TU Delft

Delft University of Technology

On the Ductility at Plastic Localisations in Steel Structures
New Insight from Routine Mechanical Test Properties

Wong, W.J.

DOI
10.4233/uuid:a0f5f105-84fa-46e2-8ea2-cc66355522ff

Publication date
2025

Document Version
Final published version

Citation (APA)
Wong, W. J. (2025). *On the Ductility at Plastic Localisations in Steel Structures: New Insight from Routine Mechanical Test Properties*. [Dissertation (TU Delft), Delft University of Technology].
https://doi.org/10.4233/uuid:a0f5f105-84fa-46e2-8ea2-cc66355522ff

Important note
To cite this publication, please use the final published version (if applicable).
Please check the document version above.

Copyright
Other than for strictly personal use, it is not permitted to download, forward or distribute the text or part of it, without the consent of the author(s) and/or copyright holder(s), unless the work is under an open content license such as Creative Commons.

Takedown policy
Please contact us and provide details if you believe this document breaches copyrights.
We will remove access to the work immediately and investigate your claim.

This work is downloaded from Delft University of Technology.
For technical reasons the number of authors shown on this cover page is limited to a maximum of 10.



WONG WEI JUN

ON THE DUCTILITY AT PLASTIC LOCALISATIONS IN STEEL STRUCTURES

New Insight from Routine Mechanical Test Properties

ON THE DUCTILITY AT PLASTIC LOCALISATIONS IN STEEL STRUCTURES

New Insight from Routine Mechanical Test Properties

PROEFSCHRIFT

TER VERKRIJGING VAN DE GRAAD VAN DOCTOR AAN DE
TECHNISCHE UNIVERSITEIT DELFT,
OP GEZAG VAN DE RECTOR MAGNIFICUS
PROF.DR.IR. T.H.J.J. VAN DER HAGEN,
VOORZITTER VAN HET COLLEGE VOOR PROMOTIES,
IN HET OPENBAAR TE VERDEDIGEN OP
DINSDAG, 16 SEPTEMBER 2025 OM 17:30 UUR

DOOR

WONG Wei jun

MASTER OF ENGINEERING IN CIVIELE TECHNIEK
IMPERIAL COLLEGE LONDON, ENGELAND
GEBOREN TE KUALA LUMPUR, MALEISIË

Dit proefschrift is goedgekeurd door de promotoren.

Samenstelling promotiecommissie bestaat uit:

Rector magnificus		voorzitter
Prof.dr.	M. Veljkovic	Technische Universiteit Delft, promotor
Dr.	C.L. Walters	Technische Universiteit Delft, promotor

onafhankelijke leden:

Prof.dr.ir.	R. Benedictus	Technische Universiteit Delft
Prof.dr.	J. Besson	Mines Paris – PSL
Prof.Dr.-Ing.	M. Feldmann	RWTH Aachen
Prof.Dr.-Ing.	A. Nonn	OTH Regensburg
Dr.	L.M. Paredes Tobar	Texas A&M University
Prof.dr.ir.	B.J. Boersma	Technische Universiteit Delft, reservelid

This research was funded by the HYSt: High Y/T Steel Joint Industry Project, and has been made possible by a financial contribution of TKI Maritime.

HYSt JIP partners: Bureau Veritas Marine & Offshore SAS, Damen Schelde Naval Shipbuilding BV, Huisman Equipment BV, Lloyd's Register EMEA, POSCO.

ON THE DUCTILITY AT PLASTIC LOCALISATIONS IN STEEL STRUCTURES

New Insight from Routine Mechanical Test Properties

WONG WEI JUN

Printed by: Ridderprint
Cover design: Flóra Kürti
Typesetting: LaTeX

A catalogue record is available from the Delft University of Technology Library.

ISBN/EAN: 978-94-6384-831-2
Copyright © 2025 by Wong Wei Jun

謹獻給父親母親。

SUMMARY

High-strength steels offer the benefit of weight, size and cost reductions in structural applications, but their use has seen limitations owing to concerns about their higher yield-to-tensile strength ratio (σ_y/σ_u) relative to lower-strength steels. A maximum limit on the σ_y/σ_u ratio is imposed as a material requirement by various steel structural design standards, product specifications and material certification rules, due to the σ_y/σ_u ratio's connection to strain hardening and the amount of plastic deformation that can be sustained without the loss of strength at locally collapsing or locally straining zones. However, the σ_y/σ_u ratio acts only as an indirect indicator of structural ductility, being one of the many factors that affect the plastic deformation capacity of a structure and whose effect and relevance vary with the structural context. This thesis hence investigates the role and applicability of the σ_y/σ_u ratio as a ductility requirement in steel design, in view of other important material and geometrical properties, with a focus on improving the assessment of ductility in steel structures, towards more efficient and confident use of steels with high σ_y/σ_u. Two mechanisms of plastic localisation that affect the structural ductility are identified as being critical to the present stipulation of σ_y/σ_u limits in design practice: local buckling in plastic hinges in stocky beams subject to bending and ultimate ductile fracture of cracked structural details.

For the plastic hinge rotation capacity of stocky beams, welded I-section high-strength steel beams are considered in this thesis, due to their widespread use in steel structures. A parametric study using a finite-element modelling approach validated by experiments in the literature, taking into account welding residual stresses, geometrical imperfections and plastic strain hardening behaviour, is performed to investigate the role of the σ_y/σ_u ratio in the plastic buckling response. Not only does the σ_y/σ_u ratio play an important role in this context, the maximum allowable σ_y/σ_u for ensuring a certain rotation capacity at a plastic hinge depends on the yield strength σ_y, the slenderness of the flange, the slenderness of the web, and the relative slenderness between the flange and web. The local ductility requirements relating to plastic hinge rotation can be made more efficient if they are made to be dependent on the σ_y, σ_y/σ_u and cross-sectional slenderness.

The maximum σ_y/σ_u ratio has also been considered to function as an indirect provision for ductility where localised tensile plastic straining is expected to occur (such as notched and cracked details). This was initially based on the concept of delaying the onset of necking instability in the structure but has subsequently come to be seen as part of a set of substitute upper-shelf toughness requirements for ensuring that the ultimate strength of structural details susceptible to cracking assumed in design can be achieved. This σ_y/σ_u requirement is implemented alongside a minimum

tensile test fracture elongation (A) and a minimum Charpy value for the avoidance of brittle fracture behaviour. However, the mechanical basis for the use of σ_y/σ_u and A in this capacity is lacking. Recently, there has been a growing trend towards the use of minimum upper-shelf Charpy energies C_v as a better upper-shelf ductility indicator, but a clear consensus on the implications of this for the use of σ_y/σ_u and A has yet to emerge. Furthermore, even C_v is not a direct measure of fracture toughness. The most direct way to assess the upper-shelf toughness is to perform fracture toughness tests, such as the pre-cracked single-edge notched bending tests, but these tests are deemed too costly and complicated to implement for general material certification purposes. Often, correlations between the upper-shelf notch toughness in terms of C_v and the fracture toughness in terms of the J-integral are used to estimate the material's fracture toughness from Charpy tests. The existing correlations, however, are predominantly based on empirical findings and have not systematically considered if and how variations in the σ_y/σ_u and A might affect the correlation between the notch toughness and the fracture toughness.

In light of this, a parametric damage-mechanics approach is used to investigate how the correlation between the notch toughness C_v from Charpy impact tests and the critical ductile fracture initiation toughness J_Q from quasi-static fracture tests is affected by changes in the fracture elongation A, yield strength σ_y and yield-to-tensile strength ratio σ_y/σ_u obtained from tensile testing. To this end, a phenomenological rate-dependent plasticity model coupled with damage and temperature effects is developed. The validity of the modelling approach is shown by its ability to simultaneously model the tensile test, the Charpy V-notch test and the precracked single-edge notched bending test. This is demonstrated for two steels, AH36 and S690QL, capturing the force-displacement responses and the characteristic ductile fracture mechanism of slant fracture in all three tests. The applicability of simplifying assumptions used to reduce the damage model complexity while maintaining its ability to simulate the mechanical response in key tests covering an important range of stress states is exemplified. The insights gained are used to reduce the calibration effort needed for the subsequent parametric study on the correlation between material certificate data (σ_y/σ_u, A, C_v), damage mechanics parameters and fracture toughness.

First, a correlation based on regression between the damage parameters and the mechanical properties from mill test certificates is found by calibrating the damage parameters assuming a range of material certiciate properties typical of S690Q steels. Then, the correlation between C_v and J_Q is assessed by simulating the single-edge notched bending test for the varying mill test certificate properties (σ_y/σ_u, A, C_v), taking into account how the damage parameters change with these mechanical properties. It is seen that although varying σ_y/σ_u and A has some effect on how the total notch energy C_v is correlated to J_Q, it does not reflect a significant effect on the ductile fracture initiation toughness but is rather associated with the fact that the C_v includes a significant portion of energy for stable ductile propagation and fracture occurring at the specimen's free surface, while J_Q primarily concerns the early, onset stage of stable ductile tunnelling behaviour at the centre of the specimen. The σ_y/σ_u and A are seen to have an even smaller effect on the correlation between J_Q and the energy (C_{vm}) dissipated up to the occurrence of the peak force in the instrumented Charpy test, in comparison with the C_v–to–J_Q correlation, especially for low C_{vm}.

As a result of the investigation of these two key mechanisms, a shift towards more context-specific ductility criteria, accounting for the structure's failure mechanism and geometry as well as properties obtained from material testing, is recommended. Additionally, the current use of σ_y/σ_u and A as part of a set of substitute upper-shelf toughness requirements has little basis, with σ_y/σ_u and A showing weak correlations to ductile fracture resistance. Instead, the use of upper-shelf notch toughness parameters like C_v and C_{vm}, which better correlate with ductile fracture initiation toughness, is recommended as a more suitable proxy for direct fracture toughness testing. Along the way, a valuable modelling approach for damage mechanics whose relevance extends beyond the present research objectives has been demonstrated, involving a calibration process that is centred around a small number of easily accessible engineering properties and realising complex fracture simulations with reduced calibration effort.

SAMENVATTING

Hoge-sterkte staalsoorten bieden het voordeel van gewichts-, grootte- en kostenreducties in constructieve toepassingen, maar het gebruik ervan loopt tegen beperkingen aan vanwege zorgen over de hogere verhouding tussen de vloeigrens σ_y en de treksterkte σ_u in vergelijking met lagere-sterkte staalsoorten. Een bovengrens voor de σ_y/σ_u-verhouding wordt opgelegd als materiaalvereiste door verschillende staalconstructienormen, productspecificaties en materiaalcertificeringsregels. Dit komt doordat de σ_y/σ_u-verhouding samenhangt met de rekversteviging en de hoeveelheid plastische vervorming die kan worden ondergaan zonder verlies van sterkte in lokaal instortende of lokaal rekkende zones. De σ_y/σ_u-verhouding is echter slechts een indirecte indicator voor de ductiliteit van een draagconstructie. De σ_y/σ_u-verhouding is één van de vele factoren die de plastische vervormingscapaciteit van een constructie beïnvloeden, zodat het effect en de relevantie van de σ_y/σ_u-verhouding variëren met de context waarin de constructiedelen zich bevinden. Dit proefschrift onderzoekt daarom de rol en toepasbaarheid van de σ_y/σ_u-verhouding als een ductiliteitseis in staalontwerp, rekening houdend met andere belangrijke materiaal- en geometrische eigenschappen. Dit wordt gedaan met een focus op het verbeteren van de beoordeling van ductiliteit in staalconstructies, waarbij wordt toegewerkt naar een efficiënter en nauwkeuriger gebruik van staalsoorten met een hoge σ_y/σ_u-verhouding. Twee mechanismen van plastische lokalisatie die invloed hebben op de ductiliteit van een draagconstructie worden geïdentificeerd als zijnde van aanzienlijk belang voor de huidige bepaling van σ_y/σ_u-limieten in het ontwerp: lokale knik in plastische scharnieren in gedrongen balken die aan buiging worden onderworpen, en ductiele breuk van gescheurde constructiedetails.

Wat betreft de rotatiecapaciteit van plastische scharnieren van gedrongen balken worden in dit proefschrift gelaste I-profiel hoge-sterkte staalbalken behandeld, vanwege hun wijdverspreide gebruik in staalconstructies. Een parametrische studie met behulp van de eindige-elementenmethode, gevalideerd door experimenten uit de literatuur en rekening houdend met lasrestspanningen, geometrische imperfecties en plastisch rekverstevigingsgedrag, is uitgevoerd om de rol van de σ_y/σ_u-verhouding in het plastische knikgedrag te onderzoeken. De σ_y/σ_u-verhouding speelt niet alleen een belangrijke rol in deze context, maar de maximaal toegestane σ_y/σ_u-verhouding voor het waarborgen van een minimale rotatiecapaciteit bij een plastisch scharnier hangt af van de vloeigrens σ_y, de slankheid van de flens, de slankheid van het lijf, en de verhouding tussen de flensslankheid en lijfslankheid. De lokale ductiliteitseisen met betrekking tot de rotatie van plastische scharnieren kunnen efficiënter worden gemaakt als ze afhankelijk worden gesteld van σ_y, de σ_y/σ_u-verhouding en de slankheid van de dwarsdoorsnede van de balk.

De maximale σ_y/σ_u-verhouding wordt ook beschouwd als een indirecte voorziening voor ductiliteit op plekken waar gelokaliseerde plastische trekvervorming wordt verwacht, zoals bij inkepingen en scheuren. Dit was aanvankelijk gebaseerd op het concept van het uitstellen van het begin van insnoering van het materiaal. Inmiddels wordt de maximale σ_y/σ_u-verhouding, samen met een minimale verlenging bij breuk A en een minimumkerfslagwaarde ter vermijding van brosse breuk, opgevat als een alternatief voor een directe breuktaaiheidseis. De breuktaaiheidseis zorgt ervoor, dat de ontwerpweerstand van ingekeepte en gescheurde constructie-elementen kan worden bereikt. Echter ontbreekt een overtuigende technische basis voor het gebruik van de σ_y/σ_u-verhouding en A in deze hoedanigheid. Recentelijk wordt het gebruik van de minimumkerfslagwaarde C_v (oftewel de minimumkerftaaiheid) bij kamertemperatuur door sommige gezien als een betere indicator voor de breuktaaiheid, maar er is nog geen consensus bereikt over de implicaties hiervan voor het gebruik van de σ_y/σ_u-verhouding en A. Bovendien is zelfs C_v geen exacte representatie van breuktaaiheid. De meest directe manier om de breuktaaiheid te beoordelen, is door breuktaaiheidsproeven uit te voeren, zoals de voorgescheurde enkelzijdige kerf-buigproef (oftewel de *crack-tip opening displacement* CTOD-proef), maar deze proeven worden als te kostbaar en ingewikkeld beschouwd voor algemene materiaalcertificering. Vaak worden correlaties tussen de kerftaaiheid in termen van C_v en de breuktaaiheid in termen van de J-integraal gebruikt om de breuktaaiheid van het materiaal te schatten op basis van kerfslagproeven. De bestaande correlaties zijn echter voornamelijk gebaseerd op empirische bevindingen en houden geen rekening met de vraag of en hoe variaties in de σ_y/σ_u en A de correlatie tussen de kerftaaiheid en de breuktaaiheid kunnen beïnvloeden.

Daarom wordt hier een benadering op basis van schade-mechanica gebruikt om te onderzoeken hoe de correlatie tussen de kerftaaiheid C_v van kerfslagproeven en de breukinitiatie-taaiheid J_Q van quasi-statische breuktaaiheidsproeven wordt beïnvloed door veranderingen in de uit trekproeven verkregen verlenging bij breuk A, vloeigrens σ_y en σ_y/σ_u-verhouding. Daartoe wordt een fenomenologisch plasticiteits- en schade-model ontwikkeld dat rekening houdt met reksnelheid, thermische verzachting en rekverzwakking. De validiteit van deze aanpak wordt aangetoond door het vermogen om de trekproef, de kerfslagproef en de CTOD-proef goed te modelleren. Dit wordt gedemonstreerd voor twee staalsoorten, AH36 en S690QL, waarbij het kracht-verplaatsingsgedrag en het kenmerkende afschuifbreukmechanisme in de drie proeven worden gesimuleerd. De validiteit van de aannames die zijn gedaan om de complexiteit van het schademodel te reduceren, zonder verlies van een goede beschrijving van het gedrag aangaande het spanningstoestandbereik dat de drie proeven betreft, wordt aangetoond. De inzichten worden ingezet om het moeizame schade-mechanica kalibratieproces, dat nodig is voor de daaropvolgende parametrische studie over de correlatie tussen materiaalcertificaatwaarden (σ_y/σ_u, A, C_v), schade-mechanica parameters en breuktaaiheid, te vereenvoudigen.

Eerst wordt een correlatie op basis van regressie tussen de schadeparameters en de materiaalcertificaatwaarden bepaald door de schadeparameters te kalibreren, uitgaande van een typisch bereik van materiaaleigenschappen voor S690Q-stalen. Vervolgens wordt de correlatie tussen C_v en J_Q bepaald door de CTOD-proef te simuleren met variërende materiaalcertificaatwaarden (σ_y/σ_u, A, C_v), waarbij rekening wordt gehouden met hoe de schadeparameters veranderen met de materiaalcerti-

ficaatwaarden. Het blijkt dat, hoewel variërende σ_y/σ_u en A enige invloed hebben op de correlatie tussen C_v en J_Q, er geen significante invloed is op de breukinitiatie-taaiheid. De invloed wordt eerder geassocieerd met het feit dat C_v een aanzienlijk deel van de energie bevat die verbonden is met stabiele scheurgroei en scheurgroei aan het oppervlak van het kerfslagproefstuk. Aan de andere kant betreft J_Q voornamelijk de initiatie van een tunnelvormige scheur die gebeurd in het midden van de proefstuk. Er wordt verder gezien dat veranderingen in σ_y/σ_u en A een nog kleiner effect hebben op de correlatie tussen J_Q en de energie C_{vm}, vooral bij lage C_{vm}. C_{vm} wordt gedefinieerd als de energie die wordt gedissipeerd tot het moment waarop de piekkracht optreedt tijdens de geïnstrumenteerde kerfslagproef.

Als resultaat van het onderzoek naar deze twee belangrijke mechanismen wordt een verschuiving naar meer contextspecifieke ductiliteitscriteria aanbevolen, waarbij het faalmechanisme en de geometrie van de constructiedelen, evenals eigenschappen verkregen uit materiaalcertificeringsproeven, worden meegenomen. Bovendien is het huidige gebruik van σ_y/σ_u en A als een alternatieve breuktaaiheideis slecht onderbouwd, aangezien σ_y/σ_u en A zwakke correlaties vertonen met breuktaaiheid. In plaats daarvan wordt het gebruik van kerftaaiheidparameters zoals C_v en C_{vm}, die beter correleren met de breukinitiatie-taaiheid, aanbevolen. Daarnaast is in dit proefschrift een waardevolle schade-mechanica-modelleringsaanpak voor complexe breuksimulaties gedemonstreerd, waarvan de relevantie verder reikt dan de huidige onderzoeksdoelen, door een vereenvoudigd kalibratieproces in te voeren dat gebaseerd is op een klein aantal gemakkelijk toegankelijke materiaalcertificeringswaarden.

CONTENTS

Summary VII
Samenvatting XI
List of Figures XVIII
List of Tables XX
Acronyms XXII
1 Introduction 1
1.1 Research objectives . . . 2
1.2 Structure of the thesis . . . 2
2 Failure modes and rules related to the yield-to-tensile strength ratio in steel structures 5
2.1 Introduction . . . 6
2.2 σ_y/σ_u limits found in rules, standards and specifications . . . 6
2.2.1 Explicit limit on the σ_y/σ_u ratio . . . 6
2.2.2 Implicit σ_y/σ_u limit arising from capacity design . . . 7
2.2.3 Design strength reduction for steels with high σ_y . . . 9
2.2.4 Use of global plastic analysis by hinge modelling . . . 11
2.3 Failure modes . . . 12
2.3.1 Tensile strain localisation . . . 12
2.3.2 Stress concentrations . . . 15
2.3.3 Ductile fracture . . . 16
2.3.4 Plastic hinges . . . 18
2.3.5 Global buckling . . . 21
2.4 Conclusions: critical areas of research . . . 22
2.5 Symbols . . . 24
3 The yield-to-tensile strength ratio and the rotation capacity of welded I-section high-strength steel beams 27
3.1 Introduction . . . 28
3.2 Rotation capacity and rotation requirements of plastic hinges . . . 29
3.2.1 The effect of the strain hardening ability on plastic local buckling and hinge rotation capacity . . . 30
3.3 Finite element model used for the parametric study . . . 31
3.3.1 Geometrical imperfections . . . 33
3.3.2 Residual stresses from welding . . . 33
3.3.3 Finite element model validation . . . 35
3.4 Parametric studies . . . 37
3.4.1 Range of material properties in the parametric study . . . 38
3.4.2 Range of geometrical properties in the parametric study . . . 38

3.4.3 Dependence of rotation capacity on σ_y and σ_y/σ_u 39
3.4.4 Dependence of rotation capacity on σ_y/σ_u and λ_p 42
3.5 Assessment of the UR I flange and web slenderness limits 44
3.6 Conclusions 47
3.7 Symbols 48
4 Correlation between material certificate data, damage mechanics parameters and fracture toughness 51
4.1 Introduction 52
4.2 The use of the Charpy notch toughness to estimate fracture toughness – limitations and challenges 54
4.3 Consistency model for viscoplasticity with damage softening and thermal softening 56
4.3.1 Plastic hardening model 57
4.3.2 Rate-dependence model 58
4.3.3 Damage model 60
4.3.4 Thermal softening model 62
4.3.5 Stress-update algorithm and return mapping for coupled thermal- and damage-softening viscoplasticity model 63
4.4 Model calibration to experiments 64
4.5 Uniaxial tensile test 67
4.6 Charpy impact tests 70
4.7 Single-edge notched bending test 71
4.8 Modelling insights 80
4.8.1 Triaxiality and Lode angle dependence (C_1, C_2 and C_3) 80
4.8.2 Softening parameters (m and D_c) 85
4.8.3 Similarities and differences between the Charpy and SENB fracture behaviour 85
4.8.4 Implications 86
4.9 Relationship between material certificate data and damage parameters 87
4.9.1 Parametric study 87
4.9.2 Regression of A and C_v on C_2 and C_3 92
4.10 Correlation between C_v and J_Q 99
4.10.1 Implications of changes in A 102
4.10.2 Implications of changes in σ_y/σ_u 105
4.11 Conclusions 105
4.12 Symbols 107
5 Conclusions and recommendations 111
5.1 Conclusions 111
5.2 Recommendations 113
A σ_y/σ_u limits found in standards, rules and specifications 117
B Stress-update algorithm for viscoplastic consistency model with damage softening and thermal softening 121

Bibliography 123
Publications 143
Acknowledgements 145

Curriculum Vitae 147

LIST OF FIGURES

Figure 2.1 Forming limit diagram. 14
Figure 2.2 Central-holed test and Central-notched test. 15
Figure 2.3 Rotation capacity definition 19
Figure 2.4 Strut buckling curve. 21
Figure 3.1 Beam boundary conditions and applied rotation. 32
Figure 3.2 Assumed residual stress distribution in welded I-beam. . . . 34
Figure 3.3 Introduction of membrane residual stresses in finite-element beam model for $\sigma_y = 890\,\text{MPa}$. 34
Figure 3.4 Simulation of experiment from Green *et al.* (2002). 36
Figure 3.5 Simulation of experiment from Lee *et al.* (2013). 36
Figure 3.6 Simulation of experiments from Yang *et al.* (2021). 36
Figure 3.7 Relationship between σ_y/σ_u and σ_y. 38
Figure 3.8 σ_y/σ_u against n_H for different σ_y. 40
Figure 3.9 R against σ_y/σ_u and σ_y. 40
Figure 3.10 Buckling modes as seen from the top. 41
Figure 3.11 Linear elastic buckling mode shapes. 41
Figure 3.12 R against σ_y/σ_u and λ_p 42
Figure 3.13 R against λ_p for $\sigma_y/\sigma_u = 0.8$; 0.89 and 0.99. 43
Figure 3.14 R against σ_y/σ_u and λ_p for $t_f = 20.0\,\text{mm}$; $t_w = 17.6\,\text{mm}$; $\lambda_w = 40.0\varepsilon$. 44
Figure 3.15 R against σ_y/σ_u and λ_f/ε for $t_f = 20.0\,\text{mm}$; $t_w = 17.6\,\text{mm}$; $\lambda_w = 40.0\varepsilon$. 45
Figure 3.16 R against λ_f for $\sigma_y/\sigma_u = 0.94$ and $\sigma_y = 690\,\text{MPa}$. 46
Figure 3.17 R against σ_y/σ_u for $\lambda_f = 10.1\varepsilon$ and $\sigma_y = 690\,\text{MPa}$. 46
Figure 3.18 R against λ_w for $\sigma_y/\sigma_u = 0.94$ and $\sigma_y = 890\,\text{MPa}$. 46
Figure 3.19 R against σ_y/σ_u for $\lambda_w = 52.5\varepsilon$ and $\sigma_y = 890\,\text{MPa}$ 46
Figure 3.20 Observed and required σ_y/σ_u against σ_y based on geometry 47
Figure 4.1 Swift-type power-law true stress-strain curve with a yield plateau. 57
Figure 4.2 Least-squares fit of rate-dependence factor R to experimental data from the literature. 59
Figure 4.3 Model parameters. 66
Figure 4.4 Experimental and simulated engineering stress-strain curves. 68
Figure 4.5 Fracture morphology in the tensile test. 69
Figure 4.6 Half model of Charpy specimen with mesh refinement . . . 70
Figure 4.7 Experimental and simulated Charpy impact force-displacement curves. 72

Figure 4.7 Experimental and simulated Charpy impact force-displacement curves. . . . 73
Figure 4.8 Fracture morphology in the AH36 Charpy test. . . . 74
Figure 4.9 Fracture morphology in the S690QL Charpy test. . . . 74
Figure 4.10 Crack length measurements from SENB tests. . . . 75
Figure 4.11 Schematic cross-section showing the crack-tip meshing. . . . 76
Figure 4.12 Half model of SENB specimen with mesh refinement. . . . 76
Figure 4.13 Experimental and simulated F-CMOD curves. . . . 76
Figure 4.14 Experimental and simulated $J - \Delta a$ curves. . . . 77
Figure 4.14 Experimental and simulated $J - \Delta a$ curves. . . . 78
Figure 4.15 Experimental and simulated Δa - CMOD curves. . . . 79
Figure 4.16 Slant fracture in the SENB test. . . . 80
Figure 4.17 Evolution of the triaxiality in key elements in the simulations. 82
Figure 4.18 Evolution of the Lode angle in key elements in the simulations. 83
Figure 4.19 σ_y/σ_u and σ_y assumed in the parametric study, based on fit to database. . . . 89
Figure 4.20 Charpy simulations of S690QL steel at $-60\,^{\circ}$C, $-20\,^{\circ}$C and $20\,^{\circ}$C. . . . 90
Figure 4.21 Average hardening slope g against σ_y/σ_u. . . . 93
Figure 4.22 Effect of varying σ_y/σ_u on the plastic strain hardening curve. 93
Figure 4.23 C_v and A against C_2 from the parametric simulations. . . . 94
Figure 4.24 C_v and A against C_3 from the parametric simulations. . . . 95
Figure 4.25 C_v and A against σ_y/σ_u from the parametric simulations. . . . 96
Figure 4.26 C_v and A against C_2 and C_3 from the parametric simulations. 98
Figure 4.27 C_2 and C_3 against C_v based on regression. . . . 99
Figure 4.28 J_Q against C_v . . . 101
Figure 4.29 J_Q against C_{vm} . . . 103

LIST OF TABLES

Table 2.1 Material factors for hollow section joint resistances from prEN 1993-1-8:2020 . . . 10
Table 2.2 Material reduction factors for ship hull girder yielding checks 11
Table 2.3 EN 1993-1-1 Cross-sectional class definitions . . . 19
Table 3.1 Range of geometrical and material properties of the beams modelled in the parametric study. . . . 37
Table 3.2 Expected σ_y/σ_u, λ_f and λ_w requirements for achieving $R = 3$ given existing classification limits. . . . 46
Table 4.1 Material parameter values for the calibrated S690QL and AH36 steels. . . . 67
Table 4.2 Uniaxial tensile test specimen properties. . . . 68
Table 4.3 Experimental and finite-element comparisons for the tensile test properties. . . . 69
Table 4.4 Experimental and simulated Charpy impact energies from the instrumented Charpy tests. . . . 71
Table 4.5 Single-edge notched bending specimen properties. . . . 71
Table 4.6 Experimental and finite-element comparisons for the SENB test. . . . 80
Table 4.7 Average triaxialities and Lode angles calculated over $0 \leq D \leq 1$ in key elements in the AH36 simulations. . . . 84
Table 4.8 Range of σ_y and σ_y/σ_u considered in the damage-mechanics parametric study. . . . 88
Table 4.9 Charpy energy values in simulations with flow stress modified to account for lower temperatures. . . . 91
Table 4.10 Fitted parameters for the regression of C_v and A on C_2, C_3 and σ_y/σ_u . . . 97
Table 4.11 Dependencies of C_v and A on C_2, C_3 and σ_y/σ_u. . . . 97
Table 4.12 Values of σ_y/σ_u for different combinations of A and C_v used for generating the simulations in the parametric study on fracture toughness from SENB testing. . . . 99
Table 4.13 Qualitative description of the strength of the interaction between the engineering parameters and material parameters. 105
Table A.1 Limits specified on the nominal values of σ_y/σ_u in design. . 117
Table A.2 Limits specified on the actual values of σ_y/σ_u obtained from testing for certification or compliance with product specification. . . . 118

Table A.3 Reduction in design strength for steels with high σ_y/σ_u in lifting appliances. 119

ACRONYMS

CMOD	Crack-mouth opening displacement
CTOD	Crack-tip opening displacement
DWTT	Drop-weight tear test
FEA	Finite-element analysis
MMC	Modified-Mohr Coulomb
SCF	Stress concentration factor
SENB	Single-edge notched bending (test)

1

INTRODUCTION

Ductility refers to the amount of plastic deformation that a structure, component or material can sustain without losing strength significantly. A structure is typically designed to fail in a ductile manner at the ultimate limit state by providing each of its components with sufficient capacity to undergo plastic deformations, such that the entire structure can achieve the design global failure load that is contingent on the sustained strength of the constituent components and materials. This could also be used to allow structural failures that happen to happen in a controlled, less catastrophic manner.

With the exception of certain contexts such as seismic and accidental limit state design, the majority of design contexts that relate to the ultimate collapse of a structure, i.e. the ultimate limit state, involves a strength-based approach. Members are sized to achieve a given minimum strength, while sufficient ductility is ensured through accompanying restrictions on the detailing and the choice of materials.

Due to the strength-based nature of the approach, the deformation-related (i.e. ductility) requirements on the materials are indirect and broad, being secondary in nature when compared to the strength criterion. They are broad in the sense that they are often applied to the material regardless of the structural context. They are indirect in a sense that rough, easily accessible engineering properties from specific material tests are often used as indicators for ductility, rather than direct measures of deformation at the structural level.

Due to the indirectness and broadness of the requirements, the actual amount of ductility that is provided in a design is not well understood in this approach. This has led to doubts on whether the present ductility requirements for structural steels are sometimes over- or under-conservative, especially with the increasing incentive to use steels which have lower ductility but higher strength than those which are traditionally used, due to technology advancements and potential weight reductions and cost benefits.

In particular, several widely used structural design standards and rules make use of ductility requirements that consist of a maximum limit on the yield-to-tensile strength ratio σ_y/σ_u of the steel and a minimum fracture elongation A obtained from the uniaxial tensile test. This is also paired with minimum Charpy impact energies C_v at specified (typically low) temperatures, meant for the avoidance of

brittle behaviour at operational temperatures. Higher-strength steels (with strength of 690 MPa and above) are sometimes found to violate the σ_y/σ_u limit, even though they might have acceptable A and C_v values and excellent strength. This calls for a clear understanding of the role of σ_y/σ_u and of how to more precisely account for the ductility of steels so that high-strength steels could be used safely with confidence.

The use of the limit on the σ_y/σ_u has its roots in its relationship to the necking behaviour in a uniaxial tensile test and its relationship to the strain hardening slope which affects plastic buckling behaviour. In general, a low σ_y/σ_u is associated with larger necking strains in the uniaxial tensile test and hence an increased amount of plastic deformation sustained before necking starts. A low σ_y/σ_u is also associated with greater strain hardening which increases the amount of deformation that can occur in plastic buckling mechanisms before significant strength is loss. However, the basis for its role as a generally applicable material requirement is lacking in the literature. Its relationship to the ultimate ductile fracture behaviour following necking has not been substantiated, and the few studies in the literature investigating fracture toughness in light of varying σ_y/σ_u have not arrived at a clear consensus on this issue.

1.1 RESEARCH OBJECTIVES

To facilitate the precise assessment of ductility and hence the safe and efficient use of high-strength steel structures, this thesis undertakes the following research objectives:

1. Quantify the role of strain hardening and σ_y/σ_u in the two main mechanisms which account for most of the motivation found in the literature for the use of the σ_y/σ_u ratio as a ductility indicator:
   a) The ductility of plastic hinges in beams.
   b) The upper-shelf toughness in details that are cracked or susceptible to cracking.
2. Develop more nuanced, context-dependent ductility criteria for plastic hinges that account for both the structure's material properties and geometrical properties.
3. Evaluate how the upper-shelf toughness in cracked details correlates with the aggregate information contributed by easily accessible material testing properties obtained from the tensile and Charpy tests, accounting for the effects reflected by variations in the combination of these properties.

1.2 STRUCTURE OF THE THESIS

Chapter 2 presents the knowledge in the literature about the use of the yield-to-tensile strength ratio as a ductility indicator. It is seen that the yield-to-tensile strength ratio is used as part of ductility considerations in various contexts and design cases involving a few distinct mechanisms. The known motivations for its

use are discussed, and two critical mechanisms (objectives 1a and 1b), to which its prevailing use as a material requirement is attributed, are identified.

Chapter 3 addresses objective 2 by studying the effect of strain hardening on the ductility capacity of plastic bending hinges as limited by the plastic buckling behaviour. Recommendations for the ductility assessment of welded I-section steel beams designed to fail plastically are given. In particular, the use of interdependent strength, strain hardening and slenderness criteria, that accounts for a trade-off between these parameters in their contribution towards the rotation capacity of the beam, is suggested in place of fixed yield-to-tensile strength ratio limits.

Chapter 4 addresses objective 3 by studying how the σ_y/σ_u and A affects the correlations between Charpy impact testing and static fracture toughness testing. For this purpose, a damage-mechanics modelling and calibration approach, which gives physical insight into the correlations, takes differences in strain rates and stress states into account, and captures the characteristic ductile fracture mechanism involved in such tests, is developed. New insights into the correlations between properties obtained from Charpy testing, fracture toughness testing and uniaxial tensile testing is found and advice is given on the the use of these properties for the assessment of ductile fracture initiation toughness.

Conclusions and recommendations towards a practicable and improved assessment of ductility in steel structures are given in Chapter 5.

2

FAILURE MODES AND RULES RELATED TO THE YIELD-TO-TENSILE STRENGTH RATIO IN STEEL STRUCTURES

This chapter is based on [1]:

W. J. Wong and C. L. Walters, 'Failure modes and rules related to the yield-to-tensile strength ratio in steel structures', *ASME 2021 40th International Conference on Ocean, Offshore and Arctic Engineering (OMAE)*, (June 21-30, 2021, Virtual, Online), ASME (The American Society of Mechanical Engineers), 2021. DOI: doi.org/10.1115/OMAE2021-61995

ABSTRACT

Upper limits on the ratio of the yield strength to the tensile strength (σ_y/σ_u ratio) and lower limits on the fracture elongation A are present in various offshore, maritime and civil engineering rules, standards and specifications for steel structures as a provision for the minimum material ductility and toughness which ensures sufficient structural ductility. In other instances, the design yield stress to be adopted in strength calculations is reduced from its nominal value if the σ_y/σ_u ratio exceeds a certain limit. Such requirements deter the use of high strength steels (nominal σ_y higher than 690 MPa), which inherently have a high σ_y/σ_u ratio. To guide subsequent efforts towards optimised and scientifically grounded σ_y/σ_u limits and wider application of high strength steels, this chapter first presents an overview of the current provisions in engineering practice relating to the σ_y/σ_u ratio and structural ductility, and it then discusses key failure mechanisms to which ductility considerations are relevant: tensile strain localisation, yielding and localisation precipitated by stress concentrations, localisation of plastic bending hinges, ductile fracture and global buckling. The reasoning behind the current provisions, the findings of previous research concerning the requirements, and the key potential areas for future research are highlighted. This chapter concludes with highlighting the two most significant and critical mechanisms that have the most impact in the use of the current ductility requirements in practice: local buckling in plastic hinges in beams and ductile fracture toughness at details susceptible to cracks.

2.1 INTRODUCTION

High-strength steels are increasingly used in construction for weight and size reduction, but they are known to have a higher ratio of yield strength to ultimate tensile strength (σ_y/σ_u ratio) than lower-strength steels. Many product specifications, rules for material certification, and design codes specify maximum allowable limits on the σ_y/σ_u ratio, which often could not be satisfied by high strength steels. This constitutes a barrier to the more widespread use of high strength steels and leads to interest in reevaluating the σ_y/σ_u requirement.

The stipulation of a maximum σ_y/σ_u ratio, together with minimum fracture elongation A, is fundamentally a ductility requirement [2–8]. These two quantities are widely used together to gauge whether the use of a material will result in ductile behaviour in the structure in general, i.e. in an arbitrary detail or member anywhere in the structure. Notwithstanding, the σ_y/σ_u ratio is the ratio of the yield strength σ_y to the ultimate tensile strength σ_u observed in a standard tensile test performed on the steel; this is a property which is specific to the standard tensile test. Therefore, the σ_y/σ_u ratio correlates to but does not directly give more fundamental material properties that relate to structural safety. Since the response behaviour which qualifies as sufficiently ductile varies for each structural configuration and failure mechanism, research on the determination of appropriate σ_y/σ_u limits, as well alternative ductility requirements, has been carried out from different perspectives and with respect to different failure mechanisms.

Hence, this chapter discusses the various σ_y/σ_u limits and related ductility requirements that have been stipulated in different contexts and forms (Section 2.2). Then, five main mechanisms are identified (Section 2.3), in which in which the ductility of the structure could be related to the σ_y/σ_u ratio obtained from the standard tensile test. Finally, Section 2.4 concludes the chapter by identifying the two most important mechanisms that have the most significant contribution towards the use of the σ_y/σ_u limit in industry practice and which subsequently become the focus of the following chapters in this thesis: buckling in plastic hinges in beams (Chapter 3) and ductile fracture (Chapter 4).

2.2 σ_y/σ_u LIMITS FOUND IN RULES, STANDARDS AND SPECIFICATIONS

2.2.1 *Explicit limit on the σ_y/σ_u ratio*

In all of the most common structural design contexts, an explicit upper limit is stipulated on the σ_y/σ_u ratio of structural steel. An extended list of such rules applied in various industries can be found in Tables A.1 and A.2 in the Appendix.

The σ_y/σ_u limit could either be stipulated on the ratio calculated from the results of the standard tensile test (Table A.1) or on the ratio based on nominal, minimum strength values (Table A.2). Where the requirement is stated in a structural design standard or in design rules, the ratio would be based on the nominal values. This is the case in the framework of Eurocode 3; σ_y/σ_u limits based on the nominal values are specified in EN 1993-1-1: 2005 [9] for the design of general steel structures, and no σ_y/σ_u requirement is specified in the related EN product specifications, e.g. [10]. An explicit σ_y/σ_u limit based on nominal strength values is also specified in Lloyd's

Register's Code of Lifting Appliances [11], though not in the Bureau Veritas Rules for the Certification of Lifting Appliances onboard Ships and Offshore Units [12].

In most other contexts, the σ_y/σ_u limits are specified in product specifications or in the material certification rules of classification societies. For example, in comparison to Eurocode 3, no limit is stipulated in the structural design standard AISC 360-22 [13], but it specifies that materials conforming to the relevant ASTM product specifications should be used. The σ_y/σ_u requirements in the ASTM product specifications [14], which are based on actual strengths, then applies.

These σ_y/σ_u limits which are evaluated on material testing results are found across a range of industries, such as:

1. Structural steel product specification for general engineering structures [14, 15].
2. Pipe specifications and standards [16–18].
3. Product specifications and class certification rules for marine and offshore steels [19–23].

The background for the stipulation of the σ_y/σ_u limits and the research on the relationship between structural ductility and the σ_y/σ_u ratio will be discussed in Section 2.3 with respect to different failure modes. Although most of these research has been done in the context of civil engineering, they give valuable insight that is no less applicable to all steel structures.

2.2.2 *Implicit σ_y/σ_u limit arising from capacity design*

Capacity design involves designing a structure so that the critical failure mode which governs is one that results in a ductile type of response. This is considered good engineering practice for structures in general, because it helps prevent sudden catastrophic collapse in extraordinary situations where the design limit of the structure is exceeded. Moreover, in the context of seismic design, capacity design is essential, because seismic design often involves allowing some degree of plastic behaviour in response to rare earthquake events, in which the ductile behaviour required for energy dissipation occurs in a controlled manner, and primary load bearing elements remain capacity-protected and undamaged [24–26].

The requirement for one failure mode to occur before another could often result in an implicit requirement on the σ_y/σ_u ratio. This is usually because the ductile failure mode involves significant yielding in the structure and is dependent on σ_y, whilst the "brittle" or sudden failure mode involves ultimate failure at areas of disturbed stress flow and is dependent on σ_u. Some typical examples are identified below. It is worth noting that some of these do not expressly prohibit the use of steels with a high σ_y/σ_u ratio; in examples 2.2.2.3 and 2.2.3, high σ_y/σ_u ratios can be achieved with appropriate choices of geometry or structural configuration.

2.2.2.1 *Capacity design in a tension member with holes*

Ductile response occurs when the yielding of the gross section occurs before ultimate failure of the cross-section with reduced area. Such provisions can be found in EN 1993-1-1 [9] and AISC 360-22 [13]. For example, in EN 1993-1-1, this is expressed as:

$$\frac{A\sigma_y}{\gamma_{M0}} < \frac{0.9 S_{net}\sigma_u}{\gamma_{M2}} \tag{2.1}$$

$$\implies \frac{\sigma_y}{\sigma_u} < 0.9 \cdot \frac{S_{net}}{S_{tot}} \cdot \frac{\gamma_{M0}}{\gamma_{M2}} \tag{2.2}$$

where γ_{M0} is the partial factor for the resistance of cross-sections; γ_{M2} is the partial factor for the resistance of cross-sections in tension to fracture; S_{tot} is the gross area of the cross-section; and S_{net} is the net area of the cross-section.

Assuming the recommended values of $\gamma_{M0} = 1.00$ and $\gamma_{M2} = 1.25$ specified in EN 1993-1-1: 2005 [9] and an upper bound of $S_{net}/S_{tot} = 1$, it can be seen that this equation results in a σ_y/σ_u limit of at most 0.72. Since when there are holes, $S_{net}/S_{tot} < 1$, it is clear that capacity design sets a stringent requirement on the σ_y/σ_u ratio. Accordingly, EN 1993-1-12: 2007 [27] and prEN 1993-1-1: 2020 [28] do not even allow capacity design for steel grades above S460.

Another aspect of the design of such tension members is the verification of the material ductility that is required to ensure that the ultimate resistance based on σ_u at the net-section can be achieved, both in the cases of smooth holes and holes with sharp cracks. This will be discussed in Section 2.3.2 and 2.3.3 below.

2.2.2.2 *Capacity design in web-bolted beam-to-column moment connections*

In web-bolted moment connections, the webs are assumed to contribute negligibly to the transfer of moments at the connection. The moments are transferred by the flanges through a force tension-compression force couple. Ductile response occurs when the plastic moment capacity (corresponding to plastic hinge formation) occurs in the beam before the flanges at the connection reach their ultimate resistance [29]. Where Z_f is the plastic section modulus of the flanges, i.e. the first moment of area of the flanges about the plastic neutral axis, and Z is the plastic section modulus of the beam, i.e. the first moment of area of the cross-section about the plastic neutral axis, this requirement for ductile response can be expressed as:

$$\frac{\sigma_y}{\sigma_u} < \frac{Z_f}{Z} \tag{2.3}$$

However, other factors such as the presence of defects, fracture toughness and quality of welding also contribute to the response of the connection. So, in practice, this is often not addressed merely by deliberate selection of steel with better σ_y/σ_u ratios or excellent toughness, which have high variability, but by careful detailing of the connection, such as the use of haunches and brackets to strengthen the connection, the reduction of the beam section to weaken the beam, or the use of welding with better fracture resistance [30]. These methods all help to ensure that inelastic action occurs in the beam rather than at the connecting interfaces.

2.2.2.3 *Capacity design in welded connections*

It is standard practice to provide full strength welding in hollow section joints, i.e. to ensure that the design resistance of the weld is greater than the design resistance of the connecting members [31, 32]. This is also a form of capacity design, in that the governing failure mode that is chosen is yielding in the member rather than fracture of the welds. In the case of fillet welds, this leads to a dependence between the required weld throat size a and the σ_y/σ_u ratio, because the strength of the welds depends on σ_y and the strength of the connecting members depends on σ_u. For example, considering a one-sided fillet weld at a T-joint subject to a tension force which is perpendicular to the weld and parallel to the web of the T, and using the directional method [32] to determine the strength of the fillet weld, the following relation arises:

$$\frac{a}{t} < \sqrt{2}\beta_w \frac{\gamma_{M2}}{\gamma_{M0}} \frac{\sigma_y}{\sigma_u} \tag{2.4}$$

where a is the size of the weld throat; t is the thickness of the web of tee; β_w is the correlation factor for fillet weld; where γ_{M0} is the partial factor for the resistance of cross-sections; and γ_{M2} is the partial factor for the resistance of welds.

The result of this is that the use of higher-strength steels lead to larger weld sizes relative to the thickness of the connected parts, where the a/t ratio could be as high as 1.73 for S960 steel. Several studies have been made towards optimising the throat thickness, and some possible reductions in throat thicknesses were suggested; however, the authors highlighted the need for further research due to the complexity of residual stresses and the non-linear relationship between the weld strength, the throat thickness and steel grade [33, 34].

2.2.3 *Design strength reduction for steels with high σ_y*

In some design rules and standards, the design yield strengths or design resistances in strength calculations involving high-strength steels are reduced from their nominal values. Although such provisions do not specify requirements on the σ_y/σ_u ratio, they are related nonetheless to the reduced ductility of high-strength steels. Three main examples are given below:

2.2.3.1 *Reduction of the resistance of hollow section joints*

A reduction of the resistance of hollow section joints is specified for steels with high σ_y/σ_u in standards addressing the design of hollow section joints, including Eurocode 3 for steel structures [27, 28, 32, 35] and standards for fixed offshore structures [36–40].

For example, prEN 1993-1-8:2020 [41] stipulates that the design resistance of joints should be multiplied by the factors shown in Table 2.1, depending on the nominal strength of the steel, and that for joint failure modes of punching shear failure and tension brace failure, the design yield strength $\sigma_{y,d}$ should not exceed $0.8\sigma_u$. The upper limit of $\sigma_{y,d} \leq 0.8\sigma_u$ is also seen in the standards for the design of offshore structures such as those by API, ISO and NORSOK [36–38], although

in these standards no further reduction factor is applied on the joint resistance for different steel grades.

Table 2.1: Material factors for hollow section joint resistances from prEN 1993-1-8:2020 [41].

Nominal stress range [MPa]	Material factor
$\sigma_y \leq 355$	1.00
$355 < \sigma_y \leq 460$	0.90
$460 < \sigma_y \leq 550$	0.86
$550 < \sigma_y \leq 700$	0.80

The reasons for these reductions in Eurocode 3 [27, 28, 32] are given by Wardenier [31]:

1. The design limit of joints that fail by plastification is defined based on a deformation limit which is given as a function of σ_y; however, disproportionately large deformations have been known to occur in joints of higher strength steels;

2. The plastic rotation capacity of higher-strength steel joints is known to be low relative to normal strength steels;

3. Capping $\sigma_{y,d}$ at $0.8\sigma_u$ allows for ample ductility in cases when punching shear failure or local yielding of brace or plate governs.

Although no explicit σ_y/σ_u limit is imposed in these provisions, it is evident that they have implications for steels with a high σ_y/σ_u ratio. These provisions could not be directly formulated in terms of σ_y/σ_u in the current framework because the joint resistances are calculated based on models where there is a horizontal yield plateau at $\sigma_{y,d}$ and no strain hardening, such as in typical yield line analyses.

2.2.3.2 *Reduction of design yield stress in lifting appliances*

Provisions for the design of lifting appliances such as EN 13001 [42], FEM 1.001 [43], and the rules by the classification societies [11, 12, 44, 45] stipulate a limit on the design yield stress $\sigma_{y,d}$ that can be utilised in strength calculations. The maximum limit is usually expressed as a fraction of the σ_u although each standard or rule might express it in slightly different ways. These are summarised in Table A.3 of the appendix. It is worth noting that lifting appliances are designed to operate predominantly in the elastic range. This limit on the of $\sigma_{y,d}$, as stated in the rules by the European Materials Handling Federation [43], is provided "to ensure a sufficient margin of safety" for steels with high σ_y/σ_u. Also, although lifting appliances are designed primarily elastically, at stress raisers such as connections and areas with changes of geometry, some inelasticity might be expected, and ductility would be required for redistribution of stresses at these areas, as in any structure.

2.2.3.3 *Reduction of design yield stress in yielding checks of ships*

The allowable stress for hull girder yielding checks in the rules for the classification of ships are subject to a material reduction factor based on the strength of the steel. The values for the material factors are very similar between the different classification societies and these are shown in Table 2.2, below [46–49]. The allowable stresses given in the rules are based on the reference case assuming steel with minimum yield stress of 235 MPa. The allowable stresses for higher-strength steels, typically up to 460 MPa, are found by dividing the reference stress by the material factor, k. The values of k are given such that the increase in the allowable stress is not proportionate to the increase in the grade of the steel. This, according to the Guidance Notes on High Tensile Steel by TSCF [50], was introduced to provide extra margin for the strength of the ship and to help account for failure modes which were not extensively considered such as fatigue. As in the case of the crane checks, these hull girder yielding checks concern global elastic behaviour, and can also help with ensuring the ductility at local stress raisers apart from giving a larger reserve strength.

Table 2.2: Material reduction factors for ship hull girder yielding checks [46–49].

Minimum yield stress MPa	k for BV, DNV, IACS CSR	k for LR	k assuming proportionate increase in design strength
235	1.00	1.00	1.00
265	-	0.92	0.87
315	0.78	0.78	0.75
355	0.72	0.72	0.66
390	0.68[2]	0.68[2]	0.60
460	0.62	0.62	0.51

[1] Intermediate values can be obtained by interpolation.
[2] BV, DNV and LR includes note for 390 MPa steel stating that 0.66 may be applied provided that a fatigue assessment as per class rules is carried out.

2.2.4 *Use of global plastic analysis by hinge modelling*

Global plastic analysis refers to the determination of design actions or forces on a structure assuming a material model which includes plastic behaviour. In general, this allows some degree of redistribution of forces to be exploited in the calculations, resulting in smaller design forces and optimised members. In the design of frames, this is commonly implemented using models where plastic rotations are concentrated at idealised hinge locations, which behave according to the moment-rotation relationship it has been assigned, although more detailed finite element modelling with finer discretisation could also be used.

Since this analysis refers only to the determination of forces based on an analytical model which is assigned an idealised material behaviour, it is justifiable only when accompanied by measures ensuring that the actual structure is able to behave in a ductile manner, as assumed. One such provision relates to the ductility of the steel itself: both the current EN 1993-1-12:2007 [27] and the latest draft of prEN 1993-1-1:2020 [28] allow the use of plastic hinge modelling only for steels up to grade S460; similarly, AISC 360-22 [13] and related ASCE guidelines [51] only recommend steels with yield stress up to 65 ksi (450 MPa). This is because high-strength steel members are known to have reduced plastic rotation capacity relative to lower-strength steels. The background and research concerning hinge-based design of high-strength steels will be discussed further under Section 2.3.4 below.

2.3 FAILURE MODES

Five failure mechanisms in which ductility considerations are relevant will be discussed in this section: tensile strain localisation, yielding and localisation precipitated by stress concentrations, localisation of plastic bending hinges, ductile fracture and global buckling.

2.3.1 *Tensile strain localisation*

Tensile strain localisation, also known as necking, is often taken as a critical limit in sheet metal forming processes, because it marks the point of plastic instability which is followed by a drop in the force and ultimately fracture. This is the fundamental, characteristically ductile mechanism that occurs at a local level in steels under tension. Accordingly, the standard tensile test, which fails by tensile strain localisation leading to ductile fracture, is widely used to give a measure of the ductility of the steel in terms of the σ_y/σ_u ratio and the fracture elongation A. However, it constitutes only one specific strain path which results in necking, i.e. uniaxial instability, amidst the various possibilities of biaxial instability. This section aims to summarise the significance of the uniaxial tensile test, and suggest the relevance of the less-considered biaxial instability.

2.3.1.1 *Uniaxial instability*

The ultimate tensile strength σ_u and the associated uniform elongation ε_u in a uniaxial tensile test corresponds to the formation of a neck. It is well known that the necking limit is dependent on the strain hardening of the material, of which the σ_y/σ_u limit is an indicator. Considère [52] derived the criterion for diffuse necking in a uniaxial tensile test as:

$$\frac{\mathrm{d}\sigma_t}{\mathrm{d}\varepsilon_t} = \sigma_t \tag{2.5}$$

where σ_t is the true stress, and ε_t is the true strain.

This is given as the point at which the rate of material hardening and the rate of geometric softening due to cross-sectional area reduction are balanced. By applying Equation (2.5), for example, to the Hollomon [53] power-hardening material law

$\sigma_t = K_H \varepsilon^{n_H}$, where K_H is the strength coefficient and n_H is the strain hardening coefficient, it can be shown that the true strain at instability equals $\varepsilon_{t,u} = n$, and the uniform elongation $\varepsilon_u = e^n - 1$. This dependence of the necking limit on strain hardening forms the basis for some of the empirical models that have been created: Yun and Gardner [54, 55] suggested empirical equations predicting ε_u from σ_y/σ_u for mild to high-strength structural hot-rolled and cold-formed steels; Bannister [56] suggested lower-bound estimates of the strain hardening exponent n_H for a range of metal alloys including high strength steels; whilst Zhu and Leis [57] suggested equations for average estimates of the σ_y/σ_u ratio based on n for pipeline steel grades.

Determining the value of ε_u is useful for describing the stress-strain models in structural analyses accounting for strain hardening, such as non-linear finite element analyses or the moment-curvature analyses used in displacement-based seismic design [58, 59]. However, as far as ductility requirements according to engineering design standards are concerned, there are usually no limits stipulated for ε_u. [1] Instead, a minimum limit is specified for the fracture elongation A, which corresponds to the complete separation of the tensile specimen following the increasing localisation of strains that begin with the onset of necking at ε_u.

The fracture elongation A is suggested [60, 61] as a better quantity to be used as an indicator of ductility than the uniform elongation ε_u, because ε_u marks specifically the point of plastic instability of the standard tensile test, but has limited comparability to the ductility of arbitrary structural configurations. The fracture elongation A is also strongly dependent on the specimen geometry, and it is an engineering strain that is calculated on the gauge length of the standard tensile test which does not reflect the true strains at failure in the material. However, in general, a high A indicates good tensile ductility and tensile toughness (specific energy to rupture) [62]. For example, Hradil and Talja [61], and Hradil et al. [63] suggested the use of a 'necking capacity', i.e. the difference between A and ε_u, as an alternative criterion for material ductility in design; and Feldmann and Schaffrath [60] considered A as a substitute measure when upper-shelf Charpy energies or fracture toughness measures are not available. These aspects will be discussed further in Section 2.3.3 on ductile fracture below. It is already worth noting that A and tensile toughness is not based cracked geometries and could only act as a very indirect indicator [64] of fracture toughness, which pertains to cracked geometries.

Another consideration relating to uniaxial instability is how after necking, the true stresses and strains deviate ever more significantly from the engineering stresses and strains of the standard tensile test. Almost all research on the tensile-test-based ductility requirements utilises finite element analyses for validation; hence, another crucial aspect is the determination of representative true stress-strain curves up to the fracture strain for use in the finite element analyses. Theoretical models exist for relating post-necking engineering stresses and strains to true stresses and strains [65], however most researchers implement a numerical, iterative method [66, 67], which proves its benefits when implementing numerical parametric studies. Also, it is worth noting that the procedure of [65] requires additional information to be measured in the experiment, including the minimum cross-sectional area and the radius of curvature after the onset of necking.

1 The minimum ε_u requirement in EN 1993-1-1 [9] has been removed in the latest draft version [28, 60].

In summary, the standard uniaxial tensile test is primarily used to obtain the following indicators:

1. σ_y: the yield strength
2. σ_u: the uniaxial tensile strength
3. σ_y/σ_u: an indicator of strain hardening, which affects the onset of local-level necking and the global-level ductility of other structural configurations
4. A: An indicator of tensile ductility and the tensile toughness (specific energy to rupture) of the material

Along with these, the gauge length must be reported and is usually kept proportional to the square root of the area, because the elongation depends on the geometry of the structure. In typical engineering design practice, ductility requirements are stipulated in terms of these quantities. Where required for numerical analyses, theoretical or numerical methods could be used to deduce the true stress-strain behaviour from the results of the standard tensile test.

2.3.1.2 *Biaxial instability*

Forming limit diagrams (Figure 2.1) are regularly used in the sheet forming industry to quantify the limits to which a metal sheet can be shaped without wrinkling, necking and tearing. Determination of the forming limits is generally well understood [68], and the forming limit strains could be found by mechanical testing or predicted by finite element analyses. Several theoretical models of the forming limits exist, such as the Swift model [69], the Hill model [70], and the Marciniak-Kuczyński model [71].

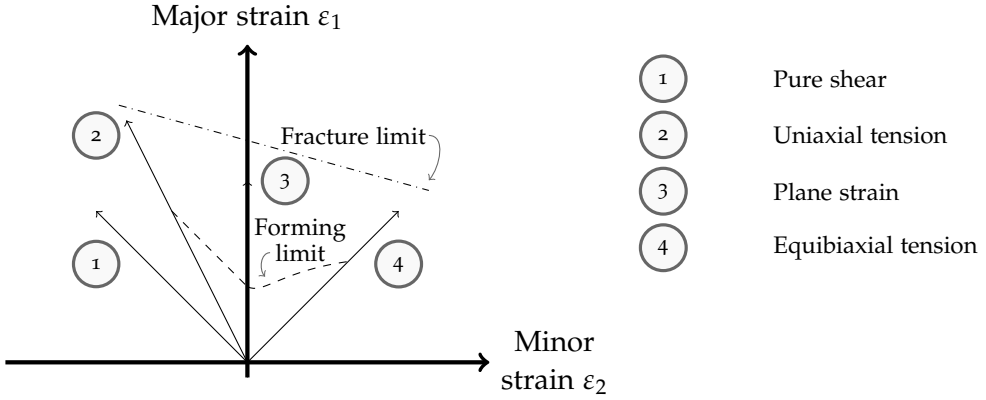


Figure 2.1: Forming limit diagram.

It can be seen that the standard tensile test, from which the σ_y/σ_u ratio is obtained, constitutes one specific strain path (i.e. $\varepsilon_1/\varepsilon_2$ ratio) leading to the necking limit (Figure 2.1), whilst the necking limits vary according to the strain path. This means that for a given material, the necking limit, and hence the equivalent σ_u, that would be obtained from biaxial loading could be expected to be different from that obtained from uniaxial tension, ultimately leading to a different equivalent σ_y/σ_u.

2.3.2 *Stress concentrations*

Details such as corners, holes, cut-outs, welded connections and notches are geometrical stress raisers that often experience plastic strains even before the yielding limit state of the global, structural member level is reached. Ductility is required at these areas to allow the redistribution of these stresses and to maintain the local load bearing capacity. In many steel design standards including the European EN 1993-1-1: 2005 [9] and the American AISC 360-22 [13], it is implied that the requirements on the σ_y/σ_u ratio and A, combined with the prevention of lower-shelf behaviour though Charpy V-notch toughness testing, are sufficient to ensure that the ultimate strength could be achieved and maintained at these locations.

A key structural configuration involving such local ductility is the tension member with an area reduction, and this has been a focus of the research relating to σ_y/σ_u in the European engineering community. There are two general conditions for this configuration: cases without sharp notches and cases with sharp notches due to fatigue cracking or severe manufacturing defects. These could respectively be represented by the central-holed test and central-notched test (Figure 2.2), which have been used as the reference components for a basis of comparison to other geometries [72]. This section concerns the unnotched case; the case with sharp notches will be discussed in Section 2.3.3 below. A similar consideration also applies to the design of beams with holes in the tension flanges [13, 73].

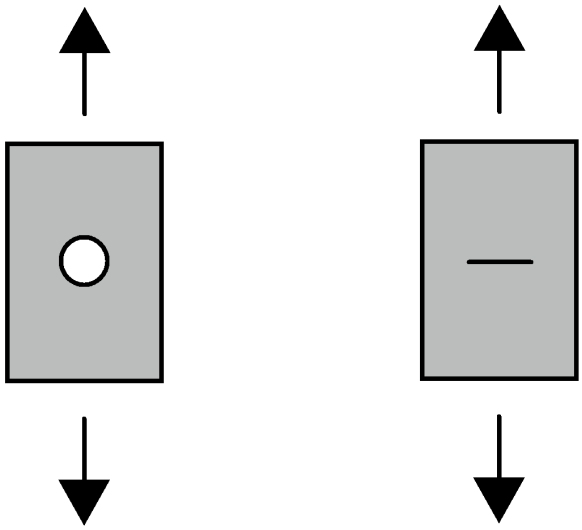


Figure 2.2: Left: Central-holed test; Right: Central-notched test.

In the current EN 1993-1-1: 2005 [9], the capacity of the tension member is found as the lower of:

$$\text{Design plastic resistance of the gross cross-section} = \frac{S_{tot}\sigma_y}{\gamma_{M0}} \tag{2.6}$$

$$\text{Design ultimate resistance of the net cross-section} = \frac{0.9S_{net}\sigma_u}{\gamma_{M2}} \tag{2.7}$$

This has been the subject of research for two major reasons: First, achieving the ultimate resistance at the net section as given by Equation (2.7) is based on the

assumption that the requirements on the σ_y/σ_u ratio, the uniform elongation and the fracture elongation ensure sufficient ductility is provided to sustain localised yielding at areas of stress concentrations, and the suitability of these assumptions has been questioned [60, 72]. Second, where capacity design is implemented, the requirement that the gross section of the tension member yields before the net section reaches ultimate failure places a tight requirement on the σ_y/σ_u ratio that could not be typically satisfied by high-strength steels. It is worth nothing that both the current EN 1993-1-12 [27] and the latest draft of prEN 1993-1-1: 2020 [28] incorporating steel grades up to S700 do not allow the use of S460 grades and above for use in capacity design. This can be related to the concerns on the limited deformation capacity that is seen in high-strength steel structures, which is discussed in Section 2.3.4 below.

Many of the stipulated σ_y/σ_u limits today (Tables A.1 and A.2) are similar to the value of 0.95 recommended by Dhalla and Winter [74] in 1974, from plane-stress bilinear-material finite-element analyses of plates with circular holes and side notches. This was in essence based on the grounds of delaying necking sufficiently to ensure a minimum level of ductility, and post-necking behaviour and fracture toughness were neglected in these considerations. A study by Može [75] involving central hole tests on S690 steel found that the use of Equation (2.7) is very conservative for unnotched cases and that the 0.9 factor could be dropped. Feldmann et al. [33] further studied the σ_y/σ_u and elongation limits in relation to central-holed tension test by carrying out parametric studies with damage mechanics models calibrated to tests performed on S700 and S960 steel, and found that even for σ_y/σ_u ratios as high as 0.97 and ε_u as low as 0.03, the full bearing capacity of the net section (i.e. without the 0.9 factor) is reached, and that occurs before the onset of ductile material damage. Similarly, experiments and numerical simulations of S690 and S1100 steel in blunt-edged notched tensile tests by Stofregen [76] also saw the onset of ductile damage occurring after the maximum tensile force was achieved.

Based on these findings, the ultimate tensile strength at net sections for the unnotched case has been updated in the latest draft of EN 1993-1-1: 2020 [28] such that the 0.9 factor has been omitted, although the factor remains important for cases with sharp notches. Furthermore, since the ultimate strength is reached before any ductile material damage occurs, these observations suggest the relevance of investigating the localisation of strains and associated stress field around smooth, unnotched stress concentrations analytically [77]. Feldmann et al. [72], from the outcome of their damage-based approach to central-holed tests, also noted that the localisation leads to the exhaustion of the strainability, and the implementation of damage models is not necessary for determining the ultimate strength of holed tensile specimens without cracks, although it could be useful for studying the post-necking behaviour.

2.3.3 *Ductile fracture*

It has been established in the previous sections that in the standard uniaxial standard test and the central-holed test representative of smooth geometrical stress raisers, ductile fracture follows after the point of instability due to the increasing localisation of strains in a necking area. The strength in these cases is then dominated by the

onset of tensile strain localisation rather than the point of fracture. However, a sharp notch, such as that caused by fatigue cracking or a severe manufacturing defect, results in an extreme state of stress concentration when loaded, which could lead to loss in strength due to crack growth, such that the ductile fracture failure mode determines the ultimate strength in cases with sharp notches.

As mentioned, the central-notched test is a key reference configuration for this condition and can be taken as a representative example for discussion. In central-notched tests, the ultimate tensile stress falls short of the uniaxial tensile strength given by the standard tensile test. This is the origin for the 0.9 factor that is seen in Equation (2.7), which was introduced based on considerations of tension tests of bolted connections and fracture mechanics safety assessments [78]. Accordingly, this is also the origin of the σ_y/σ_u limit of $1/1.10 = 0.91 \approx 0.9$ in EN 1993-1-1 [9]. Given the fracture strength criterion of $\sigma_{frac} = 0.9\sigma_u$, a minimum σ_y/σ_u of 0.9 is stipulated so that yielding of the net-section would occur reached before the fracture of the net-section [78].

However, it was also noted by Sedlacek et al. [78] that the fracture strength criterion of $\sigma_{frac} = 0.9\sigma_u$ is based on the assumption that the upper-shelf toughness is sufficient for all situations regardless of the size of the crack relative to the cross-section of the tension member, while no explicit requirement is stipulated for the upper-shelf toughness. Along these lines, Feldmann and Schaffrath [60] investigated the relationship between the ultimate strength achieved in central-notched tests as a function of the σ_y/σ_u ratio and the upper-shelf Charpy impact energy C_v which they took to be a measure of upper-shelf toughness. Based on their findings, they suggested minimum upper-shelf Charpy impact energy values to be included as a ductility requirement. Nonetheless, recognising the industry's likely reluctance to accept such a change, they identified A as a substitute for a more direct criterion on the upper-shelf toughness. Accordingly, the minimum required A has been updated from 10 % to 12 % in the latest draft of prEN 1993-1-1: 2020 [28]. However, A remains an indirect indicator for fracture toughness, corresponding to the total strain energy density from unnotched tensile tests and predominantly involving relatively low stress triaxialities [79], unlike in pre-cracked geometries.

It is worth noting that, in a similar vein, upper-shelf Charpy impact testing is used in the pipeline industry to obtain an estimate of the dynamic crack propagation energy and hence, indirectly, the ductile fracture propagation resistance. In this context, a minimum notch toughness (indicated by C_v) necessary for arresting a running ductile crack is used as a design requirement, and research to obtain an better assessment of the crack arrest toughness is ongoing [80].

Some work has been done on the role of the σ_y/σ_u ratio in relation to ductile fracture, but the literature lacks consensus on the implications of the findings on its use as an ductility indicator in design considerations. For example, although Feldmann and Schaffrath [60] indicate that a higher σ_y/σ_u leads to increased net section resistance relative to the ultimate tensile strength in centrally notched tensile tests, Nonn et al. [81] and Lu et al. [82] indicate that a higher σ_y/σ_u leads to decreased crack arrest toughness.

With respect to the use of C_v to estimate the upper-shelf fracture toughness of the material as suggested by Feldmann and Schaffrath [60] and introduced in the latest draft of EN 1993-1-10 [72, 83], although many studies and proposed

correlations exist [84–94], the role of σ_y/σ_u in these correlations has not been systematically studied, and the existing correlations have been developed using predominantly empirical methods, due to modelling complexities associated with using an analytical-numerical approach (e.g. damage mechanics and flow plasticity) to accurately simulating the ductile fracture behaviour throughout the duration of both the dynamic Charpy and static fracture tests on a given material.

2.3.4 *Plastic hinges*

2.3.4.1 *Frames*

The concept of plastic hinges first arose in the analysis of the collapse of beams and frames under bending. Observing a fixed-ended beam loaded to collapse, Kazinczy [95] identified regions of intense deformation, which acted like pin joints, as plastic hinges. He noted that the total collapse of the beam did not happen at the formation of the first hinge, but only when sufficient hinges were formed to result in a structural-level mechanism. This consideration of consecutive formation of hinges could also be applied to more elaborate frames, and it allows the redistribution of forces and the analysis of collapse mechanisms to determine the ultimate load at collapse. Since it could be applied to an arbitrary frame, this form of plastic analysis has found a wide range of applicability including, for example, the derivation of the IACS UR I [96] plastic framing requirements for polar ships [97, 98].

Besides noting the possibility of second-order effects at large structural deformations, it is important to realise that the consecutive formation of plastic hinges up till total collapse is based on the premise that the hinges are capable of maintaining those rotations without losing their strength due to local buckling at the cross-section. The ability of the joints to maintain their strength to large rotations is called the ductility of the joint, and could be quantified through the rotation capacity or curvature capacity, as shown by Figure 2.3 and Equation (2.8) to (2.9):

$$R_\kappa = \frac{\kappa_{rot}}{\kappa_{pl}} - 1 \tag{2.8}$$

$$R_\theta = \frac{\theta_{rot}}{\theta_{pl}} - 1 \tag{2.9}$$

The behaviour and ductility of the joints depends on the cross-sectional and material properties of the frame element, including the strain hardening of the material [99]. This is why the requirements on the σ_y/σ_u ratio have been investigated in the context of plastic hinges. It is well known that a high σ_y/σ_u ratio leads to a decreased rotation capacity at plastic hinges [7, 100–109], and σ_y/σ_u limits have been proposed based on this consideration (e.g. 0.91 in Steenbergen et al. [102], the same value as is used in EN 1993-1-1 [28]). However, this effect is not rigorously captured in the plastic design provisions of typical strength-based design codes such as EN 1993-1-1: 2005 [9] and EN 1993-1-12: 2007 [27], because in these codes, the ductility of the cross-sections is assessed based on broad classifications (Table 2.3). Strain hardening is not directly accounted for in the calculation of the bending resistance of the cross-section, and there is no provision for the explicit quantification of the rotation capacity of the cross-section. The ductility needed for the formation

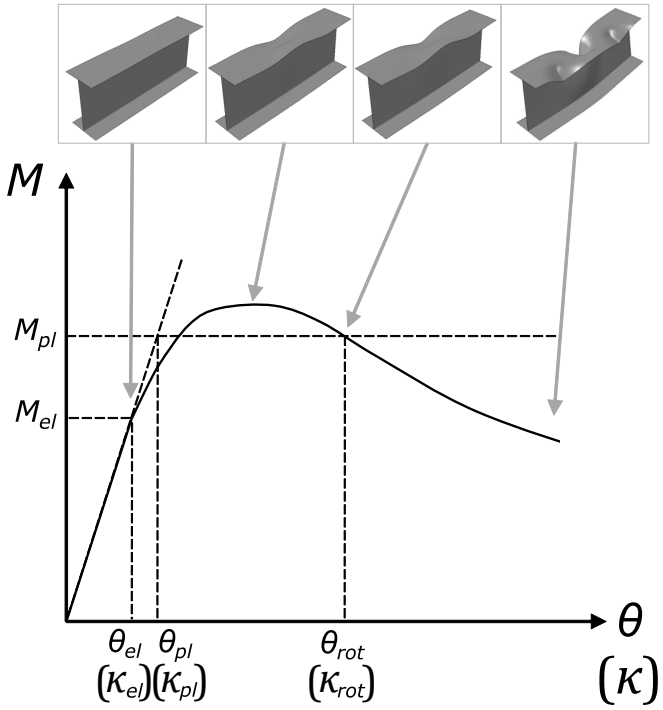


Figure 2.3: Rotation capacity (with deformation due to the application of uniform moment as example).

of an assumed plastic mechanism is accounted for by requirements such as: the cross-section at plastic hinges are to be classed 1; the location of the plastic hinge are to be laterally restrained; the tensile-test-based ductility requirements on σ_y/σ_u and A are to be satisfied; and the steel grade is not to be above S460. This constitutes a barrier to the more widespread use of high strength steels and hence the ductility capacity of plastic hinges and related requirements such as the σ_y/σ_u ratio is still being researched to this day [107, 108, 110, 111].

Table 2.3: EC3 [9] class definitions

Class	Definition
1	Forms a plastic hinge with the rotation capacity and strength required from plastic analysis of the global structure
2	Develops plastic moment resistance but have limited rotation capacity due to local buckling
3	Extreme fiber of cross-section reaches the yield stress, but local buckling prevents development of plastic moment
4	Local buckling occurs before the attainment of yield stress

Although the strength calculations in EN 1993-1-1: 2005 do not depend on strain hardening, the determination of the appropriate classification limits in EN 1993-1-1 are affected by strain hardening and hence the σ_y/σ_u ratio. Wang [112] and Taras et al. [113] reinvestigated the classification limits in light of the properties of high strength steels and proposed more stringent limits, and accordingly, some of the

classification limits have been updated in the draft prEN 1993-1-1: 2020 [28] which account for steel grades up to S700. Pavlovic and Veljkovic [114] investigated the required σ_y/σ_u limits which would be required for hollow-section steels beams up to S960 to achieve the Class 1 and 2 limits of the current EN 1993-1-1:2005 [9] and found that maximum σ_y/σ_u limits as low as 0.77 and 0.91 respectively might be needed. Studer and Taras [115] performed a similar study with focus on the transition between EN 1993-1-1 [9] Class 2 and 3 designations for welded I-section beams and proposed a method to find σ_y/σ_u-dependent cross-sectional slenderness limits for this transition.

From the discussion above, it can be seen that there are certain advantages of moving towards a strain-based design framework for the plastic design of frames which would allow for more convenient consideration of strain hardening effects and determination of deformation capacities. Such frameworks are more commonly applied in displacement-based seismic design, in which ductility is essential. In these cases, the limit states are defined in terms of strains, material behaviour accounting for strain hardening is defined, and the strength of the cross-section is found from moment-curvature analysis of the cross-section.

Recognising certain shortcomings of the classification-based design system, Gardner and Nethercot [116, 117] introduced the continuous strength method in 2004 for structural stainless steel design. In this method, the critical local buckling strain is given as a function of the cross-sectional slenderness. Like the aforementioned approaches used in seismic design, this method has the advantage that strain hardening and hence σ_y/σ_u ratio can be more directly accounted for, and that the deformation in the cross-section can be conveniently found from the strains. This method had first and foremost been developed for the design of stainless steels, but it was identified to be also particularly relevant to high-strength steels, which often exhibit hardening behaviour without yield plateaus similarly to stainless steels. Research extending the applicability of the continuous strength method to high strength steels by Lan et al. [118, 119] found more accurate and consistent prediction of strengths than other traditional codified methods.

2.3.4.2 *Plates*

The concept of a plastic point hinge in frame elements can be extended to that of a hinge-line for application to plates. The hinge-line is then a line about which large plastic rotations occur, as in a folding mechanism. This methodology was first developed in the context of concrete slab design [120, 121], but has since seen a very wide scope of application, examples of which are the analysis of basic folding mechanisms [122, 123] in the crushing of box columns [122], the failure by chord plastification [32, 124] in hollow section joints [32], and the ultimate strength of plates in ship hulls and decks [125–127]. However, in many cases, the hinge-lines used in limit analyses of the collapse state assumed rigid plastic material properties, so not much research has been done on the relationship between the ductility capacity of plates under bending and the strain hardening or the σ_y/σ_u ratio. As was seen in the plastic hinges in frames, the σ_y/σ_u ratio may be an indicator for the ductility of plates under bending, although the actual behaviour would depend on the boundary conditions and the presence of stabilising membrane behaviour.

2.3.5 *Global buckling*

2.3.5.1 *Buckling of struts under axial compression*

An ideal strut made of linear elastic material under axial compression buckles at the critical Euler buckling load, which depends on the slenderness of the strut ('elastic buckling' in Figure 2.4). An ideal strut made of an elastic - perfectly plastic material might experience yielding and plastic squashing even before the elastic buckling stress is reached if it has low slenderness ('plastic squashing' in Figure 2.4). But in a realistic strut, which not only has non-linear elastoplastic material properties but also geometric imperfections, yielding and buckling interact, and the strut may buckle at loads lower than that given by either of the ideal situations given above ('experimental points' in Figure 2.4).

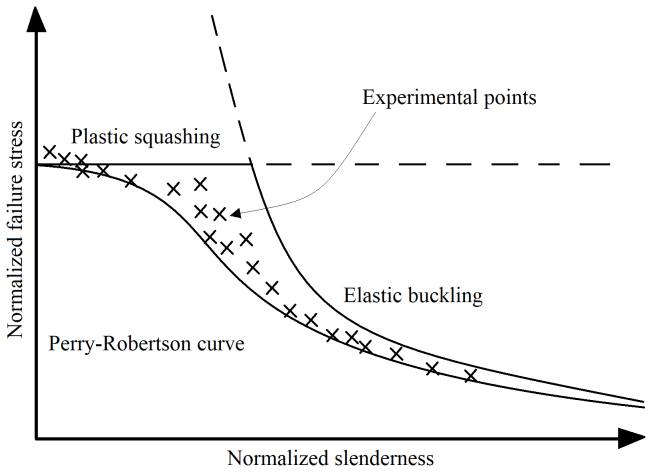


Figure 2.4: Strut buckling curve (adapted from [128]).

Strain hardening comes into effect in inelastic buckling which occurs in struts of low slenderness. As illustrated in Figure 2.4, inelastic buckling of real struts with material hardening may plot above the plastic squashing line of the perfectly plastic material. Although methods which could include strain hardening behaviour in global buckling considerations exist, such as the Engesser tangent modulus theory [129] and Shanley buckling theory [130], the effects of strain hardening is generally not included in the global buckling checks in design standards. This is because the strain hardening comes into effect at low slenderness, at which inelastic global buckling occurs, and yielding precedes inelastic buckling. Yielding is taken as the limit state because beyond yield, large deformations start to occur. To avoid large deformations, the strength is conservatively capped at the yield strength. There is generally no intention to utilise the strain hardening and no implied use of ductility or large deformations, and so there is no requirement relating to the σ_y/σ_u ratio for global buckling checks in typical design practice.

However, the other aspects of strut buckling unique to high-strength steel members are worth mentioning. In general, high-strength steel struts have better resistance to global buckling under axial compression that lower-strength steels, due to the reduced effects of residual stresses and global geometric imperfections [131].

The latest draft of prEN 1993-1-1: 2020 [28] accounts for this effect to some degree by specifying a set buckling curves for steels below S460 grade, and a different set of curves for steels of grade S460 up to S700, whilst the AISC 360-22 [13] code gives only one buckling curve for all steel grades. Hence, recent research on global buckling of high strength steels has been focused on methods to better incorporate the yield strength dependence, and modifications have been proposed which involve the use of buckling curves which vary continuously with the yield strength [132, 133].

2.3.5.2 *Lateral torsional buckling*

Typical design practice such as in EN 1993-1-1 [9] and AISC 360-22 [13] de-couple the calculations of the local buckling resistance of cross-sections and the lateral torsional buckling resistance of members; this is a valid and widely accepted practice. Nonetheless, it is known that there is interaction of local buckling and lateral torsional buckling in the inelastic range, and concerns have been raised about the applicability of this de-coupling to high-strength unrestrained steel beams in cases where plastic hinge ductility and rotation capacity are required [134, 135]. Some work has been done on the modelling interaction between local and lateral torsional buckling, in which strain hardening is accounted for [134, 136], and the importance of the σ_y/σ_u ratio to the interaction was also identified [137]. However, due to the complexity of the interaction, the practice to use standardised design frameworks to consider interactions between lateral torsional buckling and local buckling has in general not taken off (apart from full non-linear finite analyses which naturally does). In practice, concerns about the impact of this interaction on the ductility capacity of plastic hinges are eliminated by simply ensuring that areas which are designed to act as plastic hinges have sufficient lateral restraint so that lateral torsional buckling cannot happen [9]. It is also worth noting that in EC3, there is an option of applying a so-called 'general method', which has been shown to be suitable for analysing cases for combined stability issues of lateral and torsional buckling as seen in asymmetrical open sections [138, 139].

2.4 CONCLUSIONS: CRITICAL AREAS OF RESEARCH

The σ_y/σ_u ratio is used together with the fracture elongation A and minimum brittle-fracture-avoidance Charpy C_v values in current standard practice as an indirect criterion for the minimum material ductility and toughness which ensures sufficient structural ductility. Structural ductility includes both the ductility at local stress raisers which is required for distribution of stresses and aversion of premature failure at these locations, and the ductility in the global plastic mechanisms by which the structure is designed to fail.

From the rules (Section 2.2) and failure modes (Section 2.3) identified in this chapter, key trends regarding the motivations for the use of σ_y/σ_u in the industry can be highlighted. The current σ_y/σ_u limits stipulated in EN 1993-1-1 and EN 1993-1-12 [9, 27, 28] are found to be most closely linked to and influenced by the consideration of the rotation capacity at plastic hinges in beams [102, 114] (as described in Sections 2.2.4 and 2.3.4) and the upper-shelf toughness required at

structural details susceptible to cracks [60, 72, 78] (as described in Sections 2.3.2 and 2.3.3).

Notably, providing sufficient rotation capacity in plastic hinges is given by the background document to EN 1993-1-10 [72] as a reason to maintain the specification of the yield-to-tensile strength ratio in EN 1993-1-1 [9, 28]. For example, the σ_y/σ_u limit of 0.91 prescribed in the latest draft of EN 1993-1-1 [28] for the design by global plastic analysis agrees with the recommendation by Steenbergen et al. [102], which is derived from a cross-sectional treatment of classic beam mechanics and then-codified limits on the strain at uniform elongation [140]. However, this treatment neglected the role of plastic local buckling, which is a strong determinant of the ultimate failure behaviour of the hinge [99]. Recent work on the topic has been limited to hollow-section beams [114] and the transition between Class 2 and 3 designations for welded I-section beams [115]. Therefore, Chapter 3 investigates how the rotation capacity of stocky (Class 1) welded I-section beams is affected by changes in yield strength, strain hardening ability and cross-sectional slenderness in a parametric study. The σ_y/σ_u requirement is assessed together with the slenderness requirements and the yield strength σ_y, suggesting the possibility of more efficient use of high σ_y/σ_u steels when the interdependence of these variables has been accounted for.

In addition, the maximum σ_y/σ_u limit, together with the minimum fracture elongation A and minimum Charpy impact energies C_v for the avoidance of brittle fracture, is viewed as part of a set of substitute upper-shelf toughness requirements for ensuring sufficient local ductility at details that are cracked or susceptible to cracking [60, 72]. Recent research questions the mechanical basis and the suitability of the use of this set of requirements [60]. The recommended σ_y/σ_u limit can be traced back to considerations which use the uniaxial test's uniform elongation, corresponding to necking, as a critical limit state, ignoring post-necking and fracture behaviour [74] which is significant. Relatively little research has been performed on the role of σ_y/σ_u in fracture toughness considerations, and there is a lack of consensus on the implications of the findings [60, 81, 82]. The use of requirements based on the upper-shelf (instead of brittle-fracture-avoidance) C_v values, which correlate strongly to the fracture toughness, has been suggested [72, 83], but the current correlations between upper-shelf C_v and fracture toughness in use are predominantly empirical, lacking detailed mechanistic insight, and the role of σ_y/σ_u in these correlations is once again unclear. A is viewed as an indirect indicator, predominantly associated with relatively low triaxialities and significant tensile straining energy, and this differs from that which is prevalent in fracture testing, such that the role of A in this set of substitute local ductility requirements is also insufficiently clear. In view of these issues, Chapter 4 develops a simplified modelling and calibration approach for damage-plasticity modelling to investigate the correlations between upper-self C_v and the fracture toughness from single-edge-notched-bending fracture testing, taking into account variations in σ_y/σ_u, A and correspondingly varying damage-mechanics material parameters.

By addressing the two most critical mechanisms relating to the σ_y/σ_u limit and the accompanying set of ductility requirements, useful insight regarding the blanket use of σ_y/σ_u limit as an intrinsic material requirement (Tables A.1 and A.1) in the context-dependent question of structural ductility can be derived. The σ_y/σ_u limit

pertaining to plastic buckling, and the correlations between the C_v, fracture toughness, σ_y/σ_u and A, is discussed in depth in Chapters 3 and 4, respectively. Finally, overall conclusions and recommendations regarding local ductility requirements in structural steel design, steel product specification and material certification are given in Chapter 5 in view of these findings.

2.5 SYMBOLS

Latin

A	Fracture elongation over the proportional gauge length from pieced-together tensile test fragments
a	Size of weld throat
k	Material factor for ship hull girder yielding checks
K_H	Strength coefficient of the Hollomon hardening rule
K_{Ic}	Critical plane-strain fracture toughness
M_{el}	Moment at first yielding
M_{pl}	Fully-plastic bending moment
n_H	Strain hardening exponent of the power-hardening material law
S_{tot}	Gross area of cross section
S_{net}	Net area of cross-section
t	Thickness of web of tee
Z	Plastic section modulus of beam
Z_f	Plastic section modulus of beam flanges

Greek

β_w	Correlation factor for fillet weld
γ_{M0}	Partial factor for the resistance of cross-sections
γ_{M2}	Partial factor for the resistance of welds or of cross-sections in tension to fracture
ε_u	Uniform elongation
ε_t	True strain
$\varepsilon_{t,u}$	True strain at uniform elongation
θ	Cross-sectional rotation
θ_{el}	Cross-sectional rotation corresponding to M_{el}
θ_{pl}	Cross-sectional rotation corresponding to M_{pl} and assumed linear material behaviour
θ_{rot}	Cross-sectional rotation when M falls below M_{pl}
κ	Cross-sectional curvature
κ_{el}	Cross-sectional curvature corresponding to M_{el}
κ_{pl}	Curvature corresponding to M_{pl} and assumed linear material behaviour

κ_{rot}	Cross-sectional curvature when M falls below M_{pl}
σ_y	Yield stress
σ_u	Ultimate tensile stress
σ_t	True stress
$\sigma_{y,d}$	Design yield stress used in strength calculations
σ_{frac}	Average net section fracture stress from cracked tensile tests

3

THE YIELD-TO-TENSILE STRENGTH RATIO AND THE ROTATION CAPACITY OF WELDED I-SECTION HIGH-STRENGTH STEEL BEAMS

This chapter is reproduced from [141]:

W. J. Wong and C. L. Walters, 'Effect of strain hardening on the rotation capacity of welded I-section high-strength steel beams', *Ships and Offshore Structures*, pp. 1–16, 2023. DOI: 10.1080/17445302.2023.2195727

ABSTRACT

High-strength steel beams are known to have less plastic rotation capacity than beams with lower yield strengths. This has been related to the decreased strain-hardening ability of high-strength steels, and various rules and standards for steel structures stipulate maximum limits on the allowable yield-to-tensile strength ratio (σ_y/σ_u), which indirectly acts as a measure of strain hardening. While the literature suggests that there is an interdependence between strain hardening ability, yield strength, cross-sectional slenderness and rotation capacity, the presently prescribed limits on σ_y/σ_u (e.g. 0.91, 0.94, 0.95) are typically constant for a given material regardless of the other parameters mentioned. This computational study hence investigates how the rotation capacity is simultaneously dependent on yield strength, strain hardening ability and cross-sectional slenderness, and how each parameter affects the relationship between the others. The results show that, with the geometrical aspect kept constant through the use of normalised slenderness parameters, a higher yield strength leads to higher rotation capacity for a given σ_y/σ_u, while the well-known decrease of rotation capacity with higher σ_y/σ_u is confirmed. This suggests the possibility of more efficient use of high-strength steels with high σ_y/σ_u when the interdependence of all the variables are accounted for. The results also suggest the importance of accounting for the relative slendernesses of the web and the flange and whether the buckling behaviour is web- or flange-dominated, since a switch between a web- and flange- dominated buckling response could lead to a reverse in the trend between the rotation capacity and the overall cross-sectional slenderness.

3.1 INTRODUCTION

High-strength steels are increasingly used in the construction of ship and offshore structures due to their potential for reducing the weight and size of structural elements. However, such steels are known to have lower ductility, smaller reserve strength after yielding and reduced strain hardening ability relative to conventional lower-strength mild steels [4]. They are also associated with a higher tendency to localise around stress concentrations [77]. A description of the influence of the hardening capacity (frequently indicated by the yield-to-tensile strength ratio σ_y/σ_u) on four failure modes can be found in Wong and Walters [1]. Risks of these failure modes remain a concern in the application of high-strength steels, and to account for this, various offshore, maritime and civil engineering rules, standards and specifications for steel structures stipulate requirements based on the σ_y/σ_u ratio (Appendix A) and the fracture elongation. Specifically, European norms for the design of steel structures impose upper bounds of 0.91 [9, 28] and 0.95 [27, 28]. A similar value of 0.94 is stipulated in the rules for the certification of high-strength shipbuilding and offshore steels by classification societies [19–21].

Given the aforementioned benefits of using high-strength steels, efforts have been made to find improved rules to account for ductility, so that higher-strength steels might be used with confidence. For example, recommendations on the acceptable σ_y/σ_u ratio in structures have been given based on considerations of the toughness, strength and deformation capacity of pressure vessels and pipelines [4], tubular joints [2] and ties containing cross-sectional area reductions [60, 72, 74, 78]. However, the aforementioned limits of 0.91 [9, 28] and 0.95 [27, 28] correspond to recommendations which arise from the consideration of the rotation capacity at plastic hinges for steels with high σ_y and σ_y/σ_u ratios [60, 102, 114].

Although the dependence of the rotation capacity on σ_y/σ_u has been further evidenced by the work of several researchers on the topic [7, 104, 106–109], the relationship between σ_y/σ_u and the rotation capacity has yet to be quantified and explained definitively. The σ_y/σ_u limit of 0.91 prescribed in the latest draft of EN 1993-1-1 [28] for the design by global plastic analysis agrees with the recommendation by Steenbergen et al. [102], which is derived from a cross-sectional treatment of classic beam mechanics and then-codified limits on the strain at uniform elongation [140]. However, this treatment neglected the role of plastic local buckling, which is a strong determinant of the ultimate failure behaviour of the hinge [99]. Recent attempts have been made to determine the σ_y/σ_u limit appropriate for high-strength steel grades up to S960 based on experimentally-validated finite-element parametric studies considering buckling effects [114], which resulted in recommendations for more stringent σ_y/σ_u limits by the authors, but these analyses were specific to hollow-section beams.

Furthermore, the context of the existing research [105, 114] is a framework which makes use of broad, discrete cross-sectional classes to differentiate between levels of beam deformation capacity, such that the required σ_y/σ_u limit was investigated with particular focus on its relation to the separate flange and web slenderness ratios required to achieve a minimum rotation capacity. This separate classification of flange and web neglects the interactive effect between the constituent plates, and the approach of specifying a minimum rotation capacity corresponding to

a broad, discrete definition of a ductility class is not conducive for describing the full continuous relationship between σ_y/σ_u and rotation capacities. Recent developments in the design of steel beam-columns have seen the use of a strain-based framework capable of estimating the strengths and deformation capacity of stocky cross-sections above the fully-plastic bending moment M_{pl} based on regression analysis of critical buckling strains dependent on overall cross-sectional slenderness derived from finite element and experimental data [117, 119], but these critical buckling strains themselves were not analysed for their dependence on the strain-hardening behaviour. To explore the limits of acceptable σ_y/σ_u ratios dependent on both the strain hardening and overall cross-sectional slenderness, this computational study investigates how the rotation capacity varies simultaneously with the yield strength σ_y, the σ_y/σ_u ratio which is used to characterise strain hardening (Section 3.2.1), and the overall cross-section slenderness λ_p, which accounts for relative web and flange slendernesses.

This study employs parametric finite element analyses of the bending of stocky I-section beams with varying material properties and geometries to describe the relationship between varying yield strengths, strain-hardening behaviours, and achievable rotation capacities in welded high-strength steel I-section beams. This structural form is chosen for its relevance considering the commonly applied method of analysing strips of plate-stiffener combinations in ship grillages as I-sections beams [97, 127] as well as its widespread use in civil engineering structures. The parametric investigation focuses on cross sections in the stocky range, i.e. cross sections with overall cross-sectional slenderness $\lambda_p < 0.51$ [142], because this is the range in which plasticity and strain hardening is expected to occur. Naturally, the dependence of the plastic local buckling behaviour on the web and flange slendernesses is also considered. Using the results of the parametric study, the σ_y/σ_u requirement of 0.94 by the classification societies [19, 20] is assessed together with the slenderness requirements of the IACS UR I Requirements concerning Polar Class [96].

3.2 ROTATION CAPACITY AND ROTATION REQUIREMENTS OF PLASTIC HINGES

In the plastic design of structures, the ultimate strength of a structure is calculated based on the complete formation of a plastic collapse mechanism which results from a sequential formation of plastic hinges, so the rotation capacity R of a plastic hinge must be large enough so that the plastic hinge can maintain its strength until the complete collapse mechanism is formed. The rotation capacity R is defined as:

$$R = \frac{\theta_{rot}}{\theta_{pl}} - 1 \tag{3.1}$$

where θ_{rot} is the rotation at which the moment resistance drops below the full-plastic bending moment M_{pl}, which is calculated based on a perfectly-plastic, fully yielded cross-section in bending, and θ_{pl} is the beam rotation corresponding to the M_{pl} based on ideal linearised behaviour (Figure 2.3).

The minimum required value for R depends on the structural and configuration, such as the number and length of the spans and the loading distribution on the different spans [143]. Although different values have also been suggested for specific

cases [143–145], the general consensus in the literature is that an overall R requirement of 3 is sufficient for typical configurations encountered in building structures such as continuous beams and frames of typical proportions and loading [146, 147], and this was the value adopted for the structural steel code EN 1993-1-1 [148] and ANSI/AISC 360-22 [13].

In the maritime industry, hull framings and grillages subject to lateral loading by ice [96, 97], impacts [125], and blasts [149] are also designed plastically and hence require sufficient structural ductility in the plastic range. In particular, plastic framing design concepts similar to that used in the civil structural industry are used for the design of hull grillages against ice loads [96, 97]. Similarly, limits are stipulated on the plate slenderness [96] and the σ_y/σ_u ratio [19, 20]. The authors are not aware of research on the rotation requirements specific to hull grillages. However, since the plate-stiffener combination in a hull grillage designed against lateral loading can be seen as a beam spanning over transverse girders [127], the rotation requirement of 3 applicable in general to multi-span continuous beam would be a reasonable value to adopt for the framing of hull grillages.

Accordingly, in assessing the current limits on σ_y/σ_u, λ_f, and λ_w in the classification society rules and UR I [96], this work adopts the minimum rotation requirement of 3. Nonetheless, the main focus of this work is the slenderness- and strain-hardening- dependent rotation capacity rather than the rotation requirement, and the parametric studies shed light on the range of achievable rotation capacities and its influencing parameters regardless of rotation requirements.

3.2.1 *The effect of the strain hardening ability on plastic local buckling and hinge rotation capacity*

The primary failure mode that limits the strength and rotation capacity of plastic bending hinges is plastic local buckling that occurs after yielding develops over the cross section. Lateral-torsional buckling of the entire beam is excluded here, since the standard practice required by structural steel codes [9, 96] is to eliminate lateral torsional buckling by either ensuring sufficient lateral restraint or limiting the unbraced length at the plastic hinges. In some situations, the rotation capacity could be limited by fracture on the tensile flange prior to local buckling due to stress concentrations due to the welding of web stiffeners; however, this should be prevented in practice by appropriate welding and detailing practice [104]. This work hence focuses on the failure mechanism of plastic local buckling in unstiffened plastic hinges sufficiently designed against lateral torsional buckling.

Several attempts have been made to provide a physical explanation for the decreased rotation capacity of high strength steels which have high σ_y/σ_u ratios. [108] and [106] related this to the absence of the yield plateau in the stress-strain behaviour of high-strength steels, which in conventional mild steels causes a 'jump' to larger strains and curvatures at the same level of loading. This can however only be a partial explanation, since it has been shown by Pavlovic and Veljkovic [114] that even when comparing materials that all have rounded stress-strain curves, a higher σ_y/σ_u results in reduced rotation capacity. [102] related the reduction in the rotation capacity to the reduction in the plastic hinge length (the length over which yield has occurred) which accompanies higher σ_y/σ_u ratios, assuming first order

beam kinematics and a specified failure strain criterion. This can once again only be a partial explanation, because it considers only pre-buckling behaviour, ignoring the crucial geometrically non-linear buckling mechanism which causes post-buckling drop-off in the moment resistance.

The most convincing proposition on what determines this behaviour is given by Kato [150] and Schillo and Feldmann [107], who identified the strain-hardening behaviour as an important factor in determining the rotation capacity of plastic hinges, although they neglected to quantify the relation between strain hardening and the rotation capacity. Nonetheless, Zhu and Leis [57] showed that the σ_y/σ_u can be seen as a measure of the strain-hardening behaviour giving an overall measure of the slope and shape of the plastic stress-strain behaviour. By considering the uniaxial tensile test, assuming a Hollomon power curve (Equation (3.2)) which passes through the yield point for the plastic stress-strain behaviour, and applying Considère's [52] necking instability criterion, they related the σ_y/σ_u ratio and the strain hardening exponent n_H of the Hollomon law, as shown in Equation (3.3). The significance of this is that the σ_y/σ_u ratio, despite being a ratio of two stresses and seemingly not related to strains, directly relates to the overall strain hardening behaviour of the assumed material law.

$$\sigma_t = K_H {\varepsilon_t}^{n_H} \tag{3.2}$$

$$\frac{\sigma_y}{\sigma_u} = \frac{1}{1+\varepsilon_y}\left(\frac{e\ln(1+\varepsilon_y)}{n_H}\right)^{n_H} \tag{3.3}$$

where σ_t is the true stress; ε_t is the true strain; K_H is the strength coefficient; and n_H is the strain hardening exponent ε_y is the engineering strain at yield; and e is Euler's number. Since high-strength steels are the focus on this research, a power-law true stress-strain curve acts as a reasonable and common choice [60, 151] for the true-stress strain curve.

In view of this, as few as two ubiquitously used parameters are sufficient to describe idealised true plastic stress-strain curves with a range of strain-hardening behaviour: the yield strength σ_y and the σ_y/σ_u ratio. The following analyses hence use the material definition as given by Equation (3.4) combined with Equation (3.3), which is fully defined given a combination of σ_y and σ_y/σ_u. This enables the use of σ_y/σ_u, in the computational study in this work both as a strain hardening measure and as a direct variable input parameter whose effect on the model response behaviour is to be studied.

$$\sigma_t = \begin{cases} E\varepsilon_t & \text{for} \quad \varepsilon_t \leq \varepsilon_y \\ K_H {\varepsilon_t}^{n_H} & \text{for} \quad \varepsilon_t > \varepsilon_y \end{cases} \tag{3.4}$$

3.3 FINITE ELEMENT MODEL USED FOR THE PARAMETRIC STUDY

The welded I-section beam was modelled using 4-noded, reduced-integration, finite-strain shell elements (S4R) capable of capturing thick-shell behaviour and transverse shear deformation in Abaqus [152]. The flanges were assigned with an appropriate offset in Abaqus so that the web was attached to the surface rather than the midsection of the flange shell elements in the finite element calculations.

To study the behaviour of the plastic hinge localisation independently from length-dependent moment gradient and global buckling effects, the beams in this study were loaded with a uniform moment along the length (pre-buckling) and modelled such that the non-dimensional lateral-torsional-buckling slenderness (Equation (3.5)) λ_{LT} was equal to 0.1. The parameter λ_{LT} is

$$\lambda_{LT} = \frac{M_{el}}{M_{cr,LT}} \tag{3.5}$$

where M_{el} is the moment at first yielding in the cross-section, and $M_{cr,LT}$ is the elastic critical buckling load, for which an exact solution exists for a beam loaded subject to a uniform moment, as is given by Equation (3.6) [153]:

$$M_{cr,LT} = \frac{\pi}{L}\sqrt{EI_z GJ}\sqrt{1 + \frac{\pi^2}{L^2}\frac{EI_w}{GJ}} \tag{3.6}$$

where L is the length of the beam; E is the Young's modulus assumed to be 200 GPa in this chapter; I_z is the second moment of area about the minor axis; G is the shear modulus; I_w is the warping stiffness; and J is the torsion constant.

The value of λ_{LT} was arrived at by considering the threshold of $\lambda_{LT} < 0.4$ required to avoid lateral-torsional buckling [154], the reduction of computational time achieved by analysing shorter beams, and the need to model a sufficient length such that the boundary conditions at the beam ends do not interfere with the buckling localisation in the plastic hinge. The constant λ_{LT} was achieved for different cross-sectional geometries by adjusting the length L of the model accordingly, which is found by substituting Equation (3.6) into (3.5) and solving for L.

To provide a uniform moment (pre-buckling), the beams were fully fixed at one end, and all the degrees of freedom of the nodes at the other end were kinematically coupled to a reference point on the same face, to which a rotation was applied to create major axis bending (Figure 3.1). The reference point was allowed to displace perpendicular to the major axis and longitudinally, but not in the direction perpendicular to the minor axis. Rotations of the reference point around the other two axes were also prevented.

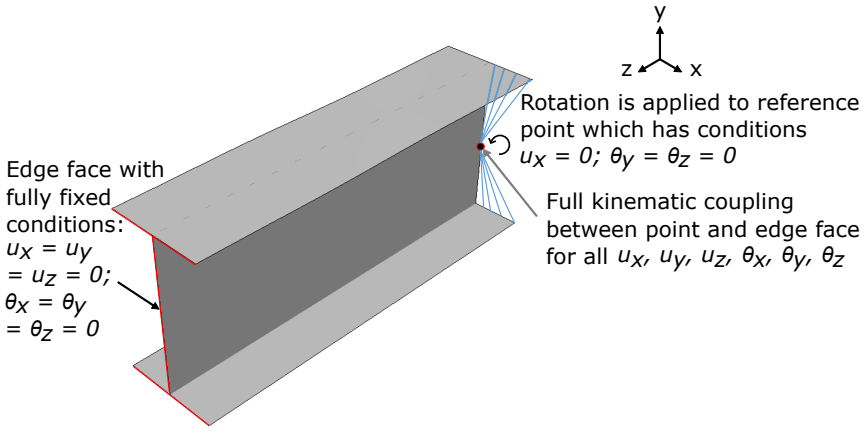


Figure 3.1: Boundary conditions and applied rotation.

The analyses are performed in displacement (rotation) control using Abaqus's general static solver, with automatic stabilisation to aid convergence in the unstable

post-buckling range, as shown in Pavlovic and Veljkovic [114]. The dissipated energy fraction was specified as 0.0001, and the viscous damping energy was checked to be no more than 2 % of the total internal energy. The through-thickness integration was performed using Simpson's rule with 25 through-thickness integration points, so that the post-buckling behaviour could be captured by the S4R elements even for the geometries with thicker walls, as shown by Sadowski and Rotter [155].

3.3.1 *Geometrical imperfections*

Geometrical imperfections arising from the manufacturing and assembly of the welded I-section were accounted for in a conservative manner by applying an initial deformation in the shape of the elastic critical buckling mode obtained from a linear bifurcation analysis (LBA) performed using Abaqus. The buckling mode was given an amplitude equal to the assumed imperfection size, which was taken as 80 % of the manufacturing tolerance, as recommended by EN 1993-1-5 [156]. The manufacturing tolerances of EN 1090-2 [157] given for the flanges and webs of welded profiles were used, which are a $B/100$ out-of-squareness for the flange tip, and a $h/100$ out-of-plane deviation for the web, where B is the flange width and h is the depth of the web. When the peak of the buckled shape arose in the flange, the buckling mode was scaled by an imperfection size equal to $0.8B/100$, and when the peak of the buckled shape arose in the web, the buckling mode was scaled by an imperfection equal to $0.8h/100$.

3.3.2 *Residual stresses from welding*

The residual stress distribution (Figure 3.2) proposed by Schaper et al. [158] for thermal-cut welded I-sections was introduced in the model. This distribution is based on studies on a range of steels including high strength steels up to grade S690 and accounts for the non-proportional relationship between the magnitude of the residual stresses and the yield strength. Furthermore, it accounts for the tensile stresses existing at the flange tips in thermal cut sections, which simultaneously causes higher compressive stresses in the flanges due to equilibrium conditions, affecting the buckling behaviour. In determining the size of the area (given by $\min\{t_w + 5a, B/5\}$) over the web-flange junction at which tensile residual stresses occur, the weld throat size a was taken to be $a = \sqrt{2}s/2 = 0.53t_w$, based on the typical conservative weld leg length of $s = 0.75t_w$ used for full-strength double-sided fillet welds [159]. However, the geometry of the weld was not included in the finite element model because it has a relatively small influence [160].

The residual stress distribution is nominally in equilibrium with itself. It was included in the model by introducing the predefined stress distribution throughout the beam (Figure 3.3) in the initial step of the analysis. This step is followed by a load-free static step to allow small stress imbalances caused by numerical inaccuracies and by the imposed geometrical imperfection to equilibrate, before any loading is applied.

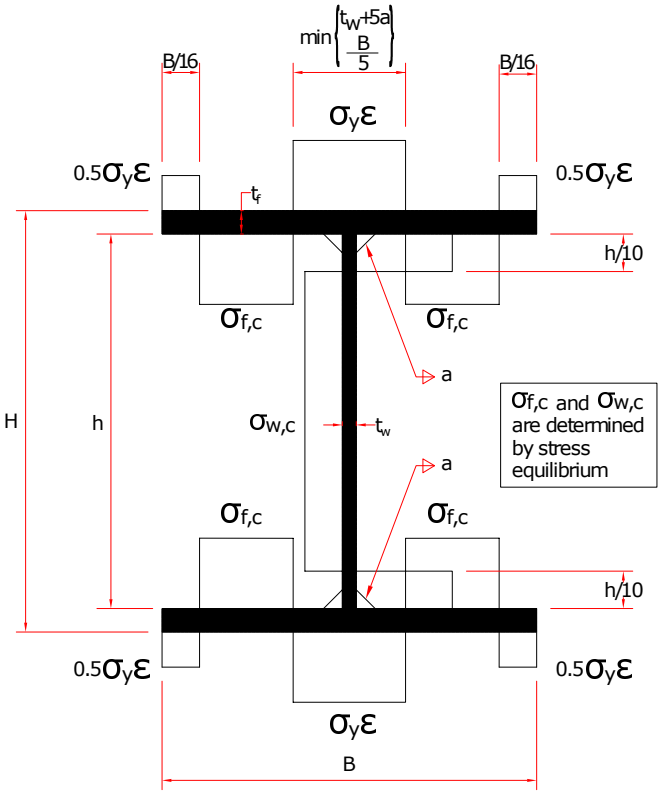


Figure 3.2: Assumed residual stress distribution [158].

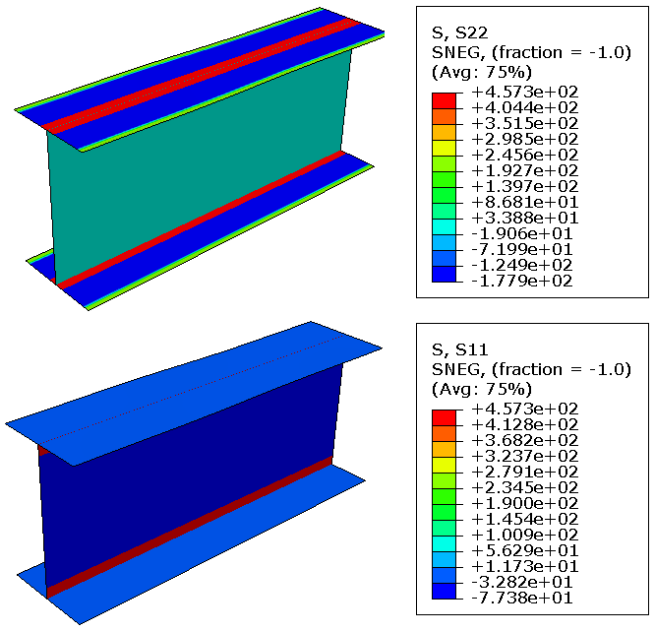


Figure 3.3: Introduction of membrane residual stresses in flange (top) and in web (bottom) in Abaqus for σ_y = 890 MPa.

3.3.3 *Finite element model validation*

The moment-rotation behaviour predicted by the finite element model is compared against that which is observed in experiments in the literature to validate the model's applicability. Four-point bending experiments on stocky high-strength welded I-section steel beams found in Green et al. [161], Lee et al. [104] and Yang et al. [162] were considered. The experiments used for validation thus have high-strength steel grades (HSLA-80, HSA800 and Q690) and slendernesses ($\lambda_f < 10.1\varepsilon$; $\lambda_w < 72\varepsilon$ [9]) which fall within the scope of the study.

The finite element model, which is subject to global bending through the application of an end rotation, is used to simulate the region between the two load application points in the four-point bending experiment, which likewise experiences a uniform moment over the length before buckling occurs. Appropriate boundary conditions are added along the length of the finite element model to match lateral restraints applied in the experimental setup. A similar strategy has been successfully applied by Chen et al. [142].

Since the experimental results were reported in terms of beam-end rotations of the 4-point bending setup while the finite element model only gives the rotations of the portion of the beam initially subjected to uniform moments, expected 4-point-bending beam-end rotations corresponding to the pure-bending model's end rotations were found using beam theory and the superimposition of the assumed-elastic response outside the pure bending region, as given by Equation 3.7.

$$\frac{\theta_{4,end}}{\theta_{pl}} = \frac{\theta_{FE} + \frac{L_{out}}{L_{in}} \min(\theta_{FE}, \theta_{pl})}{L_{out}\kappa_{pl} + L_{in}\kappa_{pl}} \tag{3.7}$$

where $\theta_{4,end}$ is the 4-point-bending end-rotation predicted by the pure-bending model; θ_{FE} is the rotation at the rotated end of the pure bending model (while the other end is clamped in a horizontal position); L_{in} is the length between the two loading points; and L_{out} is the length between a support and the closest loading point. This results in predicted 4-point-bending beam-end rotations which are then plotted against the experimental 4-point-bending beam-end rotations.

To describe the material model in the finite element simulations, the engineering stress-strain curves reported by the authors of the experimental work were converted to true stress-strain values up to the ultimate tensile stress, followed by an extrapolation using the power curve as given in Section 3.2.1, with the exception of the experiment by Green et al. [161] for which the full experimental stress-strain curve was not reported. In that case, equations (3.2) to (3.4) were used to construct the true stress-strain curve, as described in Section 3.2.1.

Geometrical imperfections and residual stresses were included using the methods described above in Sections 3.3.1 and 3.3.2, while adopting the imperfection amplitude and yield stresses corresponding to the experiments, with the exception of the unreported imperfection amplitudes for the experiments by Lee et al. [104] and Green et al. [161]. In those cases, estimates based on Eurocode recommendations [156, 157] as described in Section 3.3.1 were used.

The comparison in Figures 3.4, 3.5 and 3.6 shows that the finite element models can simulate the moment-rotation behaviour observed in the experiments reasonably well.

It can be seen from Figures 3.4 and 3.5 that both the experimental curves by Green et al. [161] and Lee et al. [104] were captured very well in shape and reasonably well quantitatively. For Specimen 7 by Green et al. [161], the model predicted the same maximum M/M_{pl} as observed in the experiment (within 0.02 %) and overestimated the R by 11.9 %. For test HSA800-C-LP-4-PHS by Lee et al. [104], the model underestimated the maximum M/M_{pl} by 3.1 % and overestimated the R by 15.3 %.

The simulation of the experiments Y13-4 and Y15-4 (Figure 3.6) by Yang et al. [162] also captured the maximum M/M_{pl} relatively well, overestimating it by 12.6 % and 5.0 % respectively. The prediction of the R showed greater deviations for these experiments, Y13-4 underestimating R by as much as 49.6 % and Y15-4 not achieving any R at all. This is related to the definition of R, which being based on the exceedance of M_{pl}, is sensitive to changes in the maximum M/M_{pl} even if the post-buckling curve and decay do not change. However, these deviations in R were both underestimations by the model, acting on the conservative side. (Experiment Y11-4 by Yang et al. [162] was not used for validation although it was stocky and tested in 4-point bending because it had a different lateral bracing system than all the other experiments modelled here and demonstrated very low R due to global buckling effects.)

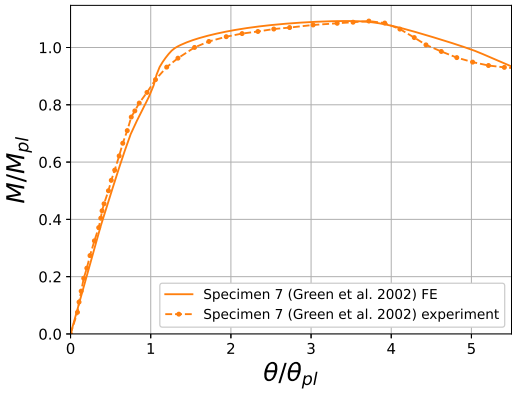


Figure 3.4: Simulation of experiment from Green et al. [161].

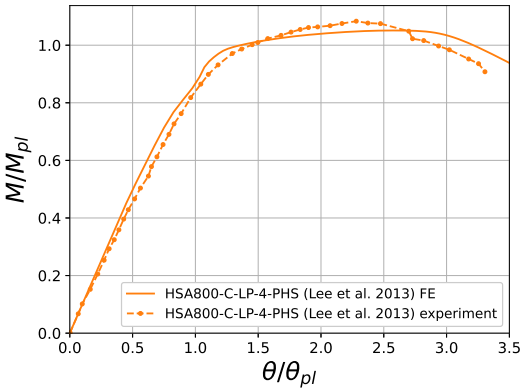


Figure 3.5: Simulation of experiment from Lee et al. [104].

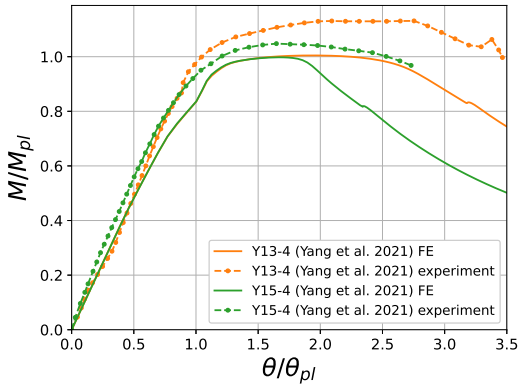


Figure 3.6: Simulation of experiments from Yang et al. [162].

The finite element modeling method has not been validated against other tests in Green et al. [161], Lee et al. [104] and Yang et al. [162] because they either did not involve 4-point-bending setups or their slenderness fell out of the range of interest. It should hence be noted that the validation is limited to the scope described above, beyond which the results of this study should not be extrapolated.

3.4 PARAMETRIC STUDIES

The finite element model was used to perform a series of imperfection-included geometrically and materially non-linear analyses (GMNIA) of beams with varying geometries and material properties. 378 beams with varying yield strength σ_y, σ_y/σ_u ratio, width B, depth H, flange thickness t_f and web thickness t_w, were analysed, as summarised in Table 3.1. The model length L was correspondingly adjusted to maintain a constant lateral-torsional buckling slenderness λ_{LT}, as explained in Section 3.3.

Table 3.1: Range of geometrical and material properties of the beams modelled in the parametric study.

Series	t_f [mm]	t_w [mm]	B [mm]	H [mm]	H/B [-]	σ_y [MPa]	σ_y/σ_u [-]	λ_f [-]	λ_w [-]	λ_p [-]
1	20.0	17.6	200.0	400.0	2.0	[460, 960]	[0.80, 0.99]	[6.4ε, 9.2ε]	[28.6ε, 41.3ε]	[0.30, 0.42]
2	20.0	17.6	[153.0, 279.1]	450.8	[1.8, 2.9]	690	[0.80, 0.99]	[5.8ε, 11.2ε]	40.0ε	[0.30, 0.46]
3	20.0	17.6	[149.6, 247.8]	401.8	[1.8, 2.7]	890	[0.80, 0.99]	[6.4ε, 11.2ε]	40.0ε	[0.33, 0.45]
4	20.0	17.6	[217.5, 306.4]	[388.3, 543.2]	1.8	[460, 960]	[0.78, 0.99]	10.1ε	40.0ε	[0.38, 0.46]
5	15.0	11.0	220.0	400.0	1.8	[460, 960]	[0.80, 0.99]	[9.7ε, 14.1ε]	[47.1ε, 68.0ε]	[0.46, 0.65]
6	12.0	11.0	220.0	400.0	1.8	[460, 960]	[0.80, 0.99]	[12.2ε, 17.6ε]	[47.8ε, 69.1ε]	[0.54, 0.77]
7	12.0	11.0	152.5	[280.0, 480.0]	[1.8, 3.1]	690	[0.80, 0.99]	10.1ε	[39.9ε, 71.0ε]	[0.48, 0.56]
8	12.0	11.0	135.6	[250.1, 431.0]	[1.8, 3.2]	890	[0.80, 0.99]	10.1ε	[40.0ε, 72.0ε]	[0.52, 0.60]
9	12.0	11.0	[130.9, 184.3]	[309.7, 436.8]	2.4	[460, 960]	[0.78, 0.99]	10.1ε	52.5ε	[0.45, 0.56]

3.4.1 *Range of material properties in the parametric study*

Figure 3.7 shows the relationship between σ_y and σ_y/σ_u as seen from existing tests from Bannister [56], together with empirical relationships proposed by different researchers [55, 163, 164] based on other test databases. The experiments of Bannister [56] involve steels that are available for different industries, including the ship and offshore industry. [165] tested several steels relevant to ships and offshore structures including steel grades A, D, AH32, DH32 and DH36, which would fall into the low-strength portion of this data cloud. The main focus of the current work concerns higher-strength steels, which are higher than most steels used in current practice in the maritime industry but well established in the offshore industry. These steels would fall into the higher strength region of the data cloud in Figure 3.7. This choice was made in order to focus on realistic steels with high σ_y/σ_u values.

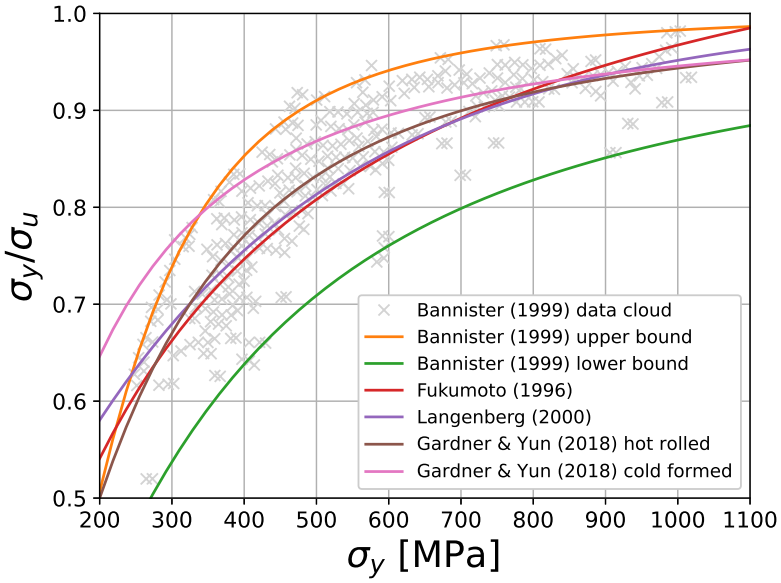


Figure 3.7: Relationship between σ_y/σ_u and σ_y.

The yield strength σ_y in the parametric study was hence varied assuming values of 460, 550, 690, 790, 890 and 960 MPa, and the σ_y/σ_u ratio was varied assuming values of 0.80, 0.84, 0.89, 0.94 and 0.99, with additional analysis points between these values when interpolating to make comparisons against the rules in UR I [96]. These ranges are common for high-strength steels, as seen in Figure 3.7. The generic stress-strain relationship that is given by the combination of Equations (3.3) and (3.4) and defined by the yield strength σ_y and the σ_y/σ_u ratio (which also directly acts as a strain hardening parameter) was utilised for this purpose.

3.4.2 *Range of geometrical properties in the parametric study*

The ranges of the parameters B, H, t_f, t_w, were chosen such that the flange slenderness λ_f , web slenderness λ_w, overall cross-sectional slenderness λ_p, and depth-to-width ratio H/B fell near the limit and within the range for stocky I-sections with constituent plates which are also individually stocky. This corresponds to $\lambda_f < 10.1\varepsilon$

[96], $\lambda_w < 72\varepsilon$ [9, 28] and $\lambda_p < 0.51$ [142]. The yield stress scaling parameter ε and the slendernesses λ_f, λ_w, and λ_p are found as:

$$\varepsilon = \sqrt{\frac{235\,\text{MPa}}{\sigma_y}} \tag{3.8}$$

$$\lambda_f = \frac{B - t_w}{2t_f} \tag{3.9}$$

$$\lambda_w = \frac{h}{t_w} \tag{3.10}$$

$$\lambda_p = \sqrt{\frac{M_{el}}{M_{cr}}} \tag{3.11}$$

where M_{cr} is the elastic critical buckling moment of the overall cross-section, which is found by performing a linear bifurcation analysis of the beam subject to bending using Abaqus. Hence, for each set of parameters B, H, t_f, t_w, σ_y and σ_y/σ_u, a linear bifurcation analysis was first performed to obtain the buckling mode to be used as the shape of the geometrical imperfection and to obtain the critical buckling moment to be used to calculate λ_p. Then, a geometrically and materially non-linear static analysis with the assumed imperfections and residual stress distribution was performed using Abaqus to obtain the rotation capacity R as defined in Equation (3.1).

3.4.3 *Dependence of rotation capacity on σ_y and σ_y/σ_u*

Figure 3.7 shows a clear trend that steels with higher yield strengths σ_y typically have higher σ_y/σ_u ratios and that steels with the same σ_y could nonetheless have a significant variation in σ_y/σ_u. It is hence important to investigate the how R varies with σ_y and σ_y/σ_u simultaneously. It is also worth noting that the relationship between the σ_y/σ_u ratio and the strain hardening coefficient n_H given by Equation (3.3) is dependent on σ_y, as plotted in Figure 3.8. Steenbergen et al. [102] presented results which showed that for a fixed σ_y/σ_u ratio, a higher σ_y leads to lower R, albeit without considering the occurrence of local buckling. The finite element analysis results plotted (Figure 3.9) and discussed below shows that the same trend is seen for failure by local plastic buckling at the plastic hinge.

In Figure 3.9, each colour map corresponds to a fixed cross-sectional geometry which has been analysed assuming a range of σ_y and σ_y/σ_u ratios. The effect of the different cross-sectional slendernesses is seen in the consistently higher R values achieved by the cross sections which are less slender. The analyses in which failure occurred before M_{pl} was reached are plotted on the figure as having R equal to 0. For the cross section with higher slenderness ($0.54 < \lambda_p < 0.77$), barely any of the analyses achieved the M_{pl}, let alone a R of 3. This agrees with the classification by Chen et al. [142] in which $\lambda_p < 0.51$ marks the range for which M_{pl} can be achieved.

Considering the cross section which falls in the stocky range indicated by the grayscale surface, the expected trend of decreasing R with increasing σ_y/σ_u is seen. As for the change in R given a fixed σ_y/σ_u and an increasing σ_y, a general decrease in R is seen, but with the presence of a small trough around $\sigma_y \approx 790\,\text{MPa}$. Furthermore, the change in R with respect to σ_y becomes more gentle for higher

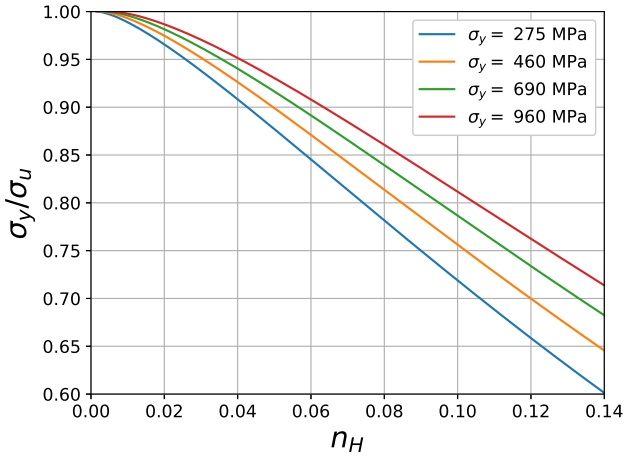


Figure 3.8: Plot of σ_y / σ_u against n_H (Equation (3.3)) for different σ_y.

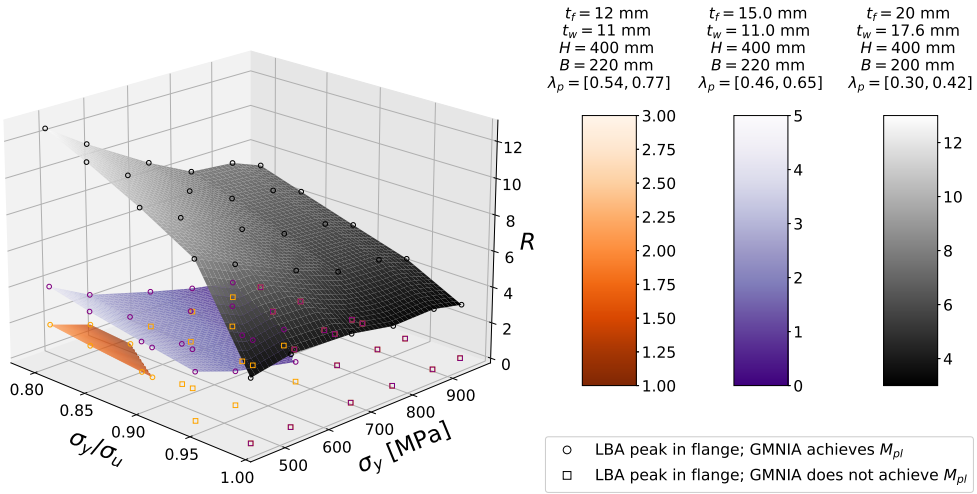
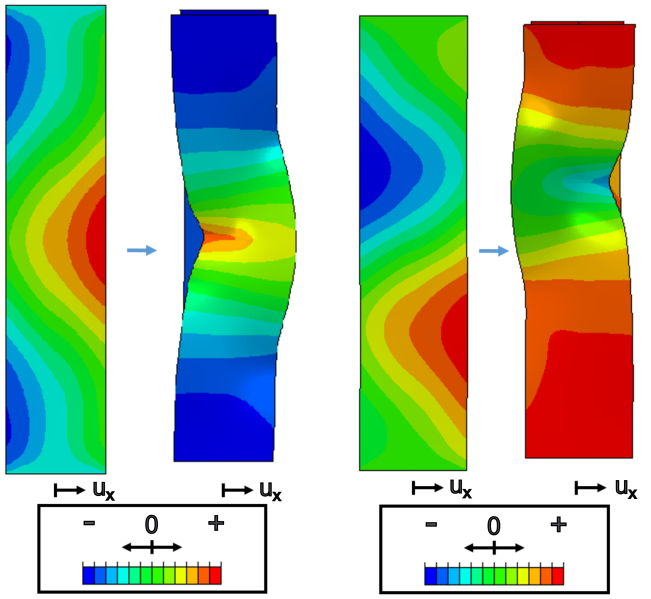


Figure 3.9: R against σ_y / σ_u and σ_y.

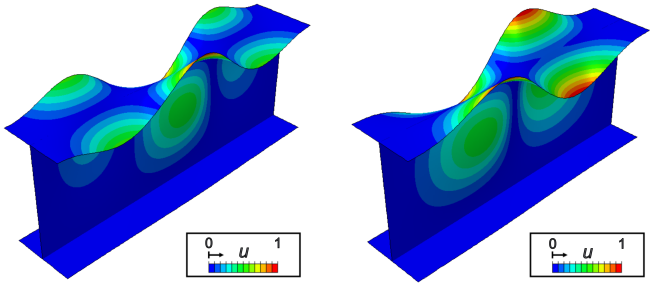
σ_y/σ_u ratios. Looking into the buckled shapes of the finite element models, it can be seen that the trough around $\sigma_y \approx 790\,\text{MPa}$ is associated with a switching between a buckling mechanism which is symmetric, with a buckle localising in the center (such as in Figure 3.10a), and a buckling mechanism which is asymmetric, with a buckle localising in one half of the beam (such as in Figure 3.10b). Furthermore, the buckled plastic mechanism is related to the number of buckling half wavelengths present in the linear buckling mode shape: a symmetric mechanism is seen to happen when the LBA mode shape has an odd number of half wavelengths (Figure 3.11a), while an asymmetric mechanism is seen to happen when the LBA mode shape has an even number of half wavelengths (Figure 3.11b).



(a) Symmetric buckling mode.

(b) Asymmetric buckling mode.

Figure 3.10: Buckling modes as seen from the top.



(a) Odd number of LBA half wavelengths.

(b) Even number of LBA half wavelengths.

Figure 3.11: Linear elastic buckling mode shapes.

This is even more clearly seen when R is plotted against λ_p in place of σ_y (Figure 3.12). Each plane of constant σ_y/σ_u gives a buckling curve showing the dependence of R on the slenderness λ_p (Figure 3.13), with mode switching causing small bumps in the curve. This is reminiscent of the plots of buckling strength against aspect

ratio or dimensionless length used in linear elastic buckling analyses [166, 167], and speaks of the suitability of using λ_p as a normalised slenderness parameter in place of the traditional engineering use of λ_f, λ_w and $\varepsilon = \sqrt{235\,\text{MPa}/\sigma_y}$ separately. For a fixed cross-section geometry, the overall cross-section slenderness λ_p increases if the σ_y increases, because λ_p is based on the normalisation of the critical elastic buckling load by σ_y (Equation (3.11)), and the critical elastic buckling load is independent of σ_y. Hence for a fixed cross-section geometry, increasing σ_y has an effect of increasing the normalised overall cross-section slenderness, which leads to a decreased R.

This buckling curve is however dependent on the σ_y/σ_u ratio. As can be seen in Figures 3.12 and 3.13, the overall height (in R) of each buckling curve decreases for higher σ_y/σ_u ratios. The switching between mode shapes is also different: around $\sigma_y \approx 550\,\text{MPa}$ ($\lambda_p \approx 0.33$) in the grayscale surface (representing stocky geometries), another switch into a different mechanism starts to occur for high σ_y/σ_u but not for lower σ_y/σ_u.

Therefore, the R does indeed decrease for increasing σ_y with increasing λ_p, and although the exact relationship is subject to the buckling mechanism and mode shape interactions, it has a decreasing trend overall. It will however be shown in the next section that an increasing σ_y paired with a constant λ_p leads instead to an increase in R.

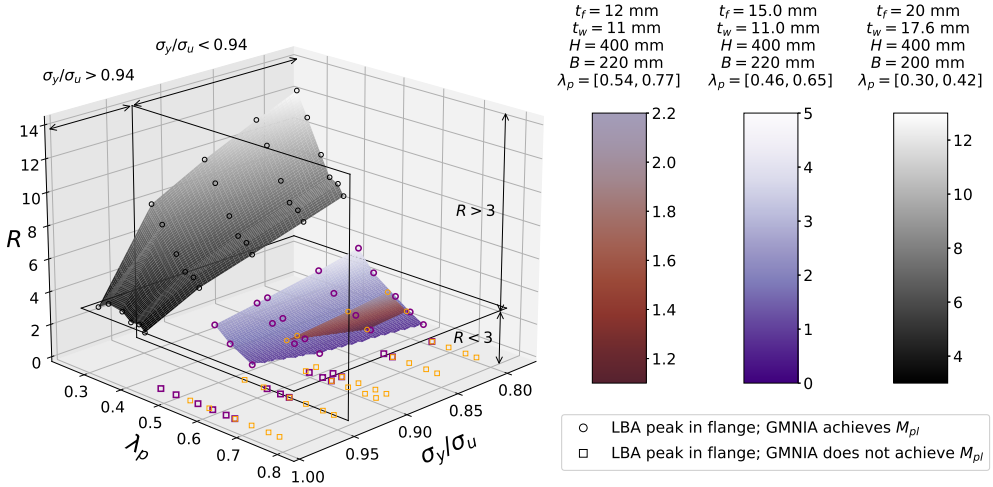


Figure 3.12: R against σ_y/σ_u and λ_p

3.4.4 *Dependence of rotation capacity on σ_y/σ_u and λ_p*

In Section 3.4.3, relationships between R, σ_y/σ_u, and σ_y (or λ_p as a monotonically increasing function of σ_y) were plotted for fixed cross-sectional geometries. In this section, the effect of varying the σ_y/σ_u ratio and the cross-sectional geometry for a fixed σ_y is investigated instead. The flange thickness t_f and the web thickness t_w are fixed at 20.0 mm and 17.6 mm respectively. The λ_p is varied by changing the flange slenderness while keeping the web slenderness λ_w fixed at 40.0ε, which corresponds to $H = 450.8\,\text{mm}$ for $\sigma_y = 690\,\text{MPa}$ and $H = 401.8\,\text{mm}$ for $\sigma_y = 890\,\text{MPa}$.

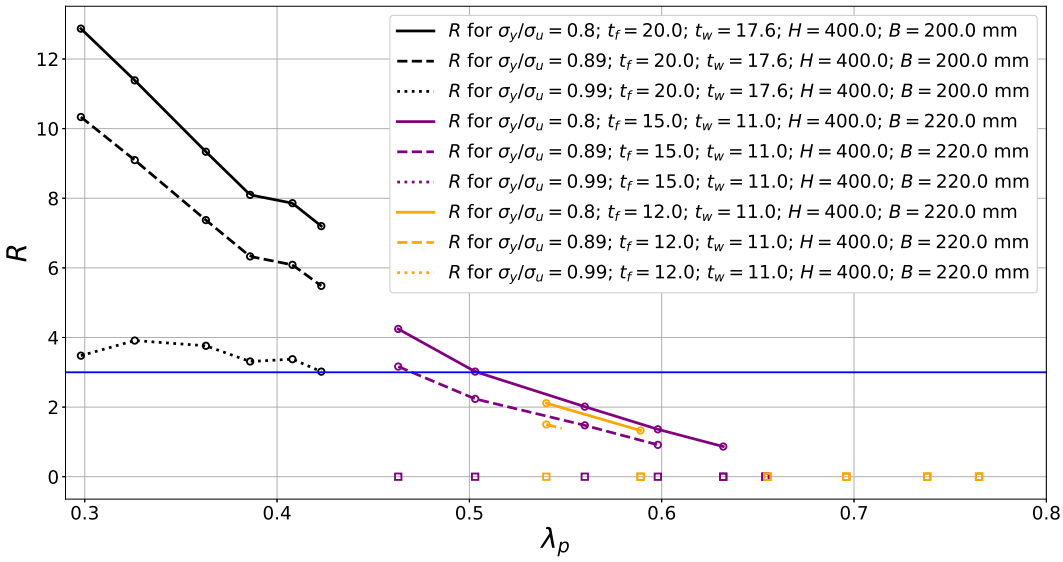


Figure 3.13: R against λ_p for σ_y/σ_u = 0.8; 0.89 and 0.99.

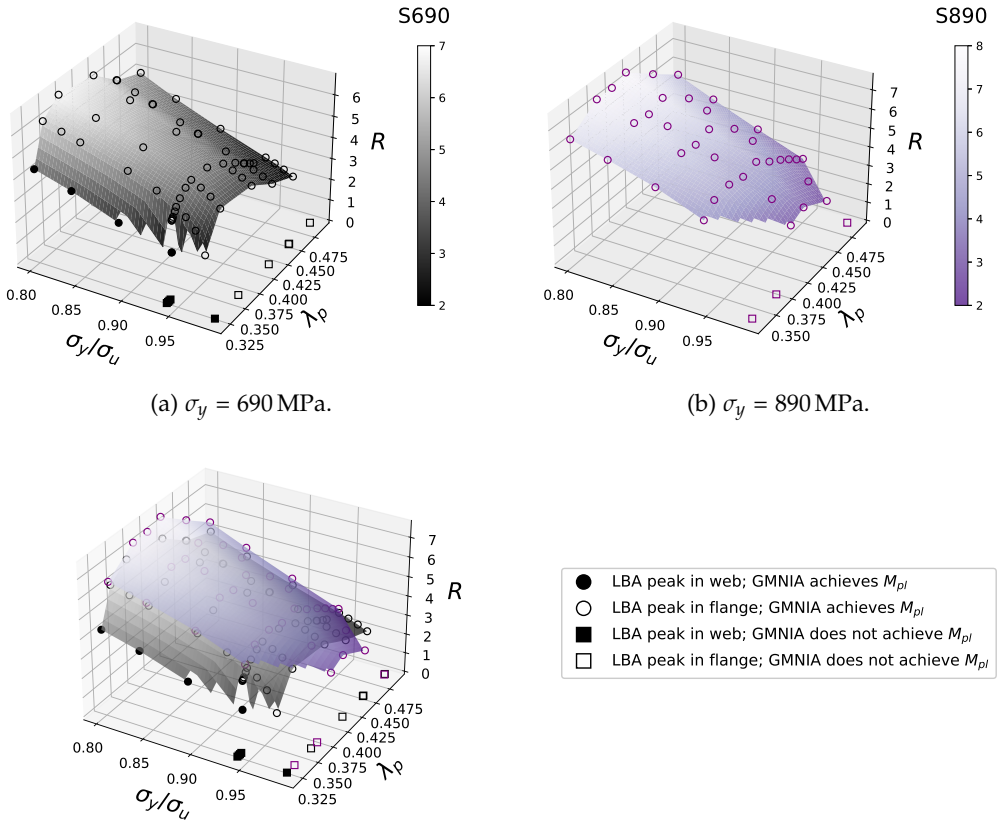
In this case, the solution of Equations (3.5) and (3.6) to maintain a constant λ_{LT} = 0.1 works out such that the analyses for a fixed σ_y have roughly the same length, i.e. between 1152.1 mm and 1152.3 mm for σ_y = 690 MPa and between 898.8 mm and 898.9 mm for σ_y = 890 MPa.

Figure 3.14a shows the resulting R-σ_y/σ_u-λ_p relationship for σ_y = 690 MPa. As before, an increase in σ_y/σ_u leads to a decrease in R for a given λ_p. A small trough is seen in the R surface with respect to λ_p at around $\lambda_p \approx 0.45$, corresponding to a switch between a symmetrical and asymmetrical buckling mode as also seen in Section 3.4.3 above. Nonetheless, there is a maximum point in the variation of R with respect to λ_p at $\lambda_p \approx 0.36$ despite there being no change in the overall buckling mode there. This can be related to the decreasing ratio of the maximum flange displacement to the maximum web displacement in the LBA mode shape with decreasing λ_f and λ_p, which culminates in a transition of the location of the peak displacement in the mode shape from being in the flange to being in the web. The latter leads to what is here termed 'web-dominated' buckling behaviour and the former to 'flange-dominated' buckling behaviour. The unexpected trend of a decreasing R with increasing stockiness (i.e. decreasing λ_p) when the imperfection peak is in the web rather than the flange demonstrates that web-dominated buckling behaviour and large web imperfections could be more detrimental to R than flange-dominated buckling behaviour, and it is necessary to consider both situations.

It is important to note that all of the analyses here have the same $\lambda_w = 40.0\varepsilon$, which satisfies the maximum web slenderness limit specified in UR I [96] to prevent local web buckling and also satisfies the EN 1993-1-1 [9, 28] Class 1 limit for web plates. The switch in the mode shape's peak location led to a change in trend and a decrease in R despite a decrease in λ_f and λ_p and a constant λ_w classified as sufficiently stocky. It is hence important to either account for the location of the buckling mode or imperfection peak or consider limits on the relative ratio between flange and web slenderness.

For σ_y = 890 MPa (Figure 3.14b), a similar overall trend to that of σ_y = 690 MPa discussed above is seen, where for a constant σ_y/σ_u, the gradient of R with respect to λ_p is positive for small λ_p and negative for large λ_p, and a small trough is seen at around $\lambda_p \approx 0.39$ which is associated with a switching from an asymmetrical buckling mode to a symmetrical buckling mode as discussed in Section 3.4.3 above.

Figure 3.14c shows the R-σ_y/σ_u-λ_p relationship assuming the same fixed t_f and t_w, for both σ_y = 690 MPa and σ_y = 890 MPa. While for a fixed cross-section geometry, an increase in σ_y leads to an increase in λ_p such that R decreases (Figure 3.12), Figure 3.14c shows that for a fixed λ_p, an increase in σ_y leads to an increase in R. This is in agreement with the idea a higher strain hardenability leads to greater R, because if the normalised slendernesses λ_{LT} and λ_p are fixed (by accordingly adjusting the cross-section geometry), any increase in σ_y is a purely material change, and for a fixed σ_y/σ_u ratio, a higher σ_y leads to a greater n_H and a greater strain hardening ability, since the behaviour of σ_y/σ_u as a strain hardening parameter is dependent on σ_y (Equation (3.3) and Figure 3.8).



(a) σ_y = 690 MPa.

(b) σ_y = 890 MPa.

(c) σ_y = 690 MPa and σ_y = 890 MPa.

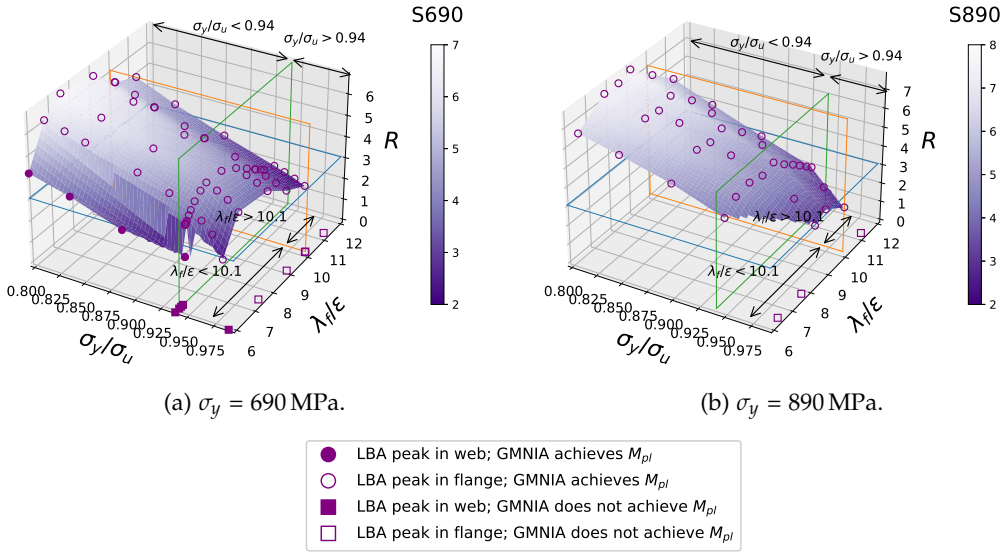
Figure 3.14: R against σ_y/σ_u and λ_p for t_f = 20.0 mm; t_w = 17.6 mm; λ_w = 40.0ε.

3.5 ASSESSMENT OF THE UR I FLANGE AND WEB SLENDERNESS LIMITS

As discussed in Section 3.2, grillages subject to ice loading in polar class ships are designed using plastic framing design concepts in which the plate-stiffener

combination is assumed to act as a frame which develops plastic hinges [96, 97]. UR I [96] specifies a maximum flange-outstand slenderness limit of $155/\sqrt{\sigma_y} = 10.1\varepsilon$ and a web slenderness limit of $282/\sqrt{\sigma_y} = 52.5\varepsilon$ (where the yield stress is in MPa) to prevent local flange and web buckling in the welded stiffeners. As an example to illustrate the significance of the trends observed from the parametric study, the aforementioned slenderness limits are assessed together with the σ_y/σ_u limit of 0.94 specified in the classification societies' rules [19, 20] for two nominal steel grades, $\sigma_y = 690\,\text{MPa}$ and $\sigma_y = 890\,\text{MPa}$. Since R is dependent on both the cross-sectional slenderness and σ_y/σ_u, the slenderness required to achieve a given R depends on the σ_y/σ_u ratio, and the σ_y/σ_u ratio required to achieve a given R depends on the slenderness. The results of the parametric study is hence used to infer a limiting slenderness corresponding to the σ_y/σ_u limit of 0.94 in the classifications societies' rules [19, 20] and similarly a limiting σ_y/σ_u ratio corresponding to the slenderness limits in UR I, based on the assumptions described in Sections 3.3 and 3.4. As shown in Figures 3.15 to 3.19, this is done by using linear interpolation of the parametric results and plotting lines describing a constant σ_y/σ_u, λ_f/ε or λ_w/ε.

The same series of parametric analyses discussed in Section 3.4.4 is considered to assess the λ_f limit, since this series has a constant and stocky web slenderness and varying flange slendernesses. As for assessing the λ_w limit, a series of finite element analyses with a fixed stocky web slenderness λ_w of 10.1ε is performed. The flange and web thicknesses are fixed at $t_f = 12.0\,\text{mm}$ and $t_w = 11.0\,\text{mm}$, and λ_{LT} is set to 0.1 as before. The values obtained are summarised in Table 3.2.



(a) $\sigma_y = 690\,\text{MPa}$. (b) $\sigma_y = 890\,\text{MPa}$.

Figure 3.15: R against σ_y/σ_u and λ_f/ε for $t_f = 20.0\,\text{mm}$; $t_w = 17.6\,\text{mm}$; $\lambda_w = 40.0\varepsilon$.

By varying the σ_y and σ_y/σ_u for beams with constant t_f, t_w, λ_f, λ_w and λ_{LT}, the σ_y/σ_u requirement with respect to σ_y for beams with constant cross-sectional slenderness classifications can be assessed. This is done by plotting the R-σ_y-σ_y/σ_u data and using linear interpolation to find the σ_y-σ_y/σ_u line corresponding to $R = 3$. To illustrate this, two series of parametric runs involving constant cross-sectional slendernesses were performed: one with $t_f = 20.0\,\text{mm}$; $t_w = 17.6\,\text{mm}$; $\lambda_w = 40.0\varepsilon$

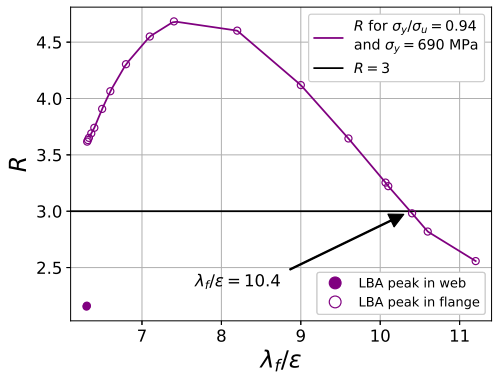


Figure 3.16: R against λ_f for $\sigma_y/\sigma_u = 0.94$ and $\sigma_y = 690$ MPa.

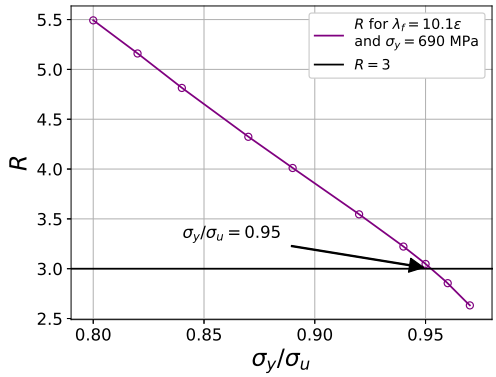


Figure 3.17: R against σ_y/σ_u for $\lambda_f = 10.1\varepsilon$ and $\sigma_y = 690$ MPa.

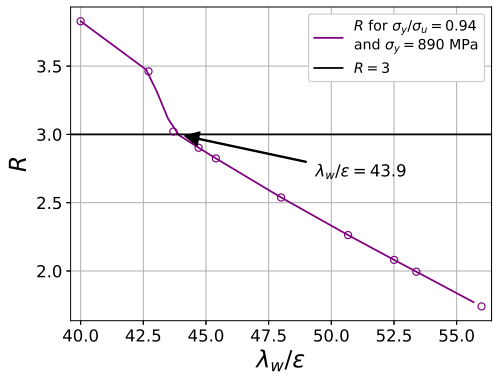


Figure 3.18: R against λ_w for $\sigma_y/\sigma_u = 0.94$ and $\sigma_y = 890$ MPa.

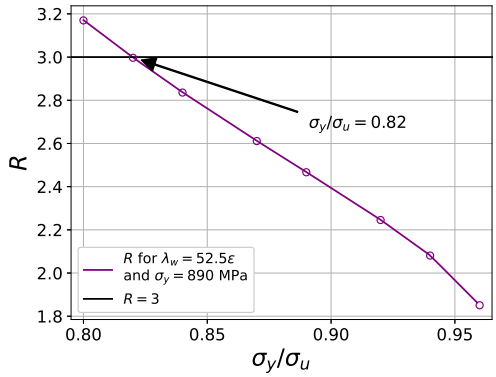


Figure 3.19: R against σ_y/σ_u for $\lambda_w = 52.5\varepsilon$ and $\sigma_y = 890$ MPa

Table 3.2: Expected σ_y/σ_u, λ_f and λ_w requirements for achieving $R = 3$ given existing classification limits.

	σ_y/σ_u	λ_f or λ_w	σ_y/σ_u	λ_f or λ_w
	690 MPa		890 MPa	
Flange limit (for t_f = 20.0 mm; t_w = 17.6 mm; λ_w = 40.0ε)	**0.94**	10.4ε	**0.94**	11.0ε
	0.95	**10.1ε**	0.97	**10.1ε**
Web limit (for t_f = 12.0 mm; t_w = 11.0 mm; λ_f = 10.1ε)	**0.94**	42.1ε	**0.94**	43.9ε
	0.80	**52.5ε**	0.82	**52.5ε**

Values in bold font are the limits specified by the rules [19, 20]; values in normal font are the inferred corresponding limits.

and $\lambda_f = 10.1\varepsilon$ (Table 3.1, Series 4); and another with $t_f = 12.0\,\text{mm}$; $t_w = 11.0\,\text{mm}$; $\lambda_w = 52.5\varepsilon$ and $\lambda_f = 10.1\varepsilon$ (Table 3.1, Series 9). The results are plotted in Figure 3.20, together with the empirically derived trends between σ_y and σ_y/σ_u observed in steels (from Figure 3.7). Thus, in Figure 3.20, the solid lines can be seen as the upper bound of what is acceptable for the given geometry based on considerations of the plastic rotation capacity, while the dashed lines can be seen as describing the range over which high-strength steel properties are found. It shows that for rotation capacity considerations, the local slenderness of the structure plays a big role on whether or not the σ_y/σ_u is adequate. Furthermore, it shows that while the observed values of σ_y/σ_u generally increases with σ_y, the highest tolerable σ_y/σ_u ratio required to achieve sufficient rotation capacity also increases, reiterating the relevance of ductility and slenderness requirements that are simultaneously dependent on σ_y and σ_y/σ_u.

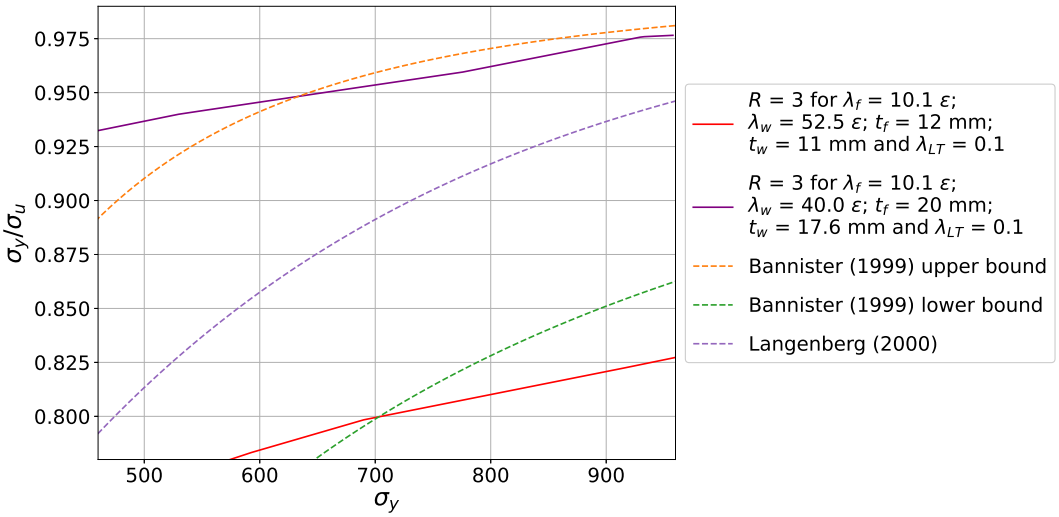


Figure 3.20: Observed and required σ_y/σ_u against σ_y based on geometry from Series 4 and 9 (Table 3.1).

3.6 CONCLUSIONS

This study has shown that the rotation capacity R is simultaneously dependent on the yield strength σ_y, the σ_y/σ_u ratio and the cross-section slenderness (λ_f, λ_w or λ_p). The following conclusions may be drawn from this study:

1. Due to the interdependence between R, σ_y, σ_y/σ_u and λ, a complete, accurate determination of the σ_y/σ_u limit would, in the ideal case, be situational and dependent on the desired rotation and specific geometries, in contrast to the current practice which typically involves a material-specific limit that is independent of the structure.

2. For a fixed σ_y/σ_u ratio, cross-sectional slenderness and lateral-torsional buckling slenderness, a higher σ_y leads to higher rotation capacities. This suggests that increased use of high-strength steels could be achieved by considering all of these factors together. For example, this could be done by introducing

cross-sectional slenderness limits that are dependent on both the σ_y and σ_y/σ_u, instead of a constant, blanket σ_y/σ_u requirement such as is currently adopted in standards and rules.

3. The trend between the rotation capacity and the cross-sectional slenderness depends on whether the buckling is web- or flange-dominated. Increasing the flange stockiness by decreasing the flange width for a beam that is experiencing web-dominated buckling does not help to increase the rotation capacities but instead decreases it, although a decrease is reflected in the cross-section slenderness parameter. This suggests the value of considering the ratio between the web slenderness and flange slenderness and of specifying independent web and flange limits that apply simultaneously, as also suggested by Chen et al. [142].

3.7 SYMBOLS

LATIN

a	Weld throat size
B	Flange width
E	Young's modulus
e	Euler's number
G	Shear modulus
H	Beam depth
h	Web depth
I_w	Warping stiffness
I_z	Second moment of area about the minor axis
J	Torsion constant
K_H	Strength coefficient of the Hollomon power-hardening rule
L	Modelled length of the beam
L_{in}	Length between the two loading points in 4-point-bending
L_{out}	Length between a support and the closest loading point
M	Moment of resistance
M_{cr}	Critical linear elastic buckling moment from linear bifurcation analysis
$M_{cr,LT}$	Critical linear elastic lateral-torsional buckling moment
M_{el}	Moment at first yielding
M_{pl}	Fully-plastic bending moment
n_H	Strain hardening exponent of the Hollomon power-hardening rule
s	Weld leg length
t_f	Flange thickness
t_w	Web thickness
u	Magnitude of displacement
$u_{x,y,z}$	Displacement along x-, y- and z-axis respectively

GREEK

ε	Yield stress scaling parameter
ε_y	Engineering yield strain
ε_t	True strain
θ	Cross-sectional rotation
$\theta_{4,end}$	4-point-bending end-rotation predicted by the pure-bending model
θ_{el}	Cross-sectional rotation corresponding to M_{el}
θ_{FE}	Total rotation from end-to-end of the pure-bending finite element model
θ_{pl}	Cross-sectional rotation corresponding to M_{pl} and assumed linear material behaviour
θ_{rot}	Cross-sectional rotation when M falls below M_{pl}
$\theta_{x,y,z}$	Rotation about x-, y- and z-axis respectively
κ	Curvature
κ_{pl}	Curvature corresponding to M_{pl} and assumed linear material behaviour
λ_f	Flange slenderness
λ_{LT}	Lateral-torsional buckling slenderness
λ_p	Overall cross-section slenderness
λ_w	Web slenderness
σ_t	True stress
σ_u	Ultimate tensile stress
σ_y	Yield stress

4

CORRELATION BETWEEN MATERIAL CERTIFICATE DATA, DAMAGE MECHANICS PARAMETERS AND FRACTURE TOUGHNESS

This chapter is based on [168] and [169]:

[168] **W. J. Wong** and C. L. Walters, 'Damage mechanics model for correlating notch toughness in Charpy impact tests with fracture toughness in cracked static fracture tests.', *Engineering Fracture Mechanics*, 2025. DOI: 10.1016/j.engfracmech.2025.111043
[169] **W. J. Wong** and C. L. Walters, 'Damage-mechanics insights into the relationship between upper-shelf Charpy testing and J-integral testing considering varying tensile test properties', Manuscript, 2025

ABSTRACT

Requirements on the yield-to-tensile strength ratio σ_y/σ_u, fracture elongation A and the Charpy energy C_v are used together as part of an indirect method of ensuring sufficient ductility at localised areas of stress and strain concentration in the design of steel structures. Recent studies have found that these indirect requirements could be inadequate in certain situations involving cracks or manufacturing defects. Furthermore, requirements on the σ_y/σ_u which are enforced regardless of the structural context and other material properties may unnecessarily constrain the use of steels which nonetheless have high strength, fracture toughness and ductility. In contrast to the σ_y/σ_u, A, and C_v, a more direct measurement of a structure's ability to resist fracture is given by fracture toughness testing, such as J-integral testing, but this is less frequently used, because these tests are significantly costlier than tension and Charpy tests. More often, Charpy tests are performed and correlations between upper-shelf C_v and J values are used to estimate the fracture toughness of the material. However, the existing correlations are predominantly based on empirical findings and have not systematically accounted for the effect of variations in the σ_y/σ_u, which has been shown in recent studies to affect the fracture toughness. This chapter hence establishes a modelling and calibration approach that in order to contribute mechanics-based insight

into the correlations between the Charpy energy, J-integral, yield-to-tensile strength ratio and tensile test fracture elongation.

First, a phenomenological rate-dependent plasticity model coupled with damage and temperature effects is developed by implementing the strain-based modified Mohr-Coulomb damage-softening model with Johnson-Cook thermal softening in a thermodynamically consistent Cowper-Symonds viscoplasticity model. The validity of the modelling framework is shown by its ability to simultaneously model the tensile test, the Charpy V-notch test and the precracked single-edge notched bending test. This is demonstrated for two steels, AH36 and S690QL, capturing the force-displacement responses and the characteristic ductile fracture mechanism of slant fracture in all three tests. Capitalising on weak triaxiality dependence in the middle-to-high triaxiality ranges in the given materials and adopting a triaxiality-independent assumption is found to be effective for reducing the damage model complexity while maintaining its ability to simulate the mechanical response in key tests covering an important range of stress states. Accounting for thermal softening due to adiabatic heating was found to be important for the accurate simulation of ductile Charpy tests involving high impact energies. Key similarities in the fracture behaviour of the Charpy and single-edge notched bending tests are identified: they span a similar range of stress states over a large range of their response despite the initial notched versus cracked difference — an insight that is then used to reduce the calibration effort needed for a parametric study on the correlation between material certificate data, damage mechanics parameters and fracture toughness.

In the parametric investigation, a correlation based on regression between the damage parameters and the mechanical properties from mill test certificates is found by calibrating the damage parameters for a large database of S690Q steels. Then, the correlation between C_v and J_Q is assessed by simulating the single-edge-notch bending test for a range of varying mill test certificate properties, taking into account how the damage parameters vary with these mechanical properties. The results are analysed to give better insight into how the notch toughness correlates to the fracture toughness, taking the σ_y/σ_u and A into account. It is seen that although varying σ_y/σ_u and A has some effect on how the total notch energy C_v is correlated to J_Q, it does not reflect a significant effect on the ductile fracture initiation toughness but is rather associated with the fact that the C_v includes a significant portion of energy for stable ductile propagation and fracture occurring at the specimen's free surface, while J_Q primarily concerns the onset stage of stable ductile tunnelling behaviour at the centre of the specimen. The σ_y/σ_u and A are seen to have an even smaller effect on the correlation between J_Q and the energy (C_{vm}) dissipated up to the occurrence of the peak force in the instrumented Charpy test, in comparison with the C_v–to–J_Q correlation, especially for low C_{vm}.

4.1 INTRODUCTION

Structural details such as corners, holes, cut-outs, welded connections and notches are geometrical stress raisers that often experience plastic strains even before the yielding limit state of the global, structural-level member is reached. Ductility is required in these areas to allow the redistribution of these stresses and to maintain the local load bearing capacity, which is sometimes also worsened by fatigue-induced cracks or manufacturing defects. In many steel design standards [9, 13, 28] and maritime classification rules [19, 20], it is implied that complying with a maximum

limit on the yield-to-tensile strength ratio σ_y/σ_u, a minimum required fracture elongation A and a minimum transition-temperature-based Charpy notch energy C_v is sufficient to ensure that the ductile fracture behaviour and strength assumed in the ultimate strength design calculations can be achieved and maintained at these locations [72]. The σ_y/σ_u limit amounts to a minimum strain hardening requirement that serves to delay necking [1, 52], which causes the occurrence of large strains leading to fracture. The minimum fracture elongation A is a provision for delaying low-triaxiality ductile fracture [60]. The transition-temperature-based minimum Charpy energy C_v is a provision for the avoidance of brittle fracture behaviour [72]. In this way, these requirements are considered to act as an indirect substitute for an upper-shelf toughness requirement that has not been explicitly specified in the design codes and rules.

Recent studies [72, 78] have found that this set of indirect requirements could be inadequate for providing sufficient upper-shelf toughness in certain situations involving cracks or manufacturing defects. On the other hand, fixed requirements on the σ_y/σ_u which are enforced regardless of the structural context and other properties may, in some situations, unduly constrain the use of steels which nonetheless have high strength, fracture toughness and ductility [60, 64]. It is found that strain hardening, as represented by the σ_y/σ_u, has a significant effect on the ductility in plastic buckling mechanisms [115, 141], but its effect on the local ductility at stress-concentration-inducing details is less clear [164]. While a maximum σ_y/σ_u limit of 0.95 was indeed initially introduced [74] based on the grounds of delaying necking sufficiently to ensure a minimum level of ductility, and similar values for the σ_y/σ_u limit are used to this day, post-necking behaviour and fracture toughness were neglected in these considerations. More comprehensive research on the effect of strain hardening on local ductility at cracked details under positive triaxiality is ongoing, but the implications thereof on the use of σ_y/σ_u as an indicator of local ductility at such details lack a consensus. For example, Feldmann et al. [72] and Feldmann and Schaffrath [60] indicate that a higher σ_y/σ_u leads to increased net section resistance relative to the ultimate tensile strength in centrally notched tensile tests, suggesting that a higher σ_y/σ_u promotes resistance at cracked details. On the other hand, Nonn et al. [81] and Lu et al. [82] indicate that a higher σ_y/σ_u leads to decreased crack arrest toughness, suggesting the contrary.

In light of this, recent developments have seen the suggestion of minimum upper-shelf C_v values [83], in addition to A, as a better primary upper-shelf toughness substitute criterion, while maintaining a minimal σ_y/σ_u for the ductility at plastic buckling localisations and the provision of a nominal minimum hardening so that plastic mechanisms can develop [64]. Although ductile Charpy tests, when compared to fracture toughness tests, are additionally affected by strain rate effects and adiabatic heating and are more influenced by plastic energy dissipation due to extensive plastic bending, they are cheaper and easier to perform. Correlations between the upper-shelf notch toughness in terms of C_v and the fracture toughness in terms of the J-integral are often used to estimate the material's fracture toughness from Charpy tests [84, 91, 170]. These correlations provide the basis for the the use of minimum upper-shelf C_v values as an indirect upper-shelf toughness requirement for local ductility at details susceptible to crack formation and ultimate ductile fracture.

The existing correlations, however, are predominantly based on empirical findings and have not systematically accounted for the effect of variations in the σ_y/σ_u on the toughness noted by Nonn et al. [81] and Lu et al. [82]. Only one existing semi-empirical correlation, proposed by Schindler [93], which will be discussed in Section 4.10 below, varies with σ_y/σ_u. Relationships based on damage-plasticity modelling do not exist in the literature primarily because calibrating such models to capture the ductile fracture mechanism well for even one material alone typically involves extensive testing and numerical modelling effort [171], and different strain rates, notch geometry and stress state distributions occur in the Charpy and SENB model, which contribute to the modelling complexity (Section 4.2). In view of this, a modelling and calibration approach is developed in this work in order to use a damage-mechanics approach to study the correlation between C_v and J_Q, by introducing effective simplifications while still capturing the different complex behaviours involved.

With the use of detailed simulations of tensile, Charpy and single-edge-notched-bending (SENB) tests on AH36 and S690QL steel using a rate-dependent, temperature-dependent, damage-softening plasticity model, Sections 4.3 to 4.8 shows how, for steels with weak triaxiality dependence in the fracture locus, these two tests could be simulated well using a 2-parameter approach for the damage locus calibration, by assuming triaxiality independence in the damage strains, a notion that is supported by observations made by Xue [172, 173] on existing experiments on structural steels [174] and aluminium alloy [175]. The reduced calibration effort afforded by this approach enables the subsequent numerical damage-mechanics investigation of the correlation between C_v and the critical J, denoted by J_Q, as predicted by the calibrated models of a database of S690Q [10] steel material certificate data provided by Huisman BV. The calibration is performed based on the data obtained from the material certificate of these steels: σ_y, σ_u, A and C_v (Section 4.9). Using regression analysis of the numerical results, a relationship between the damage parameters and material certificate data is proposed for this group of steels. Subsequently, SENB simulations, together with the corresponding J_Q, for the calibrated steels with varying material certificate properties are obtained 4.10. The results are analysed to study and give better insight into how the notch toughness C_v correlates to the fracture toughness J_Q, taking the σ_y/σ_u and A into account. This sheds light on the roles of σ_y/σ_u and A in the local ductility at cracked details under positive triaxiality by revealing how they affect the way notch and fracture toughness measures are correlated, presenting quantified effects of σ_y/σ_u and A on fracture toughness considerations.

4.2 THE USE OF THE CHARPY NOTCH TOUGHNESS TO ESTIMATE FRACTURE TOUGHNESS – LIMITATIONS AND CHALLENGES

Charpy V-notch impact tests and uniaxial tensile tests are relatively cheap and easy to perform in comparison with fracture toughness tests such as single-edge notched bending (SENB) tests which involve precracking. Although they do not provide a direct measure of the fracture toughness, the Charpy test gives a notch (uncracked) toughness, and the tensile test gives information about the strain hardening and ductility. These tests are hence often used as part of the product certification and

structural design process in the construction industry to assess fracture toughness indirectly, in addition to their usual purpose of measuring strength (tensile test) and the ductile-to-brittle transition temperature (Charpy test). This use of the uncracked properties to estimate cracked properties appears in two application contexts: the assessment of the acceptability of flaws for fitness-of-service [170] and the design for the ultimate ductile fracture strength at areas where cracks due to fatigue or manufacturing defects might be expected to induce stress concentrations and high local plastic straining [28, 83].

In the assessment of the acceptability of flaws, upper-shelf C_v values are sometimes used to estimate the upper-shelf fracture toughness value in terms of J or an equivalent stress intensity factor K_J converted from J [84, 170] based on empirical correlations when direct fracture toughness data is not available. The material's fracture toughness is then used for comparison with the applied stress intensity for the flaw to assess its safety.

In the ultimate strength design for ductile fracture in areas where fatigue or manufacturing processes might cause cracks or crack-like defects [28], the combination of limits on the Charpy impact energy C_v, the fracture elongation A and the yield-to-tensile strength ratio σ_y/σ_u is often implicitly adopted as a substitute upper-shelf toughness criterion [64, 72]. In this context, the minimum C_v functions as a provision for the avoidance of brittle behaviour, and the minimum A and maximum σ_y/σ_u act as ductility requirements that, when complemented with strength based design, are assumed to indirectly account for the upper-shelf toughness [60]. However, this has been shown to be inadequate in certain situations, and the mechanical basis for these assumptions are lacking [64, 72, 176]. The most recent developments have therefore seen minimum upper-shelf C_v values (e.g. 100 J [72, 83]) being used for some design situations as an improved but nonetheless indirect upper-shelf fracture toughness requirement. This further accentuates the need for a better understanding of $C_v - J$ correlations.

Due to the practicality and usefulness of these upper-shelf $C_v - J$ correlations, various studies have been performed to improve their accuracy [84–90]. Some studies also estimated fracture toughness using force-displacement data from the instrumented Charpy test [91, 92], instead of the total impact energy alone. However, the correlations mentioned above have been developed using predominantly empirical methods, and although the existing work on the modelling of Charpy test and precracked fracture tests using phenomenological and micromechanical material models in the literature is extensive [177–181], a few complexities need to be overcome to relate C_v and J using such numerical models.

First, the existing studies on the numerical modelling of Charpy and SENB tests are separate and based on various models of varying complexity, while correlating C_v and J necessitates a single model that has been proven to reliably and accurately simulate the behaviour in both the Charpy and SENB tests. The differences between the strain rates and the stress states experienced in these tests present notable challenges. High strain rates have an effect of increasing the plastic flow stress [182]. A Charpy test experiences plastic strain rates of up to the order of $10^4\,\mathrm{s}^{-1}$ [183, 184], while the SENB test is a quasi-static test with strain rates around the order of $10^{-2}\,\mathrm{s}^{-1}$. At the same time, the stress states occurring at the notch tip of the Charpy specimen and the crack tip of the SENB specimen are markedly different, and the

onset of fracture is known to depend on the stress state. However, a full calibration of the stress-state dependent fracture model to all possible stress states for a single material requires extensive experimentation [171]. A model that is intended for relating C_v and J for the large variety of materials and the relatively limited material characterisation data expected in the above-mentioned engineering contexts requires relative ease of calibration without losing the capability to capture the ductile and rate-dependent aspects sufficiently accurately.

Second, ductile fracture often involves slant fracture, which is fracture that occurs in a direction that is slanted with respect to the direction of the maximum principal stress. Being able to simulate slant fracture occurrence is important because it is a characteristic feature of ductile fracture behaviour, and increased slant fracture occurrence has been correlated with properties such as reduced strain hardenability [185], increased loading rate [186], and greater specimen thickness [185]. While slant fracture behaviour has been successfully captured in simulations of uncracked quasi-static [187–189], cracked quasi-static [179, 189, 190] and sharply notched[1] dynamic [191, 192] tests, simulating an uncracked, dynamic and rate-dependent Charpy test that accounts for the ductile slant fracture behaviour proves to be a challenge[2] [177, 178, 196], let alone accounting for it in both the Charpy and the static fracture toughness test using one material model.

Therefore, a model that emphasises the balance between model simplicity, generalisability and capability to simulate complex behaviour in both the Charpy and SENB test is developed and presented in this paper. A thermodynamically consistent phenomenological rate-dependent damage-softening material model is used in finite-element calculations of fracture toughness (from single-edge notched bending specimens), notch toughness (from Charpy specimens) and ductility (from uniaxial tensile specimens). The model formulation is given in Section 4.3. Sections 4.5 to 4.7 describe the calibration of the model parameters to experiments on an S690QL [10] steel and an AH36 [19] steel. The validity of the modelling framework is shown by its ability to simultaneously model the 3 mechanical tests involving different stress states, strain rates and geometries (cracked and uncracked) with the same input parameter values describing the given material, capturing the measured mechanical properties, the load-deformation response and the characteristically ductile slant fracture surfaces with reasonable accuracy. Attention is given to the effects of the material parameters on the resulting mechanical properties.

4.3 CONSISTENCY MODEL FOR VISCOPLASTICITY WITH DAMAGE SOFTENING AND THERMAL SOFTENING

In this work, the elasto-viscoplastic consistency model [197] with an associated flow rule is coupled with damage softening [187] and thermal softening [198] acting on

1 Though not precracked by fatigue, dynamic drop-weight tear tests such as those performed in [191, 192] involve a sharp chiselled notch which has a much smaller radius, between 0.013 and 0.025 mm [193], than in Charpy tests, which have a notch radius of 0.25 mm [194].

2 An earlier version of the present model has been shown to capture slant fracture in Charpy-test simulations in a recent conference paper [195] on the effect of strain hardening and of Lode dependence of the fracture strain on slant fracture in Charpy test simulations.

the plastic hardening function. Von Mises yielding is assumed such that the yield function is expressed as:

$$f = \sigma_v - \bar{\sigma} R \beta X \tag{4.1}$$

where σ_v is the von Mises equivalent stress; $\bar{\sigma}$ is the plastic strain-hardening stress (Section 4.3.1); R is the rate-dependence factor (Section 4.3.2); β is the softening coefficient (Section 4.3.3); X is the thermal softening factor (Section 4.3.4); and $\sigma = \bar{\sigma} R \beta X$ is the flow stress. Incremental stresses due to these effects coupled in Eq. (4.1) are calculated using a return mapping solution ensuring thermodynamical consistency (Section 4.3.5).

4.3.1 *Plastic hardening model*

A quasi-static undamaged true plastic stress-strain relation (Fig. 4.1) that features a yield plateau and a Swift [69] hardening curve (Eqs. (4.2) and (4.3)) is used:

$$\bar{\sigma} = \begin{cases} \sigma_y \left(\dfrac{\varepsilon_{sh} - \dfrac{\sigma_y}{E}}{\varepsilon_{sh,p}} \varepsilon_p + \dfrac{\sigma_y}{E} + 1 \right) & 0 < \varepsilon_p < \varepsilon_{sh,p} \\ K(\varepsilon_p - \varepsilon_0)^n & \varepsilon_p \geq \varepsilon_{sh,p} \end{cases} \tag{4.2}$$

$$\varepsilon_{sh,p} = \ln(1 + \varepsilon_{sh}) - \ln\left(1 + \frac{\sigma_y}{E}\right) \tag{4.3}$$

where $\bar{\sigma}$ is the plastic strain hardening stress; ε_p is the true equivalent plastic strain; ε_{sh} and $\varepsilon_{sh,p}$ are respectively the total engineering strain and the true equivalent plastic strain corresponding to the end of the yield plateau; K is the strength coefficient; n is the strain hardening exponent; and ε_0 is the Swift [69] offset parameter. The slight hardening in the yield plateau in Eq. (4.2) arises from converting a flat plateau expressed in terms of engineering stress into one that is expressed in terms of true stress.

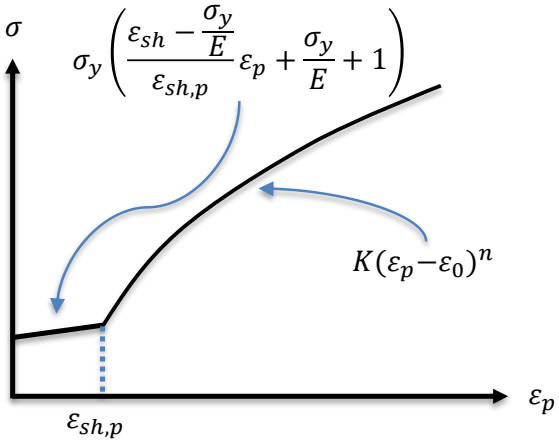


Figure 4.1: Swift-type [69] power-law true stress-strain curve with a yield plateau.

Given the Young's modulus E, yield strength σ_y, ultimate strength σ_u, yield plateau length ε_{sh} and the uniform (necking) elongation ε_u, the parameters n, K and

ε_0 of the plastic hardening model can be estimated using theoretical knowledge about the strain hardening's relation to the ultimate strength σ_u induced by necking. This is done by assuming that σ_u satisfies the Considère [52] criterion for necking, which results in Eqs. (4.4) and (4.5).

$$n = \varepsilon_{u,p} - \varepsilon_0 \tag{4.4}$$

$$K\left(\varepsilon_{u,p} - \varepsilon_0\right)^n = \sigma_u\left(1 + \varepsilon_u\right) \tag{4.5}$$

where $\varepsilon_{u,p}$ is the true plastic strain corresponding to the occurrence of necking instability and the ultimate tensile stress, which is related to ε_u by:

$$\varepsilon_{u,p} = \ln\left(1 + \varepsilon_u\right) - \ln\left(1 + \frac{\sigma_u}{E}\right) \tag{4.6}$$

In addition, considering that the power curve intersects with the yield plateau at a true plastic strain $\varepsilon_p = \varepsilon_{sh,p}$ results in Eq. (4.7):

$$K\left(\varepsilon_{sh,p} - \varepsilon_0\right)^n = \sigma_y(1 + \varepsilon_{sh}) \tag{4.7}$$

Combining Eqs. (4.3) to (4.7) enables K, n and ε_0 to be solved and the true stress-strain curve to be approximated, given σ_y, σ_u, E, ε_{sh} and ε_u. It will be seen in Section 4.5 below that these assumptions give good predictions of the engineering stress-strain response until necking, using only the experimental σ_y, σ_u, E, ε_{sh} and ε_u as input. This semi-analytical approach to the description of the true stress-strain curve is valuable for engineering applications, because in typical situations during the testing for material certification for structural steels, the entire stress-strain history is not available. However, the σ_y and σ_u are recorded in the material test certificates, while empirical relations for ε_{sh} and ε_u obtained from large databases for structural steels exist [54, 199].

4.3.2 *Rate-dependence model*

To take the effect of the strain rate on the plastic flow stress into account, the plastic stress-strain curve is scaled based on the Cowper-Symonds model [182]. The original formulation of the Cowper-Symonds [182] model is shown in Eq. (4.8):

$$R = 1 + \left(\frac{\dot{\varepsilon}}{C}\right)^{\frac{1}{q}} \tag{4.8}$$

where R is the rate-dependence factor by which the static flow stress is to be multiplied to give the rate-dependent yield stress; $\dot{\varepsilon}$ is the uniaxial strain rate; C is the Cowper-Symonds coefficient; and q is the Cowper-Symonds exponent.

To enable this to be applied to the viscoplastic consistency model presently used, two modifications are implemented. First, the strain-rate effect given by R, which is determined experimentally in the literature with respect to the uniaxial strain rate $\dot{\varepsilon}$, is assumed to act equivalently with respect to the equivalent plastic strain rate $\dot{\varepsilon}_p$. This is in accordance with the understanding that, for incompressible materials subject to uniaxial tension, $\dot{\varepsilon}_p$ is by definition equal to $\dot{\varepsilon}$ until necking. Second, the parameter $\dot{\varepsilon}_{p0}$ is introduced to enable the translation of the R versus $\dot{\varepsilon}_p$ relation

with respect to the $\dot{\varepsilon}_p$ axis by $-\dot{\varepsilon}_{p0}$, so that the gradient of R with respect to $\dot{\varepsilon}_p$ is finite for $\dot{\varepsilon}_p = 0\,\mathrm{s}^{-1}$, since this is required for the return mapping calculations (Section 4.3.5) to converge, and this gradient in the original formulation is infinite. Additionally, $R = 1$ is made to coincide with $\dot{\varepsilon}_p = \dot{\varepsilon}_{p,uni}$, the equivalent plastic strain rate corresponding to uniaxial testing through the use of a translation in the R-axis.

This results in the equation for R implemented in the present model:

$$R = 1 - \left(\frac{\dot{\varepsilon}_{p,uni} + \dot{\varepsilon}_{p0}}{C}\right)^{\frac{1}{q}} + \left(\frac{\dot{\varepsilon}_p + \dot{\varepsilon}_{p0}}{C}\right)^{\frac{1}{q}} \tag{4.9}$$

The quasi-static-uniaxial-testing equivalent plastic strain rate parameter $\dot{\varepsilon}_{p,uni}$ is here taken to be $0.000\,25\,\mathrm{s}^{-1}$ according to the ISO 6892-1 tensile testing standard [200], and the same value is assumed for the small translation $\dot{\varepsilon}_0 = \dot{\varepsilon}_{p,uni}$. Least-squares fitting to existing experimental data was performed to obtain the Cowper-Symonds parameters for structural steels with nominal strengths in the range of 345 to 355 MPa [165, 201–206] and 690 MPa [207–210] separately, as shown in Fig. 4.2, for use in the simulations of the tested AH36 and S690QL steels. The data from Dong et al. [211] was not included in the fit, due to its nature as an outlier, in which all except two points from this source plotted below the mutually overlapping data cloud formed by the other sources.

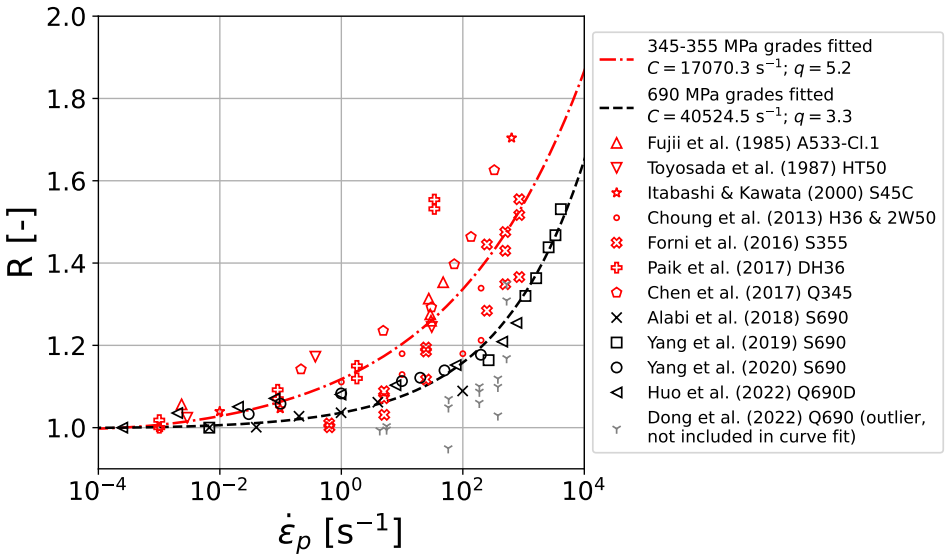


Figure 4.2: Least-squares fit of R and experimental data from the literature [165, 201–211].

In addition to accounting for the high strain rate occurring in Charpy tests, the rate dependence introduces viscosity, which has the important role of helping to eliminate the mesh sensitivity (non-convergence with mesh refinement) [197, 212] faced by local approaches to material softening such as the classic MMC damage-softening model [187].

4.3.3 *Damage model*

To describe the initiation of damage softening, the strain formulation of the modified Mohr-Coulomb (MMC) [151] fracture surface is used:

$$\varepsilon_f = \left\{ \frac{K}{c_2} \left[c_3 + \frac{\sqrt{3}}{2-\sqrt{3}}(1-c_3) \left(\sec \frac{\bar{\theta}\pi}{6} - 1 \right) \right] \times \left[\sqrt{\frac{1+{c_1}^2}{3}} \cos \frac{\bar{\theta}\pi}{6} + c_1 \left(\eta + \frac{1}{3} \sin \frac{\bar{\theta}\pi}{6} \right) \right] \right\}^{-\frac{1}{n}} \tag{4.10}$$

where ε_f is the damage initiation strain; η is the stress triaxiality; $\bar{\theta}$ is the normalised Lode-angle [213]; and c_1, c_2 and c_3 are the MMC model parameters.

The sum of the incremental equivalent plastic strains relative to the instantaneous ε_f is used to quantify the amount of damage, as given by the damage indicator D:

$$D = \int_0^{\varepsilon_p} \frac{1}{\varepsilon_f} \, d\varepsilon_p \tag{4.11}$$

Material softening starts when enough plastic straining has occurred such that $D = 1$, and complete degradation (corresponding to finite element deletion) occurs when D reaches the critical damage value D_c, as described by Eq. (4.12) [187]:

$$\beta = \begin{cases} 1 & D \leq 1 \\ \left(\dfrac{D_c - D}{D_c - 1} \right)^m & 1 < D < D_c \\ 0 & D = D_c \end{cases} \tag{4.12}$$

where β is the softening parameter in the yield function (Eq. (4.1)), and m is the softening exponent.

It is worth noting that the use of Eq. (4.12) implies that the MMC locus (Eq. 4.10) defines the damage initiation strains instead of the fracture initiation strains as assumed in the original uncoupled version of the MMC model [151]. This slight modification facilitates the coupling of softening effects to the MMC model based on stress-state-dependent damage softening initiation criterion and has been effectively applied by several others for the modelling of softening behaviour in steel [187, 214, 215] and aluminium [216].

It should be noted that here, the formulation of the MMC fracture strain surface is accepted as is, but for simplicity, the associated Lode-dependent Bai-Wierzbicki hardening rule [151, 213] used to derive the MMC strain surface is not adopted. Although a different strain hardening rule (Eq. (4.2)) is used here, the c_3 originating from the Bai-Wierzbicki hardening rule is kept as a parameter in the failure strain surface for its use in controlling the failure strain's Lode-dependence. As a result of this, the present approach uses a strain-based damage initiation criterion instead of the stress-based damage initiation criterion on which the MMC model was originally established. The stress at the occurrence of the damage initiation strain does not necessarily coincide with the stress given by the original MMC stress envelope [151]. The MMC failure strain surface is assumed to be in itself suitable for

phenomenologically describing the fracture strains regardless of the MMC stresses. This widely used phenomenological, strain-based take of the MMC fracture model has been successful in describing ductile fracture behaviour in both precracked [214, 215] and initially uncracked [187, 216, 217] geometries, performing well over a wide range of stress triaxialities and Lode angles, while involving only 3 damage initiation parameters.

The parameter c_1 determines the triaxiality dependence of the damage initiation strain. Notably, $c_1 = 0$ corresponds to the limiting case of the maximum shear stress fracture criterion which with von Mises yielding traditionally reduces to a single-parameter (c_2) fracture model. Furthermore, the parameters c_2 and c_3 can be rewritten in a normalised form that relates directly to the maximum and minimum strains on the $c_1 = 0$ fracture strain locus, for ease of comparison during strain-based calibration, as given by Eqs. (4.13) and (4.14):

$$C_2 = \left(\frac{2c_2}{K}\right)^{\frac{1}{n}} \tag{4.13}$$

$$C_3 = \left(\frac{\sqrt{3}c_2}{Kc_3}\right)^{\frac{1}{n}} \tag{4.14}$$

C_2 is given by the expression for ε_f when $c_1 = 0$ and $\bar{\theta} = \pm 1$; and C_3 is given by the expression for ε_f when $c_1 = \bar{\theta} = 0$. The effect of this is that the maximum strain in the fracture strain surface is always equal to C_2, and the minimum strain of the fracture strain surface is always equal to C_3, regardless of the values of K and n.

C_1, a normalised form of c_1, is introduced as shown in Eqs. (4.15) and (4.16), for the ease of strain-based comparison when considering the triaxiality dependence of the fracture strain locus. $C_1 = C_3$ corresponds to the triaxiality-independent $c_1 = 0$ condition, and changing C_1 introduces triaxiality dependence by adjusting the triaxiality-independent fracture strain locus to pass through $\varepsilon_f = C_1$ at $\bar{\theta} = 0$ and $\eta = 2.5$, which is the perfectly plastic, plane-strain solution for the stress state in front of the crack tip [218].

$$C_1 = \left(\frac{c_2}{c_3 K Z}\right)^{\frac{1}{n}} \tag{4.15}$$

where Z is given by:

$$Z = \sqrt{\frac{1 + {c_1}^2}{3}} + 2.5c_1 \tag{4.16}$$

A negative triaxiality cut-off value of $\eta = -1/3$ [219] for the damage initiation criterion is introduced by additionally increasing the ε_f, given by (Eq. (4.10)), quickly but continuously as η drops below $-1/3$. For high triaxialities exceeding 3.5, the ε_f is kept at a constant level determined by its value at $\eta = 3.5$, which typically only comes into effect when an element has $D > 1$ and is near deletion. The continuous nature of the addition to ε_f below the cut-off triaxiality and the constant ε_f for high η ensure that ε_f does not have extremely large or small values in those η ranges, which would cause convergence errors.

4.3.4 *Thermal softening model*

The dynamic Charpy test occurs at time scales that can be approximated as adiabatic [183]. Studies considering the effect of adiabatic heating on the Charpy impact test by Tanguy et al. [220] and Seo et al. [221] using temperature-dependent material models have shown that the thermal softening caused by adiabatic heating in the Charpy tests should not be neglected. Here, a thermal softening factor based on the Johnson-Cook [198] plasticity model is adopted in the yield function (Eq. (4.1)) for the Charpy simulation, as given in Eq. (4.17):

$$X = 1 - \left(\frac{\Theta - \Theta_r}{\Theta_m - \Theta_r} \right)^{m_x} \tag{4.17}$$

where Θ is the temperature, Θ_m is the melting temperature, Θ_r is the room temperature, and m_x is the thermal softening exponent.

The rate of change of temperature at each material point at each increment is calculated from Eq. 4.18:

$$\dot{\Theta} = \frac{\chi \dot{\mathcal{D}}_p}{c} \tag{4.18}$$

where χ is the Taylor-Quinney [222] energy coefficient, c is the specific heat capacity of the material, and $\dot{\mathcal{D}}_p$ is the rate of internal work done attributed to plastic deformation as given by Eq. (4.19) [223]:

$$\dot{\mathcal{D}}_p = \frac{\boldsymbol{\sigma} : \dot{\boldsymbol{\varepsilon}}_{\boldsymbol{vp}}}{\rho} \tag{4.19}$$

where $\boldsymbol{\sigma}$ is the Cauchy stress tensor, $\dot{\boldsymbol{\varepsilon}}_{\boldsymbol{vp}}$ is the viscoplastic strain rate tensor, and ρ is the density of the material.

The proportion χ of the internal work due to plastic deformation $\mathcal{D}_p$ that is converted to heat is assumed to be 0.9, as proposed by Meyers [224], where the remaining latent part of the work is associated with defects and changes in the physical properties of the crystalline material [222, 224] (e.g. dislocation pile-ups). Values of Θ_m, Θ_r, m_x, c found in the literature for low carbon steels with yield strength and chemical composition similar to the present steels are adopted here. For the AH36 steel, the parameters for the similarly graded low-carbon, low-alloy X52 [18] pipeline steel reported by Seo et al. [221] and Liakat and Khonsari [225] are used, being $\Theta_m = 1500\,^{\circ}\mathrm{C}$, $\Theta_r = 25\,^{\circ}\mathrm{C}$, $m_x = 0.8$ and $c = 480\,\mathrm{J\,kg^{-1}\,^{\circ}C^{-1}}$. For the S690QL steel, the parameters for Weldox 700 E steel (which fulfils the S690QL standard [10]) reported by Dey et al. [226] are used, being $\Theta_m = 1527\,^{\circ}\mathrm{C}$, $\Theta_r = 20\,^{\circ}\mathrm{C}$, $m_x = 1.071$ and $c = 452\,\mathrm{J\,kg^{-1}\,^{\circ}C^{-1}}$.

Thermal conductivity is neglected due to the short time frame and the high plastic strain rate, and thermal expansion is neglected since the adiabatic heating is primarily concentrated in areas with large plastic strains [220]. The quasi-static tensile and SENB tests are modelled as isothermal and without any temperature dependence, such that X is constant and equal to 1.

4.3.5 *Stress-update algorithm and return mapping for coupled thermal- and damage-softening viscoplasticity model*

The plasticity calculations involve solving for the stress increment which satisfies the consistency condition $\dot{f} = 0$, i.e. that when yielding, the stress state stays on the yield surface, which evolves according to the assumed plastic-hardening (Section 4.3.1), damage-softening (Section 4.3.3), and rate-dependent (Section 4.3.2) behaviour. The yield function f (Eq. (4.1)) can be expressed in terms of its variables as:

$$f(\boldsymbol{\sigma}, \varepsilon_p, \dot{\varepsilon}_p) = \sigma_v(\boldsymbol{\sigma}) - \bar{\sigma}(\varepsilon_p) R(\dot{\varepsilon}_p) \beta(D(\varepsilon_p)) X(\Theta(\varepsilon_p)) \tag{4.20}$$

The consistency condition $\dot{f} = 0$ according to the consistency model of Wang et al. [197] is then given by:

$$\dot{f}(\boldsymbol{\sigma}, \varepsilon_p, \dot{\varepsilon}_p) = \frac{\partial f}{\partial \boldsymbol{\sigma}} \dot{\boldsymbol{\sigma}} + \frac{\partial f}{\partial \varepsilon_p} \dot{\varepsilon_p} + \frac{\partial f}{\partial \dot{\varepsilon}_p} \ddot{\varepsilon}_p = 0 \tag{4.21}$$

To solve this for the present formulation, the iterative implicit Euler-backward stress-update algorithm by Wang et al. [197] for their viscoplastic model is adapted such that it is coupled with the damage-softening of Li and Wierzbicki [187] (Section 4.3.3) and the Johnson-Cook [198] thermal softening model (Section 4.3.4) and such that the rate-dependent effect can be defined according to the Cowper-Symonds model [182] (Section 4.3.2).

First, the associated flow rule [227] is assumed:

$$\dot{\boldsymbol{\varepsilon}}_{\boldsymbol{vp}} = \dot{\lambda} \boldsymbol{n} \tag{4.22}$$

where $\dot{\boldsymbol{\varepsilon}}_{\boldsymbol{vp}}$ is the viscoplastic strain rate tensor; $\boldsymbol{n} = \dfrac{\partial f}{\partial \boldsymbol{\sigma}}$ is the gradient of the yield surface; and $\dot{\lambda}$ is the plastic strain rate multiplier.

By substituting the associated flow rule (Eq. (4.22)) into the definition of the equivalent plastic strain rate, $\dot{\varepsilon}_p$ can be expressed as shown in Eq. (4.23):

$$\dot{\varepsilon}_p = \dot{\lambda} \alpha = \dot{\lambda} \tag{4.23}$$

where $\alpha = \sqrt{\dfrac{2}{3} \boldsymbol{n} \cdot \boldsymbol{n}}$, termed the plastic coefficient, is always equal to 1 in the present study, due to the assumption of von Mises yielding (Eq. (4.20)). Furthermore, substituting the associated flow rule with von Mises yielding (Eqs. (4.22) and (4.23)) into Eq. (4.19) allows $\dot{\mathcal{D}}_p$ to be expressed in terms of equivalent stress and equivalent strain (Eq. (4.24)). This makes the change in temperature a simple function of the change in equivalent plastic strain, such that Θ does not need to be solved as an extra independent variable in iterative solution of the yield and consistency functions (Eqs. (4.20) and (4.21)).

$$\dot{\mathcal{D}}_p = \frac{\sigma_v \dot{\varepsilon}_p}{\rho} \tag{4.24}$$

Substituting Eq. (4.23) into Eq. (4.21), it becomes convenient to define a hardening modulus h and a viscosity parameter s [197] for the iterative solution of Eq. (4.21), such that:

$$\dot{f}(\boldsymbol{\sigma}, \varepsilon_p, \dot{\varepsilon}_p) = \boldsymbol{n}\dot{\boldsymbol{\sigma}} - h\dot{\lambda} - s\ddot{\lambda} \tag{4.25}$$

where h and s can then be expressed in terms of the parameters of the Li and Wierzbicki [187] damage-softening model, the Cowper-Symonds [182] rate-dependence model and the Johnson-Cook [198] thermal softening model:

$$h = -\frac{\partial f}{\partial \varepsilon_p}\frac{\dot{\varepsilon}_p}{\dot{\lambda}} = R\left(\frac{\partial \beta}{\partial \varepsilon_p}\bar{\sigma}X + \frac{\partial \bar{\sigma}}{\partial \varepsilon_p}\beta X + \frac{\partial X}{\partial \varepsilon_p}\bar{\sigma}\beta\right) \tag{4.26}$$

$$s = -\frac{\partial f}{\partial \dot{\varepsilon}_p}\frac{\ddot{\varepsilon}_p}{\ddot{\lambda}} = \frac{\partial R}{\partial \dot{\varepsilon}_p}\beta\bar{\sigma}X \tag{4.27}$$

From Eqs. (4.2), (4.9), (4.11), (4.17), (4.18) and (4.24), $\frac{\partial \beta}{\partial \varepsilon_p}$, $\frac{\partial \bar{\sigma}}{\partial \varepsilon_p}$, $\frac{\partial X}{\partial \varepsilon_p}$ and $\frac{\partial R}{\partial \dot{\varepsilon}_p}$ can be expressed as shown in Eqs. (4.28) to (4.31).

$$\frac{\partial \beta}{\partial \varepsilon_p} = \begin{cases} 0 & D \leq 1 \\ -\dfrac{m\beta}{\varepsilon_f(D_c - D)} & 1 < D < D_c \end{cases} \tag{4.28}$$

$$\frac{\partial \bar{\sigma}}{\partial \varepsilon_p} = \begin{cases} \sigma_y \dfrac{\varepsilon_{sh} - \dfrac{\sigma_y}{E}}{\varepsilon_{sh,p}} & 0 < \varepsilon_p < \varepsilon_{sh,p} \\ Kn{\varepsilon_p}^{n-1} & \varepsilon_p > \varepsilon_{sh,p} \end{cases} \tag{4.29}$$

$$\frac{\partial X}{\partial \varepsilon_p} = -\frac{m_x \chi \sigma_v}{\rho c(\Theta_m - \Theta_r)}\left(\frac{\Theta - \Theta_r}{\Theta_m - \Theta_r}\right)^{m_x - 1} \tag{4.30}$$

$$\frac{\partial R}{\partial \dot{\varepsilon}_p} = \frac{1}{q(\dot{\varepsilon}_p + \dot{\varepsilon}_{p0})}\left(\frac{\dot{\varepsilon}_p + \dot{\varepsilon}_{p0}}{C}\right)^{\frac{1}{q}} \tag{4.31}$$

The expanded algorithm for the iterative solution of Eq. (4.21) to find the incremental plastic strains and updated stresses in each plastic FEA increment, implemented as a VUMAT subroutine in Abaqus Explicit [228], is shown in Appendix B. The description above highlights only the model details specific to the present formulation. Details on the other aspects of the consistency model and algorithm can be found in [197] and [229]. It is worth noting that this elasto-viscoplastic consistency model is, as its name suggests, thermodynamically consistent, because the consistency condition (Eq. (4.21)) and the Kuhn-Tucker [230] relations are satisfied in the stress-update calculations (Appendix B).

4.4 MODEL CALIBRATION TO EXPERIMENTS

The calibration of ductile damage models using conventional methods requires considerable experimental and numerical modelling effort. Since the fracture behaviour depends on the stress state, the traditional approach to calibrating damage models involves a series of experiments on specimens with geometries that induce specific stress states in order to determine the stress-state-dependent fracture locus experimentally. This is often achieved by using variations of the tension, butterfly,

notched or grooved specimens. Digital image correlation or reverse-engineering with numerical models, or both, are often required to determine obtain the fracture strains from these tests [171, 231].

Recent work in the literature has achieved some success in simplifying this calibration process for certain cases, such as the SENB-based calibration procedure proposed by Coppejans and Walters [232] and the uniaxial-tensile-test-based procedure proposed by Xin and Veljkovic [233]. In a similar vein, this work reduces the experimental effort by calibrating the model parameters using the mechanical (force-displacement and energy) response of the uniaxial tensile test, the instrumented Charpy test and the single-edge notched bending test, while ensuring that the ductile fracture mechanism observed in the slant crack propagation behaviour is captured. A considerable range of triaxialities is involved, despite the relatively low number of tests (1/3 pre-necking in the tensile test; ~ 1.7 before crack growth in the Charpy; and ~ 2.2 before crack growth in the SENB). Since tensile tests and instrumented Charpy tests are widely used and easily performed, the only significant effort arises in the single-edge notched bending test.

Fig. 4.3 summarises the material parameters of the present model and the associated calibration processes. The Young's modulus E is obtained from the linear-elastic stiffness of the uniaxial tensile test, and the Poisson's ratio ν is assumed to be 0.3. The plasticity parameters σ_y, $\varepsilon_{sh,p}$, K, n and ε_0 are found from the pre-necking tensile behaviour as described in Section 4.3.1. The rate dependence parameters C and q are estimated using a least-squares fit of the Cowper-Symonds [182] curve to empirical data in the literature, while the other rate dependence parameters $\dot{\varepsilon}_{p,uni}$ and $\dot{\varepsilon}_{p0}$ are defined based on the quasi-static uniaxial testing rate, as described in Section 4.3.2. The thermal softening parameters Θ_m, Θ_r and m_x and the specific heat capacity c are found from experiments on similar steels in the literature, as described in Section 4.3.4.

The damage parameters C_1, C_2, C_3 and D_c (with the linearity assumption of $m = 1$) are found from the fracture behaviour in the tensile (Section 4.5), Charpy (Section 4.6) and SENB (Section 4.7) test by calibrating them so that the experimental and simulated force-displacement curves agree. This involves simulating the three tests with a given set of damage parameter values, comparing the experimental and simulated force-displacement curves in all three tests, and repeating this while tuning the parameters until the force-displacement curves match for all three tests. Besides matching the overall shape of the force-displacement curves, attention is given to capturing the occurrence of slant fracture and agreement between the simulations and experiments in the fracture elongation A, the Charpy energy C_v and the maximum force of the SENB test to within 5 %. The implication of this calibration approach is that only the 5 damage parameters require calibration using finite-element simulation of only 3 tests' response histories, while the rest are taken directly from either the tensile test mechanical properties (σ_y, σ_u, $\varepsilon_{sh,p}$, ε_u) or from empirical relations (strain rate data).

Additionally, deeper investigation into the relevance of the triaxiality dependence and the nature of the softening parameters, as discussed in Section 4.8, reveals that this calibration procedure can be further reduced to be based on only 2 key parameters, C_2 and C_3, instead of all 5 damage parameters, for specific groups of steels with weak triaxiality dependence. In terms of the calibration effort required, this is

an improvement from the approaches used for other coupled viscoplastic damage models. For example, Novokshanov's [191] drop-weight tear test (DWTT) modelling approach involved 7 damage parameters and calibration to 9 different test specimen geometries. Another point of reference is Simha's [192] DWTT modelling approach, which involved 8 damage parameters and calibration to only 3 tests but which also relied on adopting 6 damage parameter values from previous calibration of a specific steel. The present approach has a smaller number of calibration parameters, requires a smaller number of tests, and does not rely on damage parameter values obtained from calibrations of other materials.

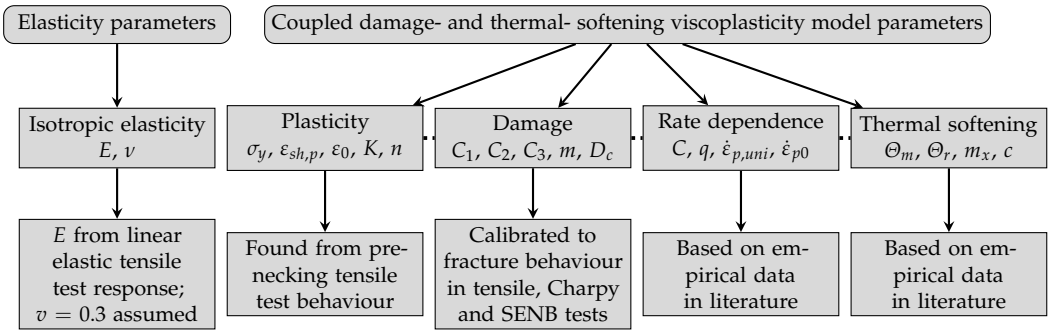


Figure 4.3: Model parameters.

The present model was separately calibrated for an S690QL [10] steel and an AH36 [19] steel to validate its capability to describe the behaviour in the 3 different mechanical tests simultaneously for a given material. The S690QL steel had a nominal thickness of 12 mm and a measured thickness varying between 12.35 and 12.80 mm. The AH36 steel had a nominal thickness of 11 mm and a measured thickness varying between 10.95 and 11.05 mm. Uniaxial tensile, Charpy and SENB specimens were made using electrical discharge machining and then tested at ambient temperature.

The specimens were modelled using C3D8R elements in Abaqus [228], which are 8-noded hexahedral elements with reduced integration and hourglass control. The density ρ of steel was assumed to be 7850 kg m^{-3}. In the simulations of the quasi-static tests, mass scaling was applied in order to model the tests within a reasonable computation time. The simulations were checked to ensure that no inertial effects large enough to influence the solution significantly were introduced. The kinetic energy was less than 1 % of the total internal energy except for the very brief period at the beginning in which the load application boundary first moves and the deformations are very small in comparison to the movement. No mass scaling was applied in the simulations of the dynamic Charpy tests. A coefficient of friction of 0.15 was assumed for the contact between the specimen and the external contact surfaces in the Charpy and SENB tests, with the exception of the two SENB support rollers, which were considered to be frictionless.

In the calibration process, it was seen that different calibration parameters led to different simulated fracture morphology, including fully flat, fully slanted and in-between situations with different amount of flat and slant fracture. However, the relationship between the calibration parameters and the transition behaviour between flat and slat fractures is outside the scope of the present study, and several

other works in the literature have been dedicated to that topic (e.g. [234–236]). All test repetitions experienced some degree of slant fracture, and as will be seen in the following sections, all the calibrated simulations had slant fracture surfaces similar in character to that observed in the experiments, although the slant fracture area in the simulations was not always the same size as that observed in the experiments. In this regard, capturing the occurrence of slant fracture is used as an indicator that the correct mechanism is being modelled and gives confidence to the calibration and the validity of the simulations.

Table 4.1 shows the parameter values for each steel, including the calibrated C_1, C_2, C_3, m and D_c, which capture the behaviour in the three tests well. The detailed results and discussion for each of the simulations are shown in Sections 4.5, 4.6 and 4.7, respectively.

Table 4.1: Material parameter values for the S690QL and AH36 steels assumed in the simulations shown in Sections 4.5 to 4.8.

(a) Plasticity and damage.

		AH36	S690QL
σ_y	[MPa]	381	836
$\varepsilon_{sh,p}$	[-]	0.0138	0.0438
ε_0	[-]	0.0077	0.0413
K	[MPa]	794.0	984.1
n	[-]	0.1409	0.0192
C_1	[-]	0.20	0.47
C_2	[-]	1.90	8.50
C_3	[-]	0.20	0.47
m	[-]	1	1
D_c	[-]	1.3	1.3

(b) Strain-rate and thermal effects and elasticity.

		AH36	S690QL
C	[s^{-1}]	17070.3	40524.5
q	[-]	5.2	3.3
$\dot{\varepsilon}_{p,uni}$	[s^{-1}]	0.00025	0.00025
$\dot{\varepsilon}_{p0}$	[s^{-1}]	0.00025	0.00025
Θ_m	[°C]	1500	1527
Θ_r	[°C]	25	20
m_x	[-]	0.8	1.071
c	[$J\,kg^{-1}\,°C^{-1}$]	480	452
E	[MPa]	208767	206064
ν	[-]	0.3	0.3

4.5 UNIAXIAL TENSILE TEST

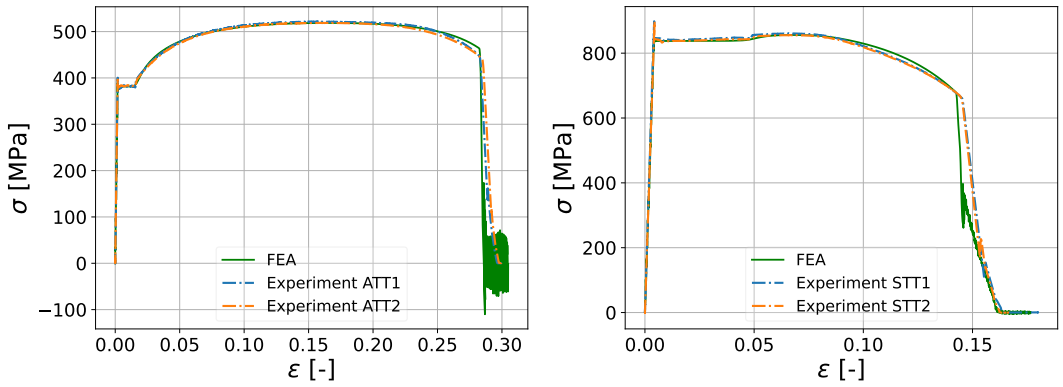
Uniaxial tensile tests were performed according to EN-ISO-6892-1 [200] on 5.5 mm and 6.0 mm thick (approximately half-thickness) specimens machined from the AH36 and the S690QL plates, respectively. The transverse material direction was tested; i.e. the rolling direction was perpendicular to the longitudinal axis of the specimens. Flat proportional dog-bone specimens with a standard width of 25 mm as given in IACS URW [237] were used. Table 4.2 shows the parallel length L_c, gauge length L_0, width W and thickness B of the specimens.

Only half the width of the specimen was modelled to save computational time, but the full specimen thickness and length up to a third of the grip area was considered in order to capture the asymmetric slant fracture mechanism. A mesh with an element size in the fracture zone of $l_c = 0.1$ mm was chosen as a result of a mesh convergence study, where l_c is the geometric-mean-based characteristic element

Table 4.2: Uniaxial tensile test specimen properties.

	Test prefix	L_c [mm]	L_0 [mm]	W [mm]	B [mm]
S690QL	STT	93.7	69.2	25.0	6.0
AH36	ATT	89.7	66.3	25.0	5.5

length, given by the cube root of the undeformed element's volume. Furthermore, a sufficiently low aspect ratio between the longitudinal dimension of the elements and the through-thickness dimension of the elements was required in order to capture slant fracture, as identified by Li and Wierzbicki [187]. In the AH36 tensile test, the ratio was 1/3, while in the S690QL tensile test which experienced greater straining, this ratio was as low as 1/5.



(a) AH36.

(b) S690QL.

Figure 4.4: Experimental and simulated engineering stress-strain curves.

The use of the hardening parameters n, K and ε_0, calculated from σ_y, σ_u, $\varepsilon_{sh,p}$ and ε_u as outlined in Section 4.3.1, combined with the empirical rate-dependence behaviour assumed in Section 4.3.2, which take into account the changing strain rates due to necking [212, 238], leads to a good estimation of both the pre-necking behaviour and the post-necking behaviour before the onset of fracture (Fig. 4.4). The onset of fracture corresponds to the start of the steep drop in the stress, which occurs when the most highly strained elements at the center of the specimen attain $D = D_c$. However, the damage initiation strains and the attainment of $D = 1$ are seen to play the largest role in determining when this drop occurs, because the material accelerates towards failure once $D = 1$ occurs. The onset of softening and the onset of fracture happens almost simultaneously in these tensile simulations, such that material softening has a small effect in the post-necking, pre-fracture regime. So, the damage parameters are calibrated by choosing parameters for which the onset of fracture and the associated slope of the degradation in the simulation plot close to those of the experiments. The A, defined as the fracture elongation over the proportional gauge length from pieced-together tensile test fragments [200], was calibrated to within $\pm 5\,\%$ of the average of the experimental values (Table 4.3). The minor discrepancy seen in the pre-damage-softening diffuse necking portion

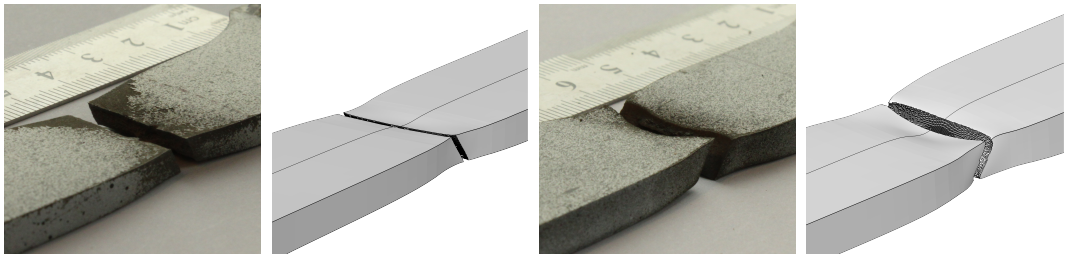
of the stress-strain curve could be attributed to the sensitivity of the localisation behaviour to the strain-rate dependence [212, 238], and the response in this region could hence be improved by more accurate strain-rate dependence modelling for the individual materials. However, since the focus of the study is on the ductile fracture behaviour, the present empirically derived curve-fitting parameters are assumed for the purpose of capturing the general trend and averaged rate-dependence behaviour for the given steels, and the calibration is performed on the damage parameters.

Fig 4.5 shows that the simulation captures key ductile fracture features observed in both the AH36 and S690QL tensile tests, such as a necking zone, through-thickness slant fracture and through-width tapering of the fracture surface. The more pronounced thickness reduction at the centre of the neck observed in the S690QL tensile test than in the AH36 tensile test was also represented in the simulation.

Table 4.3: Experimental and finite-element comparisons for the tensile test properties.

		AH36			S690QL		
		ATT1	ATT2	FEA*	STT1	STT2	FEA*
E	[MPa]	204865	208767	205142	214013	206064	204682
σ_y	[MPa]	379	381	381	840	836	837
σ_u	[MPa]	521	518	519	860	855	856
σ_y/σ_u	[-]	0.73	0.74	0.73	0.98	0.98	0.98
ε_{sh}	[-]	0.0155	0.0157	0.0147	0.0480	0.0490	0.0389
ε_u	[-]	0.1566	0.1630	0.1650	0.0671	0.0668	0.0675
A_ε	[-]	0.2967	0.2986	0.2859	0.1635	0.1624	0.1621
A	[-]	0.28	0.29	0.29	0.15	0.16	0.16

*Note these are output values from the FEA results and not the input values to the FEA. The input E, σ_y, σ_u, ε_{sh} and ε_u for AH36 and S690QL simulations are taken from the experiments ATT2 and STT2, respectively, which result in the hardening parameters shown in Table 4.1.



(a) AH36 test ATT1 (b) AH36 simulation. (c) S690QL test STT1. (d) S690QL simulation.

Figure 4.5: Fracture morphology in the tensile test.

4.6 CHARPY IMPACT TESTS

Three instrumented Charpy impact tests [194, 239] were performed on each steel grade for the transverse direction of the material, resulting in Charpy impact energies as given in Table 4.4. An MTS-E22 instrumented Charpy testing machine set up with a pendulum mass of 32.85 kg, a pendulum energy of 450 J and a striking speed of 5234 mm s^{-1} was used. Half of the Charpy specimen was simulated (Fig. 4.6), with a plane of symmetry at half thickness, so that slant fracture could be captured. The mesh was refined in a mesh convergence study resulting in a chosen characteristic length l_c of ∼0.06 mm for the elements directly above the notch.

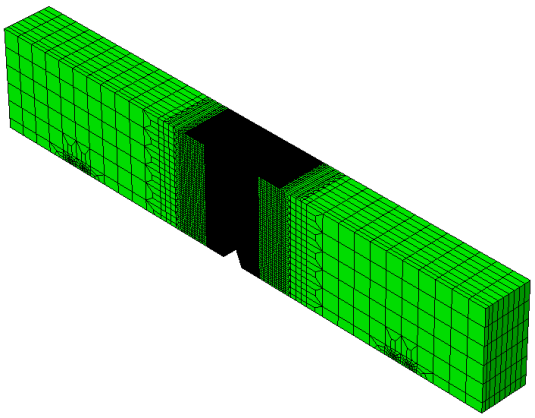


Figure 4.6: Half model of Charpy specimen with mesh refinement

For each steel grade, the force-displacement plot (Fig. 4.7) of the test giving the median impact energy of the three is used for calibration of the material parameters. The energies calculated from the force-displacement extracted from the finite-element simulations were within 5 % of the corresponding experimental Charpy impact energies (Table 4.4). Fig. 4.7 shows both the simulations with and without thermal softening due to adiabatic heating. It is seen that adiabatic heating has a negligible effect on the force-displacement curve for the AH36 simulation, while in the S690QL simulation, the effect is significant and serves to greatly improve the quality of the material model calibration, considering that a good calibration necessitates capturing the behaviour in the Charpy, SENB and tensile test simultaneously, and the SENB and tensile tests are assumed to be isothermal. The effect being greater in the S690QL steel correlates with the significantly higher notch toughness and Charpy impact energy of the S690QL steel in comparison with the AH36 steel (Table 4.4), since the adiabatic heating is caused by the dissipated energy. This also corroborates the findings in studies by Tanguy et al. [220] and [221] that the adiabatic heating effect should not be neglected in simulations of ductile Charpy tests, despite the widely adopted practice in existing work on ductile Charpy modelling, e.g. [178, 240–243], to neglect it. Hence, the adiabatic heating should be considered at least for ductile Charpy tests with high C_v.

Fig. 4.7 shows that the general shape of the force-displacement response was captured, although the post-peak drop in the force for the S690QL simulation occurred earlier than in the experiment. Figs. 4.8 and 4.9 show that the simulation captures the characteristic shear lips observed in both the AH36 and S690QL Charpy

tests, although the amount of slant fracture was not accurately represented. The simulations predict larger shear lips in the AH36 than in the S690QL Charpy tests, while the reverse is seen in the experiments. The FEA correctly predicted a full separation of the specimen for the AH36. However, it underpredicted the amount of remaining ligament in the S690QL Charpy test, giving a response in which the specimen is just on the verge of full separation by the end of the test, while the specimen remains in one piece in the experiment. The calibration process focussed on capturing the C_v and general shape of the force-displacement curve, since these are the more readily information available from Charpy tests in practice, particularly the C_v, such as is found in mill test certificates. The ability of the model to produce the approximate form of the shear lips gives confidence that the appropriate mechanism and stress state distribution shape are being accounted for. The contour plots of the stress state distributions will be discussed in more detail in comparison with the SENB fracture behaviour in Section 4.8.3.

While the fracture surface of AH36 shown in Fig. 4.8c is shiny and mostly flat, fractography with a scanning electron microscope has confirmed that it failed in a ductile, void-dominated failure mode.

Table 4.4: Experimental and simulated Charpy impact energies from the instrumented Charpy tests.

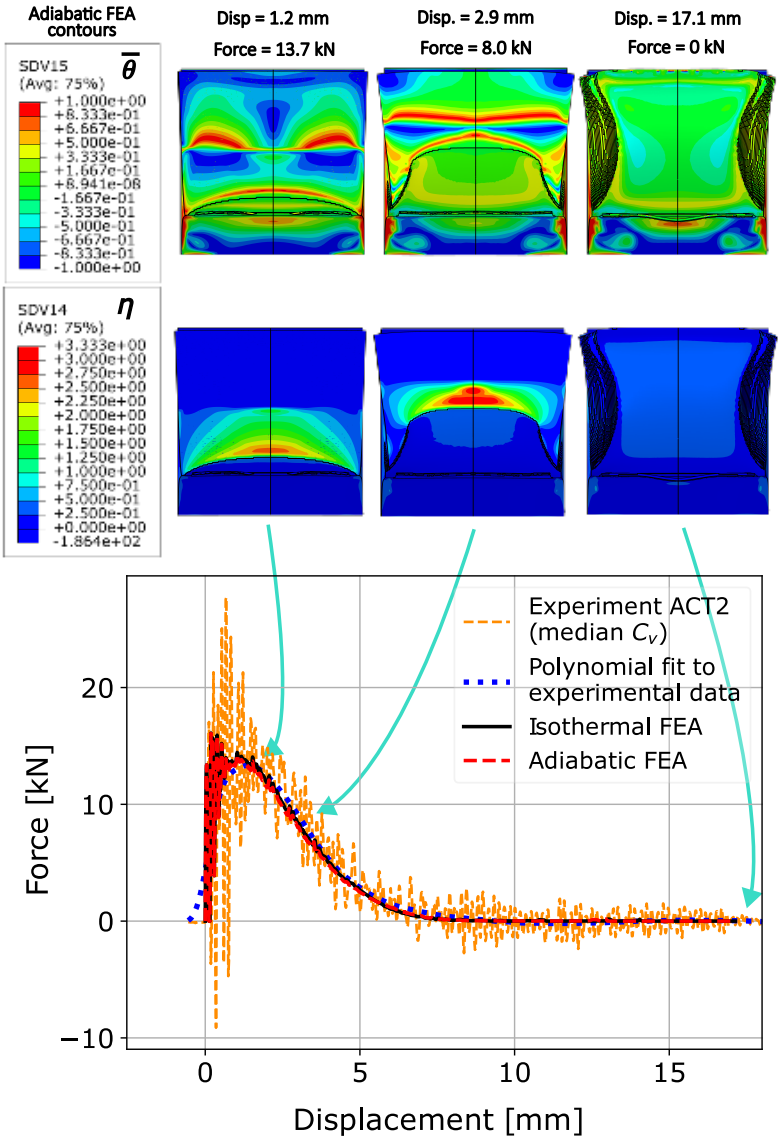
	Experimental C_v [J]				FEA C_v [J]	
	1	2	3	mean	adiabatic	isothermal
AH36	51.1	49.7	38.8	46.5	47.2	48.4
S690QL	197.2	217.7	204.2	206.4	209.4	223.2

4.7 SINGLE-EDGE NOTCHED BENDING TEST

Full-thickness SENB tests were performed on the AH36 and S690QL steels according to ASTM E1820-23b [244]. The materials were tested in the direction transverse to the rolling direction; i.e. the material's transverse direction was aligned with the longitudinal axis of the specimen. Table 4.5 shows the thickness B, width W, length L, notch-mouth opening N, notch width w, notch length a_n, measured initial cracked length a_0, compliance-estimated initial crack length a_{0q}, measured physical crack extension Δa_p and the compliance-estimated crack extension Δa_{pq} from the SENB tests. The fracture surface and the crack extension measurements are shown in Fig. 4.10.

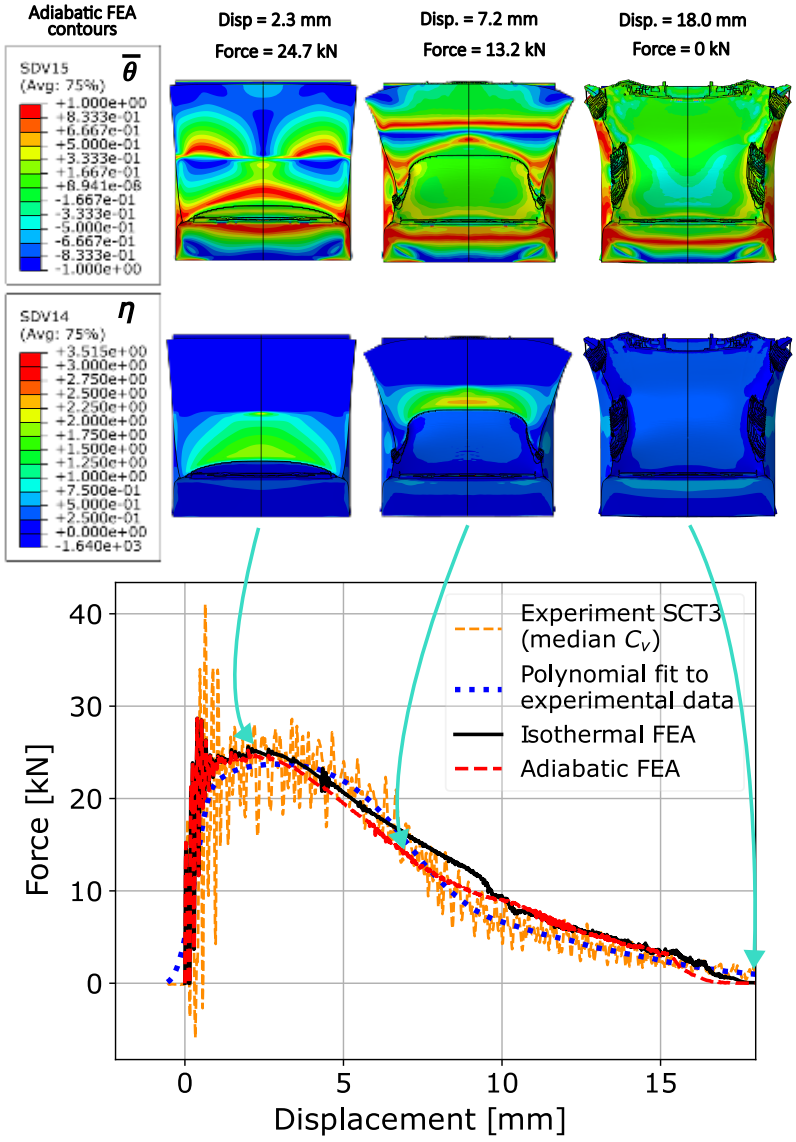
Table 4.5: Single-edge notched bending specimen properties.

Grade	Test	B	W	L	S	N	w	a_n	a_0	a_{0q}	Δa_p	Δa_{pq}
		All in [mm]										
AH36	AST3	10.9	21.9	101.1	88.0	3.0	0.32	9.7	12.47	12.57	2.57	1.42
S690	SST3	12.3	24.0	110.3	96.0	3.0	0.32	10.7	14.93	15.17	0.70	0.85



(a) AH36.

Figure 4.7: Experimental and simulated Charpy impact force-displacement curves.

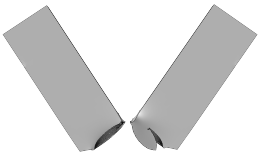


(b) S690QL.

Figure 4.7: Experimental and simulated Charpy impact force-displacement curves.



(a) Test ACT2 side view.



(b) FEA side view.



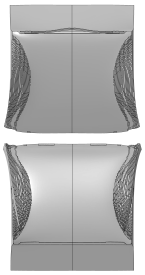
(a) Test SCT3 side view.



(b) FEA side view.



(c) Test ACT2 crack face.



(d) FEA crack face.

Figure 4.8: Fracture morphology in the AH36 Charpy test.



(c) Test SCT3 crack face.



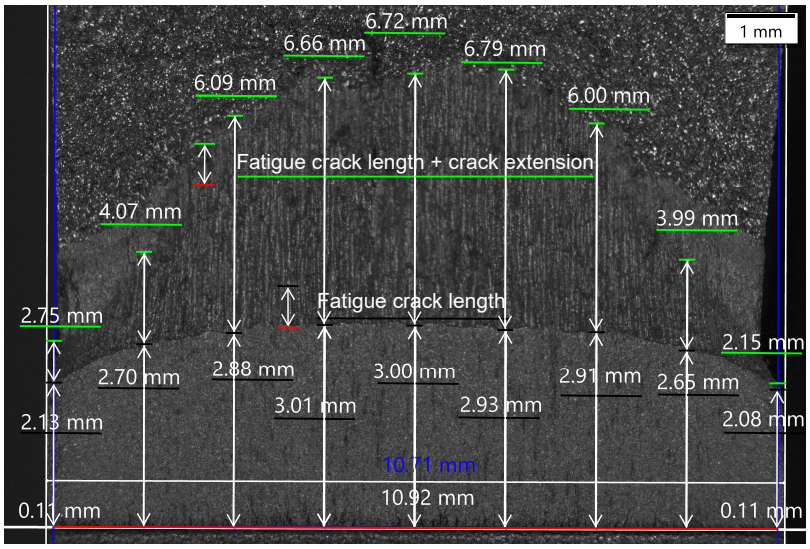
(d) FEA crack face.

Figure 4.9: Fracture morphology in the S690QL Charpy test.

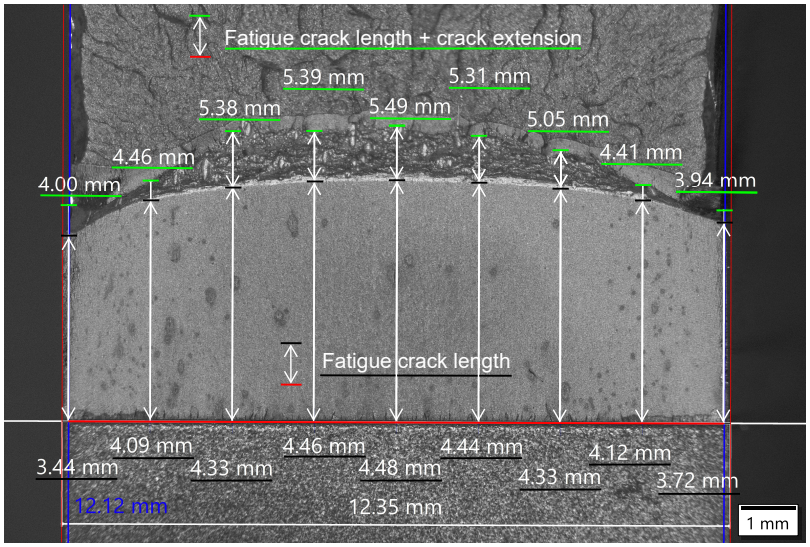
For simplicity, the initial fatigue crack in the simulations was modelled as a flat straight-through crack with a constant through-thickness length equal to the measured a_0. The sharp crack tip ended in a node, as shown in Fig. 4.11. The mesh was refined in a mesh convergence study resulting in a chosen characteristic length l_c of ~0.08 mm for the elements in the crack area. Like the Charpy simulation, a half model with a plane of symmetry at half thickness was used so that slant fracture could be captured (Fig. 4.12).

The unloading compliance method based on the crack-mouth opening displacement (CMOD) was applied to both the experiments and the simulations in order to obtain force-CMOD (Fig. 4.13) and $J - \Delta a$ curves (Fig. 4.14). Bending and rotation corrections for the SENB calculations paired with Bakker's [245] compliance equations as suggested by Wallin [246] were used.

The early-stage crack length estimates obtained from the compliance method applied to the finite-element simulation resulted in an underestimation of a of up to ~2 mm at low CMOD (Figs. 4.15a and 4.15b) in comparison to the physically measured a_0 which was also assumed in the simulation. This could be attributed to the inadequacy of the applied compliance methodology for capturing initial crack-tip blunting [247] as well as the discrepancy between the actual curved initial crack front (Fig. 4.10) and the assumed flat initial crack front in the simulation. Therefore, the ASTM E1820-prescribed [244] adjustment for a_{0q} was applied using the (a, J) data points excluding those determined at forces below the maximum precracking force, instead of using all the (a, J) data points below the maximum achieved force. The crack growth values (Fig. 4.15) were calculated with respect to the corrected a_{0q}, and a power curve was then fitted to the data points excluding Δa values outside of the 0.15 mm exclusion line in order to determine the critical J_Q from the intersection with the 0.2 mm offset line, according to standard procedure [244]. This excludes the early non-linearities and crack-tip blunting effects, which make early compliance-based a values non-realistic, from the determination of the



(a) AH36.



(b) S690QL.

Figure 4.10: Crack length measurements from SENB tests.

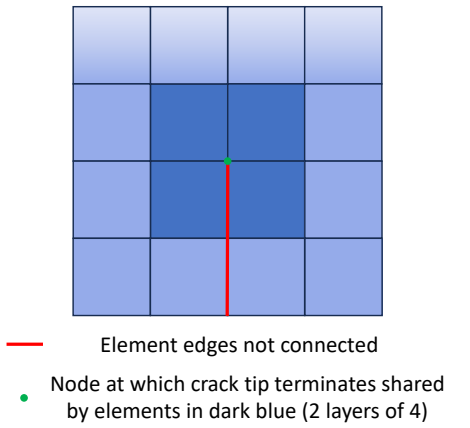


Figure 4.11: Schematic cross-section showing the crack-tip meshing.

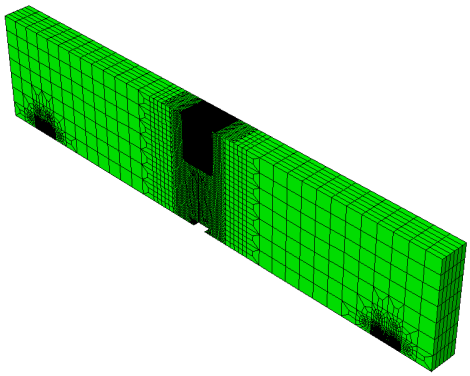
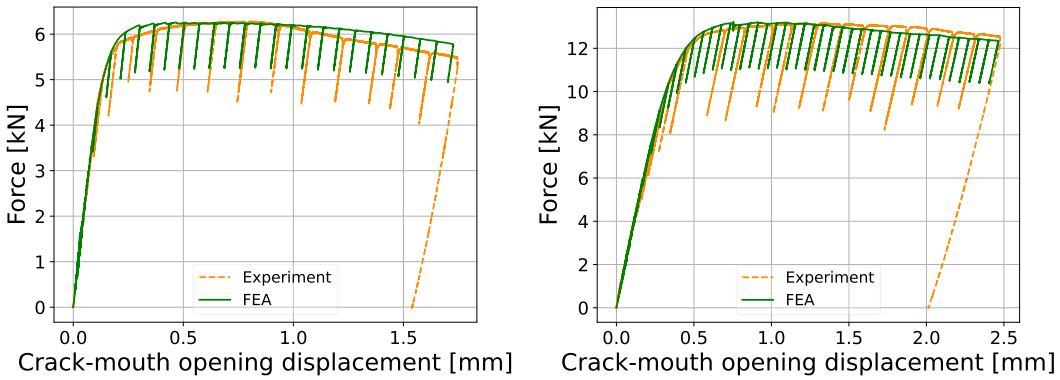


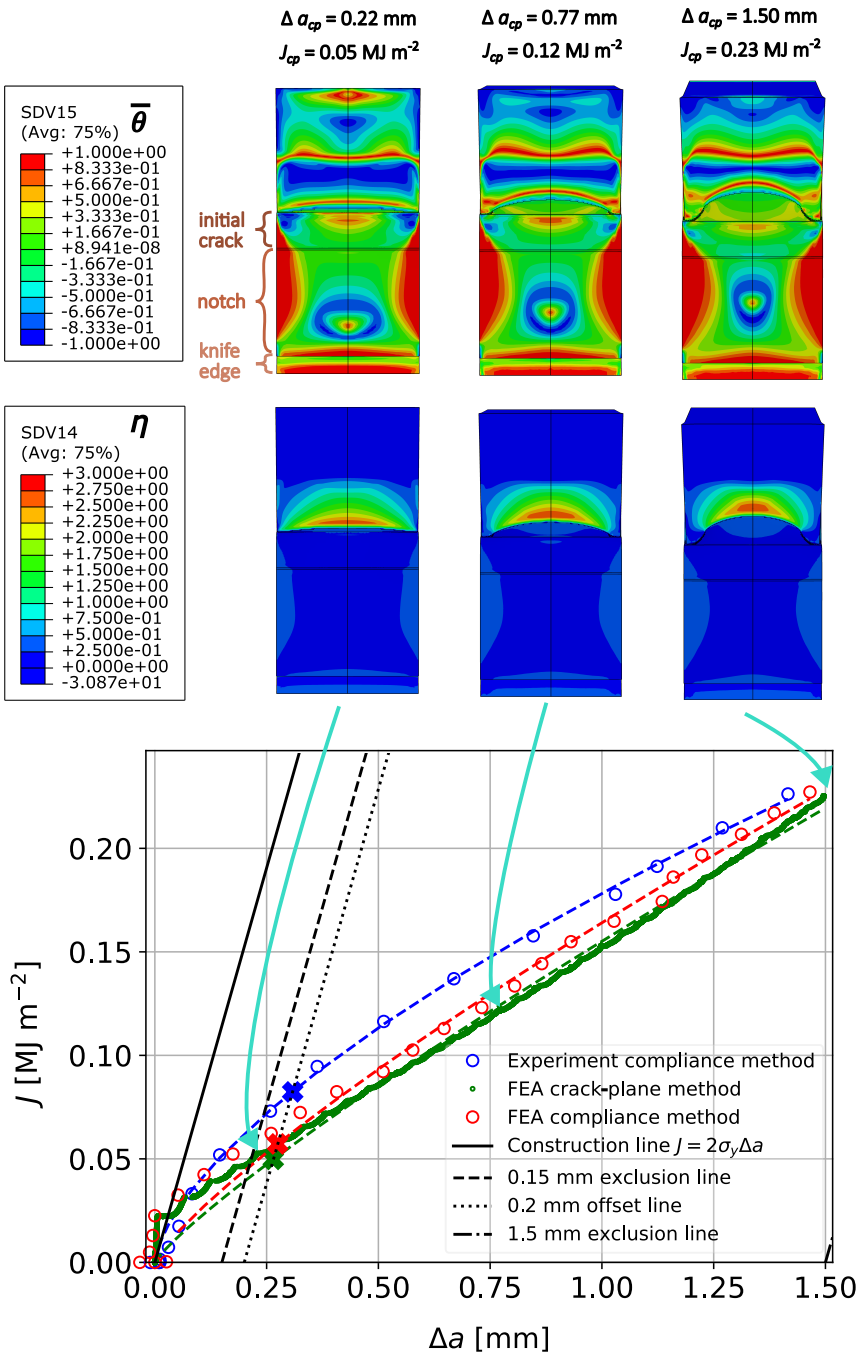
Figure 4.12: Half model of SENB specimen with mesh refinement.



(a) AH36.

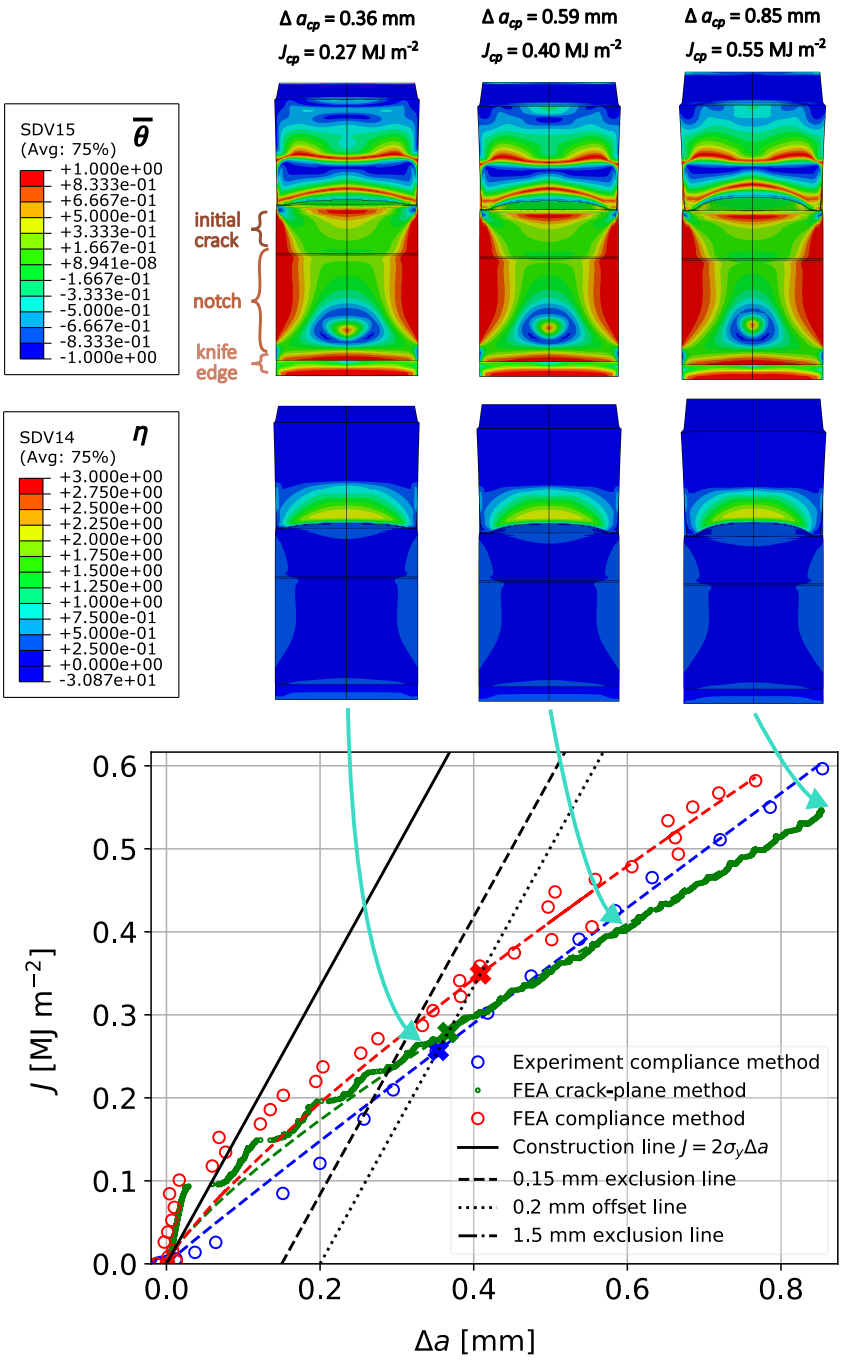
(b) S690QL.

Figure 4.13: Experimental and simulated F-CMOD curves.



(a) AH36.

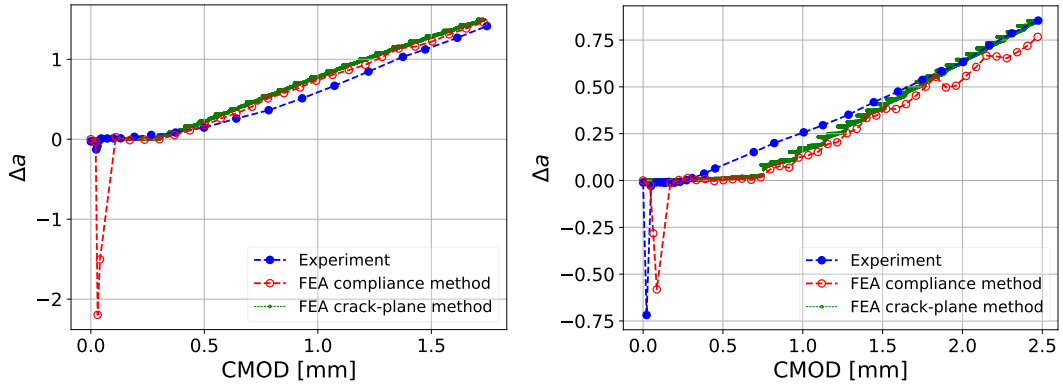
Figure 4.14: Experimental and simulated $J - \Delta a$ curves.



(b) S690QL.

Figure 4.14: Experimental and simulated $J - \Delta a$ curves.

J_Q. This procedure likewise reduces the effects of the discrepancy in the simulated early-stage crack front geometry on the construction of the $J - \Delta a$ curves.



(a) AH36.

(b) S690QL.

Figure 4.15: Experimental and simulated Δa - CMOD curves.

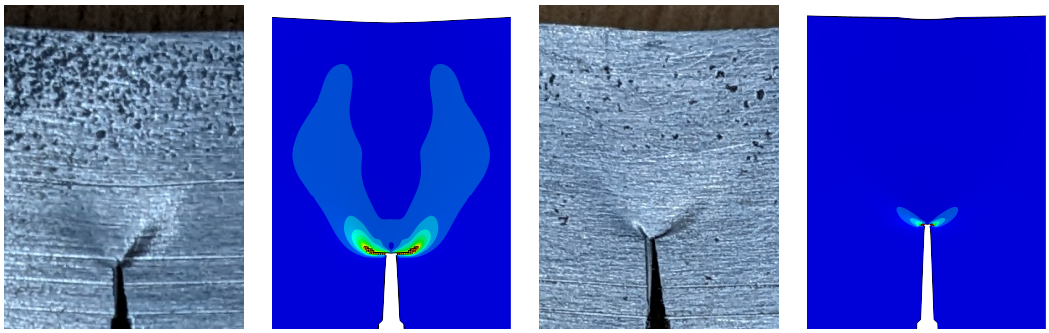
Crack lengths were also extracted from the finite-element model based on the crack plane formed by the deleted elements. The crack extension Δa was calculated by dividing the area formed by the deleted elements by the minimum width at the crack plane, which was found to give similar Δa values (within 0.05 mm) as the nine-point method. The force-CMOD compliance needed in the procedure for calculating J values were estimated from the FEA area-based Δa using the conversions given by ASTM E1820 [244]. The results are shown in Figs. 4.14 and 4.15 under the label 'FEA crack-plane method'.

Figs. 4.13 and 4.14 and Table 4.6 show relatively good overall agreement between the finite-element and experimental results. The calibration was performed based on the force-displacement curve (Fig. 4.13), hence the greater variance between the experimental and simulated J-Δa (Fig. 4.14) than between the experimental and simulated force-displacement curves. Nonetheless, the simulated J-Δa curves perform surprisingly well considering the low number of unique testing conditions (3) used for calibration of the damage parameters in comparison to that seen in the modelling of similar tests in other works (6 in [247] and 4 in [248]). Other than the purposeful simplification of the material model and calibration procedure, the difference in the experiments and simulations could also be attributed to geometrical simplifications, such as the flat instead of curved shape of the assumed initial crack front and the subsequent difference in crack front shapes between the experiments (Fig. 4.10) and simulations (Fig. 4.14). The rollers in experiment rolling away from each other also slightly changes the span between the rollers, while the inter-roller distance is fixed in the simulation.

Fig. 4.16 shows that the FEA captures slant fracture behaviour seen at the free surface of the tests. However, the slant fracture occurs relatively late in the test, such that it does not have much effect on greater part of the J-Δa curve. This and the tunneling behaviour as shown in Figs. 4.10 and 4.14 will be discussed in more detail in Section 4.8.3 in relation to the Charpy tests.

Table 4.6: Experimental and finite-element comparisons for the SENB test.

		AH36		S690QL	
		AST3	FEA	SST3	FEA
F_{max}	[kN]	6.27	6.26	13.15	13.41
J_Q compliance	[MJ m^{-2}]	0.082	0.057	0.257	0.349
J_Q crack plane	[MJ m^{-2}]	-	0.050	-	0.279



(a) AH36 test AST3. (b) AH36 simulation. (c) S690QL test SST3. (d) S690QL simulation.

Figure 4.16: Slant fracture in the SENB test.

4.8 MODELLING INSIGHTS

This section discusses key insights found from the modelling and calibration process which could help reduce the calibration effort in certain useful future situations concerning Charpy and fracture toughness correlations. First, the suitability and effectiveness of the triaxiality independent assumption for the range of stress states involved in these simulations is exemplified for the present steels with weak triaxiality dependence (Section 4.8.1). The useful similarity in the softening parameters between similar steels observed in the present work and in the literature is noted (Section 4.8.2). Consequently, it is shown how the calibration procedure could be reduced to be based on only 2 key parameters, C_2 and C_3, instead of all 5 damage parameters. Finally, the similarities and differences in the crack propagation behaviour in the Charpy and SENB fracture toughness tests are discussed, highlighting in particular how both display a similar tunnelling behaviour and a similar stress state evolution at key locations (Section 4.8.3).

4.8.1 *Triaxiality and Lode angle dependence (C_1, C_2 and C_3)*

Sections 4.5 to 4.7 show that the present model is capable of capturing the behaviour in the different mechanical tests of the AH36 and S690QL steels accurately using a fracture strain locus which is triaxiality-independent ($C_1 = C_3$), although metals are frequently found to fracture at smaller strains when subject to higher stress triaxiality [65, 171]. According to Xue's [172] investigation of Bridgman's experiments [65] on high-strength steels using a stress-based pressure- and Lode

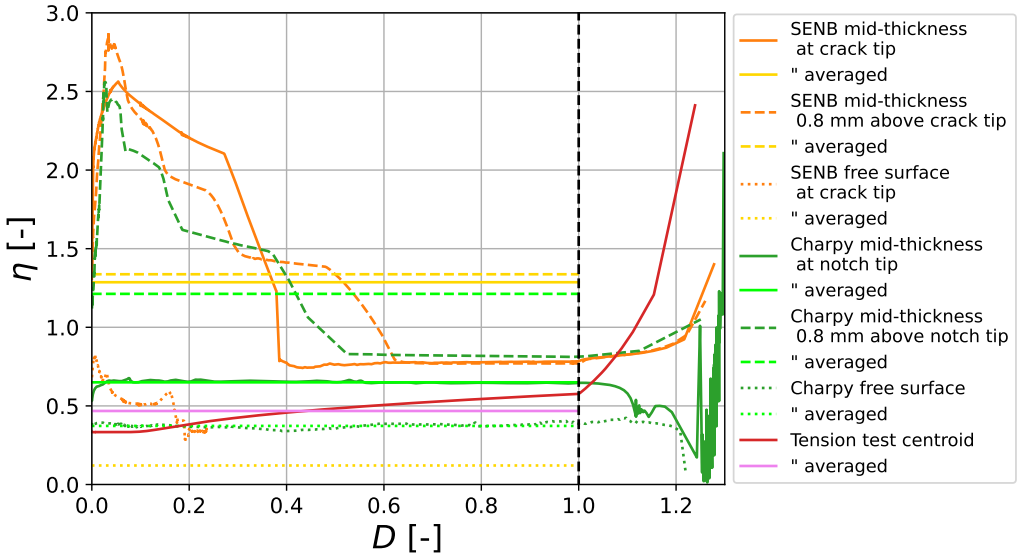
angle-dependent fracture criterion, the pressure sensitivity of steels decreases with decreasing hardenability, increasing yield stress and increasing reference fracture strain (defined at $(\eta, \bar{\theta}) = (0, 1)$). Hence, the present steels under investigation can be expected to have low pressure dependence due to the high fracture strains of both the AH36 and S690QL and the low hardenability of the S690QL, and this is corroborated by the efficacy of the present stress-independent calibration of the fracture strain locus.

It is also worth noting that although the maximum triaxiality near a sharp crack tip is high ($\eta = 2.5$ [218] in the perfectly plastic, plane-strain case), much of the damaging behaviour throughout the straining history of a typical element in the crack path of the SENB and Charpy specimens is associated with lower triaxialities due to blunting effects [249]. Fig. 4.17 shows that for elements with initially high triaxialities in the mid-thickness crack propagation path of the SENB and Charpy tests, the triaxialities drop off after the peak at a low D and has an average[3] η between around 1.1 and 1.3 (Table 4.7; 0.8 mm above tip). The stress evolution for an element at the initial crack tip as well as an element at an arbitrary distance of 0.8 mm above the initial crack tip is observed, because material at different distances from a crack or notch tip experience different regimes of behaviour in terms of stress states [79, 249, 250]. (0.8 mm corresponds to roughly 5 times the experimentally determined 0.2 mm offset critical CTOD of the AH36 and 8 times that of the S690QL). For the tensile test, the average triaxiality of the centroidal element is around 0.5 in the AH36 and 0.7 in the S690QL due to different extents of necking which cause the triaxialities to increase from their initial value of 0.33. The average triaxialities of the key elements in the different tests varying between this smaller-than-expected range of 0.5 and 1.3, combined with the trend of the pressure dependence to be weaker in higher triaxiality ranges than in the lower triaxiality ranges as shown by Xue [172], limits the effect of the material's pressure dependence on the behaviour in these tests.

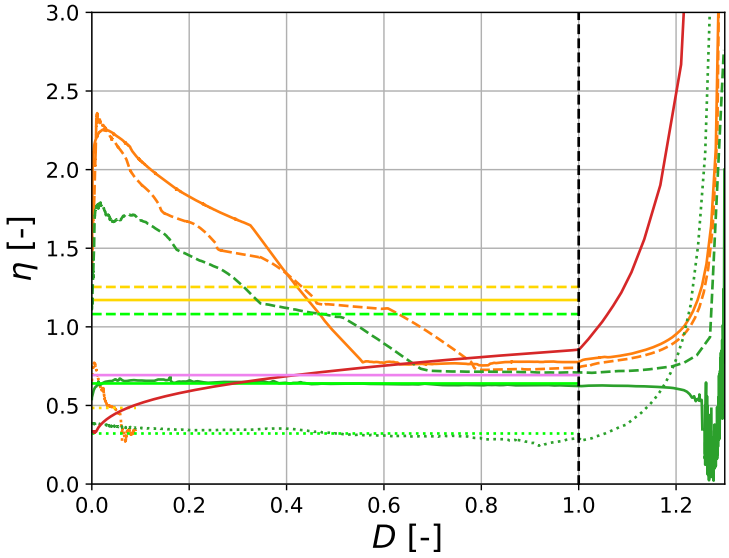
At the same time, observations have been made by Xue [172] using his stress-based model as well as existing experiments [174, 251] that a lower strain hardening capacity is accompanied by an increase in Lode-dependence in the fracture strains. From Fig. 4.18, it is clear that there are regions that are dominated by significantly different deviatoric stress states in the test, such as $\bar{\theta}$ close to 0 at the half-thickness symmetry and $\bar{\theta}$ close to 1 at the free surface in the SENB and Charpy specimens, such that this Lode-dependence in the fracture strain will have a significant effect of the fracture behaviour.

It is seen that for the present steels, pressure sensitivity is low and Lode-dependence plays the key role of distinguishing the fracture behaviour observed in different geometries, such that the assumption of a Lode-dependent only fracture strain surface is sufficient for describing the behaviour in different mechanical tests to within reasonable accuracy. This quality has also been observed in Clausing's experiments on several structural steels [172, 174] and Banabic's experiments [173, 175] on aluminum alloy. Other examples of the successful use of Lode-dependent, triaxiality-independent ductile fracture models (primarily the maximum shear stress

3 The averages are calculated only over the range of $0 \leq D \leq 1$, because once D reaches 1, deletion is imminent, with softening causing the plastic straining to accelerate and the von Mises stress to approach zero, which in turn causes the η to approach infinity.

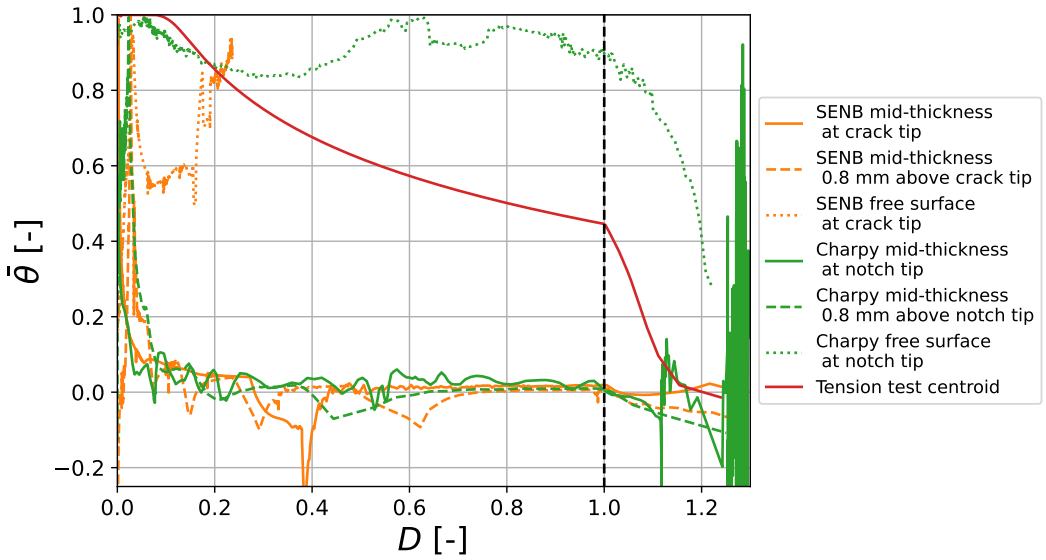


(a) AH36.

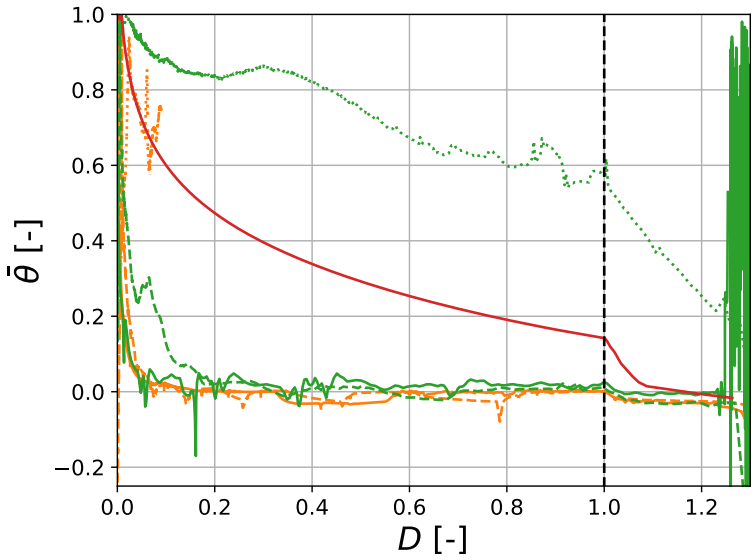


(b) S690QL.

Figure 4.17: Evolution of the triaxiality in key elements in the simulations. Unloading periods in the SENB simulations are omitted.



(a) AH36.



(b) S690QL.

Figure 4.18: Evolution of the Lode angle in key elements in the simulations. Unloading periods in the SENB simulations are omitted.

Table 4.7: Average triaxialities and Lode angles calculated over $0 \leq D \leq 1$ in key elements in the AH36 simulations.

	Plane	Element	AH36		S690QL	
			η	$\bar{\theta}$	η	$\bar{\theta}$
Tensile test	Half-thickness	Centroid	0.47	0.67	0.69	0.34
Charpy test	Half-thickness	Notch tip	0.65	0.04	0.64	0.02
	Half-thickness	0.8 mm above notch tip	1.21	0.03	1.08	0.04
	Free surface	Notch tip	0.37	0.92	0.32	0.74
SENB test	Half-thickness	Crack tip	1.29	0.02	1.25	0.00
	Half-thickness	0.8 mm above crack tip	1.34	0.01	1.25	0.00
	Free surface	Crack tip	0.51	0.65	0.48	0.67

(Tresca) model) include applications to tests involving moderate triaxialities between 0.3 and 1 [172, 231, 252–256] and even higher triaxialities such as in the compact tension test [257] and the Charpy impact test [195]. However, these (except for [195]) primarily involved the simulation of sheet metals subject to plane stress, in which the triaxiality dependence is implicitly accounted for through the one-to-one relationship between the Lode angle and triaxiality [231, 257], regardless of the pressure sensitivity of the metal's fracture behaviour.

It has been suggested by previous studies that Lode-dependence in the fracture criterion also plays a key role in capturing slant fracture behaviour in simulations [179, 189, 234, 235]. However, using the present model, it was found that neither a Lode-dependent hardening rule nor a Lode-dependent fracture strain surface is necessary for capturing slant fracture behaviour, once the mesh is sufficiently fine and softening is included in the coupled viscoplasticity model, as also seen in [195]. This is in agreement with Besson et al. [236], who attributed the formation of slant fracture to the local stress and strain state promoting additional damage, instead of a necessarily Lode-dependent damage criterion.

The major advantage of assuming triaxiality independence is the reduction of the number of calibration parameters and the model calibration effort while still capturing the slant fracture mechanism and the force-displacement response in key tests for low-pressure-sensitivity steels, at the cost of a slightly reduced model accuracy. Nevertheless, it should be noted that such models cannot capture the behaviour in axisymmetric [231, 252] tests and should only be used for steels with low triaxiality dependence in the range of the triaxialities of interest. For example, it would not work for very-low-triaxiality-dominated, pressurised situations [65] (before the cut-off value [219]), because even metals with low pressure sensitivity in the medium-to-high triaxiality ranges are generally pressure-sensitive in the very-low-triaxiality range [172].

4.8.2 *Softening parameters (m and D_c)*

For simplicity, a linear relationship is assumed for the decay of β with respect to D, such that $m = 1$. The present value of $D_c = 1.3$ for both AH36 and S690QL (both hot-rolled low-carbon structural steel plates) is close to the only other application of this version of the softening model to a hot-rolled low-carbon structural steel plate found in the literature [258], which was $D_c = 1.2$ for Q460C steel. This is significant because a trend has been identified [215] where calibrations of the softening model to different low-alloy steel pipes (X65, X70 and X100) repeatedly resulted in similar values of D_c, ranging from 2.1 to 2.3 [214, 247, 259]. Similarly, the two existing calibrations to the nickel-chromium Inconel alloy have resulted in D_c values close to each other, i.e. 1.2 [260] and 1.4 [248].

4.8.3 *Similarities and differences between the Charpy and SENB fracture behaviour*

The evolution of the triaxiality of a typical element in the crack path above the notch tip of the Charpy and the crack tip of the SENB specimen (Fig. 4.17) reveals that when tunneling starts, the triaxialities experienced in the Charpy test and the SENB are closer than would be expected based on the different sharpness of the initial crack and initial notch. Only the triaxialities of the elements at the Charpy notch tip and SENB crack tip are significantly different, where the average triaxialities in the AH36 simulations are 0.65 and 1.29, respectively, due to the difference of the notch versus crack geometry, with similar values seen in the S690QL simulations (Table 4.7). However, the other elements above the Charpy notch tip experience a very similar triaxiality evolution and tunneling process to that occurring in the SENB test. This is also seen in the η distribution shown in the second row of contour plots in Figs. 4.7 and 4.14.

In Figs. 4.7a and 4.7b, the first column of contour plots corresponds to a frame close to the occurrence of the maximum force, the second column corresponds to a frame where around 70 % of the Charpy impact energy has been dissipated, and the third column corresponds to the end of the simulation. In Figs. 4.14a and 4.14b, the first column of contour plots corresponds to a frame close to the occurrence of the 0.2 mm offset J_Q, the third columns corresponds to the end of the simulation, which is at the end of an unloading period after the simulated CMOD reaches a value close to them maximum CMOD achieved in the experiment; and the second column corresponds to a crack extension roughly halfway in between those of the two other columns. These figures show that the slant fracture in the SENB test only occurs to a small extent towards the end of the simulation, such that the J_Q and the majority of the greater part of the J-Δa curve is not affected by slant fracture, while more extensive slant fracture is seen to occur in the Charpy test. Despite this, the stress states caused by the tunnelling geometry dominates the behaviour of most of the duration of the Charpy test. Even when 70 % of the C_v has been dissipated, the amount of slant fracture in the Charpy simulations is still relatively small, such that the stress state distributions in the both Charpy and the SENB simulations are still mainly determined by the tunnelling that occurs in both simulations. The only difference is that more tearing at the free surface has occurred in the Charpy test, an observation that will be discussed Section 4.10 below in connection to the variations

in the C_v to the initiation toughness J_Q correlations. This can be seen by comparing the first and second columns of the contour plots in Figs. 4.7a and 4.7b with the contour plots in Fig. 4.14.

These plots also reveal that the Charpy simulation experiences purely tunnelling behaviour with no slant fracture until after the attainment of the maximum force, with the crack first propagating parallel to the initial crack through the whole width including the free surface. In the SENB simulation, the crack at the free surface propagates in a slant direction without first extending parallel to the initial crack. This is why the free surface crack-tip element in the SENB simulation is seen in Figs. 4.17 and 4.18 to accumulate only a small amount of damage D before it stopped straining altogether: slant fracture starts in the element right below that, causing the crack not to progress parallel to the original crack (Fig. 4.16).

4.8.4 *Implications*

It is seen that the assumption of triaxiality independence, together with the understanding of the correlation of D_c to the steel type and the assumption of linear degradation ($m = 1$), performs well in reducing the number of damage calibration parameters for weakly-triaxiality-dependent steels to only two (C_2 and C_3) while simulating the responses of the tensile, Charpy and SENB tests well. This is effectively a capitalisation on the weak triaxiality dependence of the steels in the medium-to-high triaxiality range, which is the range experienced in the tensile test as it necks and in the crack planes of the Charpy and SENB tests. A damage locus that is described by two parameters can be calibrated using only two types of tests, given that they cover distinct stress states which are in the stress-state range of interest, and material certificates provide the results of two such tests in the form of A and C_v. Furthermore, it was observed that for key portions of the behaviour in the SENB and Charpy tests, namely well beyond the occurrence of the critical J_Q and up to 70 % of the dissipation of C_v, the stress states in the Charpy and SENB are very similar, being determined by extensive tunnelling behaviour with little or no slant fracture. (In Section 4.10 below, it will be seen how the difference due to the later part of the C_v dissipation contributes to variations in the correlations between C_v and the J_Q initiation toughness.) Due to the similar tunnelling behaviour in a significant portion of the tests, a calibration based on the Charpy tests provides a similar range of stress states as is provided by the calibration to a SENB test. In light of this, this study adopts the above assumptions for a database of S690Q steel material certificate data in order to calibrate the material models for a large number of these steels, namely calibrating C_2 and C_3 based on the available A and C_v. The calibrated materials are then used to simulate the SENB test in order to construct numerically, mechanistically founded correlations between C_v and J_Q which take into account the other properties, such as σ_y/σ_u and A.

4.9 RELATIONSHIP BETWEEN MATERIAL CERTIFICATE DATA AND DAMAGE PARAMETERS

A parametric study varying the σ_y/σ_u and the key damage calibration parameters (C_2 and C_3) of the aforementioned material model in finite-element simulations of the Charpy and tensile test is performed in order to obtain sets of material certificate values with their corresponding damage parameters. For each (σ_y/σ_u, C_2, C_3) combination, both the Charpy and the tensile tests are simulated and then postprocessed to obtain the A and C_v. This allows the subsequent deduction of the relationship between (C_2, C_3) and (A, C_v, σ_y/σ_u) using regression analysis of the numerical results.

A is here found using the definition of A_ε, the engineering strain when the force first drops below zero, which has been found [168] to give a sufficiently close approximation of the value based on the standard A definition [200] of summing the length of the broken gauge section and dividing the sum by the original gauge length, i.e. it is assumed that $A = A_\varepsilon$. The Charpy energy C_v is taken to be the total kinetic energy lost from the striker by the time the force has become stable around zero.

4.9.1 *Parametric study*

The simulations are performed in Abaqus Explicit 2022 [228] with the use of a user-defined material subroutine for the implementation of the material model. Eight-noded linear solid elements with reduced integration and hourglass control (C3D8R) are used. As a result of a mesh sensitivity study, elements with characteristic sizes l_c of 0.12 mm and 0.06 mm, respectively, were used in the fracture zones of the tensile and Charpy tests, where l_c is the cube root of the volume of an undeformed element. Mass scaling was applied to the Charpy and tensile test to decrease the computational time. In the simulations of the quasi-static tensile tests, the mass was increased by a factor of 1×10^9, and the kinetic energy was checked to be less than 1 % of the total internal energy, except for the beginning of the simulation when the load application boundary accelerates to the quasi-static testing velocity. In the simulations of the dynamic Charpy tests, the mass was increased by a factor of 25, a value which is seen to produce a negligible difference in C_v in a previous mass scaling factor sensitivity study [195]. The coefficient of friction between contact surfaces in the Charpy simulations was assumed to be 0.15.

4.9.1.1 *Parametric space selection*

Table 4.8 gives the σ_y and σ_y/σ_u values that are considered in the parametric study. Although variation in the σ_y/σ_u is seen for steels with the same grade and the same σ_y, a higher σ_y is generally accompanied by a higher σ_y/σ_u. Therefore, the σ_y/σ_u is here made to vary with the σ_y in order to reduce the size of the parametric space while reflecting the general trend. Including a numerical dataset with varying σ_y/σ_u for fixed σ_y would shed further light on the separate effects of σ_y/σ_u and σ_y, but is outside the scope of this already computationally expensive study.

Table 4.8: Range of σ_y and σ_y/σ_u considered.

σ_y [MPa]	730	750	770	810	850
σ_y/σ_u [-]	0.92	0.93	0.94	0.96	0.97

The Young's modulus E, which is very similar for most structural steels, is here assumed to be 200 GPa (together with a Poisson's ratio of 0.3). The ε_{sh} and ε_u (as described in Section 4.3.1) are obtained from the relationships proposed by Yun and Gardner [54], derived from from regression analysis of 455 engineering stress-strain curves of structural hot-rolled steels with nominal grades up to S690, as shown in Eqs. (4.32) and (4.33). It is worth noting that, because of the range of σ_y/σ_u considered and the use of Eqs. (4.32) and (4.33), ε_{sh} and ε_u are assumed to be constant in this study.

$$\varepsilon_{sh} = \begin{cases} 0.0015 & \frac{\sigma_y}{\sigma_u} < 0.7 \\ 0.1\frac{\sigma_y}{\sigma_u} - 0.055 & 0.7 \leq \frac{\sigma_y}{\sigma_u} \leq 0.85 \\ 0.03 & \frac{\sigma_y}{\sigma_u} > 0.85 \end{cases} \tag{4.32}$$

$$\varepsilon_u = \begin{cases} 0.6\left(1 - \frac{\sigma_y}{\sigma_u}\right) & \frac{\sigma_y}{\sigma_u} \leq 0.9 \\ 0.06 & \frac{\sigma_y}{\sigma_u} > 0.9 \end{cases} \tag{4.33}$$

For each σ_y/σ_u, a series of simulations are run, using all the combination pairs of C_2 and C_3 values that can be made from [0.4, 2.6, 5.1, 7.6] and [0.4, 0.7], respectively, with the exception that C_2 is set to equal C_3 in pairs where $C_2 < C_3$, since $C_2 < C_3$ does not align with experimental observations (see descriptions of Eqs. (4.13) and (4.14) above). Additionally, a reduced set of runs, considering a sparser set of σ_y/σ_u values, [0.92, 0.94, 0.97], is performed for the combination pairs of C_2 and C_3 values that can be made from [0.4, 2.6, 5.1, 7.6] and [0.5], to provide more numerical data while keep the computing costs within reasonable limits.

The values chosen for σ_y and σ_y/σ_u are based on the database of material certificates provided by Huisman BV, from which 77 steels are used to form a parametric space, by discretising the σ_y domain into intervals, and taking the σ_y/σ_u predicted by a least-squares fit to these 77 steels, as shown in Fig. 4.19 and Eq. (4.34):

$$\frac{\sigma_y}{\sigma_u} = \frac{1}{1 + \left(\frac{482}{\sigma_y}\right)^6} \tag{4.34}$$

where σ_y and σ_u are expressed in megapascals.

The dataset of 77 steels is a result of the following filtering criteria applied to the database. First, only steels with the equivalent grades of StE690 and S690Q [10], which have the same minimum toughness standard, are included in the dataset. Second, only steels with a thickness between 10 and 14 mm were included in the dataset. In the tensile test simulations, the steel is assumed to be 12 mm and modelled with a standard [237] 25 mm width and proportional gauge length. The relatively small range of thicknesses in the dataset, centred around the value

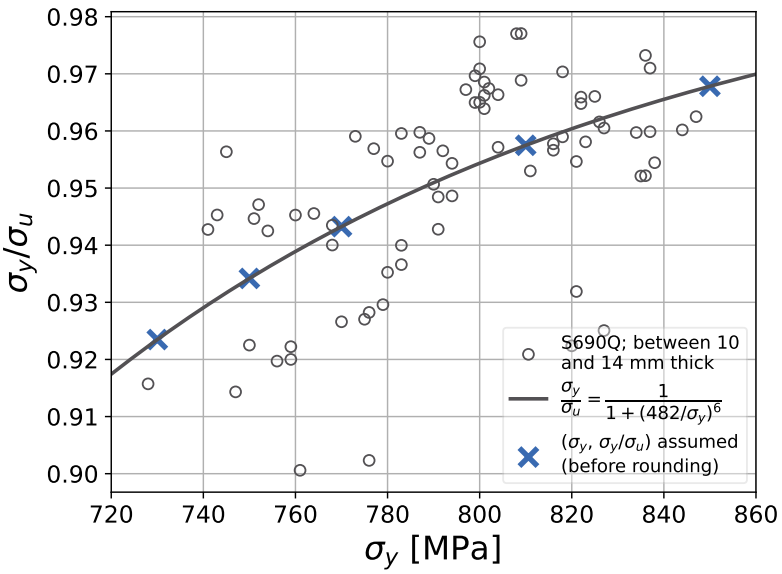


Figure 4.19: σ_y/σ_u and σ_y assumed in the parametric study, based on fit to database.

assumed in the simulations, is used so that more materials are included in the dataset while limiting any potential thickness effects that might exist despite the proportionality of the specimens [261]. Finally, only steels for which all the three C_v repetitions reported on the material certificate were larger than 100 J, and for which all three repetitions did not differ from each other by more than 50 J, were included in the dataset. This is to ensure that the Charpy tests considered in the dataset involved fully ductile behaviour even though these tests performed at $-20\,^{\circ}$C according to the corresponding material standard [10], since the simulations do not account for any transition to unstable cleavage fracture.

4.9.1.2 *Charpy testing temperature assumed in the parametric study*

The tensile tests, which are used to deduce the parameters describing the plastic strain-hardening behaviour assumed in the Charpy and tensile simulations, were performed at ambient temperature, while the Charpy tests were performed at $-20\,^{\circ}$C. The temperature affects the plastic flow stress of materials, but this temperature difference of $-40\,^{\circ}$C could be expected to make a relatively small difference in the flow stress [262]. To ascertain the significance of this difference, Charpy simulations accounting for temperatures of $-20\,^{\circ}$C and $-60\,^{\circ}$C were additionally performed for the calibrated S690QL steel investigated in [168], which was one of the materials for which detailed experimental comparisons were carried out as part of the validation of the present material modelling approach. Since the Johnson-Cook-based model described above (Eq. 4.17) is suitable only for thermal softening at temperatures above room temperature, the effect of the lower temperature is included here by directly modifying the entire plastic strain-hardening curve according to the BS 7910 [170] equation recommended for assessment temperatures below room temperature and above $-196\,^{\circ}$C, given the room temperature yield strength:

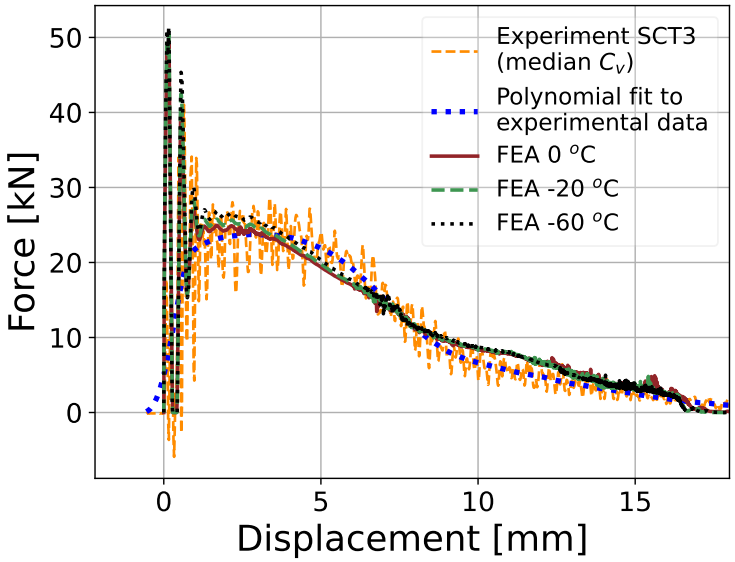


Figure 4.20: Charpy simulations of S690QL steel at −60 °C, −20 °C and 20 °C.

$$\sigma_{y,cold} = \sigma_{y,room} + \frac{10^5}{491 + 1.8\Theta} - 189 \tag{4.35}$$

where $\sigma_{y,cold}$ [MPa] is the estimated yield stress at low temperature, $\sigma_{y,room}$ [MPa] is the yield stress at room temperature, and Θ [°C] is the temperature.

For simplicity, this relationship is assumed to be applicable directly to the true plastic strain hardening stress $\bar{\sigma}$ (Eq. (4.2)), by setting $\bar{\sigma} = \sigma_{y,room}$, such that the temperatures of −20 °C and −60 °C result in a uniform increase to the $\bar{\sigma}$ of 31 MPa and 72 MPa, respectively, for all ε_p. This assumption of uniform increase is in line with the observed effect of lower temperatures on the shape of the stress-strain curves as seen in [262]. The other material parameters, including the thermal softening parameters, are kept the same (Table 4.1; S690QL), and the simulations start at room temperature with the uniformly increased plastic strain-hardening curve due to the lower temperature, such that the thermal softening model (Eq. 4.17) is assumed to act based on the temperature difference relative to the starting temperature.

The simulation results (Fig. 4.20 and Table 4.9) indicate that a testing temperature of −20 °C, and the associated 31 MPa increase in flow stress relative to room temperature conditions, makes a negligible difference to both the Charpy force-displacement curve and the Charpy energy, assuming that the Charpy test behaviour is in the fully ductile regime. In contrast, the temperature rise around the notch due to adiabatic effects, which could be as much as 350 °C [220], would lead to a 20 % decrease in the flow stress, given the present thermal softening parameters (Table 4.1; S690QL). Therefore, the Charpy simulations in the parametric study, which do take the thermal softening effects into account, are performed assuming room temperature plastic strain-hardening properties, although the Charpy tests were performed at −20 °C.

Table 4.9: Charpy energy values in simulations with flow stress modified to account for lower temperatures.

		Test	Simulations		
Θ	[°C]	~ 20	-60	-20	20
C_v	[J]	204.2	224.7	219.6	217.1

4.9.1.3 *Significance of the yield-to-tensile strength ratio σ_y/σ_u*

Classically, the σ_y/σ_u is related to the amount of strain hardening through the application of the Considère [52] uniaxial necking criterion to a Hollomon [53] power curve (Eq. (4.36)) that passes through the yield point in the true stress versus true total strains plot, which results in Eqs. (4.37) and (4.38) [57]:

$$\bar{\sigma} = K_H {\varepsilon_t}^{n_H} \tag{4.36}$$

$$n_H = \varepsilon_{u,t} \tag{4.37}$$

$$\frac{\sigma_y}{\sigma_u} = \frac{1}{1+\varepsilon_y}\left(\frac{e\ln(1+\varepsilon_y)}{n_H}\right)^{n_H} \tag{4.38}$$

where $\bar{\sigma}$ is the true stress, K_H is the Hollomon strength coefficient, n_H is the Hollomon hardening exponent, ε_y is the engineering yield strain, e is the Euler's number, ε_t is the true total strain, and $\varepsilon_{u,t}$ is the true total strain corresponding to the occurrence of necking instability.

This enables the theoretical hardening curve (i.e. strength coefficient K_H, hardening exponent n_H, and hence its slope) up to the point of necking for Hollomon-type materials to be found, given only σ_y/σ_u, σ_y and E, thereby relating σ_y/σ_u, a ratio of stresses only, to the strain hardening slope. This forms the basis for the use of σ_y/σ_u as an indicator for the strain hardening behaviour in some design rules concerning failure modes sensitive to the hardening slope, such as the plastic buckling of beams [115, 141].

Although σ_y/σ_u could function adequately as an indirect indicator for strain hardening in specifying reference limits for specific design cases, the theoretically derived Hollomon-based relationship between the necking strain and σ_y/σ_u is not generally applicable, and a range of uniform elongation values is observed for a given σ_y/σ_u in typical structural steels [54], in violation of Eqs. (4.37) and (4.38). This can be attributed to the restrictions imposed on the shape of the strain hardening curve when assuming the Hollomon rule. Therefore, a more versatile plastic strain hardening rule (Eq. (4.2)), which consists of a yield plateau followed by a Swift curve, is adopted in the present study.

Due to the presence of the Swift offset parameter in Eq. (4.2), n alone is no longer sufficient to fully describe the hardening slope. To quantify the relationship between σ_y/σ_u and the amount of hardening for the present hardening rule, an expression for the average slope g in the true stress versus true plastic strain space, between

the end of the yield plateau $\varepsilon_{sh,p}$ and the occurrence of necking instability $\varepsilon_{u,p}$, is derived:

$$\begin{aligned} g &= \frac{\int_{\varepsilon_{sh,p}}^{\varepsilon_{u,p}} \frac{\mathrm{d}\bar{\sigma}}{\mathrm{d}\varepsilon_p}\,\mathrm{d}\varepsilon_p}{\varepsilon_{u,p}-\varepsilon_{sh,p}} \\ &= \frac{\sigma_y(1+\varepsilon_{sh})}{(\varepsilon_{sh,p}-\varepsilon_{u,p}+n)^n(\varepsilon_{u,p}-\varepsilon_{sh,p})}(n^n-(\varepsilon_{sh,p}-\varepsilon_{u,p}+n)^n) \end{aligned} \tag{4.39}$$

where n is related to σ_y/σ_u by:

$$\frac{\sigma_y}{\sigma_u} = \frac{(1+\varepsilon_u)(\varepsilon_{sh,p}-\varepsilon_{u,p}+n)^n}{n^n(1+\varepsilon_{sh,p})} \tag{4.40}$$

Eqs. (4.39) and (4.40) show that the average strain hardening slope becomes dependent on ε_{sh} and ε_u, in addition to n, σ_y, σ_u and E. On the other hand, the average slope g_H for the Hollomon case depends only on n, σ_y, σ_u and E, as given by Eq. (4.41):

$$\begin{aligned} g_H &= \frac{\int_{\varepsilon_{y,t}}^{\varepsilon_{u,t}} \frac{\mathrm{d}\bar{\sigma}}{\mathrm{d}\varepsilon_t}\,\mathrm{d}\varepsilon_t}{\varepsilon_{u,t}-\varepsilon_{y,t}} \\ &= \frac{\sigma_u e^{n_H}(n_H{}^{n_H}-\varepsilon_{y,t})}{n_H{}^{n_H}(n_H-\varepsilon_{y,t})} \end{aligned} \tag{4.41}$$

where $\varepsilon_{y,t}$ is the total true strain at the initial yield point, $\varepsilon_{u,t}$ is the total true strain at the occurrence of necking instability, and e is Euler's number.

To illustrate the implication of this difference between g and g_H, the empirically obtained predictions for ε_{sh} (Eq. (4.32)) and ε_u (Eq. (4.33)) from Yun and Gardner [54] are used to calculate g, which is then plotted together with g_H, as shown in Fig. 4.21. The correlation between σ_y/σ_u and σ_y given in Eq. 4.34 is also assumed. Due to the dependence of g on ε_{sh} and ε_u, the relationship between the strain hardening slope g and σ_y/σ_u is not monotonic, in contrast with g_H. In the present study, the range of σ_y/σ_u is limited to $0.92 \leq \sigma_y/\sigma_u \leq 0.97$, which corresponds to values observed in the reference database of material certificates of S690 steels (discussed in Section 4.9.1.1). In this regime, ε_{sh} and ε_u remain constant according to Eqs. (4.32) and (4.33), and an increasing σ_y/σ_u is associated with a decreasing hardening slope (Fig. 4.21), as is normally expected. This is confirmed by the plot (Fig. 4.22) of the present hardening rule (Section 4.3.1) together with the Considère necking point, which illustrates how the hardening curve changes in the present study: the strength increases, the average hardening slope decreases, and the yield plateau length and necking strain stays constant, as σ_y/σ_u is increased from 0.92 to 0.97. However, it is important to note the range for which this applies and the presence of scatter observed in ε_{sh} and ε_u values in practice.

4.9.2 *Regression of A and C_v on C_2 and C_3*

The results of the parametric runs, together with a fitted relationship based on least-squares regression, are plotted in Figs. 4.23 to 4.26. The proposed regression

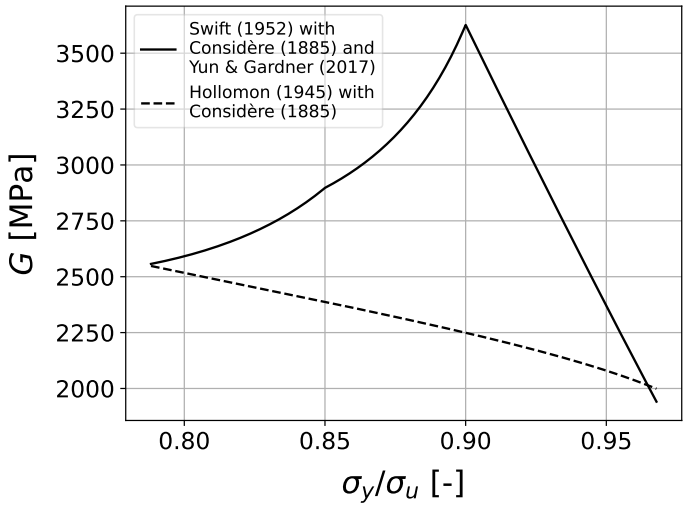


Figure 4.21: Average hardening slope g against σ_y/σ_u.

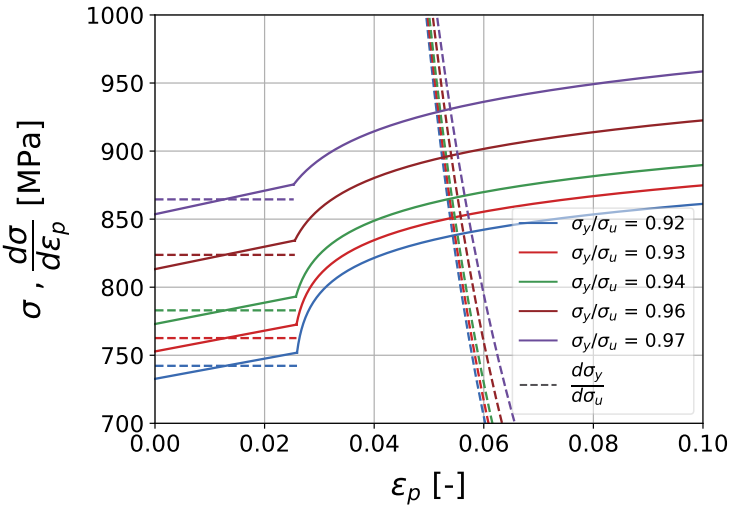
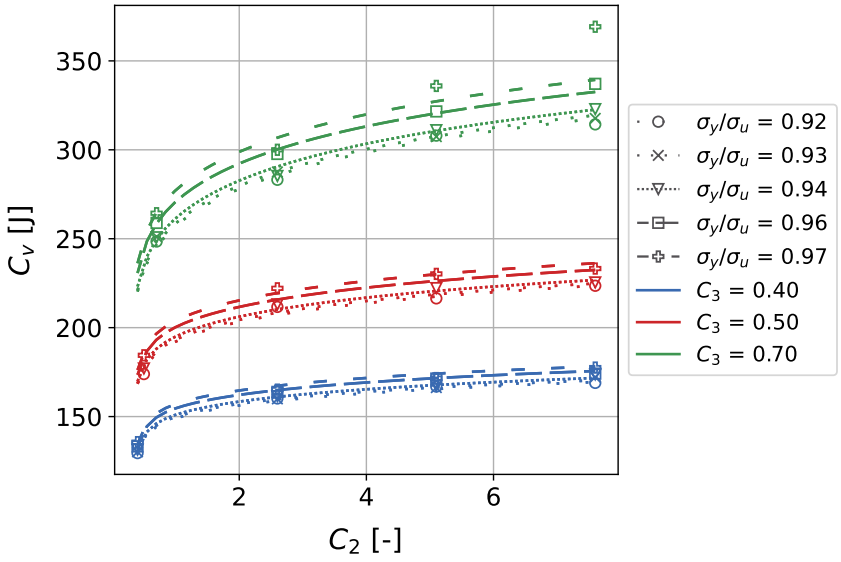
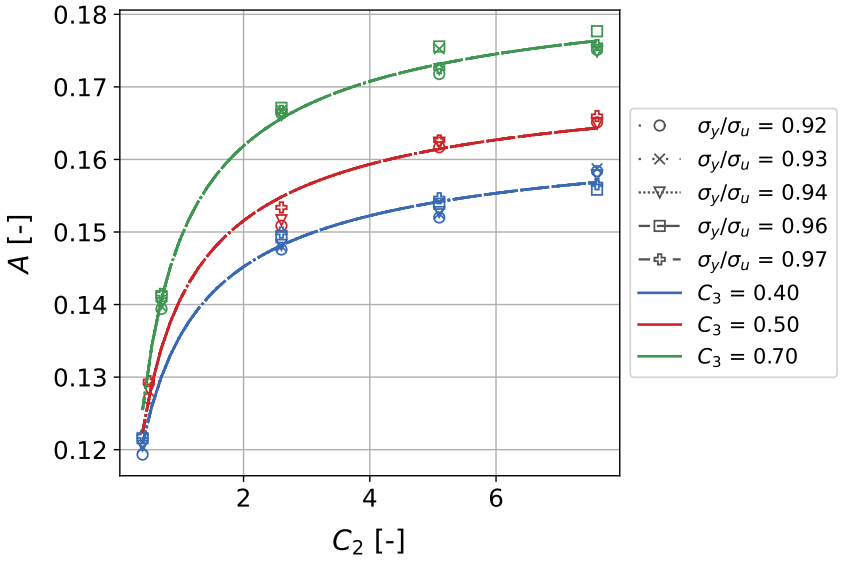


Figure 4.22: Effect of varying σ_y/σ_u on the plastic strain hardening curve.

model is given in Eq. (4.42) and is a result of fitting different trial models based on the trends observed in the data and choosing the one that best reflect the trends.



(a) C_v against C_2



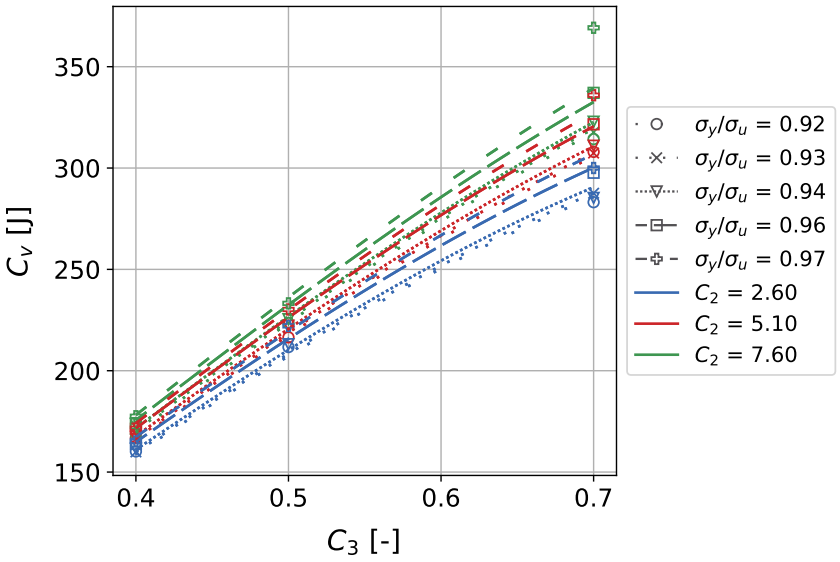
(b) A against C_2

Figure 4.23: C_v and A against C_2 from the parametric simulations.

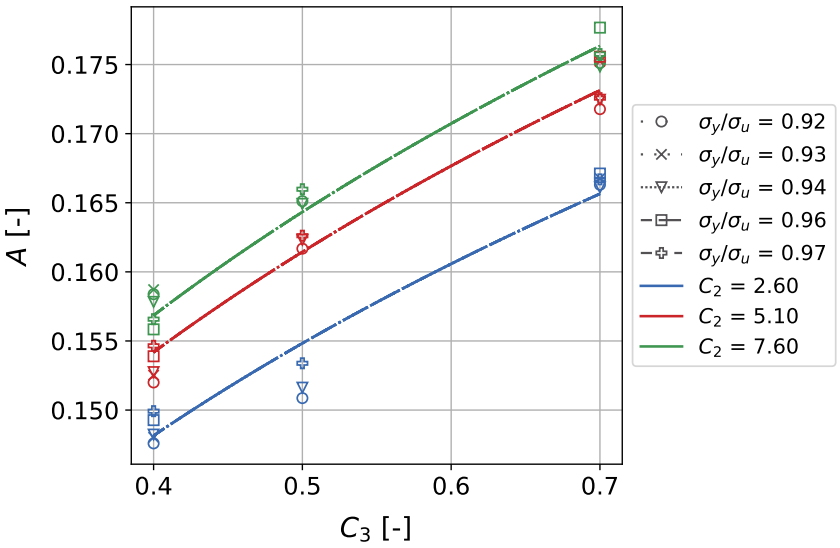
$$\begin{cases} C_v(C_2, C_3, \dfrac{\sigma_y}{\sigma_u}) = P_1 P_2{}^{(\frac{\sigma_y}{\sigma_u}-1)} C_2{}^{P_3} + P_4 P_5{}^{(\frac{\sigma_y}{\sigma_u}-1)} \dfrac{\sigma_y}{\sigma_u} C_3{}^{P_6} \\ \qquad\qquad + P_7 P_8{}^{(\frac{\sigma_y}{\sigma_u}-1)} C_2{}^{P_9} C_3{}^{P_{10}} \\ A(C_2, C_3) = Q_1 C_2{}^{Q_2} + Q_3 C_3{}^{Q_4} + Q_5 C_2{}^{Q_6} C_3{}^{Q_7} \end{cases} \tag{4.42}$$

where P_i and Q_i are the fitting parameters, as shown in Table 4.10.

The data points in Figs. 4.23b, 4.24b and 4.25b show that σ_y/σ_u has no appreciable effect on A. Because σ_y/σ_u is assumed to vary monotonically with σ_y, this also implies that σ_y has little effect on A. The tiny variations seen in A with respect

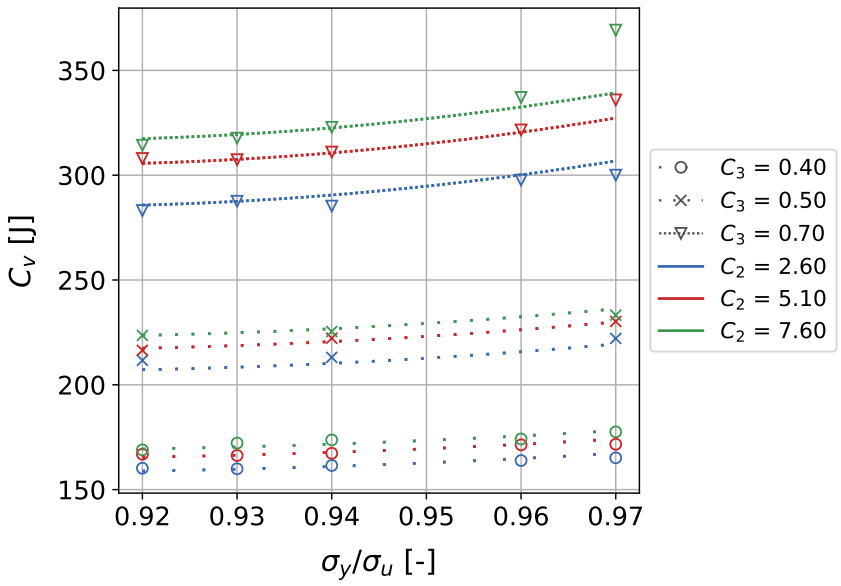


(a) C_v against C_3

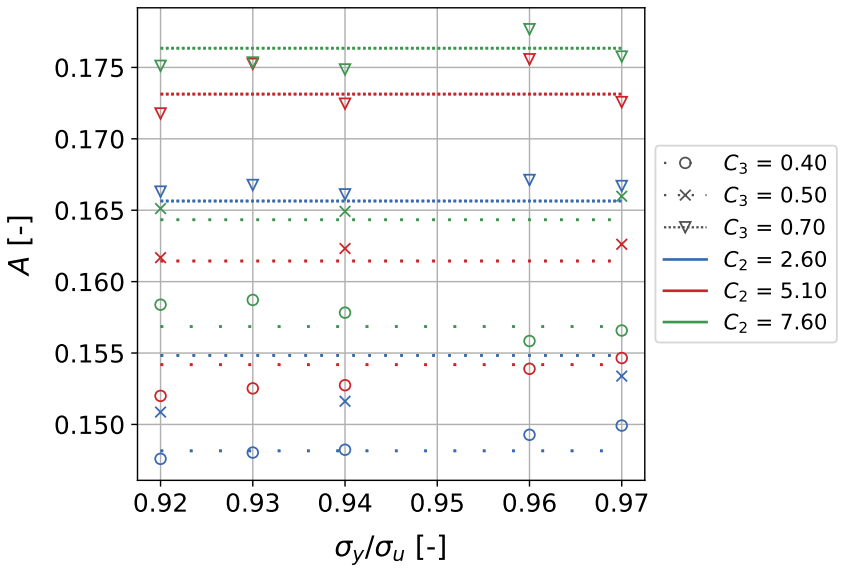


(b) A against C_3

Figure 4.24: C_v and A against C_3 from the parametric simulations.



(a) C_v against σ_y/σ_u



(b) A against σ_y/σ_u

Figure 4.25: C_v and A against σ_y/σ_u from the parametric simulations.

Table 4.10: Fitted calibration parameters.

(a) P_i parameters.

i	units	P_i
1	[J]	-0.89626
2	[-]	494.46
3	[-]	-3.2177
4	[J]	-22127
5	[-]	0.55185
6	[-]	2.0040
7	[J]	22481
8	[-]	1.6325
9	[-]	0.0027501
10	[-]	1.9707

(b) Q_i parameters.

i	units	Q_i
1	[-]	5.0212
2	[-]	-0.84337
3	[-]	0.20165
4	[-]	0.21133
5	[-]	-5.0639
6	[-]	-0.84132
7	[-]	0.0026558

to changes in σ_y/σ_u seen in these plots appear as scatter with no consistent trend. Hence, it is assumed that σ_y/σ_u has no effect on A in this regime and does not appear as a variable in the equation for A. From Figs. 4.23 and 4.24, both A and C_v appear to have a power-law relation with respect to C_2 and C_3, although this is relatively weak between A and C_3, especially when C_2 is high. Additionally, Fig. 4.25a suggests that C_v has an exponential dependence on σ_y/σ_u. The proposed nature of the dependencies between the individual variables are summarised in Table 4.11. These determine the form of constituent terms chosen in the Eq. 4.42, i.e. ${P_i}^{\left(\frac{\sigma_y}{\sigma_u}-1\right)}$ for exponential relations and $P_i {C_i}^{P_j}$ or $Q_i {C_i}^{Q_j}$ for power relations.

Table 4.11: Dependencies of C_v and A on C_2, C_3 and σ_y/σ_u.

	C_2 [-]	C_3 [-]	σ_y/σ_u [-]
C_v [J]	Power	Power	Exponential
A [-]	Power	Power	None

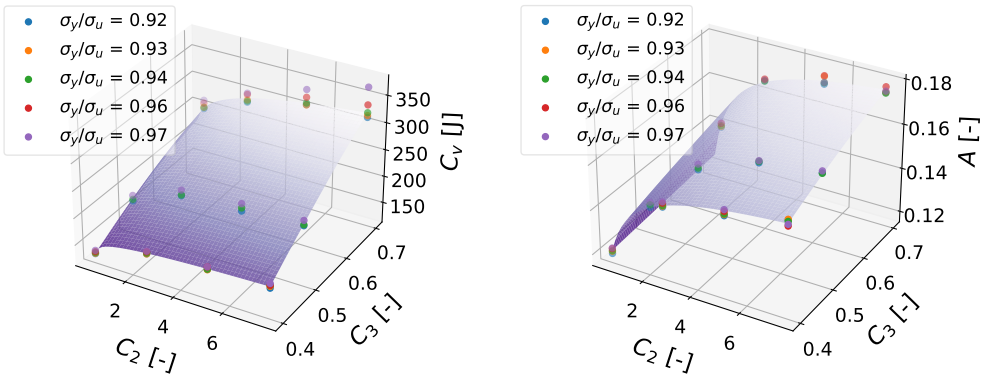
The data points in Figs. 4.23 to 4.25 also reveal information about the coupling between the plasticity parameter σ_y/σ_u and the damage parameters C_2 and C_3. It can be seen that changes in C_3 non-linearly affects the way C_v is related to C_2 (Fig. 4.23a) and changes in C_2 non-linearly affects the way C_v is related to C_3 (Fig. 4.24a). The same can be said of the relationship between A, C_2 and C_3. Therefore, the terms $P_i {C_2}^{P_j} {C_3}^{P_k}$ and $Q_i {C_2}^{Q_j} {C_3}^{Q_k}$ are included in the equation for C_v and A, respectively. From Fig. 4.23a, 4.24a and 4.25a, the coupling effect is also seen to act between σ_y/σ_u, C_2 and C_3. So, multiplicative terms between ${P_i}^{\left(\frac{\sigma_y}{\sigma_u}-1\right)}$, $P_i {C_2}^{P_j}$ and $P_i {C_3}^{P_j}$ are used in the equation for C_v.

Since C_2 and C_3 are normalised parameters representing, respectively, the maximum (at $\bar{\theta} = \pm 1$) and minimum (at $\bar{\theta} = 0$) strains in the triaxiality-independent

strain-based MMC damage locus (see section on Damage above), some physical sense could be derived from these findings.

From Figs. 4.24 and 4.26, the effect of C_3 is stronger on C_v than on A. This could be related to how the tunneling effects in the Charpy test, which have been shown to have a dominant effect in the behaviour [168], begin at mid-thickness in the specimen, where $\bar{\theta} = 0$. In contrast, $\bar{\theta}$ in the tensile test starts at 1 and gradually drops as necking occurs. The difference in the proportion of effects caused by C_2 and C_3 on C_v and A sheds light on the role played by each damage parameter in the process of calibration. While it is obvious that materials with high A and C_v are characterised by both high C_2 and high C_3, these results reveal information about the trends that characterise materials with high notch toughness C_v but low uniaxial-test fracture elongation A. Fig. 4.26 suggests that for a material with triaxiality-independent damage behaviour, the combination of high C_v and low A is characterised by combinations of high damage initiation strains at $\bar{\theta} = 0$ and low damage initiation strains at $\bar{\theta} = 1$. Conversely, a combination of low notch toughness and high uniaxial-test fracture elongation is characterised by low C_2 and high C_3.

It is also worth noting that the effect of C_2 (the maximum strain of the damage initiation locus) on C_v, which was identified as being very weak in previous work by the present authors [195], could in fact become significant if the variations in C_2 become very large (Fig. 4.23a).

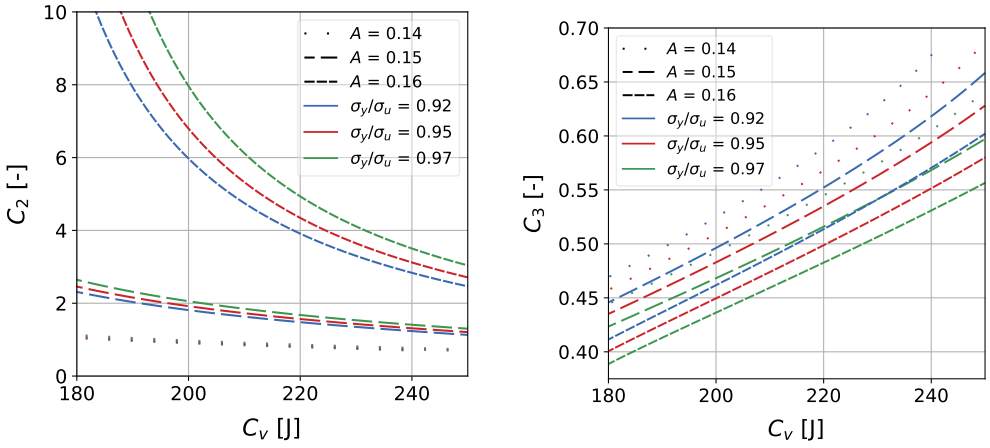


(a) C_v against C_2 and C_3

(b) A against C_2 and C_3

Figure 4.26: C_v and A against C_2 and C_3 from the parametric simulations together with fitted surface (using $\sigma_y/\sigma_u = 0.94$ as an example).

Finally, given a set of material certificate values for a steel within the range of the parametric study, Eq. (4.42) can be solved numerically to find an estimation of the calibrated damage parameters C_2 and C_3. Naturally, the range of A and C_v for which solutions exists has its bounds, as can be guessed from the surfaces shown in Fig. 4.26. Furthermore, the solution should not involve extrapolation beyond the range investigated by the parametric study. Fig. 4.27 shows the solutions of Eq. 4.42 for different C_v, σ_y/σ_u and A within the investigated range. It reveals that A has a stronger effect on the correlation between C_2 and C_v and the correlation between C_3 and C_v than does σ_y/σ_u, even when the coupling between plasticity and damage has been accounted for. To evaluate the consequences of this trend,



(a) C_2 against C_v

(b) C_3 against C_v

Figure 4.27: C_2 and C_3 against C_v obtained from solving Eq. 4.42.

Table 4.12: Values of σ_y/σ_u for different combinations of A and C_v used for generating the simulations in the parametric study on fracture toughness from SENB testing.

A [-] \ C_v [J]	150	180	190	200	210	220	250
0.14	0.97	0.97	-	-	0.97	-	-
0.15	0.92, 0.95, 0.97	-	-	0.92, 0.95, 0.97	-	-	0.92, 0.95, 0.97
0.16	-	-	0.97	-	-	0.97	0.97

observed in the internal damage parameters, for measured fracture properties, Eq. (4.42) is used in the next section to estimate the damage parameters and simulate the SENB fracture toughness test to obtain critical ductile fracture J-integral values, J_Q, for given combinations of A, C_v and σ_y/σ_u.

4.10 CORRELATION BETWEEN C_v AND J_Q

A total of 15 simulations of the SENB test were performed, for A varying between 0.14 and 0.16, σ_y/σ_u varying between 0.92 and 0.97, and C_v varying between 150 J and 250 J, as shown in Table 4.12. J_Q values were obtained from the simulations using the 'crack-plane method' described in Section 4.7. The results are plotted in Fig. 4.28, along with the upper-shelf J_Q - C_v conversion developed by Wallin [84], which has been adopted in BS7910 [170], and a similar correlation developed by Schindler

[93]. Comparison to other similar upper-self correlations [86–90, 263] is omitted due to differences in testing conditions and fracture toughness definitions used to obtain those correlations. A review on differences between the other proposed correlations can be found in Wallin [84, 264].

The Wallin [84] correlation is obtained by solving Eqs. (4.43) to (4.46):

$$J_{1\,\mathrm{mm},W} = 0.53{C_v}^{1.28} \tag{4.43}$$

$$m_W = 0.133{C_v}^{0.256} - \frac{\sigma_y}{4664} + 0.03 \tag{4.44}$$

$$\sigma_{fW} \approx \sigma_y \left(1 + \frac{150}{\sigma_y}\right) \tag{4.45}$$

$$\frac{J_{QW}}{2\sigma_{fW}} + 0.2 = \left(\frac{J_{QW}}{J_{1\,\mathrm{mm},W}}\right)^{\frac{1}{m_W}} \tag{4.46}$$

where $J_{1\,\mathrm{mm},W}$ [kJ m^{-2}] is Wallin's J-integral at 1 mm crack extension; C_v [J] is the Charpy impact energy, m_W [-] is the Wallin J-Δa curve exponent, σ_y [MPa] is the yield strength, σ_{fW} [MPa] is the average flow stress according to Wallin [265]; and J_{QW} [kJ m^{-2}] is the critical J based on the 0.2 mm crack extension offset using the Wallin [84] conversion from Charpy energy.

The Schindler [93] correlation is obtained by solving Eqs. (4.47) to (4.50):

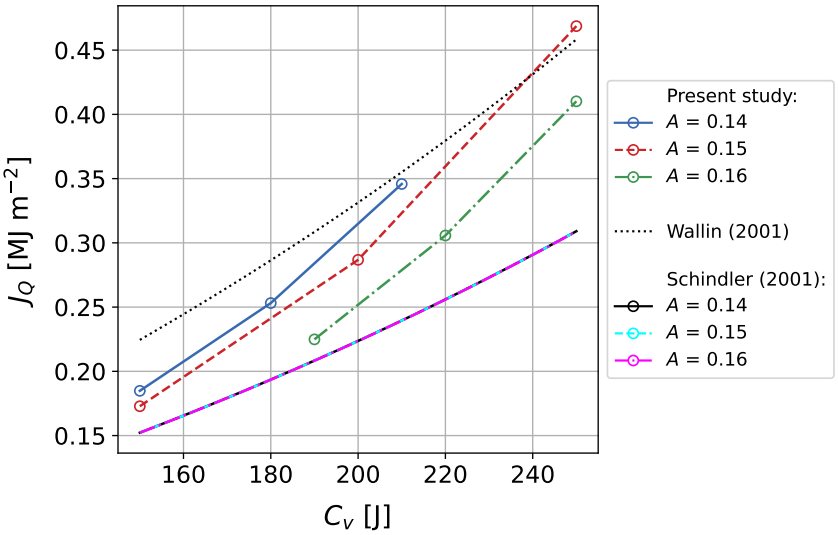
$$J_{1\,\mathrm{mm},S} = \frac{0.0250}{8^{m_S}} \left(1000C_v - 7.97U_f\right) \left(\varepsilon_u - \frac{\sigma_u}{E}\right)^{1-m_S} \tag{4.47}$$

$$m_S = \frac{3}{4}\left(1 + \varepsilon_u - \frac{\sigma_u}{E}\right)^{-1} \tag{4.48}$$

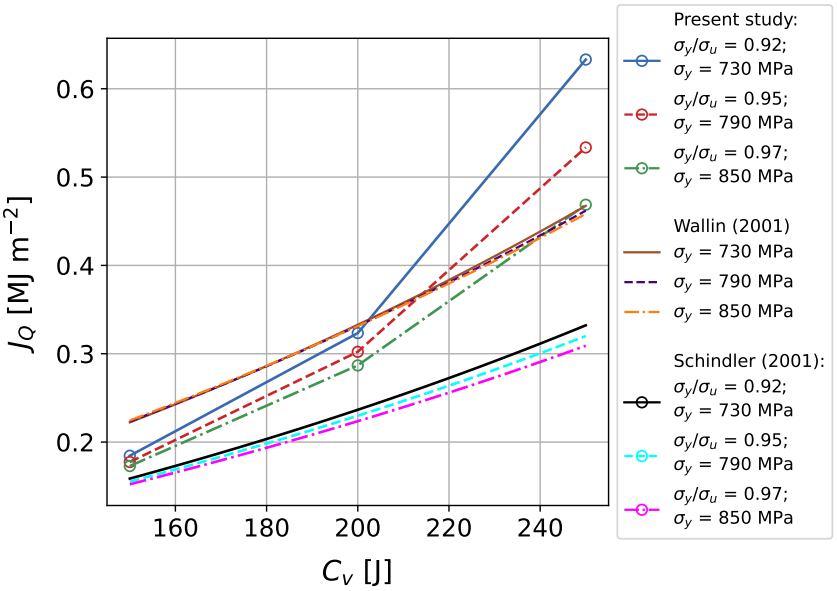
$$\sigma_{fS} = \frac{\sigma_y + \sigma_u}{2} \tag{4.49}$$

$$\frac{J_{QS}}{2\sigma_{fS}} + 0.2 = \left(\frac{J_{QS}}{J_{1\,\mathrm{mm},S}}\right)^{\frac{1}{m_S}} \tag{4.50}$$

where $J_{1\,\mathrm{mm},S}$ [kJ m^{-2}] is Schindler's J-integral at 1 mm crack extension; m_S [-] is the Schindler J-Δa curve exponent; C_v [J] is the Charpy impact energy; U_f [N mm^{-2}] is the specific energy or strain energy density of the tensile test, here approximated by the area under the engineering stress-strain curve; ε_u [-] is the uniform elongation expressed as a fraction; σ_u is the ultimate tensile strength; σ_y [MPa] is the yield strength, σ_{fS} [MPa] is the average flow stress according to Schindler [93]; and J_{QS} [kJ m^{-2}] is the critical J based on the 0.2 mm crack extension offset using the Schindler [93] conversion from Charpy energy.



(a) J_Q against C_v for different A and fixed $\sigma_y/\sigma_u = 0.97$



(b) J_Q against C_v for different σ_y/σ_u and fixed $A = 0.15$

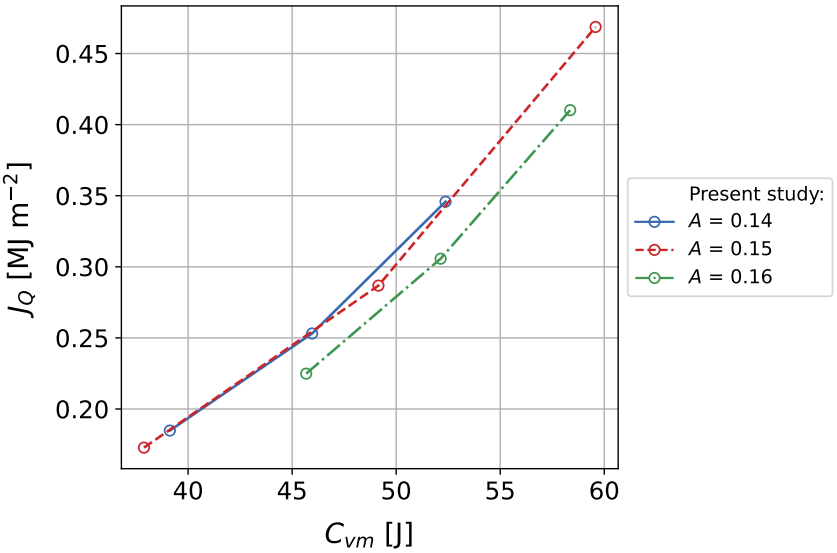
Figure 4.28: J_Q against C_v

4.10.1 *Implications of changes in A*

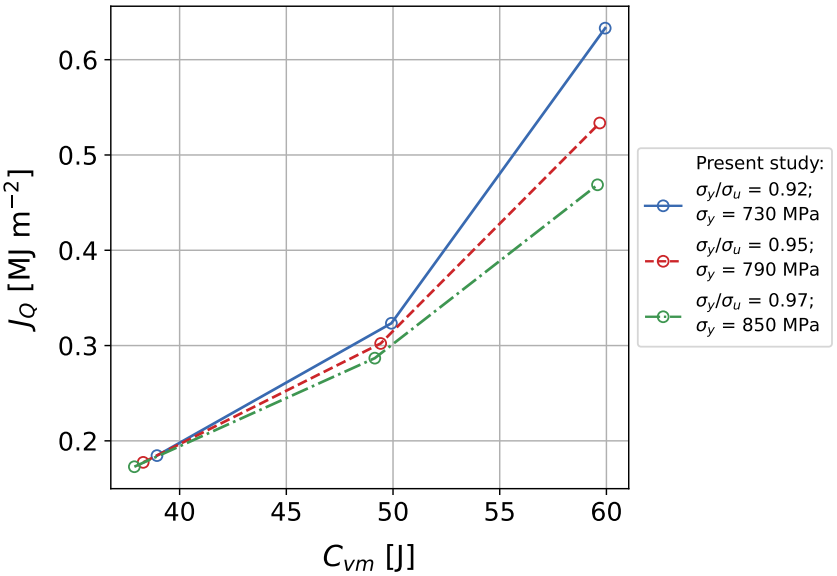
Fig. 4.28a shows how the correlation between J_Q and C_v varies for different A, when the σ_y/σ_u and σ_y are fixed. The parametric study shows that a higher J_Q is correlated with a lower A for a given C_v in this case. The Wallin [84] correlation does not include A, but the Schindler [93] correlation does show the same trend with A seen the parametric study, although its effect is so small it appears negligible. The A enters the correlation indirectly through U_f in Eq. (4.47), the specific energy of then tensile test, that is strongly correlated to A when the other engineering tensile test properties and, by extension, the plastic strain hardening properties are kept constant. From Eqs. (4.47) and (4.50), it can be seen that a decrease in U_f caused by a decrease in A leads to a increase in J_{QS} when all else is kept constant, even though this difference is so small that it is not visible in the plot (Fig. 4.28a).

Although both the present numerical results and Schindler [93] indicate a weak negative correlation between A and J_Q, many sources report a positive correlation between some measure of ductile fracture initiation toughness (such as equivalent critical plane-strain fracture toughness K_{Ic}) and either the tensile test strain energy density (associated with the area under the stress-strain curve) or the tensile test fracture elongation, for various ductile metals including steels [62, 266–268]. Taking into consideration the mechanisms assumed in Schindler's model, in which ε_u accounts for strain hardening and U_f is used based on empirical grounds to account for the difference in the energies associated with cracked and uncracked geometries, an increase in A and U_f with the other engineering test properties kept constant can be considered to be associated with an increase in the portion of the energy dissipation associated only with the initial deterioration of the uncracked notch in the Charpy test, which is not reflected in J_Q values obtained from fracture toughness testing of a the pre-cracked test, such that the remaining portion of the C_v, which is correlated to the J_Q, decreases, reflecting a decrease in J_Q. However, due to the empirical nature of this use of U_f to account for the effect of the Charpy notch and the difficulty in accounting for these energies separately, it is difficult to confirm the validity of this hypothesis using Schindler's model.

On the other hand, in the present numerical study, this trend of increasing A being accompanied by decreasing J_Q can be explained, for the assumed triaxiality-independent damage model, using mechanistic considerations relating to the fracture initiation strains and energetic considerations through partitioning of the Charpy impact energy. First, considering how all the energy attributed to ductile fracture initiation is dissipated before the force peak in a ductile Charpy impact test [269, 270] and how J_Q acts as a ductile fracture initiation measure evaluated close to the onset of stable crack extension in a fracture toughness test [244], J_Q is plotted in Fig. 4.29a against C_{vm}, the portion of the Charpy energy dissipated before the peak in the force-displacement plot from the instrumented Charpy test, instead of the total C_v. In this plot, variations due to A in the correlation between the Charpy measure and the J_Q measure dwindle. This reveals that differences in the C_v to J correlations observed for different A are related to differences in specifically the post-peak energy. This can in turn be related to the trend observed in the regression of A and C_v on C_2 and C_3 (Section 4.9).



(a) J_Q against C_v for different A and fixed $\sigma_y/\sigma_u = 0.97$



(b) J_Q against C_{vm} for different σ_y/σ_u and fixed $A = 0.15$

Figure 4.29: J_Q against C_{vm}

The regression obtained in Section 4.9 (Fig. 4.27) indicates that maintaining a constant C_v while decreasing A involves decreasing C_2, the damage initiation strain at $\bar{\theta} = 1$, and increasing C_3, the damage initiation strain at $\bar{\theta} = 0$, in the assumed triaxiality-independent damage locus. A is strongly associated with $\bar{\theta} = 1$ because damage starts building up with $\bar{\theta} = 1$, the stress state induced by the pre-necking uniaxial testing conditions. ($\bar{\theta}$ gradually drops as the neck develops and damage accumulates.) The pre-peak C_{vm} is mainly influenced by C_3 because the initial cracking in a Charpy test starts with tunnelling at the mid-thickness of the specimen, which is characterised by a plane-strain state of $\bar{\theta} = 0$. The post-peak Charpy behaviour and hence the total C_v are, in contrast, also affected by C_2 in addition to C_3, because as the tunnelling progresses outward from mid-thickness towards the free surface and as shear lips develop, damage build-up involving the $\bar{\theta} = 1$ of the free surface occurs too. As for the fracture toughness test, cracking begins with tunnelling at the mid-thickness like the Charpy test, and the stable ductile crack initiation value J_Q corresponds to only a small amount of crack extension. J_Q is therefore much more strongly affected by C_3, just like the pre-peak C_{vm} from the Charpy test. The trends observed in the influence of A on the C_v to J_Q correlations (Fig. 4.28a) and the lack thereof in the C_{vm} to J_Q correlations (Fig. 4.29a) are therefore related to the prevailing stress states involved in the determination of each of the engineering properties. A lower A for constant C_v is associated with lower damage strains for $\bar{\theta} = 1$ and higher damage strains for $\bar{\theta} = 0$, which is tied to an increase in both the C_{vm} and the J_Q.

As a conceptual aid for the above discussion, a simplified qualitative summary of the strength of the interactions between the different variables is given in Table 4.13. The evolution of the normalised Lode angle $\bar{\theta}$ at key locations in the tensile, Charpy and SENB simulations can be seen in Fig. 4.18b.

It is understood that the trend with which C_2 and C_3 changes for changing C_v or A, on which the preceding discussion is based, is limited by the assumption of triaxiality independence in the damage locus (Sections 4.8.1 and 4.8.4). If triaxiality dependence were included in the damage locus, the higher peak triaxialities in the SENB test ($\eta \sim 2.2$; $\bar{\theta} = 0$) compared to the Charpy test ($\eta \sim 1.7$; $\bar{\theta} = 0$) could be associated with lower damage initiation strains, giving combinations of damage parameters and simulations that result in a decreased J_Q and constant C_v for decreased A by virtue of decreased damage strains at high triaxiality ($\eta \sim 2.2$; $\bar{\theta} = 0$), despite the higher damage strains at peak Charpy triaxialities ($\eta \sim 1.7$; $\bar{\theta} = 0$) that would accompany the lower $\bar{\theta} = 1$ damage strains described above. This accounts for the discrepancy between the presently observed trend and that which is described in the literature [62, 266–268] for A and J_Q. The presently observed negative correlation is one that is specific to the triaxiality-independent assumption. Nonetheless, the considerations relating to the stress states and energy attributions behind these trends remain the same, and it remains that the correlation of J_Q with A is weak (Chatterjee [271] correlation coefficient $\xi = -0.02$), and the J_Q is correlated to C_{vm} so strongly ($\xi = 0.79$) in comparison that changes in A have only a very weak effect on the J_Q–to–C_{vm} correlation.

Table 4.13: Qualitative description of the strength of the interaction between the engineering parameters and material parameters as a conceptual aid.

	C_{vm} [J]	C_v [J]	A [-]	J [MJ m^{-2}]
C_2 [-]	Weak	Strong	Strong	Weak
C_3 [-]	Strong	Strong	Weak	Strong
σ_y/σ_u [-]	Strong for high C_3 Weak for low C_3	Strong for high C_3 Weak for low C_3	None	Weak

4.10.2 *Implications of changes in σ_y/σ_u*

Fig. 4.28b shows how the correlation between J_Q and C_v varies for increasing σ_y/σ_u, with a correspondingly increasing σ_y (Eq. (4.34)), when the A is fixed. The Wallin [84] correlation does not account for σ_y/σ_u, but predicts a higher J_Q for a lower σ_y, when all else is constant. The parametric study suggests that this trend still holds when the σ_y is accompanied by a higher σ_y/σ_u, with the difference that a slightly larger effect on the J_Q is predicted when the C_v is large. The effect of the increasing σ_y/σ_u and σ_y on J_Q observed here also agrees with the trend seen in the Schindler [93] correlation. Nonetheless, the change in J_Q due to changing σ_y/σ_u and σ_y is small in comparison to that due to the change in C_v. At a C_v of 200 J, a change in σ_y/σ_u from 0.92 to 0.97, a range which spans 60 % of the σ_y/σ_u range of the considered dataset (Fig. 4.19; Section 4.9.1.1), and includes 80 % of the number of observations in the dataset, leads to only a 15 % change in J_Q. The same change is effected by a change in C_v corresponding to a mere 5 % of the range spanned by the C_v values in the considered dataset.

Comparing Figs. 4.28b and 4.29b, it is worth noting that although varying σ_y/σ_u has a smaller effect on the correlation between J_Q and C_{vm} than on the correlation between J_Q and C_v for low C_{vm} and low C_v, this does not apply to high C_{vm}. This is unlike the effect of variations in A on the C_{vm}–to–J_Q correlation, where the effect of the variation in A is seen to be small for all C_{vm}. Nonetheless, considering C_{vm} instead of C_v still has the effect of reducing the influence of variations in σ_y/σ_u on the prediction of fracture toughness from the Charpy data.

4.11 CONCLUSIONS

A coupled rate-dependent plasticity model with damage softening and thermal softening has been presented and validated for the purpose of correlating Charpy V-notch toughness and SENB fracture toughness. Its ability to be calibrated using only the tensile, Charpy notch impact and SENB fracture mechanic tests and to simulate the force-displacement behaviour and ductile fracture characteristics in all these three tests simultaneously has been demonstrated for AH36 and S690QL steel.

The suitability and effectiveness of various simplifications to the model for the purpose of practical engineering application have been substantiated. Sections 4.8.1 and 4.8.2 have outlined how triaxiality independence and empirical softening parameters can be assumed for certain steels to reduce the number of damage

initiation parameters to two. Section 4.8.3 has demonstrated the strong similarities in the tunnelling behaviour and stress-state distributions in the Charpy and SENB tests at key locations and at key extents of progression of the tests, giving insight into the mechanical basis for the correlations between the two tests and suggesting that a calibration to the Charpy test effectively involves calibrating to a stress-state distribution and evolution range that is similar to that of the SENB test. It is worth noting that given its purpose, the approach has not been validated for the application to other mechanical tests and other stress state ranges: the calibration involves simplifications effective for reducing calibration effort without sacrificing the ability to capture the behaviour in specifically these three tests, given that the key differentiating factors of rate-dependence and adiabatic heating are correctly accounted for.

By virtue of the reduced calibration effort afforded by the approach presented, a numerical investigation of the correlation between J_Q and C_v and how it is affected by variations in A, σ_y/σ_u and σ_y was performed using the developed rate- and temperature- dependent damage-softening plasticity model. To this end, a parametric study, involving a range spanned by a set of material certificate data and some empirical assumptions deduced from the dataset, was carried out, in which the SENB fracture toughness test was modelled for varying A and C_v, assuming correspondingly varying damage parameters which are calibrated based on the C_v and the A. The calibration was obtained from a regression analysis of C_v and A on material parameters C_2, C_3 and σ_y/σ_u, performed on a series of Charpy and tensile simulations for each of 52 combinations of C_2, C_3 and σ_y/σ_u values spanning the parametric space. The following conclusions are drawn from this study.

The pre-peak energy from the force-displacement plot in an instrumented ductile Charpy test C_{vm} has a stronger ($\xi = 0.79$) and more independent correlation with J_Q than does C_v ($\xi = 0.57$; Figs. 4.28 and 4.29). J_Q is predominantly related to the onset of ductile crack extension, but C_v includes a significant amount of energy attributed to continued ductile crack propagation. On the other hand, C_{vm} includes less of this crack propagation energy but includes all the energy up to the onset of ductile fracture and is thus more closely tied to J_Q. Developing and making use of correlations between C_{vm} and J_Q would result in more consistent predictions of ductile fracture initiation toughness than given by correlations between C_v and J_Q.

The σ_y/σ_u ratio has a weak correlation with C_{vm} ($\xi = 0.17$) and with J_Q ($\xi = 0.17$), especially for low-value ranges of C_{vm} and J_Q. The correlation between C_{vm} and J_Q themselves is far stronger ($\xi = 0.79$), such that changes in C_{vm} can be seen to give predictions of far more significant changes in J_Q than changes in σ_y/σ_u could be related to (Section 4.10.1). The σ_y/σ_u ratio alone, without the information C_{vm} or C_v, is not useful for ductile fracture initiation toughness prediction.

For a model with a triaxiality-independent, Lode-dependent strain-based damage locus, the A is weakly and negatively correlated to J_Q for a constant C_v. Changes in A appear to affect the correlation between C_v and J_Q because A is correlated to the later-stage portion of the C_v energy, broadly associated with $\bar{\theta} = 1$, corresponding to both the uniaxial tensile pre-necking stress state and the free-surface stress state which becomes relevant with significant ductile crack propagation in the Charpy specimen. For a constant C_v, a decrease in A is correlated with a decrease in that later-stage proportion of the energy, such that the C_{vm} and J_Q associated with fracture

initiation increase. Even though the negative trend of the correlation between C_v and J_Q seen in the numerical results due to the assumption of triaxiality independence does not agree with experimental observations [62, 266–268], it remains that J_Q is much more strongly correlated to C_{vm} than to A. Differences in A only have a small effect on the correlation (Fig. 4.29a) between J_Q and C_{vm}, which acts as a more reliable indicator than C_v. Due to this, the A alone, without C_{vm} or C_v, is in general not useful for ductile fracture resistance considerations.

Although varying σ_y/σ_u and A has some effect on how the total notch energy C_v is correlated to J_Q, it does not reflect a significant effect on the ductile fracture initiation toughness but is rather associated with the fact that the C_v includes a significant portion of energy for stable ductile propagation and fracture occurring at the specimen's free surface, while J_Q primarily concerns the onset stage of stable ductile tunnelling behaviour at the centre of the specimen. The σ_y/σ_u and A are seen to have an even smaller effect on the correlation of C_{vm}–to–J_Q in comparison with the C_v–to–J_Q correlation, especially for low C_{vm}. When predicting a fracture toughness for the sake of assessing the limit state associated with the onset of stable ductile crack propagation using alternative tests in situations where direct fracture toughness testing is not an option, the advice is to use C_{vm} instead of C_v, σ_y/σ_u or A.

Two other notable findings peripheral to the central argument have been observed in the course of this work. First, the importance of the adiabatic heating effect for Charpy tests with high impact toughness and hence high C_v has been shown, while this effect has been observed to be negligible in the ductile Charpy tests with low C_v. This provides nuance to the existing discussion in the literature, in which a few have recently pointed out the importance of accounting for this effect, while many more have shown good results even while ignoring it (Section 4.6). Second, the analytical approach of finding the plastic hardening curve parameters using the Considère criterion and only key points from the engineering stress-strain curve, being the yield stress, the length of the yield plateau, the ultimate stress and the uniform elongation, instead of the full engineering stress-strain curve, has proven to be effective for modelling the behaviour up to the necking point. This leads to the recommendation to include the reporting of yield plateau length and uniform elongation in the mill test certificates, enabling the modelling of pre-necking behaviour using only point data from the mill test certificate.

4.12 SYMBOLS

LATIN

A	Fracture elongation over the proportional gauge length from pieced-together tensile test fragments
A_ε	Engineering strain at full fracture in tensile test
a_0	Measured initial crack length in SENB specimen
a_{0q}	Compliance-estimated initial crack length
a_n	Machined notch length in SENB specimen
Δa	Crack extension

Δa_{cp}	Crack extension based on FEA crack-plane method
Δa_p	Measured final crack extension
Δa_{pq}	Compliance-estimated final crack extension
B	Specimen thickness
$\mathbb{C}$	Isotropic elastic stiffness tensor
C	Cowper-Symonds coefficient
C_1	Normalised MMC parameter relating to the strain in the MMC surface when $c_1 = 0; \eta = 2.5; \bar{\theta} = 0$
C_2	Normalised MMC parameter relating to the maximum strain in the MMC surface when $c_1 = 0$
C_3	Normalised MMC parameter relating to the minimum strain in the MMC surface when $c_1 = 0$
C_v	Charpy V-notch energy
C_{vm}	Portion of the Charpy energy dissipated before the peak in the force-displacement plot from the instrumented Charpy test
c	Specific heat capacity
c_1	First MMC strain surface parameter
c_2	Second MMC strain surface parameter
c_3	Third MMC strain surface parameter
D	Damage indicator
D_c	Critical damage
$\mathcal{D}_p$	Internal work due to plastic deformation
E	Young's modulus
f	Yield function
g	Average slope for Swift hardening in the true stress versus true plastic strain space, between $\varepsilon_{sh,p}$ and $\varepsilon_{u,p}$
g_H	Average slope for Hollomon hardening rule in the true stress versus true total strain space, between $\varepsilon_{y,t}$ and $\varepsilon_{u,t}$
h	Hardening modulus
i	Iteration
i_{max}	Maximum number of iterations for the return-mapping calculations
j	Increment
J	J-integral
$J_{1\,\mathrm{mm},S}$	J at 1 mm crack extension according to Schindler's (2001) conversion from Charpy testing
$J_{1\,\mathrm{mm},W}$	J at 1 mm crack extension according to Wallin's (2001) conversion from Charpy testing
J_{cp}	J-integral based on FEA crack-plane method
J_Q	Critical J based on the 0.2 mm crack extension offset

J_{QS}	Critical J based on the 0.2 mm crack extension offset using the Schindler [93] conversion from Charpy energy
J_{QW}	Critical J based on the 0.2 mm crack extension offset using the Wallin [84] conversion from Charpy energy
K	Strength coefficient of the power law for hardening
K_H	Strength coefficient for the Hollomon hardening power law
K_{Ic}	Critical plane-strain fracture toughness
K_J	Stress intensity factor converted from J
L	Single-edge notched bending specimen length
L_0	Gauge length of tensile specimen
L_c	Parallel length of tensile specimen
l_c	Characteristic element length
m	Damage softening exponent
m_x	Thermal softening exponent
m_W	Wallin J-Δa curve exponent
N	Notch-mouth / knife-edge opening
n	Strain hardening exponent for the Swift hardening power law
n_H	Strain hardening exponent for the Hollomon hardening power law
$\boldsymbol{n}$	Gradient of the yield surface
$\boldsymbol{P}$	Pseudo-elastic material stiffness matrix
q	Cowper-Symonds exponent
R	Rate-dependence factor
S	Single-edge notched bending specimen span
s	Viscosity parameter
Δt	Time increment
T	Interpolation parameter
W	Specimen width
w	SENB machined notch width
X	Thermal softening factor
Z	Parameter for the grouped effect of the MMC c_1 terms when $\eta = 2.5$; $\bar{\theta} = 0$

GREEK

α	Plastic coefficient
β	Softening coefficient
ε	Engineering strain
ε_0	Swift offset strain
ε_f	Ductile damage initiation strain
ε_p	Equivalent plastic strain

$\dot{\varepsilon}$	Uniaxial strain rate
$\dot{\varepsilon}_p$	Equivalent plastic strain rate
$\dot{\varepsilon}_{p0}$	Equivalent plastic strain rate offset parameter
$\dot{\varepsilon}_{p,uni}$	Quasi-static-uniaxial-testing equivalent plastic strain rate parameter
$\ddot{\varepsilon}_p$	Rate of change of the plastic strain rate
ε_{sh}	Total engineering strain corresponding to the end of the yield plateau
$\varepsilon_{sh,p}$	Equivalent plastic strain corresponding to the end of the yield plateau
ε_t	True total strain
ε_u	Uniform elongation, i.e. the engineering strain at the onset of necking
$\varepsilon_{u,p}$	Equivalent plastic strain corresponding to the occurrence of necking instability
$\varepsilon_{u,t}$	True total strain at the occurrence of necking instability
$\dot{\boldsymbol{\varepsilon}}_{\boldsymbol{vp}}$	Viscoplastic strain rate tensor
$\Delta\boldsymbol{\varepsilon}_{\boldsymbol{vp}}$	Viscoplastic strain increment tensor
$\varepsilon_{y,t}$	True total strain at the initial yield point
η	Stress triaxiality
Θ	Temperature
Θ_m	Melting temperature
Θ_r	Room temperature
$\bar{\theta}$	Normalised Lode angle
$\dot{\lambda}$	Plastic multiplier as a rate
$\Delta\lambda$	Plastic multiplier as an increment
μ_D	Tolerance for $D = D_c$ when i_{max} is reached
μ_f	Tolerance for $f = 0$
ν	Poisson's ratio
ξ	Chatterjee [271] correlation coefficient
ρ	Density
σ	Flow stress taking into account plastic strain hardening, rate dependence and damage due to softening
$\bar{\sigma}$	Quasi-static undamaged stress due to plastic strain hardening only
σ_{fS}	Average flow stress according to Schindler [93]
σ_{fW}	Average flow stress according to Wallin [84]
σ_v	von Mises equivalent stress
σ_u	Ultimate tensile stress from uniaxial tensile test
σ_y	Yield stress from uniaxial tensile test
$\boldsymbol{\sigma}$	Cauchy stress tensor
χ	Taylor-Quinney energy coefficient

5

CONCLUSIONS AND RECOMMENDATIONS

The σ_y/σ_u limits presently stipulated in commonly used design rules, standards and product specifications are perceived by the industry as a barrier to the more widespread use of high-strength steels, which inherently have high σ_y/σ_u but could otherwise enable significant weight and size reductions in steel structures. These limits arise from measures to ensure sufficient structural-level ductility. Even though the minimum deformation capacity that amounts to sufficient structural ductility and even the mechanism that governs the structural ductility vary with the design context and structural configuration, the σ_y/σ_u ratio has, in some design frameworks, nonetheless assumed the role of a material ductility requirement that applies in a blanket manner (Tables A.1 and A.2).

5.1 CONCLUSIONS

To address the use of the σ_y/σ_u limit as a blanket material requirement, two critical mechanisms to which it is attributed to in the literature have been investigated in this thesis: the ductility of plastic hinges in beams and the upper-shelf toughness in cracked details.

With regard to the ductility of plastic hinges in beams, the following objectives were defined in the Introduction:

1a. Quantify the role of strain hardening and σ_y/σ_u in the ductility of plastic hinges in beams.

2. Develop more nuanced, context-dependent ductility criteria for plastic hinges that account for both the structure's material properties and geometrical properties.

By performing a parametric study using an finite-element modelling approach that was validated against experiments in the literature, accounting for σ_y/σ_u as a measure of strain hardening, Chapter 3 has shown how the rotation capacity R at a plastic hinge in a beam is simultaneously dependent on the yield strength σ_y, the σ_y/σ_u ratio and the cross-sectional slenderness. Further, the following conclusions were drawn in the study:

1. Due to the interdependence between R, σ_y, σ_y/σ_u and the cross-sectional slenderness, a complete, accurate determination of the σ_y/σ_u limit should be situational and dependent on the desired rotation and specific geometries, in contrast to the current practice which typically involves a material-specific limit that is independent of the structural context.

2. For a fixed σ_y/σ_u ratio, cross-sectional slenderness and lateral-torsional buckling slenderness, a higher σ_y leads to higher rotation capacities.

3. The trend between the rotation capacity and the cross-sectional slenderness depends on whether the buckling is web- or flange-dominated. Increasing the flange stockiness by decreasing the flange width for a beam that is experiencing web-dominated buckling does not help to increase the rotation capacities but instead decreases it, although a decrease is reflected in the cross-section slenderness parameter. This suggests the value of considering the ratio between the web slenderness and flange slenderness and of specifying independent web and flange limits that apply simultaneously, as also suggested by Chen et al. [142].

With regard to upper-shelf toughness in details that are cracked or susceptible to cracking, the following objectives were established:

1b. Quantify the role of strain hardening and σ_y/σ_u in the upper-shelf toughness in details that are cracked or susceptible to cracking.

3. Evaluate how the upper-shelf toughness in cracked details correlates with the aggregate information contributed by easily accessible material testing properties obtained from the tensile and Charpy tests, accounting for the effects reflected by variations in the combination of these properties.

To this end, Chapter 4 introduced a coupled rate-dependent plasticity model with damage softening and thermal softening. The model was validated for the purpose of correlating Charpy V-notch toughness and SENB fracture toughness by the demonstration of its ability to simulate the tensile, Charpy notch impact and SENB fracture mechanic tests' force-displacement behaviour and ductile fracture characteristics in all these three tests using a distinct set of material parameters for each material considered: an 11 mm as-rolled AH36 steel and a 12 mm quenched and tempered S690QL steel.

The suitability and effectiveness of various simplifications to the model for the purpose of practical engineering application have been substantiated, including how the assumption of triaxiality independence and empirical softening parameters can reduce the number of damage calibration parameters for steels with a weak triaxiality dependence in the medium-to-high triaxiality range to two when the objective is to simulate tensile, Charpy and SENB tests. Similarities in the tunnelling behaviour and stress-state distributions in the Charpy and SENB tests at key locations and at key extents of progression of the tests were observed, giving insight into the mechanical basis for the correlations between the two tests and suggesting that a calibration to the Charpy test effectively involves calibrating to a stress-state distribution and evolution range that is similar to that of the SENB test.

By virtue of the reduced calibration effort afforded by the approach presented, a numerical investigation of the correlation between the ductile fracture initiation toughness J_Q and the Charpy energy C_v and the implications of changes in A, σ_y/σ_u and σ_y for this correlation was performed using a two-staged parametric study. First, a calibration relationship was obtained from a regression analysis of C_v and A on σ_y/σ_u and the damage parameters C_2 and C_3, obtained from Charpy and tensile simulations for each of 52 material-parameter combinations spanning a parametric space based on a range spanned by a dataset of material certificate properties and some empirical assumptions deduced from the dataset. Then, a series of simulations of the SENB fracture toughness test was performed with varying A and C_v, assuming correspondingly varying damage parameters which are calibrated based on the C_v and the A. The following conclusions are drawn from this study:

1. The energy C_{vm} dissipated up to the occurrence of the peak force in the force-displacement plot from the instrumented Charpy test has a stronger (Chatterjee [271] correlation coefficient $\xi = 0.79$) and more independent correlation with J_Q than does C_v ($\xi = 0.57$). This is because J_Q is determined near the onset of stable ductile fracture, to which C_{vm} is more strongly related, while C_v includes significant amount of energy attributed to continued ductile crack propagation.

2. The σ_y/σ_u has a weak correlation with C_{vm} ($\xi = 0.17$) and with J_Q ($\xi = 0.17$), especially for low-value ranges of C_{vm} and J_Q. The correlation between C_{vm} and J_Q themselves is far stronger ($\xi = 0.79$), such that changes in C_{vm} can be seen to give predictions of far more significant changes in J_Q than changes in σ_y/σ_u could be related to. The σ_y/σ_u alone, without the information C_{vm} or C_v, is not useful for ductile fracture initiation toughness prediction.

3. J_Q is weakly correlated with A ($\xi = -0.02$). Differences in A only weakly affects the correlation between J_Q and C_{vm}, which acts as a more reliable indicator than C_v. The A alone, without C_{vm} or C_v, is in general not useful for ductile fracture resistance considerations.

5.2 RECOMMENDATIONS

Several recommendations can be given concerning the ductility requirements currently used in typical rules and standards for steel structures.

To begin with, considering how σ_y/σ_u is used for the sake of structural ductility and how it is a ratio of two values, specifying requirements on σ_y/σ_u based on nominal values of σ_y and σ_u is not effective for producing desired effects of increasing ductility in the actual structural response, because the actual σ_y/σ_u could be higher or lower than the stipulated limit even if the nominal σ_y/σ_u satisfies the limit. Currently, some frameworks specify it on actual values (e.g. AISC–ASTM [13–15] and some classifications societies [19, 20]), while some specify it on design values (e.g. EN [10, 28]). For a meaningful result, limits specified explicitly (Section 2.2.1) on the σ_y/σ_u in view of the ductility considerations at hand should be specified on the actual values.

Strain hardening ability, which can be indicated by the σ_y/σ_u ratio, is important for and directly correlated to the ductility of plastic hinges, such that meaningful limits on σ_y/σ_u can be proposed for given global-level deformation capacity, material strength and structural geometry. In the literature, the consideration of this mechanism has been forefront in the continued use of the σ_y/σ_u limit in its present form (Section 2.4). However, not all designs utilise the concept of plastic hinge formation in a collapse mechanism together with global plastic analysis in their ultimate limit state. Furthermore, other mechanisms which are not always applicable to all designs might also be indirectly implicated in σ_y/σ_u considerations, such as the use of capacity design (Section 2.2.2) for the avoidance of catastrophic collapse mechanisms, even though capacity design is for the most part realised by robust structural detailing. Therefore, the stipulation of limits on actual σ_y/σ_u values should be accompanied by qualifying statements that specify the mechanisms for which they apply. This allows not only the elimination of undue restriction in contexts where σ_y/σ_u is not relevant but also the possibility to specify different σ_y/σ_u limits for different mechanisms.

For the rotation capacity of plastic hinges as limited by the plastic buckling mechanism, it is seen that there are a few options for including these σ_y/σ_u ductility considerations in a more nuanced way. One way that fits within the current design framework for the local buckling of steel members is to make use of cross-sectional slenderness classification limits that account for the expected high σ_y/σ_u values for higher steel grades. Chapter 3 has given a few examples of the determination of such limits. This way, higher or lower limits for σ_y/σ_u, depending on the target rotation required, can be specified in the rules for this mechanism, through the action of low slenderness parameters that counteracts the high σ_y/σ_u. Another approach, as discussed in the literature review (Section 2.3.4), is to use strain-based design approaches that involve a more direct and continuous treatment of ductility, rather than the current widespread class-based system.

Another consideration in existing justification for the use of σ_y/σ_u in the rules involves the use of the σ_y/σ_u as part of a set of substitute upper-shelf toughness requirements, including a minimum fracture elongation A and minimum brittle-fracture-avoidance Charpy values, for ensuring the local ductility at details that are cracked or susceptible to cracking (Section 4.1). It was seen that there was a lack of a strong basis for the use of σ_y/σ_u in this regard, and recent research lacks a consensus on if and how σ_y/σ_u is correlated to ductile fracture resistance. The initial inclusion of σ_y/σ_u in this set of requirements appears to stem from the fact that lower σ_y/σ_u values are associated with larger necking strains, which mark the onset of strain localisation.

The findings of Chapter 4 reinforce the doubt cast on the use of σ_y/σ_u, which has a very weak correlation to ductile fracture initiation toughness J_Q, in the set of substitute upper-shelf toughness requirements. Furthermore, the A was also seen to have a very weak correlation to the ductile fracture initiation toughness, and the pre-force-peak energy C_{vm} is more strongly correlated to J_Q than C_v is. Due to this, and considering the scatter and range exhibited by observed values, σ_y/σ_u and A play a near-negligible role in the substitute upper-shelf toughness requirements. (However, A might have relevance for other considerations, such as when the critical structural-level ductility is determined by ultimate failure

of plastically yielding tension members.) For safety considerations for structures involving details that are cracked or susceptible to cracks, upper-shelf C_v or C_{vm} values (involving predominantly ductile behaviour in the Charpy tests) would act as a better substitute upper-shelf toughness criterion than the current ones. Also, developing and making use of correlations between C_{vm} and J_Q would result in more consistent predictions of ductile fracture initiation toughness than given by correlations between C_v and J_Q. The upper-shelf C_v-to-J_Q correlation is slightly more affected by σ_y/σ_u and A, so a potential stipulation of an upper-shelf C_v requirement would be one that is derived assuming worst-case σ_y/σ_u and A values and a target minimum ductile fracture initiation toughness.

It was also seen in Chapter 4 that the analytical approach of finding the plastic hardening curve parameters using the Considère criterion and only key points from the engineering stress-strain curve, being the yield stress, the length of the yield plateau, the ultimate stress and the uniform elongation, instead of the full engineering stress-strain curve, has proven to be effective for modelling the behaviour up to the necking point. This leads to the recommendation to include the reporting of yield plateau length and uniform elongation in the mill test certificates, enabling the modelling of pre-necking behaviour using only point data from the mill test certificate.

The recommendations can be summarised as follows:

1. Any limit specified on σ_y/σ_u for local ductility considerations should be specified on the actual rather than the nominal σ_y/σ_u.

2. Limits specified on σ_y/σ_u should be accompanied by qualifying statements specifying the mechanisms for which they apply.

3. Limits specified on σ_y/σ_u for plastic hinge rotation capacity considerations could be improved to broaden the allowable use scope of high-strength and high-σ_y/σ_u steels by considering the joint effect of the cross-sectional slenderness, the σ_y and the σ_y/σ_u on the plastic hinge rotation capacity.

4. The prevalent use of limits on the yield-to-tensile strength ratio and the fracture elongation as part of an implied set of substitute upper-shelf fracture toughness requirements should be replaced by upper-shelf Charpy-based limits, in agreement with Feldmann and Schaffrath [60]. (Note, however, that σ_y/σ_u and A might be relevant for other contexts.) Recognising that C_{vm} values are not readily available in current practice, the simplest implementation of this recommendation for the present involves the introduction of requirements in terms of minimum Charpy energies obtained from room-temperature testing.

5. Developing and making use of correlations between C_{vm} and J_Q would result in more consistent predictions of ductile fracture initiation toughness than given by correlations between C_v and J_Q.

6. Reporting the yield plateau length and uniform elongation in the material test certificates would enable the modelling of pre-necking behaviour using only point data from the mill test certificate, without a full stress-strain curve. This information is readily available from the typical uniaxial tensile test

performed in standard practice for product certification and should be added to the record due to the value it brings at no extra cost.

A

σ_y / σ_u LIMITS FOUND IN STANDARDS, RULES AND SPECIFICATIONS

Table A.1: Limits specified on the nominal values of σ_y/σ_u in design.

Application	σ_y/σ_u limit	Reference
Buildings and bridges	0.95 - elastic analysis 0.91 - plastic analysis	CEN 2020 [28]
Lifting appliances	0.94	LR 2022[1] [11]

[1] Additionally, the steel should comply with the LR Rules for the Manufacture, testing and Certification of Materials, in which limits of 0.90 or 0.94 on the actual σ_y/σ_u ratio apply to some steels (see Table A.2 below).

[2] In most other design rules or standards, although a limit on σ_y/σ_u is not stated, a requirement is set that the material should comply with relevant product specifications or material certification rules, in which limits on the actual σ_y/σ_u are stated.

Table A.2: Limits specified on the actual values of σ_y/σ_u obtained from testing for certification or compliance with product specification.

Application	Steel type	Strength [MPa]	σ_y/σ_u limit	Reference
Buildings, bridges and general structural use	General rolled and HSLA QST steel shapes	345 – 450	0.85	ASTM 2020, 2019 [14, 15]
Marine and offshore structures	Grades AH, DH, EH, FH	420 – 960	0.94	LR 2024 [19]; DNV 2021 [20]
	C-Mn steels of grades AH, DH, EH, FH – N or M	265 – 390	0.90	LR 2024 [19]
	C-Mn steels of grades AH, DH, EH, FH – QT	265 – 390	0.94	LR 2024 [19]
	Grades designated with normal weldability, improved weldability 'W' and offshore 'O'	420 - 960	0.94	DNV 2021 [21]
	Hot-rolled grades S355 – S770: NO, MO, QO	355 – 770	0.87 (355 MPa) – 0.97 (770 MPa)	CEN 2019 [22]
	QR3, QR4, QR4 (offshore mooring chains and accessories)	410 - 760	0.92	BV 2020 [23]
	High-strength steel for special applications (pressure vessels)	550 - 690	0.90 (550 MPa) - 0.92 or 0.95 (690 MPa)	LR 2024 [19]
Pipes	Grades L, X with PSL2	245 – 830	0.93 (245 MPa) – 0.99 (830 MPa)	API 2018 [18]
	Grades L, X with PSL2	245 – 555	0.80 (245 MPa) – 0.90 (555 MPa)	ISO 2019 [16]
	C-Mn steels	245 – 555	0.93	DNV 2021 [17]
	Duplex and martensitic stainless steels of grades 13Cr, 22Cr, 25Cr	450 – 550	0.92	DNV 2021 [17]

Table A.3: Reduction in design strength for steels with high σ_y/σ_u in lifting appliances.

Document	Condition	Provision
LR Code for Lifting Appliances in a Marine Environment (2022) [11]	$\sigma_y/\sigma_u > 0.85$	$\sigma_{y,d} = 0.459(\sigma_u + \sigma_y)$
DNV-ST-0378 Standard: Offshore and platform lifting appliances (2021) [45]	$\sigma_y/\sigma_u > 0.8$	$\sigma_{y,d} = 0.8\sigma_u$
ABS Guide for certification of lifting appliances (2020) [44]	$\sigma_y \leq 355$ MPa and $\sigma_y/\sigma_u > 0.72$ (For all structural steel parts of cranes apart from steel booms)	$\sigma_{y,d} = 0.72\sigma_u$
	$\sigma_y \leq 690$ MPa and $\sigma_y/\sigma_u > 0.72$ (For cargo gear)	$\sigma_{y,d} = 0.72\sigma_u$
	$\sigma_y/\sigma_u > 0.7$ (For base-mounted manriding winches)	$\sigma_{y,d} = 0.409(\sigma_u + \sigma_y)$
BV NR 526 Rules for the Certification of Lifting Appliances onboard Ships and Offshore Units (2021) [12]	$\sigma_y/\sigma_u > 0.83$ (For offshore lifting appliances in general)	$\sigma_{y,d} = 0.83\sigma_u$
	$\sigma_y/\sigma_u > 0.71$ (For unstayed masts in derrick systems)	$\sigma_{y,d} = 0.417(\sigma_u + \sigma_y)$
FEM 1.001 3rd Edition Rules for the design of hoisting appliances (1998) [43]	$\sigma_y/\sigma_u > 0.7$	$\sigma_{y,d} = 0.414(\sigma_u + \sigma_y)$
EN 13001-3-1:2012+A2:2018 Cranes - General Design - Part 3-1: Limit States and proof competence of steel structure (2018) [42]	$\sigma_y/\sigma_u > 0.95$	$\sigma_{y,d} = 0.95\sigma_u$

B

STRESS-UPDATE ALGORITHM FOR VISCOPLASTIC CONSISTENCY MODEL WITH DAMAGE SOFTENING AND THERMAL SOFTENING

This is an implementation of the viscoplastic consistency model given by Wang et al. [197] coupled with the damage-softening model of Li and Wierzbicki [187], the Cowper-Symonds rate-dependent flow stress model [182], and the Johnson-Cook [198] thermal softening model.

Subscript $j-1$ refers to quantities from the previous (converged) finite-element analysis increment, and subscript $i-1$ refers to the quantities of the previous return mapping iteration of the current increment. Symbols with neither subscript refer to the values from the most recent iteration in the current increment.

To find stress increment for current increment j:

1. Compute trial stress state: $\boldsymbol{\sigma_{trial}} = \boldsymbol{\sigma}_{j-1} + \mathbb{C}\Delta\boldsymbol{\varepsilon}_t$
2. Evaluate yield function $f(\boldsymbol{\sigma_{trial}}, \sigma_{j-1})$
   - If $f \geq 0$: continue to plastic calculations in step 3.
   - Else, check whether this is unloading:
     i. If $\dot{\varepsilon}_{vp,j-1} > 0$: previous increment was plastic; so calculate σ_t using $\dot{\varepsilon}_{vp} = 0$ and re-evaluate $f(\boldsymbol{\sigma_{trial}}, \sigma_t)$. If $f \geq 0$: continue to plastic calculations in 3.
     ii. Else, $\boldsymbol{\sigma} = \boldsymbol{\sigma_{trial}}$ and go to step 6.
3. Initialise zeroth iteration $i = 0$

$$\Delta\lambda_0 = 0$$
$$\dot{\lambda}_0 = 0$$
$$\boldsymbol{n}_0 = \left.\frac{df}{d\boldsymbol{\sigma}}\right|_{\boldsymbol{\sigma}=\boldsymbol{\sigma_{trial}}}$$

$$\alpha_0 = \sqrt{\frac{2}{3}\boldsymbol{n}\cdot\boldsymbol{n}}$$

4. For iteration $i = 1$ to $i_{max} = 50$
   - Update plastic strains and stresses (and h, s), and check yield functions based on n and $\Delta\lambda$ from last iteration:
     a) Calculate the components of plastic strain for current iteration:
        $\Delta\boldsymbol{\varepsilon_{vp}} = \left[(1-T)\dot{\boldsymbol{\varepsilon}}_{\boldsymbol{vp},j-1} + T\dot{\lambda}_{i-1}\boldsymbol{n}_{i-1}\right]\Delta t$
        where T is the interpolation parameter.
     b) Calculate components of new stress:
        $\boldsymbol{\sigma} = \boldsymbol{\sigma}_{j-1} + \mathbb{C}[\Delta\boldsymbol{\varepsilon} - \Delta\boldsymbol{\varepsilon_{vp}}]$
     c) Evaluate yield function f using updated state variables:
        i. Calculate ε_p:
           $\Delta\varepsilon_p = \alpha_{i-1}\Delta\lambda_{i-1}$
           $\varepsilon_p = \varepsilon_{p,j-1} + \Delta\varepsilon_p$
        ii. Calculate $\dot{\varepsilon}_p$:
           $\dot{\varepsilon}_p = \alpha\dot{\lambda}$
        iii. Calculate η, $\bar{\theta}$, $\bar{\sigma}$ (Eq. (4.2)), R (Eq. (4.9)), ε_f (Eq. (4.10)), D (Eq. (4.11)), β (Eq. (4.12)) and X (Eq. (4.17)).
        iv. Calculate the current flow stress $\sigma = \bar{\sigma}R\beta X$, and h and s (Eqs. (4.26) to (4.31)) using the updated state variables above.
        v. Evaluate $f(\boldsymbol{\sigma}, \sigma)$.
           - If $f < \mu_f$; where $\mu_f = 1 \times 10^{-2}$ is the tolerance on f, accept the stress update and go to step 7 (next integration point).
           - Else, use the updated stress to find new $\Delta\lambda$ and $\dot{\lambda}$ for the calculations in the next iteration:
             $\boldsymbol{n} = \dfrac{df}{d\boldsymbol{\sigma}}$
             $\alpha = \sqrt{\dfrac{2}{3}\boldsymbol{n}\cdot\boldsymbol{n}}$
             $\boldsymbol{P} = \left[\mathbb{C}^{-1} + T\Delta t\dot{\lambda}_{i-1}\dfrac{\partial\boldsymbol{n}}{\partial\boldsymbol{\sigma}}\right]^{-1}$ (Use the Sherman-Morrison [272] formula)
             $\Delta\lambda = \Delta\lambda_{i-1} + \dfrac{f}{\boldsymbol{n}\cdot\boldsymbol{P}\boldsymbol{n} + h + s/(T\Delta t)}$
             $\dot{\lambda} = \dfrac{\Delta\lambda}{T\Delta t} - \dfrac{1-T}{T}\dot{\lambda}_{j-1}$
           - Update $i = i + 1$ and go back to beginning of step 4.

5. If ($k > i_{max}$ and $f > \mu_f$) or otherwise nonconvergent (f =NaN), check whether last steps's D is within the tolerance $\mu_D = \max(0.05, 0.05\,(D_c - 1))$ from D_c. If yes, delete element.

6. Go to the next integration point and start from step 1.

BIBLIOGRAPHY

[1] W. J. Wong and C. L. Walters, 'Failure modes and rules related to the yield-to-tensile strength ratio in steel structures', *ASME 2021 40th International Conference on Ocean, Offshore and Arctic Engineering (OMAE)*, (June 21-30, 2021, Virtual, Online), ASME (The American Society of Mechanical Engineers), 2021. DOI: doi.org/10.1115/OMAE2021-61995.

[2] J. Billingham, J. Healy and H. Bolt, *The significance of yield ratio and work-hardening for structural performance* (Marine Research Review 9). Marine Technology Directorate, 1997.

[3] R.L. Brockenbrough & Associates Inc., 'Effect of yield-tensile ratio on structural behavior - high performance steels for bridge construction', Expanded draft final report ONR-AISI Agreement No. N00014-94-2-0002, 1995.

[4] A. C. Bannister and S. J. Trail, 'Structural integrity assessment procedures - Sub-task 2.1: The significance of the yield stress/tensile stress ratio to structural integrity', British Steel PLC, SINTAP report, 1996.

[5] H. Ban and G. Shi, 'A review of research on high-strength steel structures', *Proceedings of the Institution of Civil Engineers - Structures and Buildings*, vol. 171, no. 8, pp. 625–641, 2018. DOI: 10.1680/jstbu.16.00197.

[6] J. Billingham, J. V. Sharp, J. Spurrier and P. J. Kilgallon, 'Review of the performance of high strength steels used offshore', Health & Safety Executive, Research Report 105, 2003.

[7] B. Kato, 'Deformation capacity of steel structures', *Journal of Constructional Steel Research*, vol. 17, pp. 33–94, 1990.

[8] S. van Es, H. Slot, H. Steenbergen, J. Maljaars and R. Pijpers, 'Use of HSS and VHSS in steel structures in civil and offshore engineering', *Steel Construction*, vol. 11, no. 4, pp. 249–256, 2018.

[9] CEN (European Committee for Standardization), *EN 1993-1-1 Eurocode 3: Design of steel structures - Part 1-1: General rules and rules for buildings*. Brussels: CEN, 2005.

[10] CEN (European Committee for Standardization), *EN 10025-6 Hot rolled products of structural steels - Part 6: Technical delivery conditions for flat products of high yield strength structural steels in the quenched and tempered condition*. Brussels: CEN, 2019.

[11] LR (Lloyd's Register), *Code for lifting appliances in a marine environment*. London: LR, 2022.

[12] BV (Bureau Veritas), *NR 526 DT R03 E Rules for the Certification of Lifting Appliances onboard Ships and Offshore Units*. Paris La Defense Cedex: BV, 2021.

[13] AISC (American Institute of Steel Construction), *ANSI/AISC 360-22 Specification for Structural Steel Buildings*. USA: AISC, 2022.

[14] ASTM (American Society for Testing and Materials), *A992/A992M - 20 Standard specification for structural steel shapes*. West Conshohocken: ASTM, 2020.

[15] ASTM (American Society for Testing and Materials), *A913/913M - 19 Standard Specification for High-Strength Low-Alloy Steel Shapes of Structural Quality, Produced by Quenching and Self-Tempering Process*. West Conshohocken: ASTM, 2019.

[16] ISO (International Organization for Standardization), *ISO 3183 Petroleum and natural gas industries - Steel pipe for pipeline transportation systems*. ISO, 2019.

[17] DNV (Det Norske Veritas), *DNV-ST-F101 Submarine pipeline systems*. DNV, 2021.

[18] API (American Petroleum Institute), *API 5L. Line Pipe Specification 5L*. Washington, DC: API, 2018.

[19] LR (Lloyd's Register), *LR-RU-002 Rules for the Manufacture, Testing and Certification of Materials*. London: LR, 2024.

[20] DNV (Det Norske Veritas), *DNV-RU-SHIP Pt.2 Ch.2. Rules for classification: Ships: Part 2 Materials and welding 2 Metallic materials*. DNV, 2021.

[21] DNV (Det Norske Veritas), *DNV-OS-B101 Offshore standard: Metallic materials*. DNV, 2021.

[22] CEN (European Committee for Standardization), *EN 10225 Weldable structural steels for fixed offshore structures - Technical delivery conditions*. Brussels: CEN, 2019.

[23] BV (Bureau Veritas), *NR 216 Amd 002 Rules on materials and welding for the classification of marine units*. Paris: BV, 2020.

[24] G.-Q. Li, Y.-b. Wang and S.-W. Chen, 'The art of application of high-strength steel structures for buildings in seismic zones', *Advanced Steel Construction*, vol. 11, no. 4, pp. 492–506, 2015.

[25] K. S. Sivakumaran, 'Role of yield-to-tensile strength ratio in the design of steel structures', *Niobium Bearing Structural Steels*, pp. 63–76, 2010.

[26] T. Suzuki, Y. Yoshida, Y. Shimura, Y. Suzuki, S. Kubota and M. Nagata, 'Development of building structural steel with high yield ratio and high yield point leading to innovative steel structural system', Nippon Steel Technical Report No. 97, 2008.

[27] CEN (European Committee for Standardization), *EN 1993-1-12 Eurocode 3: Design of steel structures - Part 1-12: Additional rules for the extension of EN 1993 up to steel grades S700*. Brussels: CEN, 2007.

[28] CEN (European Committee for Standardization), *prEN 1993-1-1 Draft: Eurocode 3: Design of steel structures - Part 1-1: General rules and rules for buildings*. Brussels: CEN, 2020.

[29] O. W. Blodgett and D. K. Miller, 'Welded connections', *Handbook of Structural Engineering*, W.-F. Chen, Ed. CRC Press LLC, 2001.

[30] J. L. Gross, M. D. Engelhardt, C.-M. Uang, K. Kasai and N. R. Iwankiw, *Steel design guide series 12: Modification of existing welded steel moment frame connections for seismic resistance*. Chicago: American Institute of Steel Construction, 2003.

[31] J. Wardenier, Y. Kurobane, J. A. Packer, G. J. van der Vegte and X.-L. Zhao, *Design guide 1: Circular hollow section joints under predominantly static loading*. CIDECT (Comité International pour le Développement et l´Etude de la Construction Tubulaire), 2008.

[32] CEN (European Committee for Standardization), *EN 1993-1-8 Eurocode 3: Design of steel structures - Part 1-8: Design of joints*. Brussels: CEN, 2005.

[33] M. Feldmann et al., 'Rules on high strength steel (RUOSTE)', Research Fund for Coal and Steel, European Commission, Final report, 2016.

[34] T. Björk and H. Saastamoinen, 'Capacity of CFRHS X-joints made of double-grade s420 steel', *Proceedings of 14th International Symposium on Tubular Structures*, (London), L. Gardner, Ed., 2012.

[35] X. Lan, T.-M. Chan and B. Young, 'Structural behaviour and design of high strength steel RHS X-joints', *Engineering Structures*, vol. 200, 2019. DOI: 10.1016/j.engstruct.2019.109494.

[36] API (American Petroleum Institute), *API RP 2A-LRFD 2nd Ed: Planning, Designing, and Constructing Fixed Offshore Platforms—Load and Resistance Factor Design*. Washington, DC: API, 2019.

[37] ISO (International Organization for Standardization), *ISO 19902 Petroleum and natural gas industries - Fixed steel offshore structures*. Switzerland, 2020.

[38] NORSOK, *N-004 NORSOK standard: Design of steel structures*. Lysaker: NORSOK, 2004.

[39] HSE (Health and Safety Executive), 'Steel', Offshore technology report OTR 2001/015, 2001.

[40] J. Healy, J. Billingham, C. Billington and H. Bolt, 'Design implications of the high yield to ultimate ratio of high strength steels in offshore engineering', *Proceedings of the 14th International Conference on Offshore Mechanics and Arctic Engineering*, 1995, pp. 271–277.

[41] CEN (European Committee for Standardization), *prEN 1993-1-8 Draft: Eurocode 3: Design of steel structures - Part 1-8: Design of joints*. Brussels, 2020.

[42] CEN (European Committee for Standardization), *EN 13001-3-1:2012+A2:2018 Cranes - General Design - Part 3-1: Limit States and proof competence of steel structure*. Brussels: CEN, 2018.

[43] FEM (Fédération Européenne de la Manutention), *FEM 1.001 Rules for the design of hoisting appliances 3rd Edition*. 1998.

[44] ABS (American Bureau of Shipping), *Guide for certification of lifting appliances*. Spring, TX: ABS, 2020.

[45] DNV (Det Norske Veritas), *DNV-ST-0378 Offshore and platform lifting appliances Edition July 2019 Amended October 2021*. DNV, 2021.

[46] BV (Bureau Veritas), *NR 467 Rules for the classification of steel ships*. BV, 2020.

[47] DNV (Det Norske Veritas), *DNV-RU-SHIP Pt.3 Ch.3. Rules for classification: Ships: Part 3 Hull Chapter 3 Structural design principles*. DNV, 2024.

[48] IACS (International Association of Classification Societies), *Common structural rules for bulk carriers and oil tankers*. 2020.

[49] LR (Lloyd's Register), *LR-RU-001 Rules and regulations for the classification of ships*. London: LR, 2024.

[50] TSCF (Tanker Structure Cooperative Forum), 'Guidance notes on high tensile steel', TSCF IP 004/2013, 2013.

[51] ASCE (American Society of Civil Engineers), *Plastic design in steel, a guide and a commentary* (ASCE Manuals and Reports on Engineering Practice No. 41). New York, 1971.

[52] A. Considère, 'Mémoire sur l'emploi du fer et de l'acier', *Annales des Ponts et Chaussées*, vol. 9, pp. 574–775, 1885.

[53] J. H. J. Hollomon, 'Tensile deformation', *Transactions of the Metallurgical Society of AIME*, vol. 162, pp. 268–290, 1945.

[54] X. Yun and L. Gardner, 'Stress-strain curves for hot-rolled steels', *Journal of Constructional Steel Research*, vol. 133, pp. 36–46, 2017.

[55] L. Gardner and X. Yun, 'Description of stress-strain curves for cold-formed steels', *Construction and Building Materials*, vol. 189, pp. 527–538, 2018.

[56] A. C. Bannister, 'Structural integrity assessment procedures - Sub-task 2.3: yield stress/tensile stress ratio: results of experimental programme', British Steel PLC, Report SINTAP/BS/25, 1999.

[57] X.-K. Zhu and B. N. Leis, 'Influence of yield-to-tensile strength ratio on failure assessment of corroded pipelines', *Journal of Pressure Vessel Technology*, vol. 127, no. 4, pp. 436–442, 2005.

[58] ASCE (American Society of Civil Engineers), *ASCE 61-14 Seismic design of piers and wharves*. Reston, VA, 2014.

[59] CBSC/ICC (California Building Standards Commission / International Code Council), *California building code*. Washington, DC: CBSC/ICC, 2019.

[60] M. Feldmann and S. Schaffrath, 'Assessing the net section resistance and ductility requirements of EN 1993-1-1 and EN 1993-1-12', *Steel Construction*, vol. 10, no. 4, pp. 354–364, 2017.

[61] P. Hradil and A. Talja, 'Ductility limits of high strength steels', Research Report VTT-R-04741-16, 2016.

[62] N. D. Alexopoulos and M. Tiryakioglu, 'Relationship between fracture toughness and tensile properties of A357 cast aluminum alloy', *Metallurgical and Materials Transactions a-Physical Metallurgy and Materials Science*, vol. 40a, no. 3, pp. 702–716, 2009. DOI: 10.1007/s11661-008-9742-8.

[63] P. Hradil, A. Talja, J. Kurkela, L. Fülöp and P. Ongelin, 'Evaluation of ductility limits for structural steel design', *Journal of Constructional Steel Research*, vol. 135, pp. 1–10, 2017.

[64] M. Feldmann, M. Meissner, H. Bartsch, S. Münstermann, N. Fehlemann and M. Könemann, 'Stand der Untersuchungen zu Werkstoffanforderungen hochfester Stähle S700 bis S960 – FOSTA-Forschungsverbund HOCHFEST', *Stahlbau*, vol. 92, no. 8, pp. 468–483, 2023. DOI: 10.1002/stab.202300033.

[65] Bridgman and P. W, *Studies in large plastic flow and fracture with special emphasis on the effects of hydrostatic pressure*. New York: McGraw-Hill, 1952.

[66] P. Hradil, L. Fülöp, A. Talja and J. Kurkela, 'Experiences from numerical modelling of details with ductile fracture', Research Report VTT-R-01177-17, 2017.

[67] F. Yang and M. Veljkovic, 'Ductile damage model calibration for high-strength structural steels', *Construction and Building Materials*, vol. 263, p. 120 632, 2020.

[68] D. Banabic and H. J. Bunge, *Formability of Metallic Materials*. Springer Berlin Heidelberg, 2000.

[69] H. W. Swift, 'Plastic instability under plane stress', *Journal of the Mechanics and Physics of Solids*, vol. 1, pp. 1–16, 1952.

[70] R. Hill, 'On discontinous plastic states, with special reference to localized necking in thin sheets', *Journal of the Mechanics and Physics of Solids*, vol. 1, pp. 19–30, 1952.

[71] K. Kucyński and Z. Marciniak, 'Limit strains in the processes of stretch-forming sheet metal', *International Journal of Mechanical Sciences*, vol. 9, pp. 609–620, 1967.

[72] M. Feldmann, S. Schaffrath and C. Sandro, 'Draft: Background document to Eurocode 3 EN 1993 – part 1-10: Material toughness - approach for upper-shelf toughness requirements for the design of steel structures based on damage mechanics', Institute of Steel Construction RWTH Aachen University, Tech. Rep., 2020.

[73] R. J. Dexter, S. A. Alttstadt and C. A. Gardner, 'Strength and ductility of hps70w tension members and tension flanges with holes', University of Minnesota, High Performance Steel Project Report, 2002.

[74] A. K. Dhalla and G. Winter, 'Suggested steel ductility requirements', *Journal of the Structural Division*, vol. 100, no. 2, pp. 445–462, 1974. DOI: 10.1061/jsdeag.0003717.

[75] P. Može, D. Beg and J. Lopatič, 'Net cross-section design resistance and local ductility of elements made of high strength steel', *Journal of Constructional Steel Research*, vol. 63, no. 11, pp. 1431–1441, 2007.

[76] M. Stofregen, 'Static tensile strength of s1100 steel', Master Thesis, Delft University of Technology, 2004.

[77] S. F. P. M. Obers, J. J. Overal, W. J. Wong and C. L. Walters, 'The effect of the yield to tensile strength ratio on stress/strain concentrations around holes in high-strength steels', *Marine Structures*, vol. 84, p. 103 205, 2022. DOI: 10.1016/j.marstruc.2022.103205.

[78] G. Sedlacek et al., 'Commentary and worked examples to en 1993-1-10 "material toughness and through thickness properties" and other toughness oriented rules in en 1993 - background documents in support to the implementation, harmonization and further development of the eurocodes', European Commission Joint Research Centre, Tech. Rep., 2008.

[79] J. R. Rice and G. F. Rosengren, 'Plane strain deformation near a crack tip in a power-law hardening material', *Journal of the Mechanics and Physics of Solids*, vol. 16, no. 1, pp. 1–12, 1968. DOI: 10.1016/0022-5096(68)90013-6.

[80] A. Cosham, D. G. Jones, B. N. Leis, P. Hopkins and J. Barnett, 'Not another Charpy V-notch correction factor...?', *6th International Pipeline Technology Conference*, (Ostend, Belgium), 2013.

[81] A. Nonn, M. Paredes, V. Keim and T. Wierzbicki, 'Comparison of fracture models to quantify the effects of material plasticity on the ductile fracture propagation in pipelines', *2018 12th International Pipeline Conference*, (Calgary, Alberta, Canada), vol. Volume 3: Operations, Monitoring, and Maintenance; Materials and Joining, ASME, 2018. DOI: 10.1115/IPC2018-78366.

[82] C. Lu, G. Michal and P. Venton, 'A new fracture velocity model for high grade gas pipelines', *20th Joint Technical Meeting on Pipeline Research*, (Paris), 2015.

[83] CEN (European Committee for Standardization), *prEN 1993-1-10 Draft: Eurocode 3: Design of steel structures - Part 1-10: Material toughness and through-thickness properties*. Brussels: CEN, 2023.

[84] K. Wallin, 'Low-cost J-R curve estimation based on CVN upper shelf energy', *Fatigue & Fracture of Engineering Materials & Structures*, vol. 24, no. 8, pp. 537–549, 2001. DOI: 10.1046/j.1460-2695.2001.00405.x.

[85] C. Kuckertz, *Korrelation der Ergebnisse des Aufschweißbiegeversuchs an Stahl S355J2G3 mit Prüfverfahren nach europäischen Produktnormen* (Berichte aus dem Institut für Eisenhüttenkunde). RWTH Aachen, 2005, vol. 2005,2.

[86] P. Gioielli, J. Landes, P. Paris, H. Tada and L. Loushin, 'Method for predicting j-r curves from charpy impact energy', *Fatigue and Fracture Mechanics: 30th Volume*, K. L. Jerina and P. C. Paris, Eds. West Conshohocken, PA: ASTM, 2000, pp. 61–68. DOI: 10.1520/STP13395S.

[87] E. D. Eason, J. E. Wright and E. E. Nelson, 'Multivariable modeling of pressure vessel and piping J-R data', U.S. Nuclear Regulatory Commission, Tech. Rep., 1991.

[88] E. D. Eason and E. E. Nelson, 'Improved model for predicting J-R curves from charpy data', U.S. Nuclear Regulatory Commission, Tech. Rep., 1989.

[89] K. Kussmaul and E. Roos, 'Statistical evaluation of post-yield fracture mechanics properties on the basis of the notched bar impact test', *Nuclear Engineering and Design*, vol. 87, pp. 123–137, 1985. DOI: 10.1016/0029-5493(85)90101-3.

[90] J. G. Merkle and R. E. Johnson, 'Example calculations illustrating methods for analyzing ductile flaw stability in nuclear pressure vessels', *International Journal of Pressure Vessels and Piping*, vol. 18, no. 1, pp. 35–53, 1985. DOI: https://doi.org/10.1016/0308-0161(85)90025-0.

[91] R. Chaouadi and R. Gérard, 'Development of a method for extracting fracture toughness from instrumented Charpy impact tests in the ductile and transition regimes', *Theoretical and Applied Fracture Mechanics*, vol. 115, 2021. DOI: 10.1016/j.tafmec.2021.103080.

[92] R. Chaouadi and J. L. Puzzolante, 'Procedure to estimate the crack resistance curve from the instrumented Charpy V–notched impact test', *12th International Conference on Fracture*, (Ottawa, Canada), 2009.

[93] H. J. Schindler, 'Abschätzung von Bruchzähigkeitskennwerten aus der Bruch- oder Kerbschlagarbeit', *Materialwissenschaft und Werkstofftechnik*, vol. 32, no. 6, pp. 544–551, 2001. DOI: 10.1002/1521-4052(200106)32:6<544::Aid-mawe544>3.0.Co;2-k.

[94] D. Schäfer, B. Eichler, L. Amlung, I. Vayas, V. Karlos, A. Spiliopoulos, M. Lippe, Z. Kubon and L. Kander, 'Modern plastic design for steel structures', Research Fund for Coal and Steel, European Commission, Tech. Rep., 2010.

[95] G. Kazinczy, 'Bemessung von statisch unbestimmten Konstruktionen unter Berücksichtigung der bleibenden Formanderungen', *Betonszemle*, pp. 4–6, 1914.

[96] IACS (International Association of Classification Societies), *IACS UR I Requirements concerning polar class*. IACS, 2019.

[97] C. G. Daley, 'Derivation of plastic framing requirements for polar ships', *Marine Structures*, vol. 15, pp. 543–559, 2002.

[98] C. G. Daley, 'Application of plastic framing requirements from polar ships', *Marine Structures*, vol. 15, pp. 533–542, 2002.

[99] V. Gioncu and D. Petcu, 'Available rotation capacity of wide-flange beams and beam-columns part 2. experimental and numerical tests', *Journal of Constructional Steel Research*, vol. 43, no. 1-3, pp. 219–244, 1997. DOI: 10.1016/s0143-974x(97)00045-x.

[100] R. Spangemacher, 'Zum rotationsnachweis von stahlkonstruktionen, die nach dem traglastverfahren berechnet werden', PhD Thesis, RWTH Aachen, 1992.

[101] O. D. Dijkstra and H. Botter, 'Integrity of high strength steel structures - deformation capacity', Netherlands Organisation for Applied Scientific Research (TNO), TNO Report 2005-BSC-R0367, 2005.

[102] H. M. G. M. Steenbergen, F. S. K. Bijlaard and B. J. Daniels, 'The influence of material properties on plastic hinge rotational capacity and strength', Netherlands Organisation for Applied Scientific Research (TNO), TNO Report 96-CON-R1224, 1996.

[103] J. F. McDermott, 'Plastic bending of A514 steel beams', *Journal of the Structural*, vol. 95, no. 9, pp. 1851–1871, 1969.

[104] C. H. Lee, K. H. Han, C. M. Uang, D. K. Kim, C. H. Park and J. H. Kim, 'Flexural strength and rotation capacity of I-shaped beams fabricated from 800 MPa steel', *Journal of Structural Engineering*, vol. 139, no. 6, pp. 1043–1058, 2013. DOI: 10.1061/(ASCE)ST.1943-541X.0000727.

[105] J. M. Ricles, R. Sause and P. S. Green, 'High-strength steel: Implications of material and geometric characteristics on inelastic flexural behavior', *Engineering Structures*, vol. 20, pp. 323–335, 1998.

[106] N. Schillo and M. Feldmann, 'The rotational capacity of beams made of high-strength steel', *Proceedings of the Institution of Civil Engineers - Structures and Buildings*, vol. 170, no. 9, pp. 641–652, 2017.

[107] N. Schillo and M. Feldmann, 'Experiments on the rotational capacity of beams made of high-strength steel', *Steel Construction*, vol. 11, no. 1, pp. 42–48, 2018.

[108] Y. Shi and K. Xu, 'Experimental and analytical study on local buckling behavior of high strength steel welded i-section beams', *International Journal of Steel Structures*, vol. 19, no. 4, pp. 1171–1190, 2019.

[109] V. Gioncu and F. Mazzolani, *Ductility of Seismic Resistant Steel Structures*. London: Spon Press, 2002.

[110] U. Kuhlmann, M. Knoblock, J. Linder, A. Taras, F. Jörg and A.-L. Bours, 'Neue entwicklungen in pren 1993-1-1:2020', *Stahlbau-Kalender 2020: Neue Normung im Hochbau – Leichtbau*. Ernst & Sohn GmbH & Co, 2020, pp. 511–609. DOI: 10.1002/9783433610053.ch8.

[111] M. Gkantou, M. Theofanous and C. Baniotopoulos, 'Plastic design of hot-finished high strength steel continuous beams', *Thin-Walled Structures*, vol. 133, pp. 85–95, 2018. DOI: 10.1016/j.tws.2018.09.002.

[112] J. Wang, 'Behaviour and design of high strength steel structures', PhD Thesis, Imperial College London, 2016.

[113] A. Taras, R. Greiner and H. Unterweger, 'Proposal for amended rules for member buckling and semi-compact cross-section design', SC3 Evolution Group 1993-1-1, Technical Report, 2013.

[114] M. Pavlovic and M. Veljkovic, 'Compact cross-sections of mild and high-strength steel hollow-section beams', *Proceedings of the Institution of Civil Engineers*, vol. 170 SB11, pp. 825–840, 2017.

[115] P. Studer and A. Taras, 'Strain-hardening dependent cross-sectional slenderness limits for the plastic resistance of steel beams', *Journal of Constructional Steel Research*, vol. 205, 2023. DOI: 10.1016/j.jcsr.2023.107879.

[116] L. Gardner and D. Nethercot, 'Structural stainless steel design: A new approach', *Structural Engineer*, vol. 82, no. 21, pp. 21–28, 2004.

[117] L. Gardner, 'The continuous strength method', *Proceedings of the Institution of Civil Engineers: Structures and Buildings*, vol. 161 SB3, pp. 127–133, 2008.

[118] X. Lan, J. Chen, T.-M. Chan and B. Young, 'The continuous strength method for the design of high strength steel tubular sections in compression', vol. 162, pp. 177–187, 2018.

[119] X. Lan, J. Chen, T.-M. Chan and B. Young, 'The continuous strength method for the design of high strength steel tubular sections in bending', *Journal of Constructional Steel Research*, vol. 160, pp. 499–509, 2019.

[120] K. W. Johansen, *Brudlinieteorier*. Copenhagen, Denmark: Jul. Gjellerups Forlag, 1943.

[121] C. Goodchild and G. Kennedy, *Practical yield line design*. Surrey: The Concrete Centre, 2004.

[122] T. Wierzbicki and W. Abramowicz, 'On the crushing mechanics of thin-walled structures', *Journal of Applied Mechanics*, pp. 727–734, 1983.

[123] J. Amdahl, 'Energy absorption in ship-platform impacts', The Norwegian Institute of Technology, Report UR-83-34, 1983.

[124] J. Wardenier, 'Hollow section joints', PhD Thesis, Delft University of Technology, 1982.

[125] L. Zhu, J. Gao and Y. Li, 'Numerical analysis on the response of deck plates laterally impacted by a rectangular indenter', *ASME 2018 37th International Conference on Ocean, Offshore and Arctic Engineering. Madrid, Spain*, (Madrid), 2018. DOI: 10.1115/OMAE2018-78023.

[126] E. Appolonov, 'IACS unified requirements for polar ships - background notes to shell plating thickness', IACS Ad-Hoc Group on Polar Class Ships, Tech. Rep., 2000.

[127] O. F. Hughes and J. K. Paik, *Ship structural analysis and design*. New Jersey: The Society of Naval Architects and Marine Engineers, 2010.

[128] T. V. Galambos, *Guide to stability design criteria for metal structures*. John Wiley & Sons, Inc., 1998.

[129] F. Engesser, 'Über die knickfestigkeit gerader stäbe', *Zeitschrift des Architekten- und Ingenieurvereins zu Hannover.*, p. 455, 1889.

[130] F. R. Shanley, 'Inelastic column theory', *Journal of Aeronautics Science*, p. 261, 1947.

[131] H. P. Günther, 'Use and application of high-performance steels for steel structures', Structural Engineering Documents 8, 2005.

[132] X. Meng and L. Gardner, 'Behavior and design of normal- and high-strength steel shs and rhs columns', *Journal of Structural Engineering*, vol. 146, no. 11, p. 04 020 227, 2020.

[133] T.-C. Stan and J. Jönsson, 'Yield stress independent column buckling curves', *Ce/papers - EUROSTEEL 2017: 8th International Conference on Steel and Composite Structures*, (Copenhagen), vol. 1, Ernst & Sohn Verlag für Architektur und technische Wissenschaften GmbH & Co., 2017, pp. 3761–3770.

[134] C. J. Earls, 'Influence of material effects on structural ductility of compact I-shaped beams', *Journal of Structural Engineering*, vol. 126, no. 11, pp. 1268–1278, 2000.

[135] C. J. Earls, 'On the inelastic failure of high strength steel I-shaped beams', *Journal of Constructional Steel Research*, vol. 49, no. 1, pp. 1–24, 1999.

[136] A. R. Kemp, 'Inelastic local and lateral buckling in design codes', *Journal of Structural Engineering*, vol. 122, pp. 374–382, 1996.

[137] C. J. Earls, 'Geometric factors influencing structural ductility in compact I-shaped beams', *Journal of Structural Engineering*, vol. 126, no. 7, pp. 780–789, 2000.

[138] N. Schillo and M. Feldmann, 'Interaction of local buckling and lateral torsional buckling of t-shaped cantilevering beams', *Thin-Walled Structures*, vol. 81, pp. 236–241, 2014.

[139] N. Schillo and M. Feldmann, 'Local buckling behaviour of welded box sections made of high-strength steel', *Steel Construction*, vol. 3, 2015.

[140] NEN (Nederlands Normalisatie-instituut), *NEN 6770 TGB 1990 - Staalconstructies - Basiseisen en basisrekenregels voor overwegend statisch belaste constructies*. Delft: NEN (Nederlands Normalisatie-instituut), 1990.

[141] W. J. Wong and C. L. Walters, 'Effect of strain hardening on the rotation capacity of welded I-section high-strength steel beams', *Ships and Offshore Structures*, pp. 1–16, 2023. DOI: 10.1080/17445302.2023.2195727.

[142] S. Chen, H. Fang, J.-z. Liu and T.-M. Chan, 'Design for local buckling behaviour of welded high strength steel i-sections under bending', *Thin-Walled Structures*, vol. 172, p. 108 792, 2022. DOI: 10.1016/j.tws.2021.108792.

[143] U. Kuhlmann, 'Definition of flange slenderness limits on the basis of rotation capacity values', *J. Construct. Steel Research*, vol. 14, pp. 21–40, 1989.

[144] R. M. Korol and J. Hudoba, 'Plastic behavior of hollow structural sections', *Journal of the Structural Division*, vol. 98, no. 5, pp. 1007–1023, 1972. DOI: 10.1061/jsdeag.0003221.

[145] A. R. Kemp, 'Slenderness limits normal to the plane of bending for beam-columns in plastic design', *Journal of Constructional Steel Research*, vol. 4, no. 2, pp. 135–150, 1984. DOI: 10.1016/0143-974x(84)90023-3.

[146] N. Stranghöner, G. Sedlacek and P. Boeraeve, 'Rotation requirement and rotation capacity of rectangular, square and circular hollow section. Melbourne, Australia', *6. Int. Sympos. on Tubular Struct.*, (Melbourne, Australia), 1994.

[147] J. A. Yura, T. V. Galambos and M. K. Ravindra, 'The bending resistance of steel beams', *Journal of the Structural Division*, vol. 104, no. 9, pp. 1355–1370, 1978. DOI: 10.1061/jsdeag.0004982.

[148] G. Sedlacek and M. Feldmann, 'Background document 5.09 for chapter 5 of Eurocode part 1.1 - the b/t ratios controlling the applicability of analysis models in Eurocode 3 part 1.1', Tech. Rep., 1995.

[149] Y. Yuan and P. J. Tan, 'On large deformation, damage and failure of ductile plates to blast loading', *International Journal of Impact Engineering*, vol. 132, p. 103 330, 2019. DOI: 10.1016/j.ijimpeng.2019.103330.

[150] B. Kato, 'Buckling strength of plates in the plastic range', *International Association for Bridge and Structural Engineering (IABSE) Publications*. Zürich: Verlag Leemann, 1965, vol. 25, pp. 127–141. DOI: doi.org/10.5169/seals-20352.

[151] Y. Bai and T. Wierzbicki, 'Application of extended Mohr–Coulomb criterion to ductile fracture', *International Journal of Fracture*, vol. 161, no. 1, pp. 1–20, 2010. DOI: 10.1007/s10704-009-9422-8.

[152] DS Simulia (Dassault Systèmes Simulia), *ABAQUS 2019.HF2. Commercial Finite Element Software.* Computer Program, 2019.

[153] Z. P. Bažant and L. Cedolin, *Stability of Structures*. Singapore: World Scientific Publishing Co. Pte. Ltd., 2010. DOI: 10.1142/7828.

[154] N. S. Trahair, M. A. Bradford, D. Nethercot and L. Gardner, *The Behaviour and Design of Steel Structures to EC3*, 4th ed. Oxon: Taylor & Francis, 2008.

[155] A. J. Sadowski and J. M. Rotter, 'Solid or shell finite elements to model thick cylindrical tubes and shells under global bending', *International Journal of Mechanical Sciences*, vol. 74, pp. 143–153, 2013. DOI: 10.1016/j.ijmecsci.2013.05.008.

[156] CEN (European Committee for Standardization), *EN 1993-1-5 Eurocode 3: Design of steel structures - Part 1-5: Plated structural elements*. Brussels: European Committee for Standardization, 2006.

[157] CEN (European Committee for Standardization), *EN 1090-2 Execution of steel structures and aluminium structures - Part 2: Technical requirements for steel structures*. Brussels: European Committee for Standardization, 2018.

[158] L. Schaper, T. Tankova, L. Simões da Silva and M. Knobloch, 'A novel residual stress model for welded i-sections', *Journal of Constructional Steel Research*, vol. 188, 2022. DOI: 10.1016/j.jcsr.2021.107017.

[159] O. W. Blodgett, *Design of Weldments*. Cleveland, Ohio: The James F. Lincoln Arc Welding Foundation, 1963.

[160] M. Kucukler and L. Gardner, 'In-plane structural response and design of duplex and ferritic stainless steel welded i-section beam–columns', *Engineering Structures*, vol. 247, 2021. DOI: 10.1016/j.engstruct.2021.113136.

[161] P. S. Green, R. Sause and J. M. Ricles, 'Strength and ductility of HPS flexural members', *Journal of Constructional Steel Research*, vol. 58, no. 5-8, pp. 907–941, 2002. DOI: 10.1016/s0143-974x(01)00102-x.

[162] B. Yang, M. Dong, Q. Han, M. Elchalakani and G. Xiong, 'Flexural behavior and rotation capacity of welded i-beams made from 690-MPa high-strength steel', *Journal of Structural Engineering*, vol. 147, no. 2, 2021. DOI: 10.1061/(asce)st.1943-541x.0002871.

[163] Y. Fukumoto, 'New constructional steels and structural stability', *Engineering Structures*, vol. 18, no. 10, pp. 786–791, 1996. DOI: 10.1016/0141-0296(96)00008-9.

[164] P. Langenberg, T. Nießen and W. Dahl, 'Bruch- und verformungsverhalten von hochfesten stählen mit streckgrenzen von 690 bis 890 MPa', *Stahlbau*, vol. 69, no. 4, pp. 283–291, 2000. DOI: 10.1002/stab.200000860.

[165] J. K. Paik, K. J. Kim, J. H. Lee, B. G. Jung and S. J. Kim, 'Test database of the mechanical properties of mild, high-tensile and stainless steel and aluminium alloy associated with cold temperatures and strain rates', *Ships and Offshore Structures*, vol. 12, no. sup1, S230–S256, 2017. DOI: 10.1080/17445302.2016.1262729.

[166] S. P. Timoshenko and J. M. Gere, *Theory of Elastic Stability*, 2nd. New York: McGraw-Hill, 1961.

[167] N. Yamaki, *Elastic stability of circular cylindrical shells* (North Holland Series in Applied Mathematics and Mechanics). Amsterdam: Elsevier Science Publishers BV, 1984.

[168] W. J. Wong and C. L. Walters, 'Damage mechanics model for correlating notch toughness in Charpy impact tests with fracture toughness in cracked static fracture tests.', *Engineering Fracture Mechanics*, 2025. DOI: 10.1016/j.engfracmech.2025.111043.

[169] W. J. Wong and C. L. Walters, 'Damage-mechanics insights into the relationship between upper-shelf Charpy testing and J-integral testing considering varying tensile test properties', Manuscript, 2025.

[170] BSI (British Standards Institution), *BS 7910 Guide to methods for assessing the acceptability of flaws in metallic structures*. BSI, 2019. DOI: 10.3403/30369478.

[171] T. S. Cao, 'Models for ductile damage and fracture prediction in cold bulk metal forming processes: A review', *International Journal of Material Forming*, vol. 10, no. 2, pp. 139–171, 2015. DOI: 10.1007/s12289-015-1262-7.

[172] L. Xue, 'Stress based fracture envelope for damage plastic solids', *Engineering Fracture Mechanics*, vol. 76, no. 3, pp. 419–438, 2009. DOI: 10.1016/j.engfracmech.2008.11.010.

[173] L. Xue, 'Localization conditions and diffused necking for damage plastic solids', *Engineering Fracture Mechanics*, vol. 77, no. 8, pp. 1275–1297, 2010. DOI: 10.1016/j.engfracmech.2009.12.008.

[174] D. P. Clausing, 'Effect of plastic strain state on ductility and toughness', *International Journal of Fracture Mechanics*, vol. 6, no. 1, pp. 71–85, 1970. DOI: 10.1007/bf00183662.

[175] D. Banabic, H. Aretz, L. Paraianu and P. Jurco, 'Application of various FLD modelling approaches', *Modelling and Simulation in Materials Science and Engineering*, vol. 13, no. 5, pp. 759–769, 2005. DOI: 10.1088/0965-0393/13/5/009.

[176] B. Eichler and M. Feldmann, 'Ein hochlagenorientiertes und duktilitätsgesteuertes Stahlgütewahlkonzept', *Stahlbau*, vol. 85, no. 1, pp. 25–36, 2016. DOI: 10.1002/stab.201610349.

[177] P. Thibaux, S. Müller, B. Tanguy and F. van den Abeele, 'Ductile fracture characterization of an X70 steel: Re-interpretation of classical tests using the finite element technique', *2008 7th International Pipeline Conference*, (Calgary, Alberta, Canada), vol. 3, 2009, pp. 179–186. DOI: 10.1115/IPC2008-64291.

[178] B. Tanguy, T. T. Luu, G. Perrin, A. Pineau and J. Besson, 'Plastic and damage behaviour of a high strength X100 pipeline steel: Experiments and modelling', *International Journal of Pressure Vessels and Piping*, vol. 85, no. 5, pp. 322–335, 2008. DOI: 10.1016/j.ijpvp.2007.11.001.

[179] L. Xue and T. Wierzbicki, 'Ductile fracture initiation and propagation modeling using damage plasticity theory', *Engineering Fracture Mechanics*, vol. 75, no. 11, pp. 3276–3293, 2008. DOI: 10.1016/j.engfracmech.2007.08.012.

[180] Y. Shinohara, Y. Madi and J. Besson, 'Anisotropic ductile failure of a high-strength line pipe steel', *International Journal of Fracture*, vol. 197, no. 2, pp. 127–145, 2016. DOI: 10.1007/s10704-015-0054-x.

[181] Y. Zu, Y. Cao, Y. Zhen, F. Li and G. Wu, 'Determination on the fracture toughness of the welded joints of X80 pipeline steels based on small punch test', *Engineering Fracture Mechanics*, vol. 291, 2023. DOI: 10.1016/j.engfracmech.2023.109525.

[182] G. R. Cowper and P. S. Symonds, 'Strain hardening and strain-rate effects in the impact loading of cantilever beams', Office of Naval Research, Tech. Rep. no. 28, 1957.

[183] D. M. Norris, 'Computer simulation of the Charpy V-notch toughness test', *Engineering Fracture Mechanics*, vol. 11, no. 2, pp. 261–274, 1979. DOI: 10.1016/0013-7944(79)90003-1.

[184] T. R. Wilshaw, 'Deformation and fracture of mild steel specimens', *The Journal of the Iron and Steel Institute*, vol. 204, no. 9, 1966.

[185] A. Asserin–Lebert, J. Besson and A. F. Gourgues, 'Fracture of 6056 aluminum sheet materials: Effect of specimen thickness and hardening behavior on strain localization and toughness', *Materials Science and Engineering: A*, vol. 395, no. 1-2, pp. 186–194, 2005. DOI: 10.1016/j.msea.2004.12.018.

[186] F. Rivalin, A. Pineau, M. Di Fant and J. Besson, 'Ductile tearing of pipeline-steel wide plates', *Engineering Fracture Mechanics*, vol. 68, no. 3, pp. 329–345, 2001. DOI: 10.1016/s0013-7944(00)00107-7.

[187] Y. Li and T. Wierzbicki, 'Prediction of plane strain fracture of AHSS sheets with post-initiation softening', *International Journal of Solids and Structures*, vol. 47, no. 17, pp. 2316–2327, 2010. DOI: 10.1016/j.ijsolstr.2010.04.028.

[188] L. Xue, 'Damage accumulation and fracture initiation in uncracked ductile solids subject to triaxial loading', *International Journal of Solids and Structures*, vol. 44, no. 16, pp. 5163–5181, 2007. DOI: 10.1016/j.ijsolstr.2006.12.026.

[189] H. Huang and L. Xue, 'Prediction of slant ductile fracture using damage plasticity theory', *International Journal of Pressure Vessels and Piping*, vol. 86, no. 5, pp. 319–328, 2009. DOI: 10.1016/j.ijpvp.2008.11.027.

[190] W. Lan, X. Deng, M. A. Sutton and C.-S. Cheng, 'Study of slant fracture in ductile materials', *International Journal of Fracture*, vol. 141, no. 3-4, pp. 469–496, 2006. DOI: 10.1007/s10704-006-9008-7.

[191] D. Novokshanov, B. Döbereiner, M. Sharaf, S. Münstermann and J. Lian, 'A new model for upper shelf impact toughness assessment with a computationally efficient parameter identification algorithm', *Engineering Fracture Mechanics*, vol. 148, pp. 281–303, 2015. DOI: 10.1016/j.engfracmech.2015.07.069.

[192] C. H. M. Simha, S. Xu and W. R. Tyson, 'Non-local phenomenological damage-mechanics-based modeling of the drop-weight tear test', *Engineering Fracture Mechanics*, vol. 118, pp. 66–82, 2014. DOI: 10.1016/j.engfracmech.2014.01.009.

[193] ASTM (American Society for Testing and Materials), *E436 - 03 (Reapproved 2021) Standard Test Method for Drop-Weight Tear Tests of Ferritic Steels*. West Conshohocken, 2021. DOI: 10.1520/e0436-03r21.

[194] ISO (International Organization for Standardization), *ISO 148-1 Metallic materials - Charpy pendulum impact test - Part 1: Test method*. ISO, 2016.

[195] W. J. Wong and C. L. Walters, 'Effects of strain hardening and the Lode dependence of the fracture strain locus on slant fracture in Charpy V-notch impact testing', *ASME 2024 43rd International Conference on Ocean, Offshore and Arctic Engineering (OMAE)*, (Singapore), ASME (The American Society of Mechanical Engineers), 2024. DOI: 10.1115/OMAE2024-125635.

[196] J. Hure, A. Parrot and S. Meunier, 'Numerical prediction of the effect of irradiation on the Charpy upper shelf energy of reactor pressure vessel steels', *Journal of Nuclear Materials*, vol. 570, 2022. DOI: 10.1016/j.jnucmat.2022.153956.

[197] W. M. Wang, L. J. Sluys and R. de Borst, 'Viscoplasticity for instabilities due to strain softening and strain-rate softening', *International Journal for Numerical Methods in Engineering*, vol. 40, no. 20, pp. 3839–3864, 1997. DOI: 10.1002/(sici)1097-0207(19971030)40:20<3839::Aid-nme245>3.0.Co;2-6.

[198] G. R. Johnson and W. H. Cook, 'Fracture characteristics of three metals subjected to various strains, strain rates, temperatures and pressures', *Engineering Fracture Mechanics*, vol. 21, no. 1, pp. 31–48, 1985. DOI: 10.1016/0013-7944(85)90052-9.

[199] A. C. Bannister, J. Ruiz Ocejo and F. Gutierrez-Solana, 'Implications of the yield stress/tensile stress ratio to the SINTAP failure assessment diagrams for homogeneous materials', *Engineering Fracture Mechanics*, vol. 67, no. 6, pp. 547–562, 2000. DOI: 10.1016/s0013-7944(00)00073-4.

[200] ISO (International Organization for Standardization), *ISO 6892-1 Metallic materials - Tensile testing - Part 1: Method of test at room temperature*. Geneva: ISO, 2019.

[201] E. Fujii, I. Ohkuma, Y. Kawaguchi and M. Tsukamoto, 'Effects of temperature and strain rate on dynamic fracture toughness of steel', *Journal of the Society of Naval Architects of Japan*, vol. 158, pp. 619–629, 1985.

[202] M. Toyosada, E. Fujii, K. Nohara, Y. Kawaguchi, K. Arimochi and K. Isaka, 'The effect of strain rate on critical CTOD and J integral', *Journal of the Society of Naval Architects of Japan*, vol. 1987, no. 161, pp. 343–356, 1987. DOI: 10.2534/jjasnaoe1968.1987.343.

[203] M. Itabashi and K. Kawata, 'Carbon content effect on high-strain-rate tensile properties for carbon steels', *International Journal of Impact Engineering*, vol. 24, no. 2, pp. 117–131, 2000. DOI: 10.1016/s0734-743x(99)00050-0.

[204] J. Choung, W. Nam and J.-Y. Lee, 'Dynamic hardening behaviors of various marine structural steels considering dependencies on strain rate and temperature', *Marine Structures*, vol. 32, pp. 49–67, 2013. DOI: 10.1016/j.marstruc.2013.02.001.

[205] D. Forni, B. Chiaia and E. Cadoni, 'Strain rate behaviour in tension of s355 steel: Base for progressive collapse analysis', *Engineering Structures*, vol. 119, pp. 164–173, 2016. DOI: 10.1016/j.engstruct.2016.04.013.

[206] J. Chen, W. Shu and J. Li, 'Constitutive model of Q345 steel at different intermediate strain rates', *International Journal of Steel Structures*, vol. 17, no. 1, pp. 127–137, 2017. DOI: 10.1007/s13296-016-0122-8.

[207] A. A. Alabi, P. L. Moore, L. C. Wrobel, J. C. Campbell and W. He, 'Tensile behaviour of S690QL and S960QL under high strain rate', *Journal of Constructional Steel Research*, vol. 150, pp. 570–580, 2018. DOI: 10.1016/j.jcsr.2018.08.009.

[208] X. Yang, H. Yang and S. Zhang, 'Rate-dependent constitutive models of S690 high-strength structural steel', *Construction and Building Materials*, vol. 198, pp. 597–607, 2019. DOI: 10.1016/j.conbuildmat.2018.11.285.

[209] X. Yang, H. Yang, Z. Lai and S. Zhang, 'Dynamic tensile behavior of S690 high-strength structural steel at intermediate strain rates', *Journal of Constructional Steel Research*, vol. 168, 2020. DOI: 10.1016/j.jcsr.2020.105961.

[210] J.-S. Huo, X. Zeng and H.-T. Wang, 'Tensile behaviour of TMCP Q690D high-strength structural steel at strain rates from 0.00025 to 760 s-1', *Advanced Steel Construction*, vol. 18, no. 1, pp. 488–494, 2022. DOI: 10.18057/IJASC.2022.18.1.7.

[211] J. Dong, M. Elchalakani, D. Li, G. Xiong and B. Yang, 'Dynamic hardening behavior and ductile fracture of high-strength steel at intermediate strain rates', *Journal of Structural Engineering*, vol. 148, no. 9, 2022. DOI: 10.1061/(asce)st.1943-541x.0003416.

[212] A. Needleman, 'Material rate dependence and mesh sensitivity in localization problems', *Computer Methods in Applied Mechanics and Engineering*, vol. 67, no. 1, pp. 69–85, 1988. DOI: 10.1016/0045-7825(88)90069-2.

[213] Y. Bai and T. Wierzbicki, 'A new model of metal plasticity and fracture with pressure and Lode dependence', *International Journal of Plasticity*, vol. 24, no. 6, pp. 1071–1096, 2008. DOI: 10.1016/j.ijplas.2007.09.004.

[214] L. Xue, M. Paredes, A. Nonn and T. Wierzbicki, 'Modeling of crack propagation in defective X100 line pipes', *ASME 2020 39th International Conference on Ocean, Offshore and Arctic Engineering*, vol. Volume 3: Materials Technology, 2020. DOI: 10.1115/omae2020-18048.

[215] C. Sakonder, L. Xue, M. Paredes, R. Savioli and D. F. B. Sarzosa, 'Directional dependence of critical axial strain in X65 pipeline steel subject to combined internal pressure and bending loading', *International Journal of Pressure Vessels and Piping*, vol. 196, 2022. DOI: 10.1016/j.ijpvp.2022.104610.

[216] A. M. Beese, M. Luo, Y. Li, Y. Bai and T. Wierzbicki, 'Partially coupled anisotropic fracture model for aluminum sheets', *Engineering Fracture Mechanics*, vol. 77, no. 7, pp. 1128–1152, 2010. DOI: 10.1016/j.engfracmech.2010.02.024.

[217] M. Dunand and D. Mohr, 'On the predictive capabilities of the shear modified Gurson and the modified Mohr–Coulomb fracture models over a wide range of stress triaxialities and Lode angles', *Journal of the Mechanics and Physics of Solids*, vol. 59, no. 7, pp. 1374–1394, 2011. DOI: 10.1016/j.jmps.2011.04.006.

[218] T. L. Anderson, *Fracture Mechanics: Fundamentals and Applications*, 4th ed. Boca Raton: CRC Press, 2017. DOI: 10.1201/9781315370293.

[219] Y. Bao and T. Wierzbicki, 'On the cut-off value of negative triaxiality for fracture', *Engineering Fracture Mechanics*, vol. 72, no. 7, pp. 1049–1069, 2005. DOI: 10.1016/j.engfracmech.2004.07.011.

[220] B. Tanguy, J. Besson, R. Piques and A. Pineau, 'Ductile to brittle transition of an A508 steel characterized by charpy impact test', *Engineering Fracture Mechanics*, vol. 72, no. 3, pp. 413–434, 2005. DOI: 10.1016/j.engfracmech.2004.03.011.

[221] K.-W. Seo, J.-Y. Kim, Y.-J. Kim and K.-S. Kim, 'Finite element ductile fracture simulation of Charpy and drop weight tear tests for API X52', *Theoretical and Applied Fracture Mechanics*, vol. 133, 2024. DOI: 10.1016/j.tafmec.2024.104629.

[222] G. I. Taylor and H. Quinney, 'The latent energy remaining in a metal after cold working', *Proceedings of the Royal Society of London. Series A, Containing Papers of a Mathematical and Physical Character*, vol. 143, no. 849, pp. 307–326, 1933. DOI: 10.1098/rspa.1934.0004.

[223] J. F. Besseling and E. van der Giessen, *Mathematical Modelling of Inelastic Deformation*. 1994. DOI: 10.1007/978-1-4899-7186-9.

[224] M. A. Meyers, *Dynamic Behavior of Materials*. John Wiley & Sons Inc., 1994. DOI: 10.1002/9780470172278.

[225] M. Liakat and M. M. Khonsari, 'Rapid estimation of fatigue entropy and toughness in metals', *Materials & Design*, vol. 62, pp. 149–157, 2014. DOI: 10.1016/j.matdes.2014.04.086.

[226] S. Dey, T. Borvik, O. S. Hopperstad, J. R. Leinum and M. Langseth, 'The effect of target strength on the perforation of steel plates using three different projectile nose shapes', *International Journal of Impact Engineering*, vol. 30, no. 8-9, pp. 1005–1038, 2004. DOI: 10.1016/j.ijimpeng.2004.06.004.

[227] R. Hill, *The Mathematical Theory of Plasticity*. Oxford: Clarendon Press, 1950.

[228] DS Simulia (Dassault Systèmes Simulia), *ABAQUS 2022. Commercial Finite Element Software.* Computer Program, 2022.

[229] R. de Borst, M. A. Crisfield, J. J. C. Remmers and C. V. Verhoosel, *Nonlinear Finite Element Analysis of Solids and Structures*, 2nd ed. West Sussex, United Kingdom: John Wiley & Sons Ltd, 2012.

[230] H. W. Kuhn and A. W. Tucker, 'Nonlinear programming', *Second Berkeley Symposium on Mathematical Statistics and Probability*, 1951, pp. 481–492.

[231] T. Wierzbicki, Y. Bao, Y.-W. Lee and Y. Bai, 'Calibration and evaluation of seven fracture models', *International Journal of Mechanical Sciences*, vol. 47, no. 4-5, pp. 719–743, 2005. DOI: 10.1016/j.ijmecsci.2005.03.003.

[232] O. Coppejans and C. L. Walters, 'Determination of parameters for the damage mechanics approach to ductile fracture based on a single fracture mechanics test', *ASME 2017 36th International Conference on Ocean, Offshore and Arctic Engineering*, (Trondheim, Norway), OMAE, 2017. DOI: 10.1115/OMAE2017-61425.

[233] H. Xin and M. Veljkovic, 'Evaluation of high strength steels fracture based on uniaxial stress-strain curves', *Engineering Failure Analysis*, vol. 120, 2021. DOI: 10.1016/j.engfailanal.2020.105025.

[234] L. Xue and T. Wierzbicki, 'Numerical simulation of fracture mode transition in ductile plates', *International Journal of Solids and Structures*, vol. 46, no. 6, pp. 1423–1435, 2009. DOI: 10.1016/j.ijsolstr.2008.11.009.

[235] T. F. Morgeneyer and J. Besson, 'Flat to slant ductile fracture transition: Tomography examination and simulations using shear-controlled void nucleation', *Scripta Materialia*, vol. 65, no. 11, pp. 1002–1005, 2011. DOI: 10.1016/j.scriptamat.2011.09.004.

[236] J. Besson, C. N. McCowan and E. S. Drexler, 'Modeling flat to slant fracture transition using the computational cell methodology', *Engineering Fracture Mechanics*, vol. 104, pp. 80–95, 2013. DOI: 10.1016/j.engfracmech.2013.02.032.

[237] IACS (International Association of Classification Societies), *IACS UR W Requirements concerning material and welding*. IACS, 2023.

[238] A. K. Ghosh, 'The influence of strain hardening and strain-rate sensitivity on sheet metal forming', *Journal of Engineering Materials and Technology*, vol. 99, no. 3, pp. 264–274, 1977. DOI: 10.1115/1.3443530.

[239] ISO (International Organization for Standardization), *ISO 14556 Metallic materials - Charpy V-notch pendulum impact test - Instrumented test method*. Geneva: ISO, 2023.

[240] A. Hosseinzadeh, S. H. Hashemi, H. Rastegari and M. R. Maraki, 'Investigation of the notch depth effect on Charpy fracture energy and fracture surface features of API X65 steel', *Canadian Metallurgical Quarterly*, vol. 62, no. 1, pp. 36–48, 2022. DOI: 10.1080/00084433.2022.2066241.

[241] A. Nonn and H. Brauer, 'Establishing the correlation between charpy impact energies for different sized specimens of modern pipeline steels', *Proceedings of the 10th International Pipeline Conference - 2014, Vol 3*, 2014. DOI: 10.1115/IPC2014-33164.

[242] J. Besson, T. T. Luu, B. Tanguy and A. Pineau, 'Anisotropic plastic and damage behavior of a high strength pipeline steel', *The Nineteenth International Offshore and Polar Engineering Conference*, (Osaka, Japan), 2009.

[243] W. Schmitt, I. V. Varfolomeyev and W. Böhme, 'Modelling of the Charpy test as a basis for toughness evaluation', *European Structural Integrity Society*, vol. 30, pp. 45–56, 2002. DOI: 10.1016/S1566-1369(02)80005-X.

[244] ASTM (American Society for Testing and Materials), *E1820 - 23b Standard Test Method for Measurement of Fracture Toughness*. West Conshohocken: ASTM, 2023. DOI: 10.1520/E1820-23B.

[245] A. Bakker, 'Compatible compliance and stress intensity expressions for the standard three-point bend specimen', *Fatigue & Fracture of Engineering Materials & Structures*, vol. 13, no. 2, pp. 145–154, 1990. DOI: 10.1111/j.1460-2695.1990.tb00586.x.

[246] K. Wallin, 'Rotation and bending corrections for the SE(B) specimen', *Materials Performance and Characterization*, vol. 3, no. 3, 2014. DOI: 10.1520/mpc20130031.

[247] M. Paredes, T. Wierzbicki and P. Zelenak, 'Prediction of crack initiation and propagation in X70 pipeline steels', *Engineering Fracture Mechanics*, vol. 168, pp. 92–111, 2016. DOI: 10.1016/j.engfracmech.2016.10.006.

[248] D. F. B. Sarzosa, M. Paredes, R. Savioli, C. Ruggieri, L. G. T. S. Leite, N. S. da Silva and A. G. Garmbis, 'Experimental and numerical study on the ductile fracture response of X65 girth-welded joint made of Inconel 625 alloy', *Theoretical and Applied Fracture Mechanics*, vol. 121, 2022. DOI: 10.1016/j.tafmec.2022.103533.

[249] R. M. McMeeking, 'Finite deformation analysis of crack-tip opening in elastic-plastic materials and implications for fracture', *Journal of the Mechanics and Physics of Solids*, vol. 25, no. 5, pp. 357–381, 1977. DOI: 10.1016/0022-5096(77)90003-5.

[250] J. W. Hutchinson, 'Plastic stress and strain fields at a crack tip', *Journal of the Mechanics and Physics of Solids*, vol. 16, no. 5, pp. 337–342, 1968. DOI: 10.1016/0022-5096(68)90021-5.

[251] A. A. Benzerga, J. Besson, R. Batisse and A. Pineau, 'Synergistic effects of plastic anisotropy and void coalescence on fracture mode in plane strain', *Modelling and Simulation in Materials Science and Engineering*, vol. 10, no. 1, pp. 73–102, 2002. DOI: 10.1088/0965-0393/10/1/306.

[252] H. Li, M. W. Fu, J. Lu and H. Yang, 'Ductile fracture: Experiments and computations', *International Journal of Plasticity*, vol. 27, no. 2, pp. 147–180, 2011. DOI: 10.1016/j.ijplas.2010.04.001.

[253] T. B. Stoughton and J. W. Yoon, 'A new approach for failure criterion for sheet metals', *International Journal of Plasticity*, vol. 27, no. 3, pp. 440–459, 2011. DOI: 10.1016/j.ijplas.2010.07.004.

[254] H. Zhu and X. Zhu, 'A mixed-mode fracture criterion for AHSS cracking prediction at large strain', *SAE International Journal of Materials and Manufacturing*, vol. 4, no. 1, pp. 10–26, 2011. DOI: 10.4271/2011-01-0007.

[255] N. Habibi, A. Ramazani, V. Sundararaghavan and U. Prahl, 'Failure predictions of DP600 steel sheets using various uncoupled fracture criteria', *Engineering Fracture Mechanics*, vol. 190, pp. 367–381, 2018. DOI: 10.1016/j.engfracmech.2017.12.022.

[256] L. M. Ribas, M. L. Gipiela, S. F. Lajarin, R. A. C. Filho and P. V. P. Marcondes, 'Comparative study of six failure criteria via numerical simulation of stamped DP600 steel', *The International Journal of Advanced Manufacturing Technology*, vol. 121, no. 3-4, pp. 2427–2435, 2022. DOI: 10.1007/s00170-022-09440-5.

[257] K. Pack, M. Luo and T. Wierzbicki, 'Sandia fracture challenge: Blind prediction and full calibration to enhance fracture predictability', *International Journal of Fracture*, vol. 186, no. 1-2, pp. 155–175, 2014. DOI: 10.1007/s10704-013-9923-3.

[258] A. Chen, P. Zhang, B. Chen, Y. Li and J. Xing, 'A new ductile fracture model for Q460C high-strength structural steel under monotonic loading: Experimental and numerical investigation', *Engineering Fracture Mechanics*, vol. 288, 2023. DOI: 10.1016/j.engfracmech.2023.109358.

[259] P. Fudlailah and M. Paredes, 'Fracture behavior of X65 Q&T seamless pipeline steel under different strain rates and stress states', *ASME 2020 39th International Conference on Ocean, Offshore and Arctic Engineering*, (Virtual, Online), 2020. DOI: 10.1115/OMAE2020-18032.

[260] M. Algarni, Y. Bai and Y. Choi, 'A study of Inconel 718 dependency on stress triaxiality and Lode angle in plastic deformation and ductile fracture', *Engineering Fracture Mechanics*, vol. 147, pp. 140–157, 2015. DOI: 10.1016/j.engfracmech.2015.08.007.

[261] ASTM (American Society for Testing and Materials), *E8/E8M - 24 Standard Test Methods for Tension Testing of Metallic Materials*. West Conshohocken: ASTM, 2024.

[262] J.-B. Yan, J. Y. R. Liew, M.-H. Zhang and J.-Y. Wang, 'Mechanical properties of normal strength mild steel and high strength steel S690 in low temperature relevant to arctic environment', *Materials & Design*, vol. 61, pp. 150–159, 2014. DOI: 10.1016/j.matdes.2014.04.057.

[263] P. R. Sreenivasan, 'Estimation of quasi-static J–R curves from Charpy energy and adaptation to ASTM E 1921 reference temperature estimation of ferritic steels', *Nuclear Engineering and Design*, vol. 269, pp. 125–129, 2014. DOI: 10.1016/j.nucengdes.2013.08.017.

[264] K. Wallin, 'Critical assessment of the Rolfe-Novak CVN-KIC upper shelf correlation', *Engineering Fracture Mechanics*, vol. 258, 2021. DOI: 10.1016/j.engfracmech.2021.108117.

[265] K. Wallin, 'Proposal for unified rules for selection of Charpy toughness criteria for both low and extra high strength steels. IIW document X-1318-95.', (Stockholm), 1995.

[266] H. F. Li, J. L. Wei, S. P. Yang and Y. Q. Liu, 'The relationship between fracture toughness and tensile property in high-strength steels', *Engineering Failure Analysis*, vol. 131, 2022. DOI: 10.1016/j.engfailanal.2021.105854.

[267] B. Shashank Dutt, M. Nani Babu, V. Ganesan, G. Shanthi and A. Moitra, 'Prediction of fracture resistance from tensile properties and validation with experimental data for 316 type stainless steels', *Journal of Materials Engineering and Performance*, vol. 34, no. 2, pp. 1526–1539, 2025. DOI: 10.1007/s11665-024-09140-z.

[268] J. P. Hirth and F. H. Froes, 'Interrelations between fracture toughness and other mechanical-properties in titanium-alloys', *Metallurgical Transactions a-Physical Metallurgy and Materials Science*, vol. 8, no. 7, pp. 1165–1176, 1977. DOI: 10.1007/Bf02667402.

[269] A. Fabry, E. Walle, R. Chaouadi, J. Wannijn, A. Verstrepen, J. Puzzolante, T. van Ransbeeck and J. van de Velde, 'RPV steel embrittlement: Damage modeling and micro-mechanics in an engineering perspective', *AEA/OECD Specialists Meeting on Irradiation embrittlement and optimisation of annealing*, (Paris), 1993.

[270] R. Chaouadi and A. Fabry, 'On the utilization of the instrumented charpy impact test for characterizing the flow and fracture behavior of reactor pressure vessel steels', *European Structural Integrity Society*, D. François and A. Pineau, Eds. Elsevier, 2002, vol. 30, pp. 103–117. DOI: 10.1016/S1566-1369(02)80011-5.

[271] S. Chatterjee, 'A new coefficient of correlation', *Journal of the American Statistical Association*, vol. 116, no. 536, pp. 2009–2022, 2020. DOI: 10.1080/01621459.2020.1758115.

[272] J. Sherman and W. J. Morrison, 'Adjustment of an inverse matrix corresponding to a change in one element of a given matrix', *The Annals of Mathematical Statistics*, vol. 21, no. 1, pp. 124–127, 1950. DOI: 10.1214/aoms/1177729893.

[273] A. J. Sadowski, W. J. Wong, S. C. S. Li and C. Málaga-Chuquitaype, 'Dataset on the tested and simulated response of thick cold-formed circular hollow sections under cyclic loading', *Data in Brief*, vol. 53, p. 110 122, 2024. DOI: 10.1016/j.dib.2024.110122.

[274] W. J. Wong and C. L. Walters, 'Effect of strain hardening on the bending capacity of high-strength welded I-section beams', *International Conference on Ship and Offshore Structures*, H. Piehl, S. Ehlers and J. K. Paik, Eds., 2022.

[275] W. J. Wong and C. L. Walters, 'Correlation between material certificate data and damage mechanics parameters in the upper-shelf regime for S690Q steels', *The 35th International Ocean and Polar Engineering Conference*, (Seoul, Korea), 2025.

PUBLICATIONS

Journal articles

- *As part of this thesis:*

(1). **W. J. Wong** and C. L. Walters, 'Effect of strain hardening on the rotation capacity of welded I-section high-strength steel beams', *Ships and Offshore Structures*, pp. 1–16, 2023. DOI: 10.1080/17445302.2023.2195727

(2). **W. J. Wong** and C. L. Walters, 'Damage mechanics model for correlating notch toughness in Charpy impact tests with fracture toughness in cracked static fracture tests.', *Engineering Fracture Mechanics*, 2025. DOI: 10.1016/j.engfracmech.2025.111043

(3). **W. J. Wong** and C. L. Walters, 'Damage-mechanics insights into the relationship between upper-shelf Charpy testing and J-integral testing considering varying tensile test properties', Manuscript, 2025

- *Other:*

(4). S. F. P. M. Obers, J. J. Overal, **W. J. Wong** and C. L. Walters, 'The effect of the yield to tensile strength ratio on stress/strain concentrations around holes in high-strength steels', *Marine Structures*, vol. 84, p. 103 205, 2022. DOI: 10.1016/j.marstruc.2022.103205

(5). A. J. Sadowski, **W. J. Wong**, S. C. S. Li and C. Málaga-Chuquitaype, 'Dataset on the tested and simulated response of thick cold-formed circular hollow sections under cyclic loading', *Data in Brief*, vol. 53, p. 110 122, 2024. DOI: 10.1016/j.dib.2024.110122

Conference papers

(6). **W. J. Wong** and C. L. Walters, 'Failure modes and rules related to the yield-to-tensile strength ratio in steel structures', *ASME 2021 40th International Conference on Ocean, Offshore and Arctic Engineering (OMAE)*, (June 21-30, 2021, Virtual, Online), ASME (The American Society of Mechanical Engineers), 2021. DOI: doi.org/10.1115/OMAE2021-61995

(7). **W. J. Wong** and C. L. Walters, 'Effect of strain hardening on the bending capacity of high-strength welded I-section beams', *International Conference on Ship and Offshore Structures*, H. Piehl, S. Ehlers and J. K. Paik, Eds., 2022

(8). **W. J. Wong** and C. L. Walters, 'Effects of strain hardening and the Lode dependence of the fracture strain locus on slant fracture in Charpy V-notch impact testing', *ASME 2024 43rd International Conference on Ocean, Offshore and Arctic Engineering (OMAE)*, (Singapore), ASME (The American Society of Mechanical Engineers), 2024. DOI: 10.1115/OMAE2024-125635

(9). **W. J. Wong** and C. L. Walters, 'Correlation between material certificate data and damage mechanics parameters in the upper-shelf regime for S690Q steels', *The 35th International Ocean and Polar Engineering Conference*, (Seoul, Korea), 2025

ACKNOWLEDGEMENTS

I thank first and foremost my supervisor and promotor Carey Walters, without whom I would not have even started on this PhD. You have been a great teacher, incredibly supportive and kind. Thank you for the abundance of good advice, for your faith in me, for giving me the opportunity to explore and find my way in the research, and for looking out for me.

I also thank my promotor Milan Veljkovic, especially for the guidance and perspective on the project in terms of engineering practicality and with regard to the design standards, which fine-tuned the outcomes to become even more efficient and meaningful.

I am grateful to the HYSt project partners; the bright colleagues from Bureau Veritas, Damen, Huisman, Lloyd's Register and POSCO. Beyond project funding, you have given invaluable technical insight and support. Thank you for the many discussions we have had that made the project interesting, challenging and relevant to the industry.

I would also like to thank Virginia Bertolo, Elise Reinton, Ton Riemslag, Ton Veer and Pascal for helping me get my experiments running and generously sharing your knowledge and resources. Siemen Obers, thank you for the collaborative work and for sparking ideas together which helped me on my way.

Mohammed, Ali and Apostolos, thank you for all the intense and silly conversations, not least those that ended with the conclusion that it was time for a holiday, and for the most illustrious use of our whiteboard for deeply philosophical purposes. I have learned more from you than all the papers that I have read throughout the PhD.

I have been blessed by a multitude of kind, lovely colleagues and friends at the TU, both past and present. In particular, I would like to thank Abdu, Anna, Avery, Bart, Bernat, Cecilia, Esma, Filippo, Gabriele, Hugo, Isabelle, Jacob, Jordi, Fang Pan, Laurens-Jan, Marko, Martin, Nikos, Pengpeng, Romain, Roy, Ruben, Ton, Tzu-Yao, Valentin and Vasu for the many times you have helped me and for sharing part of your journey with me. Annabel, you positively changed my life by introducing me to swing dancing, something I will be forever grateful for. Thank you, Arno and Manuel, both for the many good times we shared and for being there with very practical help.

Ashraf, Yaya, Jun Jie and Adeline, you have been reliable and unassuming support to me throughout. I especially appreciate the kindred perspective you provide here in a context foreign to our origins. With you I could speak in my own language, all connotations conveyed by the slightest intonation. This has been all the therapy I ever need. Thank you too, Sherman, Vivek, Imran, Zhen Cong, Leong, Amira,

Enning, Farhan, Shlagha, Yusuf and Ariana, for bringing a home away-from-home to me.

I am aware of what a blessing it is to have shared a home here with an inspirational, diverse group of lovely people over the past few years: Yee Yonn, Shri, Kesong, Flóra, Katie, Fabienne, Tea, Meadhbh and Tamar. From sharing meals to spending time out and about, to travelling together, to celebrating milestones, to sharing little slices of life, I have learned a little bit about you and even more about myself. Each one of you has motivated and encouraged me more than you might know towards completing the PhD.

My family, my dear Mi and Di, Vanessa, Wei Quan and Aunt Joy, thank you for always being there. I still remember the conversations we had, both when I was considering to start an engineering degree and again when I was considering to start a PhD. Your blessing, support and love then, which were deeply significant, have in hindsight only become even more meaningful, and remain an enduring constant. Thank you for your care and love that radiate from so far away.

Wong Wei Jun
Delft, May 2025

CURRICULUM VITAE

2020–2025	PhD research *on the Ductility at Plastic Localisations in Steel Structures* at Delft University of Technology
2019–2020	Structural engineer at Arup, Kuala Lumpur
2015–2019	Master of Engineering in Civil Engineering at Imperial College London
2014–2015	A-levels at Taylor's College, Subang Jaya
1996	Born in Kuala Lumpur, Malaysia

